UNREINFORCED MASONRY (URM) WALLS RETROFITTED WITH REINFORCED POLYUREA FOR BLAST LOAD PROTECTION

Kelechi Ezekiel

Thesis submitted to the University of Ottawa

in partial fulfillment of the requirements

for the degree of

Doctor of Philosophy

in Civil Engineering

Department of Civil Engineering

Faculty of Engineering

University of Ottawa

March 2025

Abstract

Unreinforced masonry (URM) walls are commonly used in the construction of buildings both as external walls and internal partitions because they are cost-effective and meet many functional building requirements. However, URM walls have low flexural capacity as they are designed to resist gravity loads. This weakness and their brittle nature make them extremely vulnerable to blast loads when exposed to accidentally or intentionally generated shock waves. Consequently, their failure mode could be catastrophic, collapsing quickly and disintegrating into fragments of high-impact velocities capable of causing severe injury and death to occupants and damage to the contents of buildings. Thus, improving the performance of these walls against explosions has become necessary for public safety. As such, this research attempts to provide a possible way of enhancing the wall resistance to blast attacks using reinforced membrane retrofits.

The research has two phases: experimental and analytical. The experimental work involved tests of six URM walls, consisting of four concrete masonry unit (CMU) and two stone walls. The dimensions of each wall were 2 meters by 2 meters, and it was built with 4-inch hollow blocks for the CMU walls and solid concrete stone blocks for the stone walls. The walls were categorized into non-load bearing and load bearing, with two CMUs and one stone wall in each category. Also, they were retrofitted with the combination of two materials: the XS-350 polyurea and SS304 welded 76.2 mm x 76.2 mm stainless-steel wire mesh with either 4.1 mm or 3.1 mm wire diameters.

The retrofitted walls were exposed to blast loads of varying intensity during the tests using a shock tube. The test parameters included the percentage of stainless-steel mesh, type of URM, axial loading, arching action, and pressure-impulse combinations. The results were assessed using dynamic mid-height deflections, failure mode, ductility, load-carrying capacity, and energy absorption capacity. The analytical research involved developing resistance functions and single-degree-of-freedom (SDOF) dynamic inelastic analyses. The SDOF models predicted the dynamic mid-span deflection of the hardened URM walls reasonably well, illustrating the effectiveness of the analysis technique for blast load analysis. A parametric investigation was carried out with varying wall thickness, axial load, aspect ratio, and percentage of steel. Finally, a design procedure was developed for use in engineering practice.

Acknowledgments

First and foremost, I express my profound gratitude to God Almighty for blessing me with life, health, and the resources needed to complete this research.

I am also sincerely grateful to my supervisor, Dr. Murat Saatcioglu, whose exceptional guidance transformed this research into a significant contribution to the engineering practice. His foresight, insight, and financial support turned a simple idea into a remarkable reality.

I am grateful to the technical officers at the structural engineering laboratory, Dr. Gamal Elnabelsya and Dr. Muslim Majeed, for their invaluable support during the experimental tests. Their assistance was instrumental in the successful completion of this project.

I acknowledge the contributions of Ottawa Brick and Stone for supplying the masonry blocks, Gerard Daniel Worldwide for fabricating the 304 stainless-steel meshes, and Line-X Gatineau for expertly applying the polyurea XS-350 to the walls. This program was initiated with funding from the Petroleum Technology Development Fund (PTDF) in Abuja, Nigeria, and further supported by the International and Admission Scholarships from the University of Ottawa. I sincerely appreciate this financial assistance.

Finally, I express my profound love to my wife, Ruth, and my beloved children, Enoch, Amanda, and David, for their unwavering support throughout this journey. Thank you, to my parents and siblings for your encouragement and prayers. I also thank my colleagues and friends, including Osamah, Eshan, Emre, Rasha, Abdul, Sola, and Bita, for their invaluable support and contributions. You are all truly appreciated.

Thank you, God; thank you, Dr. Murat Saatcioglu; and congratulations to me. Peace.

Notations

M_e = equivalent mass of the SDOF
C_e = equivalent damping coefficient of the SDOF
K_e = equivalent stiffness of the SDOF
F_e = equivalent force acting on the wall
F_e (t) = equivalent load-time history applied to the SDOF
K_M = mass factor
K_L= load factor
F_h = uniform load
R_e = Resistance of the element
K_{LM} = ratio of the mass factor to the load factor
$\varphi(x)$ = displacement shape function
w = uniform load
Z = Displacement
$\dot{Z}$ = Velocity
$\ddot{Z}$ = acceleration
h = height of the wall
T = period
H = Horizontal reaction
R = Internal vertical reaction
p = lateral pressure
P = vertical support reaction
Δ = lateral deflection at wall center
y = crack depth through the thickness
α = degree of fixity at the supports
t = thickness of wall
W_i = weight of wall
E_C = Elastic modulus of concrete masonry
I_g = Uncracked gross moment of inertia
Δ_{cr} = deflection at the onset of cracking
Δ_{crG} = deflection as crack grows
β = curvature ratio
a = width of arching compression region
R = summation of the compressive forces in the wall
V_{Top} = arching force exerted at the top support
x = distance from the wall centerline to R
s = length of the parabolic formed shape
Δ = deflection
A = anchorage force
T= resultant axial force/membrane force
P_D = driver pressure
L_D = driver length of the shock tube
P_r = reflected pressure and the

t_d = positive phase duration
I_r = reflected impulse
d_{max} = maximum deflection
d_{res} = residual deflection
θ_{max} = maximum angle of rotation
P_o = ambient pressure
P_{so} = incident pressure
P_{re} = reflected pressure
t_A = arrival time
t_e = positive phase duration
P_{SO}^- = peak negative value incident pressure
P_{re}^- = peak negative value, reflected pressure
SS= stainless steel
t_e^- = negative phase duration

Acronyms

AFRL = Air Force Research Laboratory
ANFO = Ammonium Nitrate Fuel Oil
CFRP = carbon fiber reinforced polymer
CMU = concrete masonry unit
DAS = Data Acquisition System
DBT= Design Basis Threat
DOF = degrees of freedom
FE = Finite Element
LAM = Linear Acceleration Method
LOP= Levels of Protection
LVDT = Linear Variable Displacement Transducers
NPREM= nanoparticle reinforced elastic materials
NRC = National Research Council
POSS = reinforced polyurea and polyhedral oligomeric silsesquioxanes
PVC = polyvinyl chloride
SDOF = single degree of freedom
SFRS = steel fiber-reinforced shotcrete
SMRS = steel mesh-reinforced shotcrete
SS304 =stainless steel 304
URM = unreinforced masonry

Table of Contents

List of Figures

List of Tables

CHAPTER 1. INTRODUCTION

1.1 Background

Unreinforced masonry (URM) walls constitute a significant portion of the construction of buildings worldwide. They are cost-effective, durable, aesthetically pleasing with sound control, insulated against temperature fluctuations, and provide excellent fire resistance. URM is typically made of bricks, hollow clay tiles, stones, concrete blocks, calcium silicate, or adobe. URM walls are primarily designed to resist gravity loads with little or no provision for lateral loads. Thus, they are frequently used as load-bearing elements or infills and veneers in domestic and framed construction. Unreinforced masonry has great resistance to compressive loads but performs poorly to loads causing tensile stresses, like seismic and blast loads, as they are heavy brittle materials with low tensile strength, exhibiting little out-of-plane resistance when subjected to out-of-plane horizontal forces, as shown in Figure 1.1.

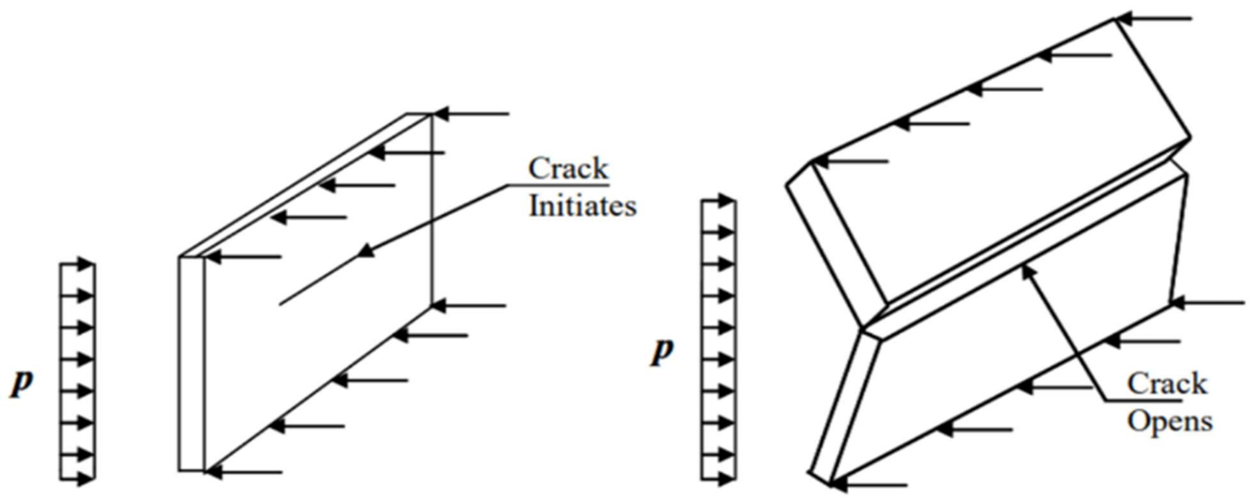

Figure 1.1. URM subjected to blast load (Moradi et al. 2011)

Many infrastructures, ancient buildings, and monuments of national, economic, and historic importance were built long ago with mostly URM. In Canada, for instance, these buildings will include government facilities like the Federal Parliament Building, Ontario Legislature

Building, Quebec Legislature Building, British Columbia Legislature, and Victoria Museum of Nature (Abass 2013). Newer buildings such as embassies, schools, churches, theatres, and shopping malls might not be internally partitioned using URM walls due to the development of more convenient wall systems; however, their facades are mainly constructed using URM walls.

The recent increase in bombings with explosives made from readily available and cheap materials (for instance, the monetary value of the bomb that struck the World Trade Center in 1993 was less than $400) accounts for 46% of all terrorist attacks (National Research Council (NRC) 1995, Thornburg 2004, Gagnet 2013) perpetrated by radical groups and political separatists around the world, which have placed these facilities of great societal relevance to high risk as they are frequent targets of these malicious threats. Generally, modern terrorism tends to cause the most unexpected physical damage to structures and psychological trauma or even death to people in their path. At the same time, accidental explosions could also similarly impact infrastructures and persons.

The Alfred P. Murrah Federal Building in Oklahoma City was subjected to a terrorist truck bombing on April 19, 1995 (Terrorism 2004). The truck was loaded with explosives equivalent to 5000 Ibs (2300kg) of TNT and was parked by the building's front view. The detonation that followed led to a partial collapse of more than one-third of the building, which killed 168 people and left almost a thousand injured (Oklahoma 1996). About 324 other buildings were damaged or destroyed within a 16-block radius, spontaneous glass breakages were experienced in 258 nearby buildings, and a 9.0 m wide by 2.4 m deep crater was created in front of the building. Also, a 22-story high apartment block called Ronan Point Tower, built in Canning Town in Newham, East London, in May 1968, had a gas explosion and blew out some load-bearing walls. This event led to the collapse of one entire corner of the building and left 4 people dead and injured 17. Furthermore, attacks on the Twin Towers at the World Trade Center in New York City and Pentagon in Washington, DC, in September 2001, the London Subway bombing in 2005, and the foiled attempt of 'Toronto 18" targeted at three distinct locations of southern Ontario on Canadian soil in the year 2006 has triggered the consciousness to protect our infrastructures against unexpected attacks or explosions actively.

Different perimeter security like stand-offs, walls and fences, natural barriers (berms, gullies, boulders, trees), and man-made barriers (benches, planters, bollards, Jersey) have been designed to protect exterior walls of buildings from bomb blasts. Although all these perimeter securities are adequate, a security breach could make pedestrian gates and vehicular gates made as exit and entry points to vicinities vulnerable pathways to convey improvised explosive devices. Often, bombs had been concealed and delivered in vehicles, packages, and even on foot. Therefore, the low resistance of URM to blast loads and the vulnerability of perimeter security to adequately protect the building's exterior and interior walls raise the need to develop other suitable blast protection measures.

1.2 Research Needs

With their low flexural capacity and brittle failure mode, masonry walls are susceptible to shock waves caused by explosions. Intentional bombings and accidental explosions generate shock waves that induce extreme tensile stresses on URM structures, flexing them beyond their elastic limit, resulting in fragmentation of great velocities (Davidson 2011, Bazhenov et al. 2012, Aghdamy et al. 2013). Most existing and newer buildings are not built to withstand blast loads, as building codes for ordinary structures have no provisions for blast loads. Since demolishing and rebuilding blast-deficient URM buildings is not feasible, their blast resistance is ensured by applying appropriate retrofitting (hardening) techniques.

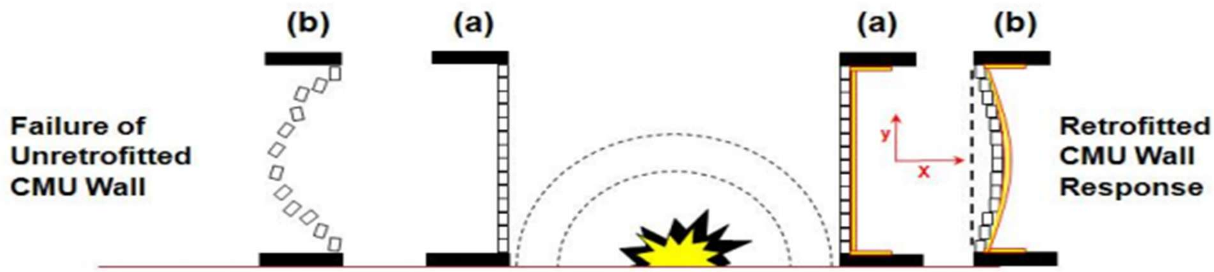

Figure 1.2. Unretrofitted and retrofitted CMU walls responses to blast load. (a) Each wall before the blast load. (b) Each wall's response to blast load (Johnson 2013)

Figure 1.2 schematically depicts unretrofitted and retrofitted CMU walls. Historically, the conventional retrofitting method, commonly known as blast hardening, involved adding steel or concrete elements on the protected side. However, this was found to be time-consuming, expensive, and difficult to apply with limited control of fragmentation, as these techniques primarily focus on overall strength improvement (Johnson 2013). Consequently, effective alternative materials are being sought and investigated in recent times.

The efficacy of URM hardening methods focuses on strengthening the out-of-plane capacity of wall elements as well as reducing or eliminating fragmentation. Some of the techniques used in practice include the application of unreinforced elastomers such as spray-on and trowel-on polyurea, reinforced elastomers such as nanoparticle reinforced polymer (having glass, carbon, or aramid fibers), reinforced polyurea, steel sheets and fiber reinforced polymer (FRP) plating (Knox et al. 2000, Davidson, El-Domiaty et al. 2002, Johnson, et al. 2004, Ciornei 2012). FRP provides sound strengthening systems and increases the flexural capacity of masonry substrate. However, studies have shown that in some circumstances, the excessively thin sheets of FRP require an impracticable number of layers on structural members to function acceptably. Also, the FRP retrofits lack proper shear capacity and wall-to-frame connections. Further, they exhibit debonding easily and suffer tensile rupturing, which might lead to premature brittle failure under high-intensity blast loads (Myers et al. 2004, Lunn et al. 2013). An investigation into the performance of spray-on polyurea on URM walls as a blast-resistant material has shown that the elastomer exhibits excellent adhesion to the walls and forms a seamless, monolithic, tough elastic membrane. Polyurea coated to a thickness range of 3 mm to 6 mm on walls can resist a peak pressure of about 450kPa (65 psi) in one application but also suffers extensive debonding and tearing that allow the escape of debris, especially at the middle height of the wall (Davidson and Moradi 2004, Davidson et al. 2005, Ciornei 2012). This implies that searching for the most suitable material or combinations for blast mitigation is ongoing. Researchers like Johnson et al. (2004), Aghdamy et al. (2013), and Ciornei (2012) were driven by this passion for reinforcing polyurea further to increase its overall material performance. Their results suggested that the reinforced elastomer significantly increases the ultimate flexural resistance of walls compared to their unreinforced counterparts, depending on the strength and orientation of reinforcement. However, limited work has been done in this area. The hazard mitigation research group at the University of Ottawa has been looking at developing a new type of reinforced polyurea using stainless-steel mesh to significantly enhance the flexibility and resilience of masonry wall systems and mitigate debonding and tearing of the polyurea under intense blast pressures. The current research forms a new phase of an ongoing project at the University of Ottawa involving the use of stainless steel and polyurea to harden URM walls. The materials used in this research project include SS304 stainless steel and XS-350 polyurea.

1.3 Objective

The objective of the current research project is to develop a blast hardening/retrofit technology for unreinforced masonry (URM) walls which involves stainless steel welded wire fabric and spray-on polyurea. The objective also includes developing a design procedure for the technology using experimental and analytical research for use in engineering practice.

1.4 Scope

The scope of research consists of four primary parts:

1. Background study, concepts, and literature review on past experimental and analytical approaches on related retrofitting techniques.
2. An experimental program to determine the performance of reinforced polyurea. This includes the construction of six URM walls: three non-load bearing and three load-bearing walls with the application of axial load. Three of the walls were retrofitted with 3.1mm diameter SS304 mesh reinforcement and polyurea (reinforced polyurea-3.1 mm) while the remaining three were retrofitted with 4.1mm diameter SS304 mesh in combination with polyurea (reinforced polyurea-4.1 mm). Blast loading was simulated using the University of Ottawa Shock Tube Facility. In addition, material tests were conducted to establish the properties of CMU, stone masonry, stainless steel mesh, and XS-350 polyurea.
3. Resistance function development for use in single degree of freedom (SDOF) dynamic analysis of walls. Dynamic analysis was conducted to validate the models against experimental results, followed by an analytical parametric investigation.
4. Development of design procedure to be used in engineering practices.

1.5 Thesis Organization

This thesis is organized into seven chapters.

Chapter 1-Introduction

- Introduction to the background, identification of research needs, objective, and scope of research.

Chapter 2-Literature review

- Focuses on the concepts and literature review of previous work done.

Chapter 3-Experimental program

- Description of the experimental program, test setup, test specimens, testing protocols, instrumentation, and material testing.

Chapter 4-Experiment results

- Description of the behavior of test specimens and observed behavior.

Chapter 5-Experimental results discussion

- Analyses and discussions of experiment results.

Chapter 6-Analytical program

- Development of resistant functions.
- Development and validation of Single Degree of Freedom (SDOF) models.
- Parametric study.
- Development of design procedure.

Chapter 7-Conclusion

- Summary, conclusions, and recommendations.

CHAPTER 2. LITERATURE REVIEW

2.1 General

The subject of masonry resistance to blast loading has been a research interest in many research groups for several decades, and its relevance cannot be overemphasized. Recently, efforts have been made to improve its blast resistance further using easy-to-install retrofit materials. To elaborate, this chapter presents insight into explosion and blast load concepts, a brief history of masonry, and its different classifications. Also, it describes the relevant retrofit materials used in this research and provides technical information on previous works on masonry blast resistance.

2.2 Explosion and Blast Load Concept

An explosion is a very fast chemical reaction accompanied by rapid and sudden release of hot gases and energy (Stone and Engebretsen 2001). Its source could be solid, liquid, or gas (Ngo et al. 2007), and when they detonate, they explode, discharging heat and producing gases under very high temperatures and pressures in milliseconds. As the hot, dense gases produced expand outward from the blast's center, so does the air around the explosion, and its molecules build up, traveling in radial directions faster than the speed of sound, resulting in what can be called a *blast load*. The intensity of the blast load on the structures along its path would depend on the type and quantity of explosives used, the angle of incidence, and the stand-off distance, which is simply the distance between the structure and the point of detonation. A simple and typical pressure-time history for a free air blast wave when it reaches a structure at a certain distance from the center of detonation can be seen in Figure 2.1.

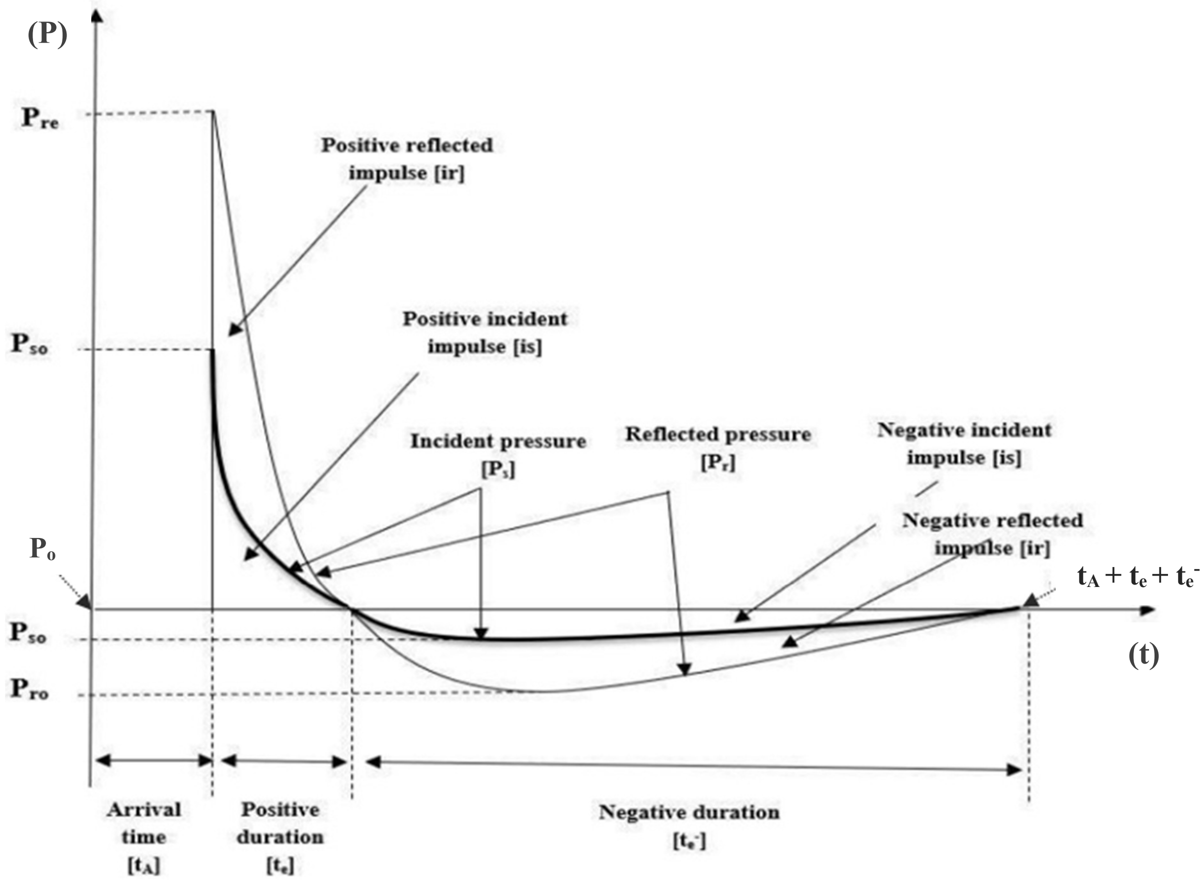

Figure 2.1. Blast phenomena (Dinesh et al. 2020)

Pressure (P) in Figure 2.1 is represented on the y-axis, and time duration (t) is plotted on the x-axis. The ambient pressure P_o is the initial pressure surrounding the structure before the arrival of the shock front (blast load), and it is used as a reference pressure for the positive and negative pressure values. After an explosion, an abrupt increase in pressure to peak values occurs. This in-air pressure is referred to as incident pressure, P_{so}. Upon interaction with an object, the incident pressure reflects on the object while generating increased reflected pressure, P_{re}. The incident and reflected blast wavefronts reach the target element at an arrival time t_A. The time required for the pressure to rise to its peak value is usually minimal and considered zero for design. The peak pressure is also known as the peak overpressure. The shock front results in side-on overpressure along the sides and the roof of a building. The side-on pressure is equal to the incident pressure if the building does not have protruding objects to cause reflection. As the distance from the detonation center increases, the shock velocity decreases with exponentially decaying pressure until it reaches the atmospheric pressure, P_o, at time t_A+t_e, where t_e is the positive phase duration. The duration of pressure is usually very small, measured in milliseconds. The pressure drops further into the negative phase until it reaches the peak negative value, P_{SO}^- and P_{re}^-, then finally restores itself to the ambient pressure. The negative phase has a longer duration of t_e^-. During this phase, suction forces are exerted on the structure, which explains why broken pieces of glass particles from failed facades are found outside of the building instead of inside during the blast loadings.

The area of the positive-phase duration under the curve gives the impulse, which dictates the amount of energy transmitted to the structure during the blast event. The explosion takes many parts of the structure beyond their elastic limits into the plastic loading region. Thus, structural members must be designed to undergo permanent plastic deformations, and the measures should be kept within the deflection tolerances while effectively withstanding the energy of a given shock wavefront (Dinan 2005, Fitzmaurice 2006). This indicates that considering the non-linear response of materials under dynamic blast loading is of utmost importance. Another factor that may influence the capacity of a member is the high strain rates imposed on the material subjected to blast shock waves. Typically, blast loads generate strain rates between 10^2 - 10^4 s^{-1}, while materials are often subjected to ordinary strain rates of 10^{-6} – 10^{-5} s^{-1} under quasi-static loads, as shown in Figure 2.2.

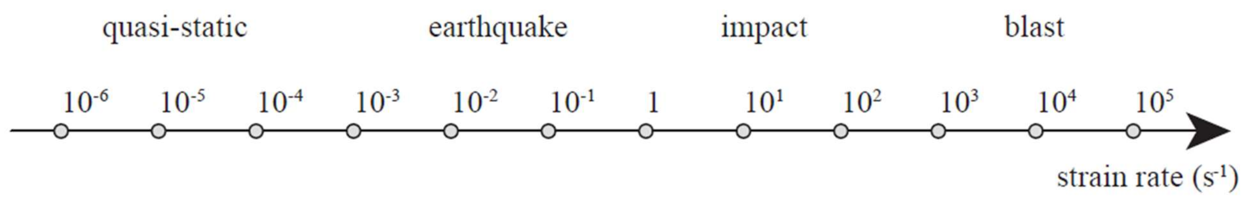

Figure 2.2. Strain rates associated with different types of loading (Godio et al. 2021)

2.3 Masonry Units

Masonry is a term used to describe the laying and bonding together of individual units with mortar to form a masonry structure. These units, called masonry units, could be clay brick, concrete brick or block, calcium silicate, mudbrick (Adobe), glass brick, cast stone, or natural stones like granite, marble, sandstone, and limestone.

Masonry units were first used as construction materials from dried mud thousands of years ago in Mesopotamia. Stone masonry and fired clay bricks started as far back as 10,000 BC and 3000 BC, respectively. Then, in the late 19th century, the rapid production of calcium silicate units on an industrial scale became possible through pressurized steam developed in Germany in 1894. Concrete masonry units also came into play in the mid-1800s with the invention of Portland cement (Drysdale and Hamid 2005).

These materials have many advantages that have made them relevant to date in the construction industry worldwide. These include their versatile functionality, which provides weather protection, thermal and sound insulation, and fire protection; durability, which keeps them serviceable for many decades and centuries; strength, ease of construction, cost-effectiveness, and low maintenance.

2.3.1 Types and Classifications of Masonry Walls

There are three types of masonry walls: unreinforced, reinforced, and prestressed masonry. Unreinforced masonry, or plain masonry, is constructed with no steel reinforcement other than light mortar joint reinforcement for tying and shrinkage crack control. They are used in low-rise and medium-rise buildings. Reinforced masonry is constructed with steel reinforcement incorporated into the units to increase tensile and shear strength and improve ductility. In prestressed masonry, high-strength steel rods are inserted centrally into the masonry and tightened against end plates to uniformly induce compressive stresses on the wall. This approach is sometimes preferable to reinforcing the masonry.

There are two significant classifications of masonry walls in terms of bearing conditions. The first is the *load-bearing walls*. They are part of the structural member of a building, supporting and transferring loads, including their weight from one structural member to another. They are primarily exterior walls resisting wind and seismic loads and sometimes could be used as interior walls. They often run perpendicular to ceiling joists supporting them at their ends and as internal walls supporting slabs/floor joists. The properties of masonry units and mortar are essential in correctly estimating the load-bearing capacity of the wall. The second is non-load bearing walls. They are partition walls or dividers that divide a building's internal space into rooms. They do not support or distribute any load but contribute their own weight to loads of structural members and are, as such, non-structural members. They often appear as infill panels within structural frames. They help with the arrangement and functionality of a space.

2.3.2 Historic Stone Masonry

Historic stone masonry is another type of masonry construction. Many landmark buildings of socio-economic importance in Canada are constructed with load-bearing or non-load bearing stone or brick masonry. These buildings have heritage value, political importance, or cultural significance to Canadians. They give a picture of past events and create awareness of the present realities and reasons to prepare for a better society (Lefebvre 2009, ASTM 2012). Examples of some of these buildings include but are not limited to the Federal Parliament Buildings, Quebec Legislature Building, British Columbia Legislature Building, and Ontario Legislature Building. The risk factor of these buildings could be high if exposed to terrorist bombings, as they were built many years ago when there were no provisions for blast-resistant design. However, efforts are being made to protect and preserve these buildings' integrity through retrofitting/hardening. Generally, the construction of these historic stone masonry walls was not uniform. They were built purely from acquiring experience from several years of practice, rules-of-thumb, transfer of knowledge, and skills of master artisan to apprentice when there were no building regulations. In constructing historic masonry walls, the coursing of blocks (stone or brick) could be a wet or dry layup. The wet layup has coursing of stone or brick units held together by mortar beds. The mortar helps fill up voids and distribute compressive pressure in the layup. The dry layup, on the other hand, has no mortar between successive courses and brick units. The direct surface interaction between adjacent courses generates stresses that reduce the compressive strength of the wall when compared to its wet layup counterpart (Felice 2011). Usually, the block coursing is laid as single-wythe or double-wythe with or without rubble core infill. The stone and mortar are two essential constituents of historic stone masonry. Their properties and the method of construction employed would significantly affect the behavior and mechanical properties of the masonry structure. The mechanical properties of stone and brick can be obtained from test samples taken from buildings, but it might not be easy to get an appreciable size of mortar samples for testing.

2.3.3 Concrete Masonry Unit

A concrete masonry unit (CMU), also referred to as a concrete block, is a rectangular block made from cast concrete. Its solid content identifies CMU as hollow, semi-solid, or full solid. These three identifications of CMU are well-defined by the CSA A165.1 standard and the related CSA masonry standards. The percentage difference between their net cross-sections and gross cross-sections differentiates them. A hollow unit has a net cross-section of over 25% less than its gross cross-section measured in the same plane. Also, a semi-solid unit has hollow cores that reduce its net cross-section by at least 25% of its gross cross-section measured in the same plane. Furthermore, a full solid unit has a net cross-section equal to its gross cross-section measured in the same plane.

CMU is specified based on its nominal dimensions rather than its actual dimensions (manufactured dimensions). The nominal dimension is the actual dimension plus the mortar joint's width (by standard 10mm). The standard nominal widths are available in 100, 150, 200, 250, and 300 mm. The typical nominal heights are 200 mm and 100 mm. The standard nominal lengths are 400 mm and 200 mm, respectively.

Based on density, CMUs can be classified into lightweight, medium, and normal-weight units. The light-weight units have a unit weight of less than 1680 kg/m^3 with water absorption of 288 kg/m^3 and are made from light-weight aggregates like pumice, scoria, and cinders. The medium-weight unit has a unit weight between 1680-2000 kg/m^3. The normal-weight unit has a unit weight of 2000 kg/m^3 and above, with 208 kg/m^3 water absorption, made from well-graded sand, gravel, or crushed stones.

2.4 Failure Mechanisms in Unreinforced Masonry

URM walls' behavior and failure mechanisms can be viewed in two categories: in-plane and out-of-plane failures. The in-plane failure mechanism is further classified into four modes: diagonal tension (shear), sliding shear, rocking, and toe crushing. These responses are affected by vertical (axial) stresses, shear stresses, the wall aspect ratio, and the compressive strength of the masonry unit (Lee et al. 2008). *Diagonal shear failure* occurs when the principal tensile stresses that develop in the wall exceed its diagonal tensile strength. These stresses are developed under simultaneous vertical and horizontal load applications. The resultant effect of these stresses is a diagonal split in the wall with an appreciable loss in strength and stiffness (Tomazevic 2008, Salmanpour et al. 2012). The *sliding shear failure* involves the wall shearing into two parts with the formation of a horizontal crack. The upper part of the masonry unit slides onto its lower part as the shear stresses generated exceed its direct shear strength. This could happen when a wall subjected to seismic forces is built with poor mortar quality and subjected to low vertical loads. This failure is very stable with high energy dissipation and displacement capacity (Salmanpour et al. 2012). The rocking failure occurs on slender walls (high moment/shear ratio). The wall is seen to tilt as the horizontal force increases and wide flexural cracks are seen at the top and bottom of the wall. The compressed zone carries the shear, and the wall crushes in the compression zone as the horizontal force increases. This is called toe-crushing (Panto et al. 2015).

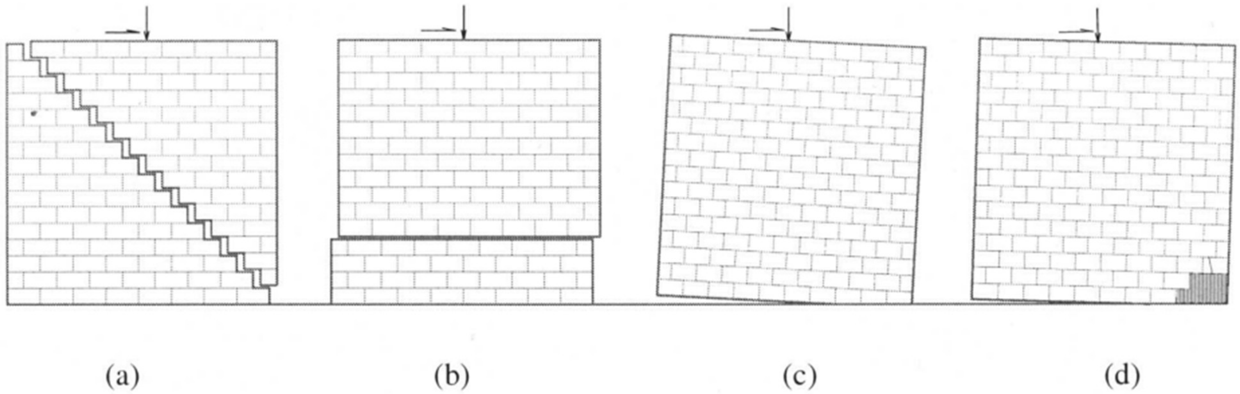

Figure 2.3. In-plane failure mechanisms of a URM wall: (a) shear failure, (b) sliding failure, (c) rocking failure, and (d) toe crushing

The out-of-plane failure of the URM wall under lateral blast loads is well described in Davidson et al. (2005). In their research, seven explosive tests were conducted that involved a total of 12 polymer-reinforced masonry walls. Some wall panels were coated on both sides; some were only coated on the interior part, while others were not coated (control walls). Some walls were constructed with window and door openings; some were built without mortar and with polymer reinforcement isolated from the block (i.e., no bond) with a plastic membrane on the interior face. The overlap of the polymer with the support varied between 15cm and 30cm. The walls were constructed following standard practices and materials by masonry contractors. Also, the top and bottom of the walls were restrained laterally, but movements were allowed along their vertical edges, enabling one-way flexural response. The blast test on these wall panels presented an overview of the failure mechanism on the various retrofitted walls. Static analysis methods like traditional beam and yield line cannot analyze loading from blast reflective pressure as the wall components fracture and its overall geometry break down. Also, predicting polymer retrofitted wall resistance to lateral blast pressure can be challenging as certain factors like variability in mortar joint flexural bond strength, inconsistencies in polymer thickness, continuity over surface irregularities, and fracture of the front face shell of the masonry blocks in early stages of the response needed to be considered. A common failure mechanism was consistently observed in front face fracture, which involves breaking the face shell into several pieces or shearing from the webs and falling as one piece. This failure was notably observed near the supports because of the high stress generated at these points. Figure 2.4 shows the failure modes. Arching, a compression membrane action of the front side of the wall, developed as flexural stresses caused by the blast, contributed to the front face fracture. Another critical failure mechanism was the mortar joint separation due to bond, flexure, or shear failure.

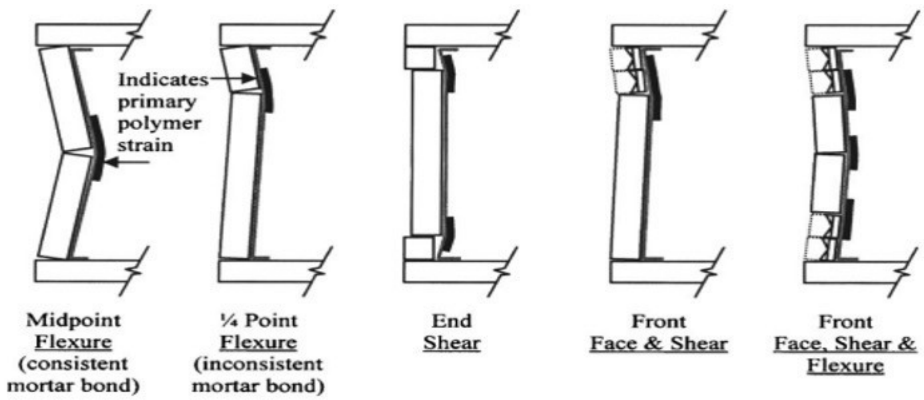

Figure 2.4. Observed failure mechanisms in URM walls exposed to blast test (Davidson et al. 2005)

The post-test analysis revealed that these two failure mechanisms were responsible for the loss of structural integrity. Shear distress developed in the polymer coating at rough block edges and the polymer was torn sooner in these situations than in those predominantly subjected to tension.

2.5 Relevant Codes and Standards for Masonry Structures

Some of the relevant Canadian codes and standards for masonry structures are CSA S304-14 (R2019), CSA A370-14 (R2023), CSA A371-14 (R2024), CSA A82-14 (R2023), CSA A165 SERIES-14 (R2024), CAN/CSA A179-14 (R2024), CAN/CSA-B354.1-04(R2016), CSA S850-23.

2.5.1 Design Standards

CSA A304-14 (R2019) Design of masonry structures: This standard makes provisions for the structural design of all engineered masonry structures and components. It recommends limit states design methods for their design by the National Building Code of Canada (NBCC) requirements. Additionally, it allows an empirical design approach for unreinforced masonry (Korany 2010).

CSA A370-14 (R2023) Connectors for masonry: This standard provides minimum requirements for the design of masonry connectors in the form of ties, anchors, fasteners, and repair connectors used to interconnect the wythes of a masonry wall or attach masonry veneer to its structural backing. Furthermore, these connectors may connect masonry walls to intersecting walls or other structural members and attach the stone to its structural support or interconnect stone. They can also be used to secure a masonry tie or anchor to a structural member, interconnect components of a multi-component tie or anchor, and restore or improve masonry construction.

2.5.2 Construction Standards

CSA A371-14 (R2024) Masonry construction for buildings: This prescriptive standard ensures that the safety and serviceability requirements of all types of masonry construction are met and that they follow CSA S304 and CSA A370 provisions. It is mainly directed at masonry contractors.

2.5.3 Material Standards

CSA A82-14 (R2023) Fired masonry brick made from clay or shale: This Standard specifies provisions for brick made from fired clay or shale to be used as structural and facing components in masonry. It includes testing and other requirements on freeze-thaw durability, finish, texture, color, compressive strength, absorption, efflorescence, size, warpage, and out-of-square.

CSA A165 SERIES-14 (R2024) CSA Standards on concrete masonry units: This series consists of three Standards.

(a) CSA A165.1 covers concrete block masonry units suitable for load-bearing and non-load-bearing applications.

(b) CSA A165.2 covers both hollow and solid concrete brick units. Solid units are suitable for load-bearing and non-load bearing applications, whereas hollow units are limited to non-load bearing applications.

(c) CSA A165.3 covers the properties of masonry units prefaced during manufacturing.

CAN/CSA A179-14 (R2024) Mortar and grout for unit masonry: This standard outline the requirements for mortar used in bedding, jointing, and bonding masonry units, as well as grout for filling core, cell, or cavity spaces in unit masonry construction.

2.5.4 Other Relevant Codes and Standards

CAN/CSA-B354.1-04 (R2016) Portable Elevating Work Platforms: This Standard specifies minimum requirements for portable, integral frameworks of aerial platforms with bases that cannot be driven or moved horizontally while the platform is elevated.

CSA S850-23 Design, and assessment of buildings subjected to blast loads: This Standard specifies minimum requirements for analyzing, designing, and assessing buildings to resist blast loading to protect human lives and reduce property damages.

2.6 Arching Action in Unreinforced Masonry

Arching action is an effective way of improving the lateral resistance of URM walls against blast loads. This action introduces compressive force on the wall within a restraining rigid frame after it cracks. McDowell et al. (1956) stated from their work that when a one-way URM wall is built within a rigid frame and subjected to out-of-plane loads, the tensile stresses generated would cause the wall to crack at its mid-height and along its supports. The cracks initiated at its mid-height divide the wall into two equal parts, and the two identical segments rotate about their supports, developing coupled forces that provide additional resistance. Accordingly, it was observed that the wall could fail in either of the two ways once the coupled forces diminish: snapping at the center or crushing completely of the masonry at the support. From their investigation, it could be stated that arching action would increase the load-bearing capacity of the wall up to six times that of a plain CMU wall with the positive effect of reduced deflection at the mid-span. Consequently, when the wall collapses, it will be two rigid sections with no ejection of fragments of high velocities. Over the years, many researchers have tested and validated this phenomenon using experiments, analysis, and numerical approaches.

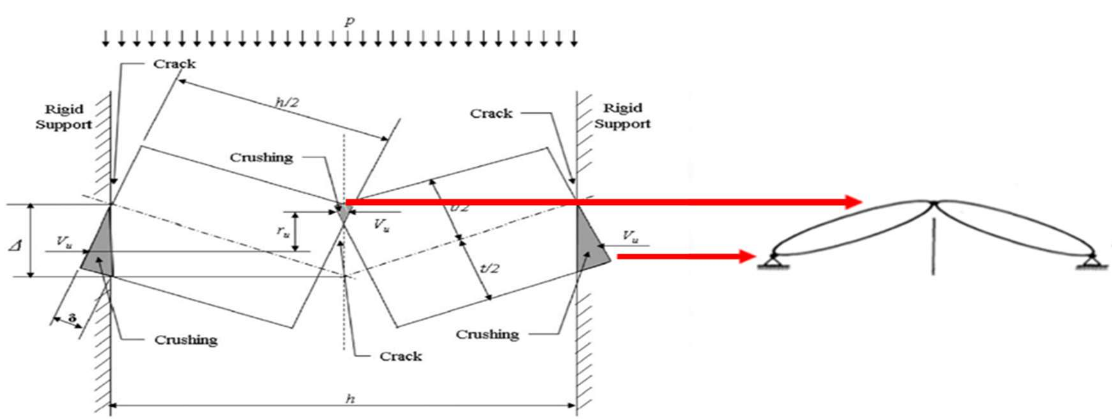

Figure 2.5. Arching action (McDowell et al. 1956, Abou-Zeid et al. 2011, Moradi et al. 2008)

Abou-Zeid et al. (2011) examined the effect of arching action on the resistance of masonry walls to blast loading. Two walls with a width of 990 mm and height of 2190 mm were constructed using standard 190 mm two-cell concrete blocks and Type-S mortar of 10 mm thickness. The walls were built to have tight contact with their top and bottom hollow steel rigid frames to enhance the arching action, and no restraints at the sides to allow one-way bending. The test was carried out on the walls using live explosives (surface burst detonated at ground level) of varied charge weights between 15 kg and 250 kg of Ammonium Nitrate Fuel Oil (ANFO) with stand-off distances between 3.0 m and 20 m. The first wall, W1, was exposed to six shots, and the second wall, W2, was subjected to three shots. The shots were applied in an increasingly successive manner until failure. W1 and W2 walls absorbed peak pressures of 174 kPa and 500 kPa and displayed maximum mid-displacements of 34 mm and 69 mm at standoff distances of 17.0 m, respectively. Therefore, providing rigid support and close contact of the walls to the supports could yield a membrane thrust force (arching action), significantly contributing to the wall's resistance against the blast loads.

Gagnet et al. (2017) studied the effect of arching and non-arching supports on masonry walls when exposed to blast loads. Four test walls of exact dimensions, 3.05 m high and 200 mm thick, were constructed for this experiment. Walls 1 and 3 had arching support, while Walls 2 and 4 had non-arching support. The walls were all exposed to the same intensity of explosive weight of exact standoff distance without the intent of collapsing them. The results revealed that walls with arching support had reduced peak displacements by over 2 times less than those with non-arching action.

2.7 Polyurea

In recent times, the elastomeric-thermoset polyurea, used as a protective coating in many industrial applications, has been increasing in relevance in the field of construction, especially in the aspect of making structures stronger and safer for occupants against blast impact, ballistics, and other impact loadings. The polyurea elastomer is a product of the rapid chemical reaction of two components, isocyanate, and polyamine, mixed by a pneumatic device in their appropriate ratio under controlled high temperature and high pressure. The polyurea is a chain structure with "n" molecules strongly bonded together, which accounts for the material's high-rate energy absorption, dissipation without permanent damage, durability, ductility, tensile strength, tensile stiffness, impact resistance, and other extraordinary properties that provide the retrofitting and strengthening capabilities when applied to new and existing structures.

2.7.1 Rate-Dependent Stress-Strain Behavior of Polyurea

The polyurea is exposed to a wide range of loading rates as a protective coating. Its dynamic mechanical behavior at different strain rates has interested many researchers. By using a universal testing machine and Split-Hopkinson pressure bar (SHPB), Yi et al. (2005) examined polyurea in both the quasi-static (< 1 s^{-1}) and high strain rate regimes (10^3 to 10^4 s^{-1}). The researchers discovered that polyurea displayed rubbery behavior at low strain rates and leathery or glassy-like behavior at very high rates. However, polymeric pressure bars of polymethylmethacrylate (PMMA) and hollow aluminum transmission bars give better high strain rate characterization of polyurea than SHPB as it could give erroneous results due to the low impedance of polyurea (Iqbal et al. 2016). Sarva et al. (2007) also studied the transition of polyurea's mechanical behavior. They used equipment like Yi et al. (2005) and considered a strain rate as low as ~0.001 s^{-1} and a very high rate as much as~5000 s^{-1}, and they came to a similar result as Yi et al. Further, Zhao et al. (2007) found that within total strains less than 3% and strain rate as high as 10^3 s^{-1} using the Time-Temperature Superposition principle, the dynamic behavior of polyurea could be modeled from the constitutive data derived from quasi-static conditions. Youssef and Gupta (2012) used a Laser Spallation Facility to obtain the stress-strain curve of polyurea at low strains and high strain rates, which agreed with the findings of Zhao et al. (2007) and discovered that the Time-Temperature Superposition principle could be extended to strain rates as high as 1.1 x 10^5 s^{-1}, which further justifies that the dynamic behavior of polyurea can be modeled using the master relaxation curve based on quasi-static loading. The energy absorption ability of polyurea is traceable to its mechanical behavior under high strain-rate loadings.

2.7.2 Polyurea as a Masonry Retrofit

Dinan et al. (2003) suggested three ways spray-on polyurea can be applied to a masonry wall. These are pure flexure, pure membrane, and combined configurations. In pure flexure configuration, the polyurea is sprayed directly on the wall to form a composite action with the wall, but this is not extended to the supporting roof or slab. The pure membrane configuration describes the scenario where the polyurea is sprayed so that it doesn't have direct contact with the wall yet protects it by forming a strong bond with the supporting structure. Further, the combined configuration has the polyurea sprayed directly on the wall and the supporting structures, as shown in Figure 2.6.

Moradi et al. (2010) reduced the spray-on polyurea application to two approaches: catcher membrane and fully bonded material. The catcher membrane is the same as the pure membrane configuration described by Dinan et al. (2003). Also, the pure flexure and combined methods discussed earlier can be grouped under the fully bonded application. The catcher membrane involves the materials being installed not having a direct connection to the masonry; this gives a uniform strain distribution over the membrane height with lowered maximum strain magnitude for a given level of effectiveness, while in the case of a fully bonded approach, materials are applied directly to the tension side of the masonry with the aid of commercially available epoxies and highly localized strains are produced where the tension cracks occur on the wall.

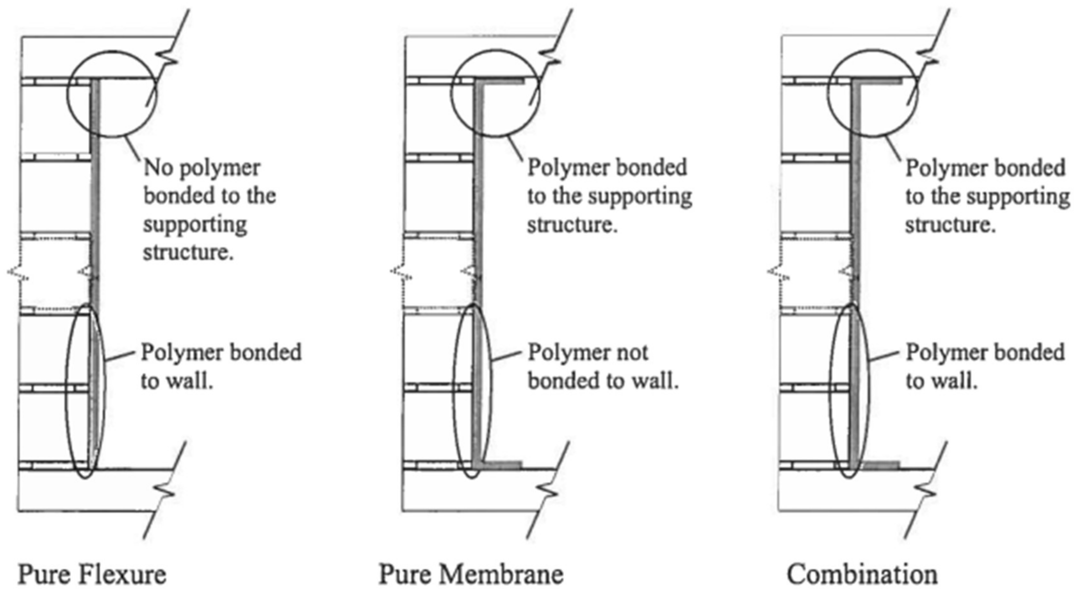

Figure 2.6. Spray-on polyurea application approaches on masonry walls (Dinan et al. 2003)

Knox et al. (2000) described conventional retrofitting methods as adding steel or concrete to improve the structure's overall strength, which is a time-consuming and expensive approach. This led the Air Force Research Laboratory (AFRL) to research and develop easier, less expensive, and lightweight retrofitting methods to introduce ductility and resilience to CMU walls. In the fall of 1999, AFRL researched by coating the inside and outside of 8 feet by 8 feet with a commercial spray-on truck bed liner product (an elastomeric polymer). The coated wall was subjected to a blast pressure of 80+ psi. Ordinarily, the CMU wall would shatter and fail between 2-4 psi pressures. Although the wall suffered from severe damage and developed large deformations, the polymer could contain shattered wall fragments, indicating safety for occupants. With the success of this experiment, AFRL decided to apply the same elastomeric polymer to a lightweight modular structure to improve its blast resistance. The inside and outside of the 10-foot by 20-foot construction trailer were coated with elastomeric polymer and exposed to a 500-pound ammonium nitrate fuel oil (ANFO) explosive, generating 12 psi pressure on the trailer. Large deformations were seen on the trailer walls, and some tears were in the membrane, but the fragments were also contained. Based on the success of the proof-of-concept testing, AFRL-Tyndall initiated a polymer retrofit program to discover polymers with enhanced structural properties, affordable and free from fire and environmental effects, and a total of 21 prospective polymers were evaluated. It included 13 spray-on materials, 7 extruded thermoplastic sheet materials, and 1 brush-on material. All the polymers were structurally tested, and only the 13 spray-on polymers were found suitable. They had fast gel and cure times, making their application to vertical and overhead surfaces feasible. The 13 spray-on polymers comprise seven polyurethanes, one polyurea, and five polyurea/urethanes. The polyurea was preferred for further testing as a retrofit material because of its strength, flammability, and cost.

The single-degree-of-freedom (SDOF) approach was developed to give a mathematical representation of the dynamic response of external walls to blast loading at various yields and standoffs. It involved developing a static resistance function based on the wall construction details, transforming the properties of the wall into an equivalent SDOF model, and solving the equation of motion to determine the response of the critical response point, which is taken to occur at the center of the wall section.

The polyurea polymer was used in three experiments: Component wall test, Structure 1 test, and Structure 2 test (Davidson et al. 2004). The component wall test involved two 8-foot by 8-foot lightweight walls with different coating thicknesses. Structures 1 and 2 tests were a long construction-style trailer and house trailer, both reinforced with an interior frame of 1 in by 1 in the tubing. The polymer retrofit generally worked well in the first two experiments, although Structure 1 suffered severe damage. Structure 2 suffered extensive failure as a larger explosive was used to push the envelope of the retrofit technique. The reinforced steel tubing reduced the ceiling deflections of the trailers but had little effect on their wall deflections.

Three explosive tests (Test 1, Test 2, and Test 3) were conducted by Davidson et al. (2004) without specifying the explosive charge sizes and distances from the reaction structure for security reasons. Two unreinforced masonry wall panels constructed for each test had dimensions of 2.24m by 3.66m with a W12 by 35 I-beam separating the two panels. A 19.1 mm foam insulation was applied on both sides of the wall panels. The exterior top of each panel was secured using a steel plate, while the interior top, interior bottom, and exterior bottom were all secured with similar steel angles. The support conditions provided for the panels enabled only one-way bending.

Test 1 had two panels, a control, and a retrofitted wall with a layer of polymer only on the interior. In test 2, panels like those in test 1 were still used. Test 3 had the interior and the exterior of one of the panels retrofitted. The panels without the polymer retrofits were taken as the ‘Control walls’, and they were needed for comparison purposes to evaluate the effectiveness of the polymers. In Test 1, it was revealed that a peak pressure of 393 kPa was impacted on the walls. The laser deflection gauge indicated that the control wall panel failed at its mid-height, which led to its total collapse. Still, the polymer held the retrofitted wall panel in place, though it suffered severe damage to the front faces of its top two courses. Also, there was no evidence of secondary fragmentation from the two walls during the blast. Test 2 involved doubling the explosive charge, and the standoff distance was shortened by about 14% because the retrofitted wall of Test 1 did not reach its capacity limit. Greater energy impacted the structure as the reflected pressure at the wall surface tripled approximately that of Test 1. Although the polymer held much of the retrofitted wall together, the wall broke off at the supports, and the polymer also got torn at mid-height along the mortar joint, where the wall flexed and fell on top of itself into two pieces. In test 3, four walls were used with variations in the application of the polymer. Wall 1 (the left wall in the reaction structure) had an interior coating of 9.5mm thick polymer, and it overlapped 0.305m into the roof and floor slab, respectively. Wall 2(right wall) was retrofitted inside and outside with the polymer with a coating thickness of 3.2mm and a floor and roof overlap of 0.305m. Wall 3 and Wall 4 were coated on their interior parts with a polymer thickness of 3.2mm. However, they had different roofs and floor overlaps of 0.152m and 0.305m, respectively. The walls were positioned to allow a one-way flexural response. The same explosive charge as Test 2 was used. The standoff distance increased by approximately 30% over Test 1. All the walls suffered major damage; however, the polymer held the walls in place and prevented fragmented particles from flying into the test structure and cubicles. Wall 3 and Wall 4 suffered serious exterior facial damage; Wall 1 also suffered significant damage at the top layers of its exterior face, while Wall 2 bulged at the top layers on both the inside and outside faces. It was noted that retrofitting both sides of the wall had little effect in increasing the protection of occupants. Although it provided additional strength against blast loading, the extra cost was unnecessary. The tests showed that peak pressures greater than 400 kPa can be resisted for one-way action retrofitted walls, compared to a capacity of less than 35 kPa for unreinforced masonry walls.

Irshidat et al. (2011) used nanoparticle-reinforced composites to retrofit masonry structures against blast loading. The research was done experimentally, numerically, and analytically. Scaled-down brick units were used to construct three-quarter scale model walls, which were retrofitted individually with three different nanoparticle-reinforced elastic materials (NPREM). The NPREM included using polyurea alone, XGnP reinforced polyurea, and Polyhedral oligomeric silsesquioxane (POSS) reinforced polyurea with a thickness of 1.5mm, 1.5mm, and 1.8mm, respectively. FE models were developed using the finite-element software AUTODYN to replicate the experimental response of walls with reasonable accuracy. Also, iso-damage (pressure-impulse) curves were generated from the SDOF model and used to predict the response of retrofitted masonry walls under blast loads. The experimental result showed that all three nanoparticle polymers increased the ultimate flexural resistance of the masonry walls when exposed to blast peak pressure within the range of 208 kPa to 225 kPa. However, nano-reinforced polyurea with POSS wall achieved the best performance for blast loading, while the others exhibited slight improvement. FE model results were compared with the wall failure mechanisms, midpoint deflection, and debris velocity obtained from the experimental data. The study revealed that the model generated results like those of the data obtained from the experiment in terms of mode of failure, midpoint deflection, and break line location.

Johnson (2013) carried out a subscale static and dynamic experimental approach. He reinforced the spray-on polyurea with fiber reinforcement as a retrofit system for CMU walls.

The reinforcement placement was considered in two orientations, 0/90-deg, and ±45-deg, respectively. Although the two fiber orientations increased the stiffness of the polyurea material, which translated into lesser deflections, it was observed that the 0/90-deg fiber orientation produced a retrofit system that was too stiff and experienced failures at lower dynamic load levels than the ±45-deg fibers. Therefore, the fiber orientation greatly affected the polyurea's ductility.

A computer program was developed by Jacques et al. (2013) to conduct dynamic inelastic response history analysis of reinforced concrete elements subjected to blast-induced shock waves. The program consists of the SDOF analysis module and the structural analysis module. While the former can generate dynamic time history analysis for a given impulsive forcing function and element resistance curves, the latter computes the force–deformation characteristics of symmetric one-way reinforced concrete elements subjected to uniformly distributed blast pressures. The program incorporates appropriate material constitutive models for concrete confinement, reinforcement strain hardening, and compression bar buckling, as well as the progression of hinging, deformations resulting from anchorage slip, and the effects of variable axial loads, hence resulting in improved accuracy of force–deformation resistance curves. It also incorporates the impact of FRP retrofitting as one of the most common techniques used in practice for blast retrofitting. The computer program "RC Blast" can be used through a user-friendly interface to generate dynamic response results and to establish PI diagrams for use in design. The results have been verified extensively against shock tube testing, indicating good correlations with experimental data and considering future improvements to the numerical procedure.

Using the University of Ottawa Shock Tube Facility, Ciornei (2012) researched four URM walls of dimensions 100 mm by 2000 mm by 2000 mm. The walls were named URM-1(control), URM-2, URM-3, and URM-4 sequentially. URM-1 and URM-2 were built and tested as infill, non-load bearing walls. However, the difference between the walls is that the second wall, URM-2, was retrofitted on the tension side with a 3mm thick layer of spray-on polyurea. Further, the third and fourth walls, URM-3 & URM-4, were designed as load-bearing walls subjected to an axial loading of 122kN with two hydraulic jacks applied from the top of the frame. URM-4 was retrofitted with 6mm thick spray-on polyurea, reinforced with vertical steel wires having a spacing of 100mm on the tension side. URM-1 was exposed to four shots from the shock tube with a starting driver's pressure of 40 kPa and increased progressively. The control wall failed at a reflected pressure/impulse combination of 30.7 kPa/265.1 kPa-ms and reached a maximum deflection of 56.5mm at mid-height. Although arching action was developed, the failure mode was brittle, with the disintegration of the wall into flying fragments. Also, a total of ten shots were fired at URM-2. The wall accommodated a reflected pressure/impulse combination of 78.1 kPa/723.4 kPa-ms and displayed a maximum mid-height deflection of 253.5 mm at failure. The polyurea membrane effectively contained the fragments but developed an extensive tear, which allowed some debris to fly in. The third wall, URM-3, recorded a reflected pressure/impulse combination of 51 kPa/414.6 kPa-ms while developing a maximum mid-height deformation of 41.7 mm after resisting seven blast shots. The application of axial loading increased the compressive force on the wall, improving its resistance to flexure before developing hinging at its mid-height, leading to the wall's collapse with flying debris. Also, the fourth wall, URM-4, received eight shots and resisted a high reflected pressure/impulse combination of 97.3 kPa/1995 kPa-ms at a mid-height maximum displacement of 261 mm. Its failure mode was ductile, and the reinforced polymer proved to be the most efficient approach for increasing the ductility of the wall and constraining fragmentation. For all the shots, the driver's length (L_D) was kept constant at 1829mm, except for the last shot on URM-4, where the driver's length was extended to 4877mm to increase the impulse to reach the wall's capacity.

2.8 Steel

Steel used in the construction industry can be classified into four groups: carbon steel, alloy steel, stainless steel, and tool steel. However, this literature review will discuss only carbon and stainless steel in the following sections.

2.8.1 Stainless Steel and Carbon Steel Comparisons

Stainless steels are manufactured by adding a minimum quantity of 10.5% chromium and a maximum of 1.2% carbon and other alloying elements to their chemical composition. Carbon steel is a combination of iron and carbon, with a carbon content of up to 2%.

Stainless steels have superior corrosion resistance to carbon steels because of their chromium content, which can be further enhanced by adding molybdenum and nitrogen. They can be categorized into five groups: austenitic, ferritic, duplex (austenitic-ferritic), martensitic, and precipitation-hardening. The construction industry mainly uses austenitic, ferritic, and duplex stainless steel (Tylek et al. 2014, Gardner 2005).

The primary difference in the structural behavior between stainless steel and carbon steel is in the shape of their stress-strain curve. As shown in Figure 2.7, stainless steel exhibits a rounded non-linear stress-strain response with no clearly defined yield stress and shows no plateau before attaining strain hardening (Baer n.d). Two methods could overcome this complexity: a generally accepted approach of equivalent yield point corresponding to 0.2 %

proof stress, which gives an overly conservative design, or a more accurate material model proposed by Ramberg and Osgood and modified by Hill as expressed in Eq. 2.1 (Vaghani et al. 2014, Gardner 2005). Carbon steel, on the other hand, has a linear stress-strain response with a clearly defined yield strength and shows a considerable yield plateau before strain hardening.

$$\varepsilon = \frac{\sigma}{E_0} + 0.002 \left(\frac{\sigma}{f_y}\right)^n \qquad 2.1$$

where E_0 is the modulus of elasticity of the material, f_y is the 0.2% proof stress, $\boldsymbol{n}$ is a strain hardening coefficient while σ and Ɛ are stress and strain, respectively.

Stainless steels, particularly austenitic stainless steels, are much more ductile than carbon steel. Their elongation may be 40-60%, while the elongation for the carbon grade is around 25%. Also, ferritic and duplex stainless steels have good flexibility of similar magnitude. Still, austenitic stainless steel exhibits the best ductility performance, with an elongation about two times larger than theirs (Gardner 2005, Tylek et al. 2014).

Austenitic stainless steels are more strain rate sensitive than carbon steels, exhibiting higher strength values and lower rupture strain at higher strain rates. This characteristic makes them relevant materials under dynamic conditions as their design strength is multiplied by a dynamic increase factor due to high strain rates to maximize their strength increase at higher strain rates (Tylek et al. 2014).

Stainless steel displays better strength retention and stiffness at elevated temperatures than carbon steel. Although stainless steel is more expensive than carbon steel, its long-lasting benefits, such as durability, aesthetics, low maintenance, strength enhancement and impact resistance, and re-use and recycling nature, offset the higher initial cost (Gardner 2005).

2.8.2 Strain Rate of Austenitic Stainless Steel

Lee et al. (2000) studied the dynamic behavior of 304L stainless steel using a Split Hopkinson bar and TEM (transmission electron microscopy). They conducted dynamic compression tests on the specimens at room temperature. The tests were conducted from a strain range of 0.05 to 0.3 and within the strain rate range of 800 s^{-1} to 4800 s^{-1}. It was observed that at high strain rates (dynamic state) and large strains, the stainless steel attained higher strengths due to Martensite formation. Also, their research revealed a 65% overall stress enhancement increase in 304L stainless steel under impact-induced loading as its strain rate increased from 800 s^{-1} to 4800 s^{-1}. When subjected to explosions, this type of steel can exhibit a strain rate as high as 10^6 s^{-1}, a dynamic behavior that makes it highly suitable for wall retrofitting against blast loads.

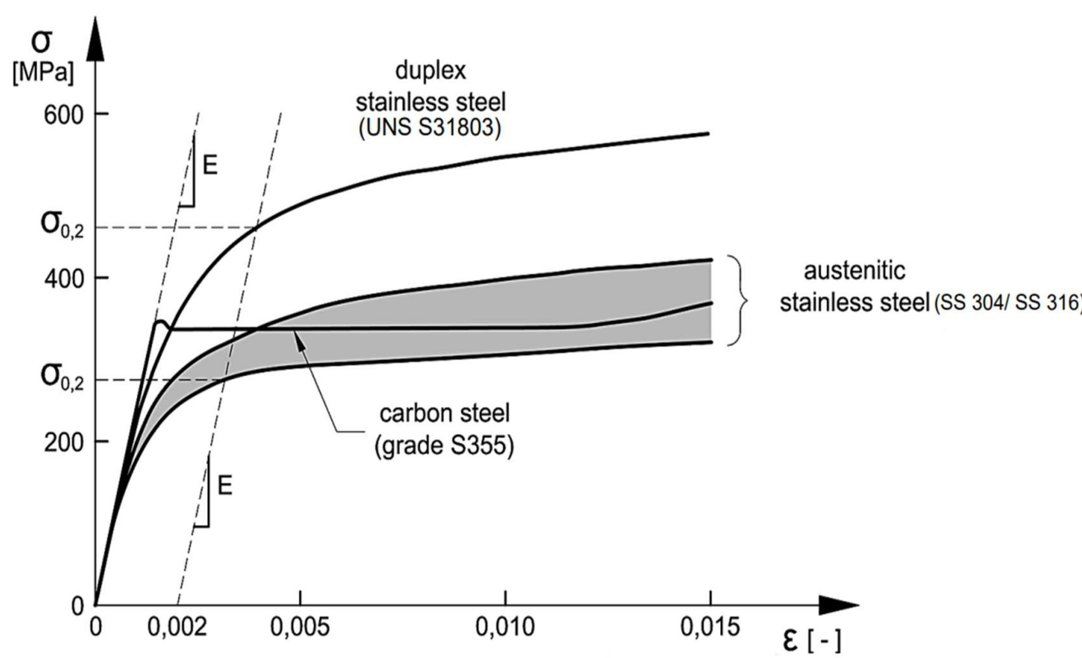

Figure 2.7. Typical experimental stress-strain curves of carbon and stainless steel (Baddoo et al. 2001, Tylek et al. 2014)

2.8.3 *Steel Mesh as Concrete Reinforcement*

Ceylan (2014) compared steel mesh, steel fiber, and high-performance polypropylene fiber-reinforced concrete in concrete plates and beams in terms of their toughness, ductility, load carrying, and energy absorption capacities. The experiments revealed that the steel mesh performed best among the materials regarding the above-tested properties. Li and Wu (2007) conducted similar research; in which case they compared the performance of steel wire mesh reinforced concrete slab to high-performance steel fiber-reinforced concrete slab. The two slabs were exposed to a 12 kg TNT detonation from a standoff distance of 1.5m. After the experiment, it was observed that the steel fiber-reinforced concrete slab failed at its mid-span with a permanent deflection of 70 mm. In contrast, the steel wire mesh reinforced concrete slab had a uniform deformation and showed little deflection.

2.8.4 *Steel Mesh for Masonry Retrofitting*

Chen et al. (2014) conducted a comparative study to define the best-suited materials needed to retrofit masonry infill walls. Three materials of interest were selected: steel wire mesh, CFRP, and laminated steel bars. Each material was used to retrofit a URM wall, and the walls were exposed to a series of explosions. The performance of the retrofits was checked in terms of displacement response and failure mode. When the walls were subjected to a charge weight of 34.2 kg, the control wall's peak displacement and maximum residual deformation were about 88mm and 58mm, respectively. However, steel mesh retrofit decreased the peak and residual displacements to 67.76mm and 19.14mm, respectively. Furthermore, the peak displacement and the residual deformation of the CFRP strip wall retrofit were reduced to 50.16mm and 4.64mm. Due to the instrumentation errors, measuring the displacement of the laminated steel retrofitted wall was impossible. None of the retrofitted walls were damaged during the detonation of the 34.2kg charge weight. The control wall experienced spalling while exhibiting significant mid-height deformation and an inward base shift of about 25mm. The specimens were further subjected to a 21.2 kg charge weight detonation. It was observed that a big opening was created in the control wall, releasing many flying fragments. Although the retrofitted walls performed well, the CFRP and the laminated steel bars retrofitted walls experienced shear rupture and delamination of CFRP. However, minor damage was seen on the back of the steel mesh retrofitted wall. More so, the walls were exposed to another detonation of 30kg charge weight; consequently, the control wall collapsed, releasing flying fragments up to 34.2 m; the CFRP strips and laminated steel bars retrofitted walls exhibited significant damage, shear rupture of the strips and bars, plaster mortar and connection delamination, but no fragments were released. Surprisingly, the steel mesh retrofitted wall just suffered slight damage on its back from the previous detonation.

Cengiz and Turanli (2004) in their research compared the performance of steel mesh-reinforced shotcrete (SMRS) and steel fiber-reinforced shotcrete (SFRS) in terms of their load-carrying capacity and energy absorption capacity. The steel mesh used in SMRS had a diameter of 8mm, intervals of 150 mm, and a weight of 23.5kg/$m^{3,}$ while the steel fiber contents used in SFRS were 35kg/m^3 and 50 kg/m^3, and their volume percentages in 1m^3 of shotcrete were 0.45% and 0.64%, respectively. Also, the fiber had a diameter of 0.6 mm and a length of 30 mm.

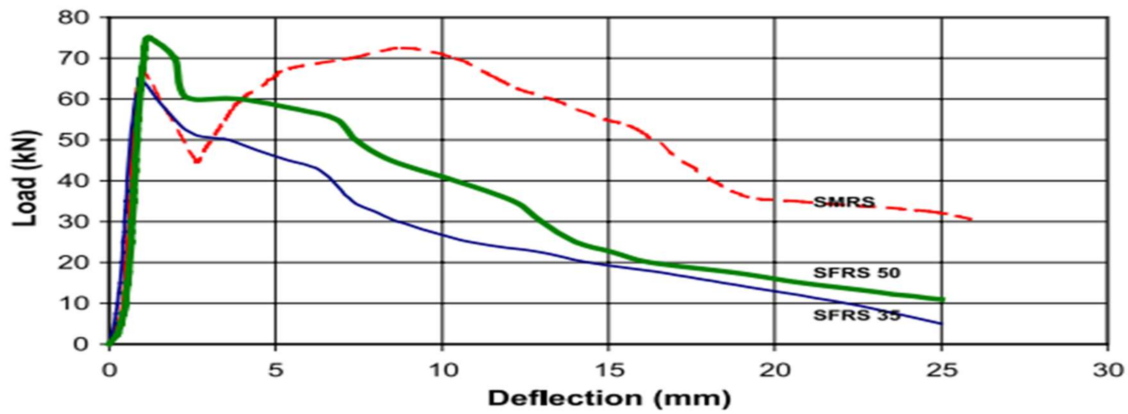

Figure 2.8. Comparison of the load-deflection curves for SMRS, SFRS 35, and SFRS 50 panels at the age of 28 days (Cengiz and Turanli 2004)

Although SFRS 50 gave the highest first peak and ultimate load resistance, it began losing it load carrying capacity faster than SMRS, which indicated an unstable zone. Despite SMRS displaying an initial drop in load-carrying capacity up to a deflection of 2.5 mm, it gradually increased its load resistance in the plastic zone between 2.5 mm and 9 mm. Also, the energy absorption of SMRS was about 1.5 times that of SFRS 50 when the areas under the two curves were compared. The SM had better bond length, bond, and friction stresses with the shotcrete matrix than SF, which exhibited strain hardening after yielding (better load-carrying capacity) and higher energy absorption.

2.8.5 Steel Mesh Orientation Effect on Impact Load

Prem Pal Bansal et al. (2008) studied the effect of steel mesh orientation on the beam capacity. The beams examined were stressed up to 75% of the safe load resistance and retrofitted with ferrocement jackets. Eight beams of 127 mm x 227 mm x 4100 mm were prepared and retrofitted with 15 mm thick ferrocement jackets reinforced with 40 mm x 40 mm single-layer square welded steel mesh. The beams were categorized into four sets, two beams per set, starting with the control beams, followed by the other three sets that had wire mesh with orientations of 0, 45, and 60 degrees, respectively, in the ferrocement jackets.

When the beams were loaded to failure, the results indicated that in terms of maximum load capacity, the ferrocement jackets reinforced with 45-degree-oriented steel mesh performed the best, followed by the 60 and the zero degrees, respectively. However, the zero-degree mesh gave the highest ductility ratio and energy absorption capacity, followed by 45 and 60 degrees. Thus, a rise in the ductility ratio and energy absorption capacity of the retrofitted beams make them appropriate for dynamic load applications.

2.9 Dynamic Analysis

URM walls or any structural elements/systems subjected to dynamic loadings develop a multiple-degree-of-freedom response, which can be simplified as a single-degree-of-freedom (SDOF) system for analysis. SDOF analysis is commonly used for blast load investigations.

2.9.1 Single Degree of Freedom Model Development

Under time-varying loadings, the displacement-time configuration of a structural system at any instant is determined by an infinite independent coordinate system called the number of degrees of freedom (DOF). However, these multiple coordinate systems can be reduced to SDOF through idealization. SDOF uses a singular independent coordinate to analyze complex dynamic systems. The simplicity of model formulation, obtaining input parameters, and minimal effort required in computing numerous calculations make the SDOF model a useful method for idealizing one-way masonry walls (Moradi 2009, Johnson 2013, Biggs 1964). SDOF is represented by a mass-spring-damper system, as shown in Figure 4. The general equation of motion for the SDOF system subjected to forced vibration is given in Eq. (2.2):

$$M_e\ddot{Z}(t) + C_e\dot{Z}(t) + K_eZ(t) = F_e(t) \tag{2.2}$$

Where M_e = equivalent mass of the SDOF; C_e = equivalent damping coefficient of the SDOF; K_e = equivalent stiffness of the SDOF; and F_e (t) = equivalent load-time history applied to the SDOF. The mid-height deflection of a CMU wall can be used as the unknown parameter to solve for. The equivalent parameters enable easy measurement of the mid-span deflection of a CMU wall in one direction.

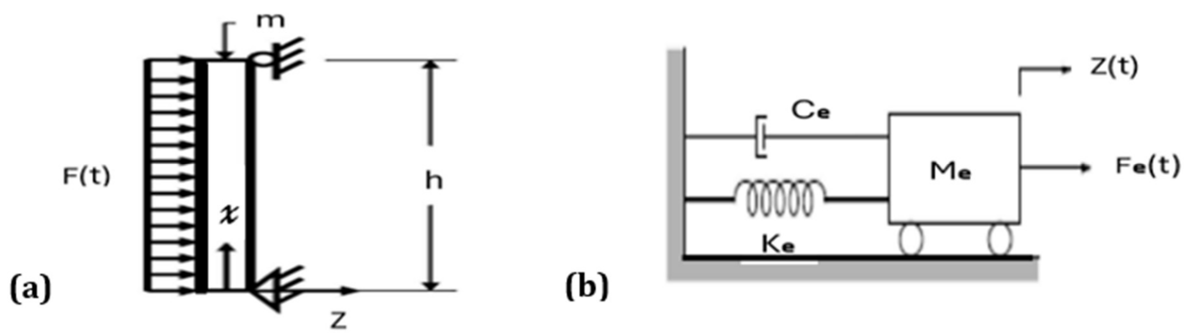

Figure 2.9. Wall idealized as spring-mass system: (a) uniformly loaded simply supported wall (b) single degree of freedom spring-mass system

The effect of damping for blast loading is usually considered to be negligible. This is because the blast occurs within a very short time frame, and the wall attains maximum response with a small reduction in a single cycle of displacement. However, significant energy dissipation by plastic deformation of the wall takes place as structural damping. Larger deflection generation by ignoring damping has been validated by experimental evaluation (Kiger and Salim 1998, Chopra 2001, Davidson et al. 2004, Al-Bayti 2017). Hence, the damping coefficient can be considered zero, which reduces Eq. (2.2) to:

$$M_e\ddot{Z}(t) + K_eZ(t) = F_e(t) \tag{2.3}$$

Further, it is necessary to determine the equivalent mass and stiffness of the system by assuming the first elastic mode of the system to be represented by an approximate deflected shape. This can be done by a fourth-order polynomial.

$$\varphi(x) = \frac{16}{5h^4}(h^3x - 2hx^3 + h^4) \tag{2.4}$$

The equivalent mass M_e of the SDOF system representing a uniformly distributed mass m is given by Eq. (2.5).

$$M_e = \int_0^h m\varphi^2(x)dx \tag{2.5}$$

Consequently, the mass factor, K_M , which is the ratio of the equivalent mass to the actual total mass of the structure is used to transform a distributed mass system into a lumped mass system.

$$K_M = \frac{M_e}{M_h} \tag{2.6}$$

Considering a wall with a constant mass, m along its height, h, the total mas becomes $M_h = mh$. The ratio of equivalent lumped mass to total mass gives the mass factor, which is used to convert distributed mass to a lumped mass. The mass factor, K_M, can be written as shown below.

$$K_M = \frac{\int_0^h m\varphi^2(x)dx}{mh} = \frac{\int_0^h \varphi^2(x)dx}{h} \tag{2.7}$$

Similarly, the equivalent concentrated force resulting from uniformly applied blast pressure can be written as:

$$F_e = \int_0^h w(x)\varphi(x)dx \tag{2.8}$$

The load factor, K_L , is the ratio of the equivalent force, F_e, to the total force of $F_h = w(x)h$. The load factor transforms distributed force into an equivalent single-point load:

$$K_L = \frac{F_e}{F_h} = \frac{\int_0^h w(x)\varphi(x)dx}{wh} = \frac{\int_0^h \varphi(x)dx}{h} \tag{2.9}$$

The internal force that restores the element to its unloaded static position is referred to as resistance R (Biggs 1964). This internal force is a function of the stiffness of the system.

known as the resistance R of the element. The stiffness of the element is defined as the ratio of the rate of resistance to the incremental change in deflection:

$$K = \frac{\Delta_R}{\Delta_Z} \text{ and } K_e = \frac{\Delta_{R_e}}{\Delta_Z} \tag{2.10}$$

Moreover, for the wall to be in equilibrium, resistance must always be equal to the applied force. Hence the transformation factor for stiffness, K_K becomes equal to the force transformation factor K_L.

$$\frac{F_e}{F_h} = \frac{R_e}{R_h} \tag{2.11}$$

$$K_L = \frac{K_e Z}{KZ} = \frac{K_e}{K} = K_K \tag{2.12}$$

Substituting the transformation factors into the equation motion given in Eq. (2.3) leads to Eq. (2.13). Dividing all terms by K_L rests in load-mass factor, K_{LM}, which is the ratio of the mass factor to the load factor.

$$K_M M_h \ddot{Z}(t) + K_L K Z(t) = K_L F(t) \tag{2.13}$$

$$\frac{K_M}{K_L} M_h \ddot{Z}(t) + KZ(t) = F(t) \tag{2.14}$$

$$K_{LM} M_h \ddot{Z}(t) + KZ(t) = F(t) \tag{2.15}$$

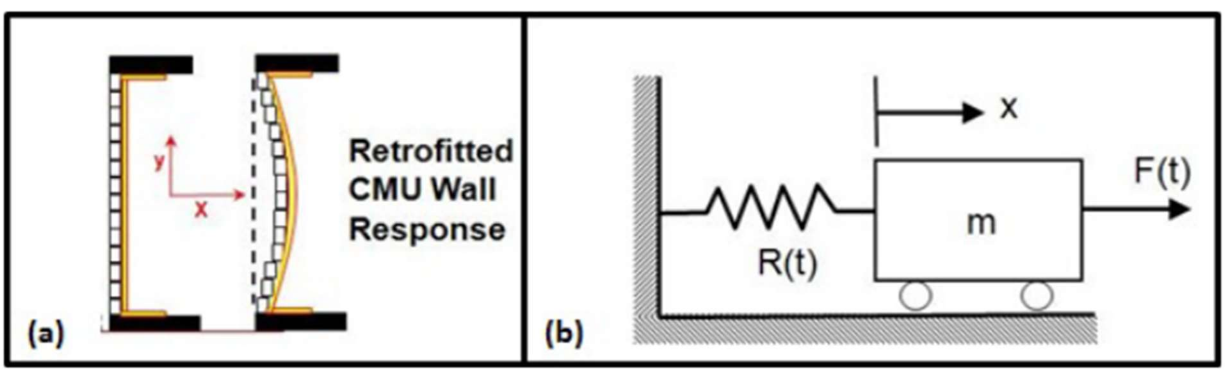

Figure 2.10. Blast response (a) retrofitted CMU wall (b) equivalent SDOF model (Johnson 2013)

The resistance function, *R(z),* describes the relationship between the out-of-plane force (or pressure) and mid-height displacement of the URM wall subjected to blast loading.

$$K_{LM} M_h \ddot{Z}(t) + R[Z(t)] = F(t) \tag{2.16}$$

$$\ddot{Z}(t) = \frac{F(t)}{K_{LM} M_h} - \frac{R[Z(t)]}{K_{LM} M_h} \tag{2.17}$$

This equation of motion can now be solved for z(t) numerically using the central difference formula, Eq. (2.18), or any other numeric computational procedure applicable:

$$Z(t + \Delta t) = \frac{F_t \Delta t^2}{K_{LM} M_h} + \left(2 - \frac{R_Z \Delta t^2}{K_{LM} M_h}\right) Z(t) - Z(t - \Delta t) \tag{2.18}$$

The results from Eq. (2.18) will be meaningful if the time step, Δt, is constant and small enough. Chopra (2007) suggested that the time step over the natural period should be less than 0.1 for the response to be acceptable and his suggestion was based on Eq. (2.19):

$$\frac{\Delta t}{T} < \frac{1}{\pi} \tag{2.19}$$

Where ***T***, the natural period of the system is given by Biggs 1964 as:

$$T = 2\pi \left(\frac{K_{LM} M_h}{K}\right)^{\frac{1}{2}} \tag{2.20}$$

Furthermore, the resistance function of the unreinforced concrete masonry wall with the membrane-bonded system can be used as R_z in Eq. (2.18) to calculate the wall response to blast loads. Thus, the resistance at a given displacement is the sum of the individual resistance of the wall and retrofit parts at that displacement (Gagnet 2013).

Several researchers have used SDOF modeling in different analyses: historic masonry (Rosen 2013), one-way bending behavior of retrofitted concrete masonry walls (Moradi et al. 2009, Gagnet et al. 2017, Gandia 2019, Jung 2020), reinforced concrete columns (Lloyd 2010), collapse study of a URM bearing wall (Zapata et al. 2008), in-fill steel-stud wall systems (Salim et al. 2005), anchorage design of blast-resistant windows (Alameer 2020).

2.9.2 Resistance Functions

Jacques et al. (2013), in their work, developed a computer program to conduct SDOF dynamic analysis. The program is called RC-blast and consists of the SDOF analysis module and the structural analysis module. The SDOF analysis module can be used to perform dynamic inelastic time history analysis. It can also generate pressure-impulse (PI) diagrams for structural elements exposed to blast loads. The structural analysis module computes the load-deformation characteristics of symmetric one-way reinforced concrete elements subjected to uniformly distributed blast pressures. This information is used in the SDOF analysis as a resistance function.

Gagnet et al. (2017), in their study *"Assessment of resistance definitions used for blast analysis of unreinforced masonry walls,"* discussed and compared the three standard methods used to develop resistance functions for SDOF analysis of unreinforced masonry walls. The three methods were the Wiehle, SBEDS, and Moradi. The distinction in these methods is influenced by the support conditions of the wall (non-arching or arching). The simply supported wall is described with a non-arching support condition, while a wall built between rigid supports might develop restraint at its supports as it deforms, which could create membrane compressive forces (arching action) in the plane of the wall while generating shear forces at the supports (Hrynyk and Myer 2008). The three methods were compared based on definitions of non-arching and arching resistance, with the work focusing on non-load bearing infill URM. Three parameters were considered regarding the non-arching resistance function: the wall thickness, the masonry type, and the axial load. A baseline case was first constructed using a concrete masonry unit (CMU) wall with dimensions of 3.66 m height and 200 mm thickness, and it had zero axial load. Although all three methods resulted in similar shapes with a linear initial stiffness, the SBEDS method displayed the largest peak resistance while the Moradi method gave the lowest resistance. The Moradi method assumes that the wall's tensile strength is negligible, thus giving conservative results. Additionally, the Moradi approach gave less than half of the ultimate deflection compared to the other two methods.

A comparison of arching methods used by the three researchers for a 200mm (thick) by 3.66m (high) CMU brick wall indicated differences in wall resistance. The area under the resistance curve for the Wiehle method was the largest compared to the other methods, indicating it has the highest blast energy absorption capacity. In contrast, the SBEDS method generated the least.

Moradi et al. (2011) indicated that the catcher membrane system of an unreinforced CMU wall has two phases involved in its resistance to blast pressure. Phase one is the flexural resistance provided by the concrete masonry with or without the arching effect, and phase two is governed by the ultimate strain of the retrofit material due to the large displacements associated with the membrane. Each phase has its resistant function, expressed as pressure versus deflection. The superposition of the two resistance functions is used to obtain the total resistance function of the system. The three sets of resistance equations of unreinforced CMU walls suggested by Moradi et al. (2011) are discussed below. Figure 2.11 illustrates free-body diagrams of URM walls with and without arching.

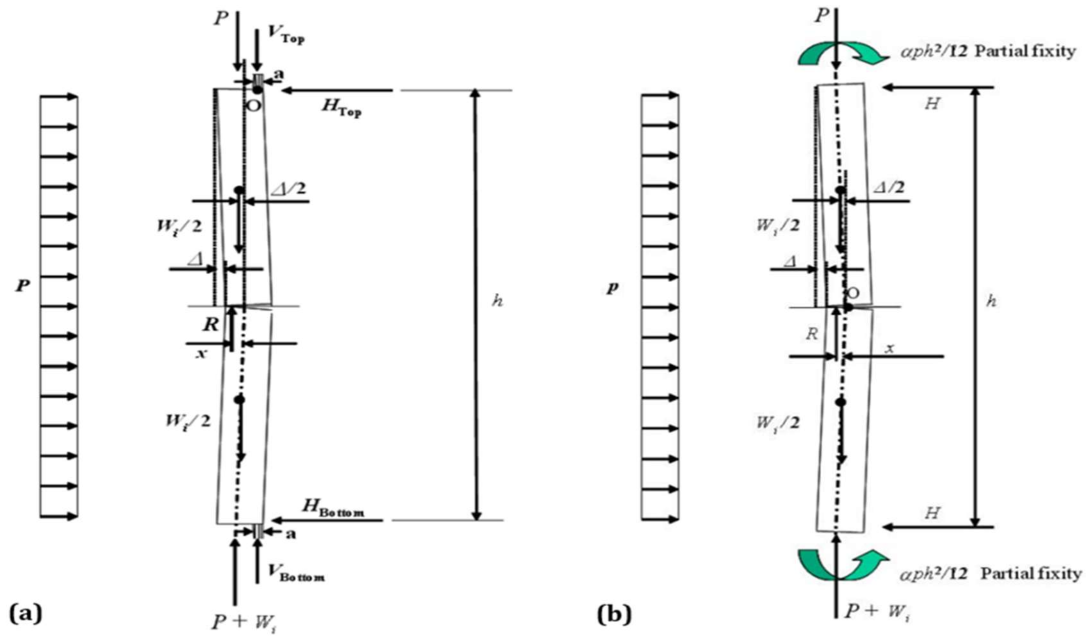

Figure 2.11. Free-body diagram of unreinforced concrete masonry wall (a) with arching and (b) without arching (Moradi et al. 2011)

(a) URM without arching

The following equations define the resistance function for URM walls without arching.

$$H = \frac{ph}{2} + \frac{W_i\Delta}{2h} \tag{2.21}$$

$$R = \frac{W_i}{2} + \mathbf{P} \tag{2.22}$$

$$\Delta = \frac{t}{6} + \frac{y}{3} - \frac{(3-2\alpha)ph^2}{12W_i + 24\mathbf{P}} \tag{2.23}$$

$$Before\ crack, \mathrm{y} = 0 \qquad \Delta_{max.elastic} = \frac{(5-4\alpha)ph^4}{384E_C I_g} \tag{2.24}$$

$$After\ crack, \mathrm{y} > 0 \qquad \Delta_{crG} = \beta\Delta_{cr} \tag{2.25}$$

where; H = Horizontal reaction, R = Internal vertical reaction, p = lateral pressure, **P** = vertical support reaction, Δ = lateral deflection at wall center, y = crack depth through the thickness, α = degree of fixity at the supports, t = thickness of the wall, W_i = weight of the wall, h = height of the wall, E_C = Elastic modulus of concrete masonry, I_g = Uncracked gross moment of inertia, Δ_{cr} = deflection at the onset of cracking, Δ_{crG} = deflection beyond the initial crack as crack grows, and β = curvature ratio.

At the crack initiation, when y = 0, the problem is reduced to two equations, Eqs. (2.23) and (2.24), and two unknowns (Δ and p). As the crack widens, y>0, Δ is calculated using Eq. (2.25), and *p* is subsequently calculated using Eq. (2.23).

(b) URM with arching action

The resistance equations for URM walls with arching action:

$$H_{Top} = \frac{ph}{2} - (\mathbf{P} + W_i)\left(\frac{t-a}{2h}\right) + \frac{W_i\Delta}{2h} \tag{2.26}$$

$$H_{Bottom} = \frac{ph}{2} + (\mathbf{P} + W_i)\left(\frac{t-a}{2h}\right) - \frac{W_i\Delta}{2h} \tag{2.27}$$

$$R = \mathbf{P} + V_{Top} + \frac{W_i}{2} \tag{2.28}$$

$$p = \frac{8}{h^2}\left(\mathbf{P}\left(\frac{t-a}{2}\right) + \frac{W_i}{2}\left(\frac{t-a}{2} - \frac{\Delta}{2}\right) - \left(\mathbf{P} + V_{Top} + \frac{W_i}{2}\right)\left(x + \frac{t-a}{2} - \Delta\right)\right) \tag{2.29}$$

$$\Delta = \frac{\left(\mathbf{P} + \frac{W_i}{2}\right)\left(\frac{t}{6}\right) - \frac{ph^2}{8}}{P + \frac{W_i}{4}} \tag{2.30}$$

$$\Delta = \frac{ph^4}{384E_C I_g} \tag{2.31}$$

$$p = \frac{\left(\mathbf{P} + \frac{W_i}{2}\right)\left(\frac{t}{6}\right)}{\left(\frac{h^4}{384E_C I}\right)\left(\mathbf{P} + \frac{W_i}{4}\right) + \frac{h^2}{8}} \tag{2.32}$$

Where ***a*** = width of arching compression region, R = summation of the compressive forces in the wall, V_{Top} = arching force exerted at the top support, *x* = distance from the wall centerline to R, and all other symbols remain the same as earlier mentioned. At y = 0, the arching forces are taken to be zero, and Eq. (2.30) can be derived from the equations of moment and force equilibrium; deflection could be calculated from Eq. (2.31).

Pressure, p, can be determined from Eq. (2.32), a derivative of Eqs. (2.30) to (2.31) at y = 0, and subsequently, the value of p is used to calculate Δ: Again, it was taken that central curvature of the wall was proportional to the extent of displacement, which makes Eq. (2.24) applicable in this case. The resistance function can be developed using an iterative method. Only two equations, i.e., Eqs. (2.31) and (2.32) become applicable immediately after cracking (y = 0), and two unknowns, Δ and *p,* can be computed. As crack progresses (y > 0), Δ is calculated using Eq. (2.24), and *p* is determined using Eq. (2.29).

(c) The catcher membrane resistance

During this loading stage, the masonry fragments due to the blast and loses its flexural resistance. The membrane resistance is activated as it behaves like an elastic bag containing debris from the broken wall. A significantly large displacement is seen in this phase. The length, s, of the formed parabolic shape, can be determined using Eq. (2.33), which is used to determine the strain of the membrane. Subsequently, the strain is used in the true stress-strain relationship of the retrofit material to get its stress.

$$S = 2\left(\frac{h^2}{16\Delta}\right) In\left[4\frac{\Delta}{h} + \sqrt{1 + \left(4\frac{\Delta}{h}\right)^2}\right] + \frac{h}{2}\sqrt{1 + \left(4\frac{\Delta}{h}\right)^2} \qquad (2.33)$$

Eq. (2.34) can compute the Resistance Provided by the catcher membrane. The resistance functions of the URM wall and catcher membrane are shown in Figure 2.12.

$$p = \frac{8\Delta t_r \sigma}{h^2} \qquad (2.34)$$

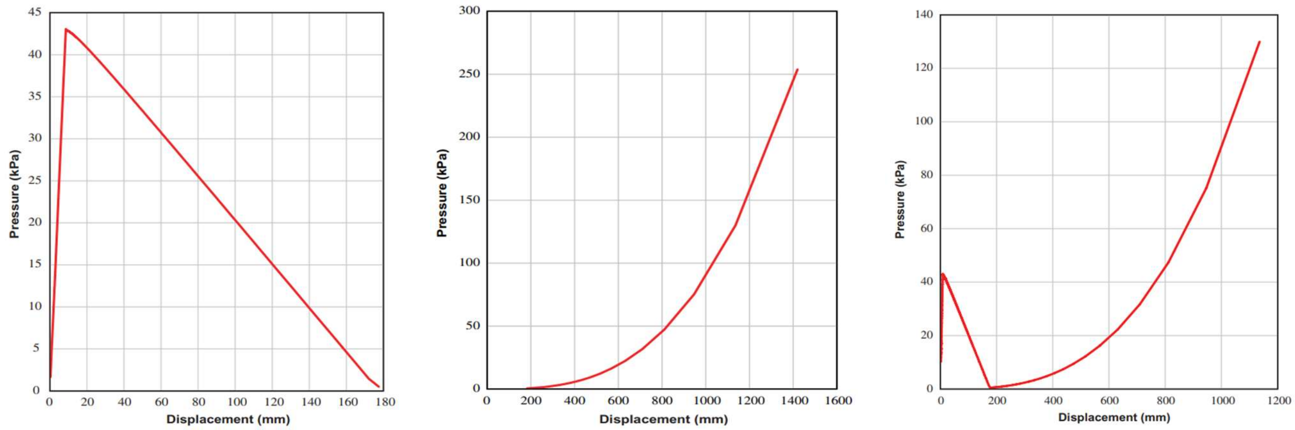

(a) (b) (c)

Figure 2.12. Resistant functions of (a) unretrofitted URM wall with arching action, (b) catcher membrane, (c) wall and membrane (Moradi et al. 2010)

Moradi et al. (2008) researched the resistance to blast pressure provided by a membrane material bonded to concrete masonry walls. In their work, they developed formulas that relied on the procedures presented by Paulay and Priestly (1992) and Drysdale et al. (1994). These formulas address different phases of masonry wall response to out-of-plane forces, including elastic response, response at crack initiation, nonlinear rocking response, large displacements, and potential collapse. Furthermore, the work was extended to develop formulations for bonded membrane retrofit on URM walls. They proved that developing the bond between the retrofit material and the wall significantly increased wall resistance to lateral pressure. The researchers developed expressions to generate resistance functions for each phase of bonded membrane retrofit as given below:

(a) URM with membrane retrofit but Without arching:

After crack, $y > 0$

$$\Delta = \frac{Rx}{\frac{w_i}{2} + P} - \frac{(3-2\alpha)ph^2}{12w_i + 24\mathbf{P}} + \frac{Tt}{w_i + 2\mathbf{P}} \tag{2.35}$$

$$x = \frac{t + 2y}{6} \tag{2.36}$$

$$R = \frac{W_i}{2} + \mathbf{P} + T \tag{2.37}$$

$$T = \frac{4E_r t_r t\Delta}{lh} \tag{2.38}$$

$$\Delta = \frac{\frac{t}{6} + \frac{y}{3} - \frac{(3-2\alpha)ph^2}{12W_i + 24\mathbf{P}}}{1 - \left(\frac{4E_r t_r t}{lh}\right)\left(\frac{4t + 2y}{3w_i + 6\mathbf{P}}\right)} \tag{2.39}$$

(b) URM with membrane retrofit and arching:

The following equations can be used to define the resistance function of a URM wall with a bonded membrane experiencing arching action (see Fig. 2.13).

Before crack, $y = 0$

$$\Delta = \frac{ph^4}{384E_C I} \tag{2.40}$$

$$p = \frac{\left(\mathbf{P} + \frac{W_i}{2}\right)\left(\frac{t}{6}\right)}{\left(\frac{h^4}{384E_C I}\right)\left(\mathbf{P} + \frac{W_i}{4}\right) + \frac{h^2}{8}} \tag{2.41}$$

After crack, $y > 0$

$$\Delta_{crG} = \beta\Delta_{cr} \tag{2.42}$$

$$p = -\frac{8}{h^2}\left(\mathbf{P}\left(\frac{t-a}{2}\right) + \frac{W_i}{2}\left(\frac{t-a}{2} - \frac{\Delta}{2}\right) - \left(T + \mathbf{P} + V_{Top} + \frac{W_i}{2}\right)\left(x + \frac{t-a}{2} - \Delta\right) - T\left(\frac{a}{2} + \Delta\right)\right) \tag{2.43}$$

$$a = 0.1\,t \tag{2.44}$$

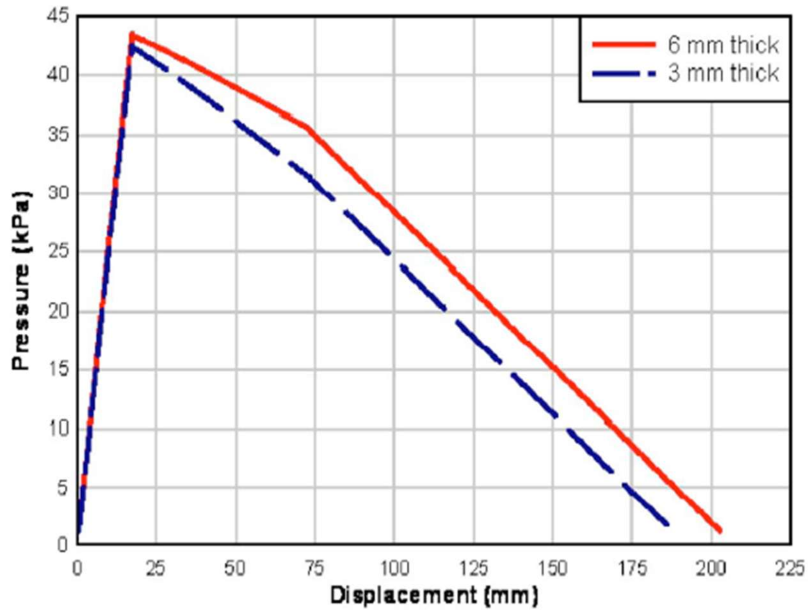

Figure 2.13. A typical resistance function of a URM wall with membrane retrofit experiencing arching action (Moradi et al. 2008)

2.10 Support Connection

Hoemann et al. (2010) identified three cases in which a workable connection can be detailed and designed, as illustrated in Figure 2.14. The first case is for an anchorage force, A, equal to the resultant axial force in the membrane, T. No prying action is created in this case as no moment arm exists within the connection plate.

Case two involves the anchorage force, A, equal to twice the resultant axial force, T (A=2T). The membrane force T is multiplied by the moment arm d creates a prying action on the anchorage.

Case three occurs when the connection plate bends and reduces the moment arm, d, to zero, which leads to direct loading of the anchorage by the membrane. It was recommended that case three could be avoided when designing the connection by amplifying the resultant axial force, T, by a factor of safety. The researchers tested a polyvinyl-chloride (PVC) liner and a steel sheet. The PVC was found to apply to case 1 because of its low modulus in which the membrane force T was easily resisted. The anchors were expected to be fixed along the leading edge of the connection plate to sustain their rigidity. This was validated by a finite element (FE) simulation. Case 2 and case 3 were found to apply to the high-modulus steel sheet material. Moment arm, rigid connection plate, and pivot point all exist in this case requiring large diameter concrete screws for anchorage and about 3 inches from the wall. They suggested that case 2 be employed when designing connections as it was taken to be more conservative because of the amplification of the anchorage force (i.e., A=2T).

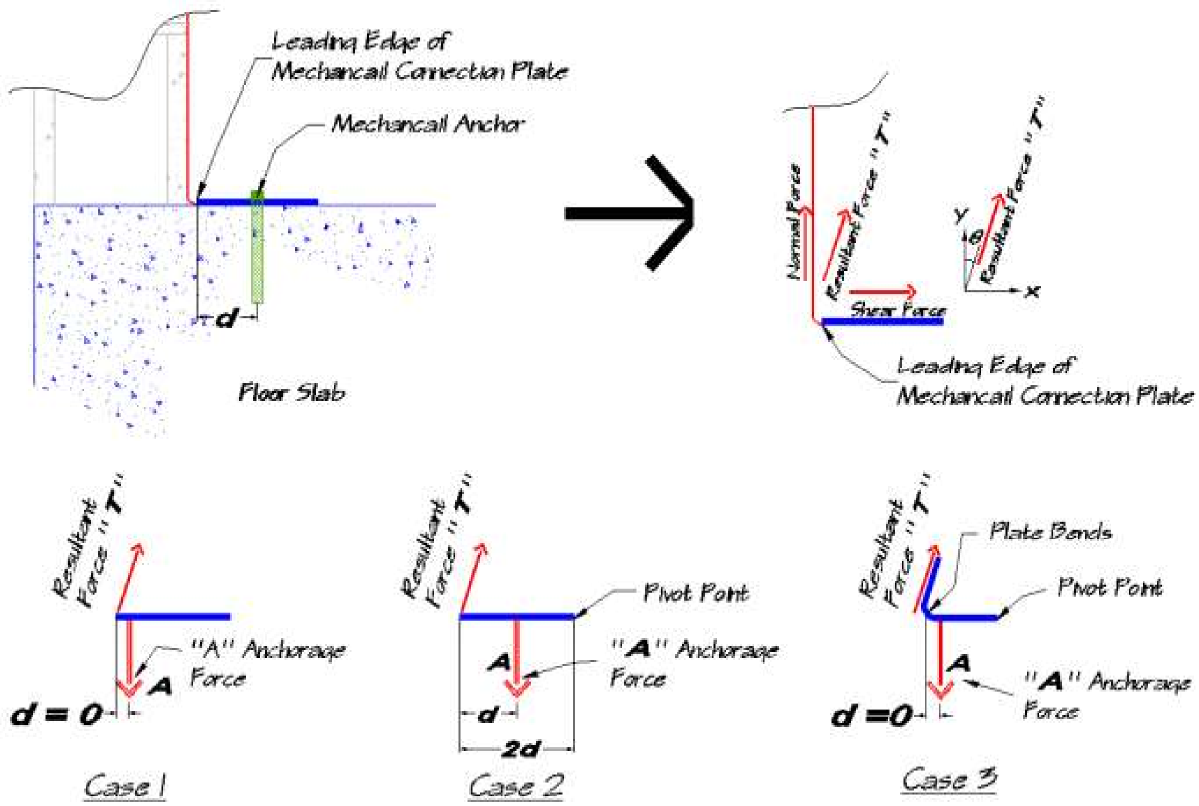

Figure 2.14. Free body diagram of connection plates (Hoemann et al. 2010)

2.11 Summary of Literature Review

The review of previous research helped identify research gaps. Essential conclusions that can be drawn from previous literature are summarized below:

- Blast load can exceed the capacity of structural and non-structural elements designed under ordinary gravity loads, including lateral seismic and wind loading. Therefore, elements must be designed to develop inelastic deformations and remain within the deflection tolerances.
- Arching action increases the resistance of masonry walls to lateral blast pressures. Arching action develops in infill walls that are restrained by enclosing rigid frame elements. Axial compressive forces develop as the wall flexes in the out-of-plane direction, developing cracks that tend to increase in length as the wall presses on its rigid frame supports (top and bottom). These arching forces increase wall resistance multiple times. Although arching introduces a measure of resistance to the wall, it is not sufficient to protect the wall against high blast loads. Therefore, there is a need to seek methods that could further increase the resistance of URM walls against lateral loads.
- Membrane retrofits on masonry walls can be applied as a catcher element or fully bonded material forming a composite action. The catcher membrane is installed not to have a direct connection to the masonry. They are designed to catch the fragments of the damaged wall. On the other hand, fully bonded membrane materials are applied directly on the tension side of the masonry, enhancing wall resistance. Bonded membrane materials affect the resistance functions of walls in a different way than the catcher membranes.

- Bonded membrane retrofits form a composite action with the URM wall and increase its blast resistance appreciably. Polyurea has proven to be an excellent membrane material for blast retrofitting URM walls. However, under intense blast loads, it could tear or partially de-bond with limited fragmentation control. Therefore, there is a need to develop reinforced membrane retrofit materials. Reinforced polyurea offers the potential for blast-hardening applications.
- The use of steel mesh to strengthen URM out-of-plane capacity was proven to be an effective material. Different orientations of steel mesh have been researched in the past, with 45^0 orientations giving a higher wall capacity, while $0^0/90^0$ orientations provide impact and higher energy absorption capacity. Stainless steel mesh provides higher resistance under higher strain rates, enhanced ductility, and stiffness at elevated temperatures. Hence, it is an excellent material to explore further, especially for use with polyurea to harden URM walls.
- SDOF dynamic analysis is a proven technique for accurately analyzing walls subjected to blast loads. A critical step in such an analysis is computing the resistance function, especially for walls made of composite materials.
- In retrofitting, *extend* the membrane to the surrounding supporting elements (slab/roof or beams) by 3in (76 mm) with a mechanical connection plate. For adequate safety, *the connections should have twice the membrane capacity.*

CHAPTER 3. EXPERIMENTAL PROGRAM

3.1 Test Matrix

Tests of large-scale URM walls were conducted as experimental investigations using the University of Ottawa shock tube as a blast simulator. *The experimental program involved six URM walls* built with 4" (100mm) blocks, retrofitted with steel wire mesh covered by spray-on polyurea. All the walls were built to introduce *instant arching actions* when subjected to blast loads. The walls were designed and tested in two categories: *non-load bearing and load bearing,* with slight differences in their retrofit designs. The non-load-bearing walls represented infill walls inside a structural frame, and the load-bearing walls were subjected to axial loads before blast testing, simulating the effects of existing vertical gravity loads. Blast loads were applied at different pressure levels using a shock tube. This chapter discusses the test specimens, material properties, test set-up, instrumentations, and loading protocols.

3.2 Details of Test Specimens

The laboratory work focused on testing six URM walls retrofitted with XS-350 polyurea reinforced with SS304 stainless steel mesh. Two block units, I) *solid stone blocks* and II) *CMU hollow blocks*, were used to construct the walls. Two walls were constructed with solid concrete stone blocks, while the remaining four were built with CMU hollow blocks. The CMU blocks were the same nominal size of 100 mm x 200 mm x 400 mm (with the actual size of 90 mm x 190 mm x 390mm), as shown in Figures 3.1a and 3.1b. The stone blocks were of four nominal sizes: 100 mm (W) x 180 mm (H) x 400 mm (L); 100mm x 180 mm x 330 mm;

100 mm x 100 mm x 300 mm; and 100 mm x 100 mm x 400 mm, as shown in Figure 3.1c. In some cases, the stones were hammered and chiseled to other sizes suitable for construction.

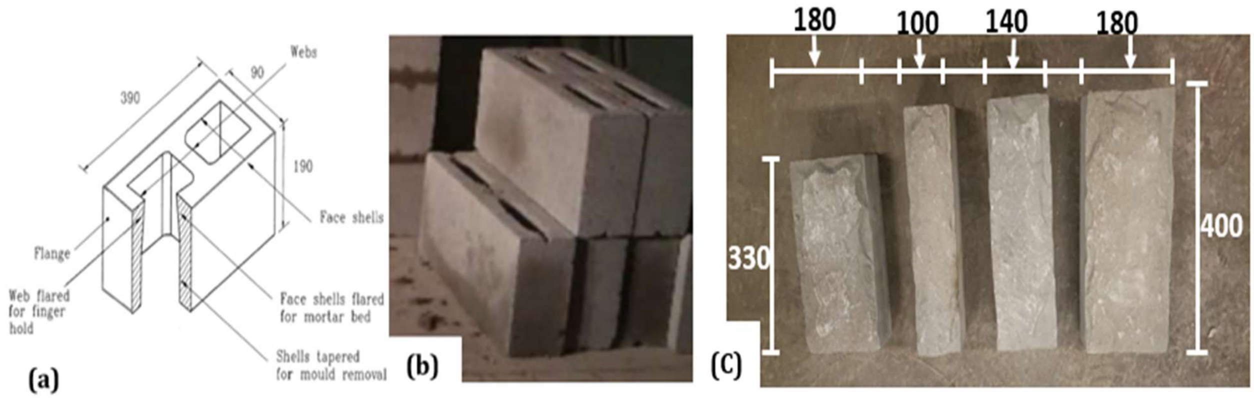

Figure 3.1. (a) Standard 100 x 200 x 400 CMU block (Glanville et al. 1996) (b) Typical CMU blocks used in the current test (c) Typical stone blocks of varying sizes used in current tests

All the test walls were built to have overall dimensions of 100mm x 2000mm x 2000mm (Figure 3.2). Type S and N mortars were used to lay block units. The walls were built separately into two reinforced concrete beams of 200mm x 200mm x 2400mm positioned at their top and bottom, respectively. This was done to create a real-life scenario of walls between concrete slabs/beams. The hardening/retrofitting was done by placing the stainless-steel mesh (SS304) on the tension side of the wall. Subsequently, the polyurea (XS-350) membrane was sprayed on the same side, bonding the mesh firmly to the wall. The XS-350 spray on polyurea was selected because of its high performance and physical properties, which are suitable for impact and abrasion resistance. SS304 mesh was chosen because of its high ductility (about 2 times more ductile than the typical low-carbon steel used in the construction industry). Two SS304 mesh wires of different sizes, 4.1mm, and 3.1mm, were used. These sizes resulted in the percentage of steel closer to that used in the earlier phase of research, which showed favorable performance. The mesh opening size was the same in all cases, with a square opening size of 76.2mm by 76.2mm. The mesh was placed on the wall surface such with the longitudinal wires (main flexural reinforcement) being closer to the wall surface for increased bond with masonry. The walls were classified based on the type of masonry, mortar, axial load, and the area of stainless-steel mesh used. All the hardened walls had a 6 mm thick polyurea layer. This thickness is considered maximum practical thickness in practice for maintaining uniform application by the polyurea professionals. Table 3.1 summarizes the properties of the wall specimens tested. The table also includes two control walls, one non-load bearing and the other load bearing, which Ciornei (2012) tested earlier for the same overall research program.

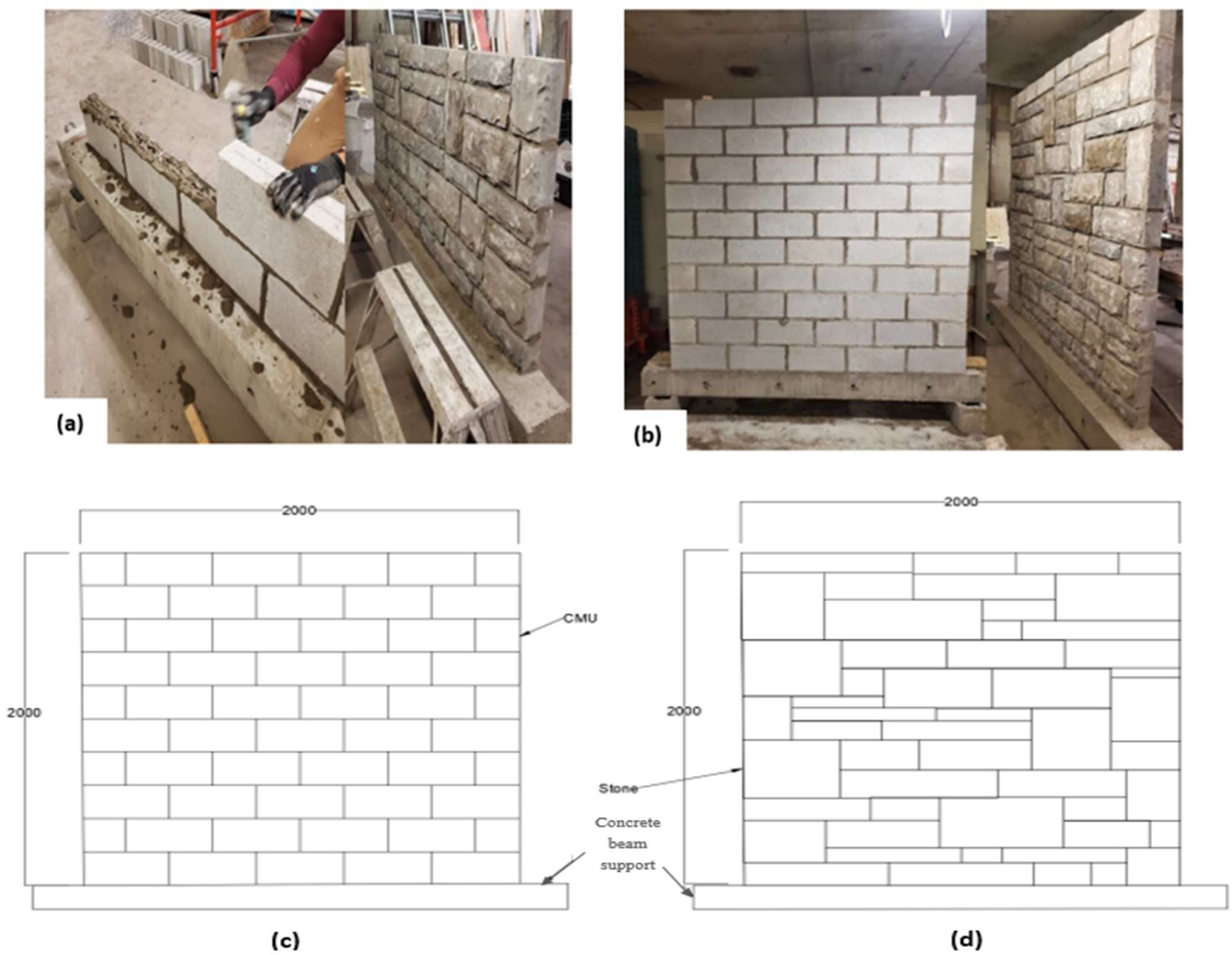

Figure 3.2. (a) Construction of CMU and stone wall in progress (b) Completely built CMU and stone walls (c) CMU wall with dimensions (d) Stone wall with dimensions

Certified masons were hired to construct the walls. Each wall was built such that the top gap (the gap between the wall and the top reinforced concrete beam) was filled with high-strength mortar to instantly activate the arching action upon applying blast loads. The walls were cured over 28 days. The stability of the walls was ensured by bracing them with wooden frames until they were hardened.

Table 3.1: Description of control and retrofitted URM walls

Test Walls	Group	URM Type	Polyurea/ Thickness (mm)	SS304 Size (mm)	Axial Load (kN)
***URM-1**	Non-load bearing	CMU	-	-	-
Wall-1		Stone	XS-350/6	3.1	-
Wall-2		CMU		4.1	-
Wall-3		CMU		3.1	-
***URM-3**	Load-bearing	CMU	-	-	122
Wall-4		Stone	XS-350/6	4.1	120
Wall-5		CMU		3.1	120
Wall-6		CMU		4.1	180

*Tested by *Ciornei (2012)*

Fifty hollow CMU blocks were used to construct each CMU wall in a stretcher bond pattern, whereas the stone walls were built using different-sized stones in an uncoursed pattern. The non-load bearing walls were built using Type N mortar, and the load-bearing walls were built using Type S mortar.

The following steps were used for hardening the walls with polyurea:

1. The wall surfaces were kept clean, dry, and free of oil or other substances that could weaken adhesion.
2. The stainless-steel meshes were mounted and held in place on each wall at an orientation of 0/90 degrees to the horizontal mortar joint of the wall with the aid of construction glue.
3. A wooden frame was mounted across the wall's surface to ensure that the construction glue tightly held the stainless-steel mesh to the wall. The frame was kept for over 24 hours to allow the binder to properly dry and establish a firm bond between the mesh and the wall.
4. SS304L (3.1mm dia.) mesh was mounted on Wall-1, Wall-3, and Wall-5, while SS304 (4.1mm dia.) mesh was mounted on Wall-2, Wall-4 and Wall-6.
5. After 48 hours, the wooden frames were removed, and a layer of 6 mm XS-350 polyurea was sprayed on the wall using a high-pressure spray gun. This process ensured full composite action between the stainless-steel mesh, the masonry wall, and the polyurea membrane. Because of the material's toxicity, precautions were taken to prevent air pollution while applying polyurea.

Figure 3.3 illustrates each step of the hardening process. After the wall hardening was completed, the walls were placed in the square opening of the expansion chamber of the shock tube for testing. Two hydraulic jacks placed on their top reinforced concrete beam subjected the load-bearing walls to vertical axial loads. Figures 3.4a and 3.4b illustrate typical load-bearing and non-load-bearing test specimens before testing. The axial load was readjusted after each shot to maintain constant level of axial compression in all tests.

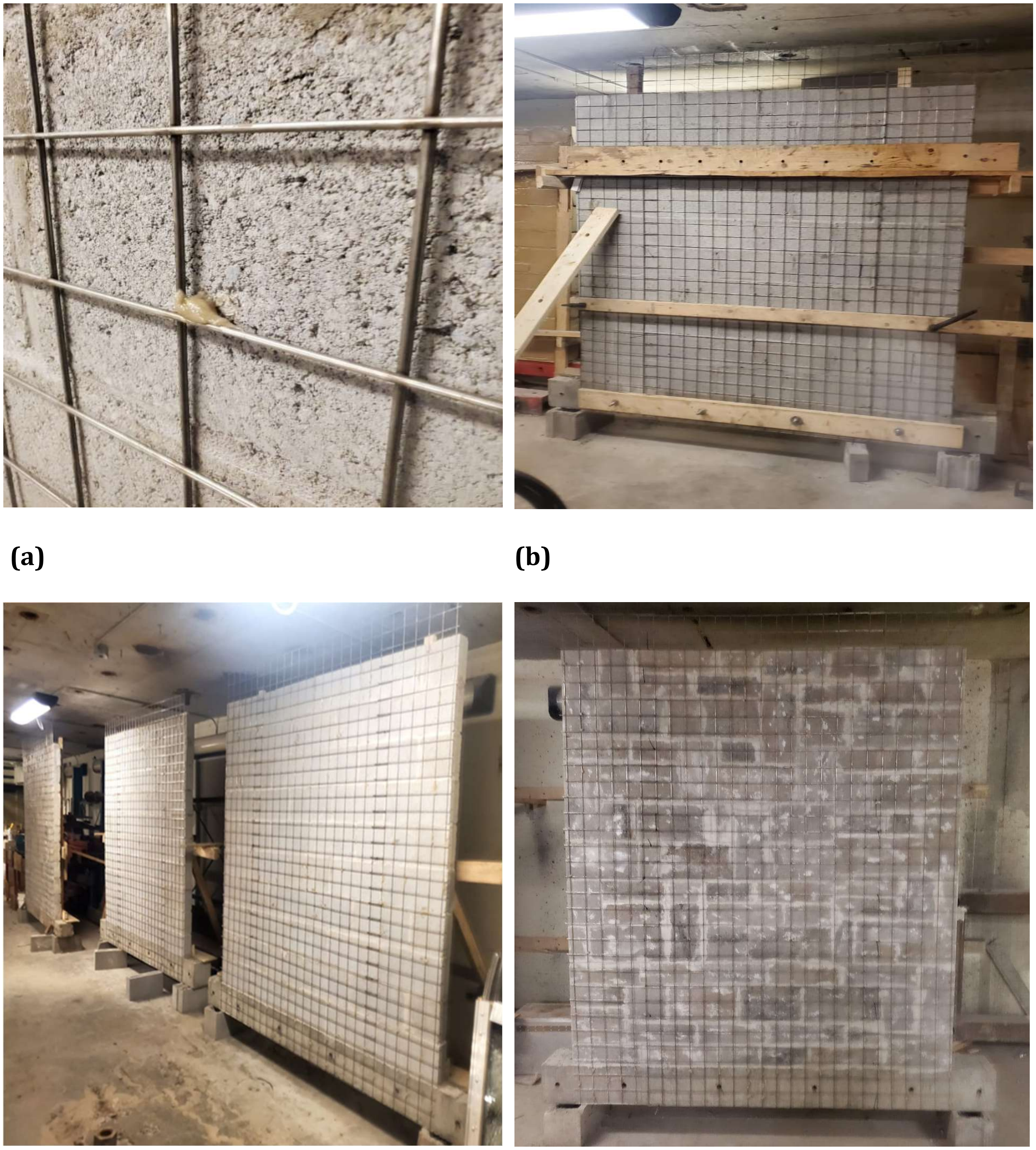

(a) (b)

(c) (d)

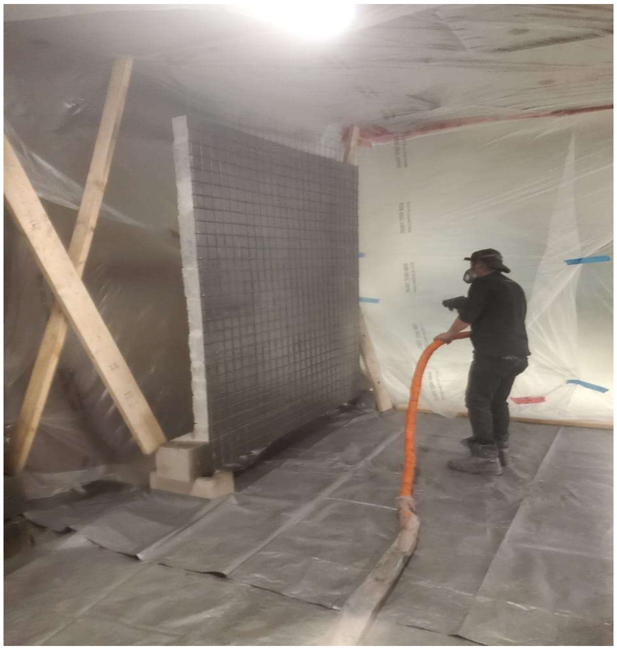

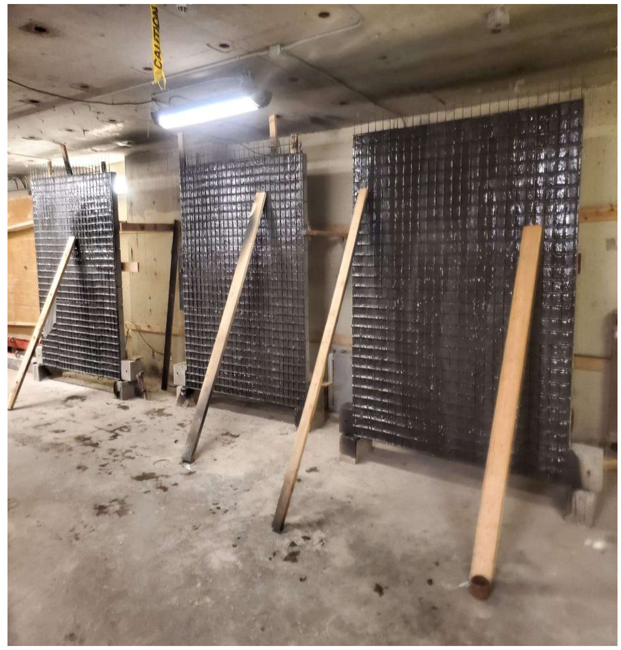

(e) **(f)**

(g) **(h)**

Figure 3.3. (a) Mesh held in place with construction glue on the wall (b) Mesh held tightly in place to the wall with wooden frames (c) Mesh firmly in place on CMU walls without wooden frames (d) Mesh mounted on stone wall (e) Spraying of XS-350 polyurea on the wall with mesh (f) Complete wall retrofitting (g) Placing retrofitted wall into the shock tube opening (h) Retrofitted wall set for test

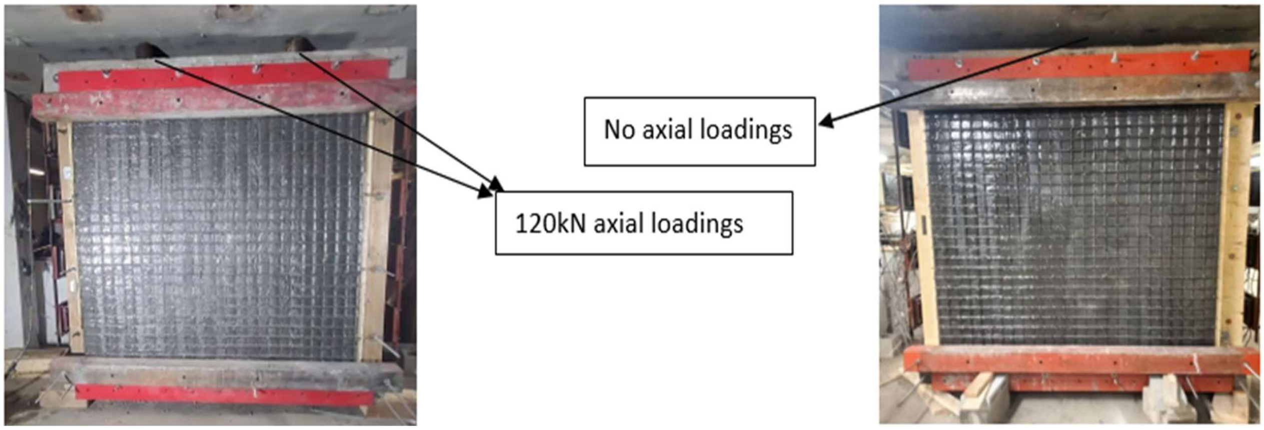

Figure 3.4. (a) Retrofitted wall with axial loading (load bearing) (b) Retrofitted wall without axial loading (non-load bearing)

3.3 Material Properties

3.3.1 Compressive Strength of Mortar Cubes (CSA A179)

The two types of mortar, N and S, were mixed with water to produce a 100% to 115% flow. Per mortar type: Six 50 mm mortar cubes were prepared, cured for 28 days, and tested using the concrete cylinder testing machine at the structures laboratory. Type N mortar cube strengths were measured to be 4.4 MPa, 5.7 MPa, 5.1 MPa, 4.5 MPa, 4.9 MPa, and 5.0 MPa, given an average compressive strength of 5.0 MPa. Also, Type S mortar cube strengths were measured to be 13.0 MPa, 12.2 MPa, 11.9 MPa, 12.4 MPa, 13.5 MPa, and 12.5 MPa, given an average compressive strength of 12.4 MPa. Figure 3.5 shows the mortar test.

Figure 3.5. Compressive strength test of mortar cubes

3.3.2 Specified Compressive Strength of CMU (CSA S304-19, Annex D, CSA A165.1)

The specified compressive strength of CMU prisms was determined using CSA S304-19, Annex D. The prisms were tested as ungrouted assemblages of 400mm hollow stretcher units. The following steps were taken:

The masonry prisms were constructed with face shell bedded only and in a running bond pattern using saw-cut stretchers as half units, with saw cuts facing outward, one unit in length, and three courses tall.

The dimensions of the whole unit CMU blocks were 90mm (W) x 190mm (H) x 390mm (L), while that of the half unit was 90mm (W) x 190 mm (H) x 195 mm (L).

Prisms were constructed using type S mortar according to the proportion specifications of CSA A179-19 (7.1.1).

The strength of the prisms was measured to be 12.9 MPa, 12.6 MPa, 11.5 MPa, 11.0 MPa and 11.2 MPa. The specified compressive strength, f'_m, was determined to be 10.4 MPa according to the statistical method specified by CSA S304-19, Annex C.

The preparation and testing of the prisms are illustrated in Figure 3.6. The compressive stress-strain curves of CMU prisms are presented in Figure 3.7.

(a)

(b)

Figure 3.6. CMU prism (a) before the test and (b) after failure

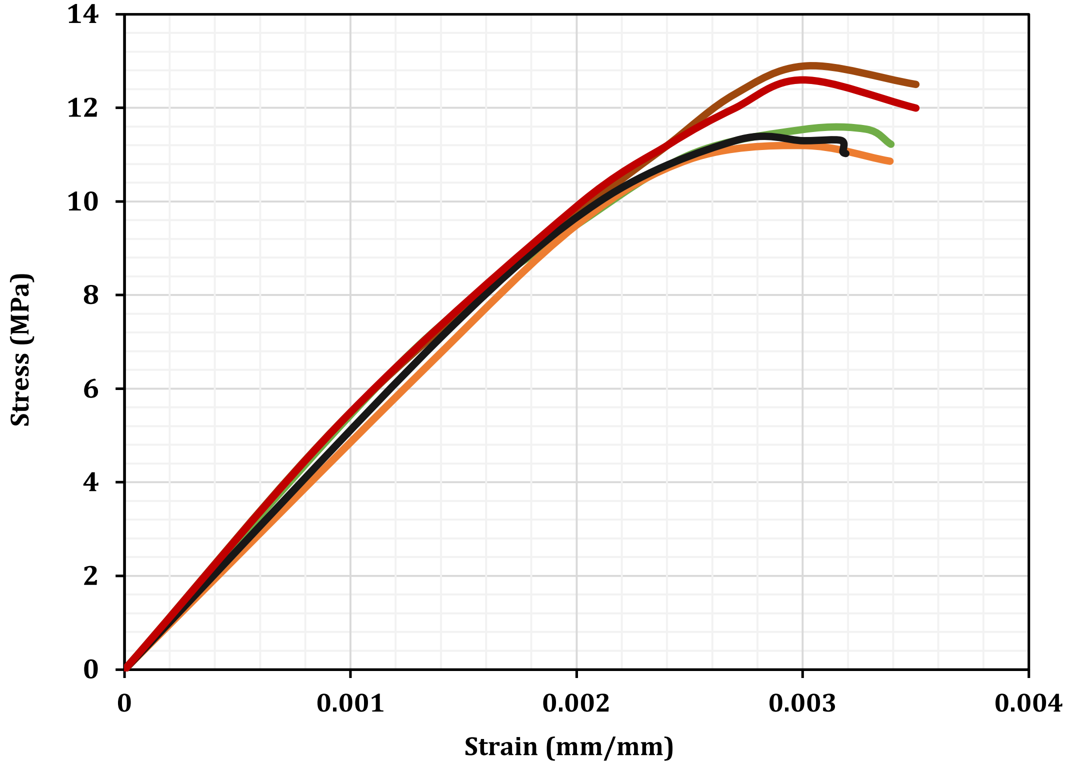

Figure 3.7. Compressive stress-strain curves of CMU prisms

3.3.3 Stone Prism Test (CSA S304.1-04 Annex D)

Five stone prisms were constructed. Each prism comprised four blocks of different sizes laid in an uncoursed pattern to replicate the stone test walls. The prisms were built to be two-course tall using type S mortar and tested under concentric compression. The results were 11.2 MPa, 11.9 MPa, 12.9 MPa, 11.1 MPa and 11.0 MPa. The specified masonry strength, f'_m, was determined to be 10.3 MPa according to the statistical method specified by CSA S304-19, Annex C. Figure 3.8 illustrates typical prism tests before and after the failure and the compressive stress-strain curves of stone prisms can be seen in Figure 3.9.

(a)

(b)

Figure 3.8. Stone prism (a) before test and (b) after failure

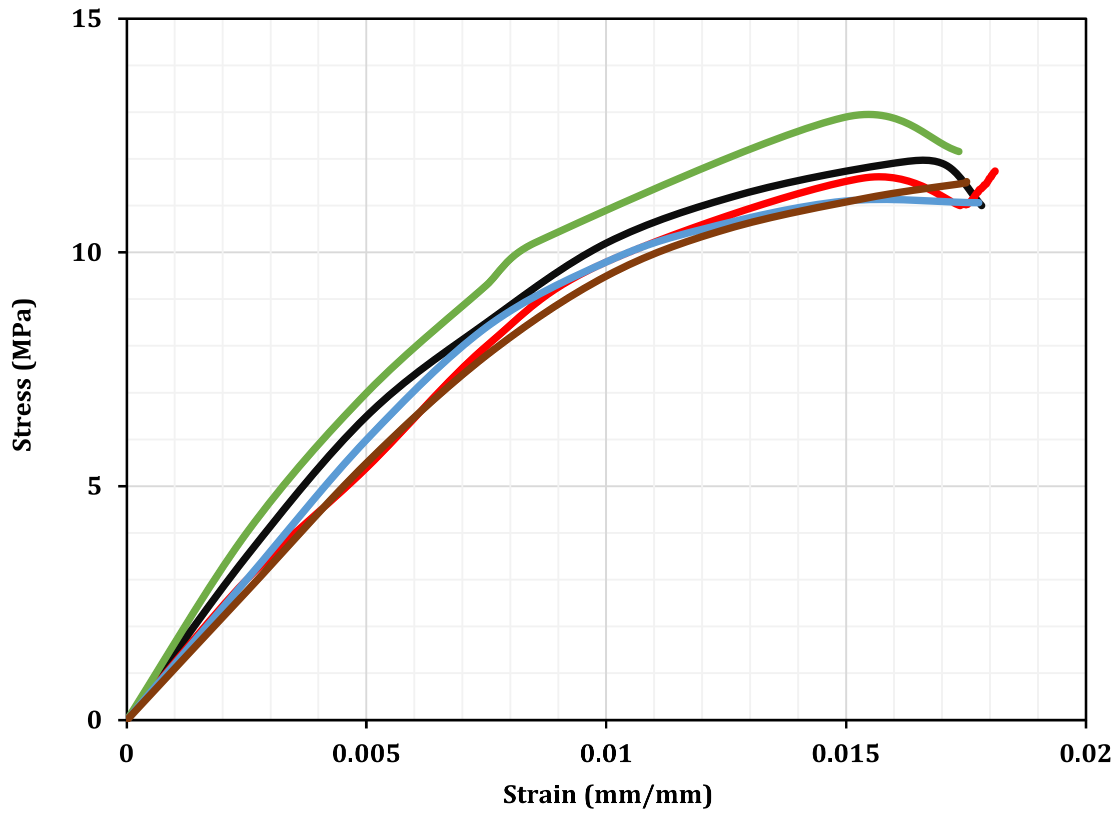

Figure 3.9. Compressive stress-strain curves of stone prisms

3.3.4 XS-350 Polyurea Coupon Test (ASTM D412-06a)

Three coupons were prepared to establish stress-strain relationships of the polyurea used in the wall tests. Each coupon was cut into a dumbbell shape and placed in the grips of the universal testing machine with tension applied symmetrically across its section and 50 mm extensometer was attached to the center of each coupon for accurate measurement. Figure 3.10 shows the configuration, testing, and rupture of the coupons. Figure 3.11 shows the stress-strain characteristics for the three coupons tested in tension. Furthermore, Table 3.2 summarizes the mechanical properties of the XS-350 polyurea material.

Figure 3.10. XS-350 polyurea coupon test

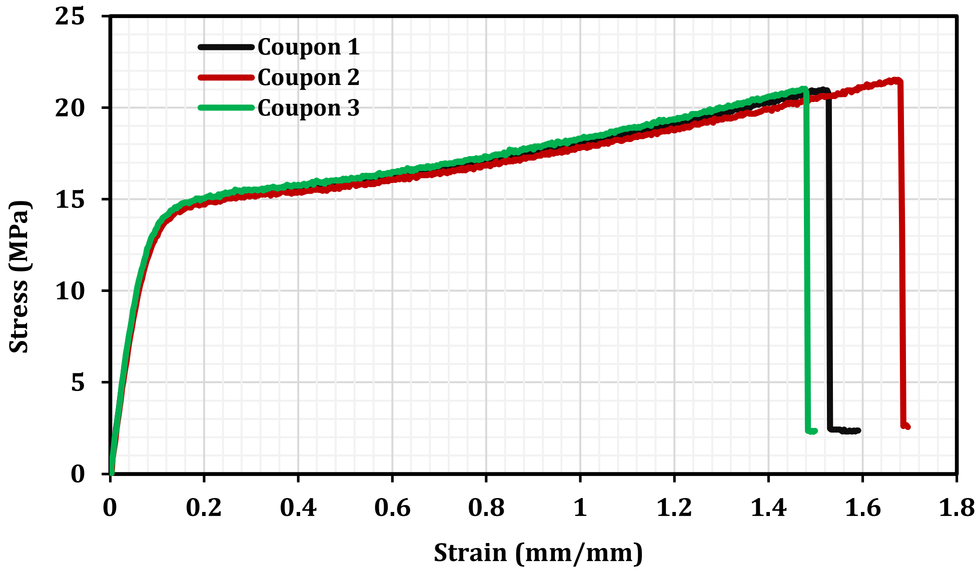

Figure 3.11. Stress-strain curve from XS-350 polyurea coupon test

Table 3.2: Material properties of XS-350 polyurea

Material Properties	Coupon 1	Coupon 2	Coupon 3
Yield Strength (MPa)	10.9	10.7	11.4
Tensile Strength (MPa)	21.0	21.5	21.0
Ductility %	152.0	168.0	148.0
Toughness (MPa)	25.3	28.8	25.1
Elastic Modulus (MPa)	247.7	247.9	241.5

3.3.5 Tensile Test for SS304-Mesh (ASTM E8)

Direct tension tests were performed on both mesh reinforcement sizes (Dia. 3.1mm and Dia. 4.1mm mesh sizes). Each mesh was cut into three wires of 700 mm in length. They were each placed in the grips of a universal testing machine, and a 50 mm extensometer was attached to the center of each wire. The tests were conducted at a speed of 15 mm/min. Figure 3.12 shows the test setup and the ruptured strands. Figure 3.13 shows the stress-strain curves for both types of wire. Using the 0.2% offset method, the dia. 3.1 mm yielded at 510 MPa, while the dia. 4.1mm wire yielded at 530 MPa. Further, the larger diameter wire had a higher ultimate strength at a lower strain than the smaller one. Table 3.3 shows the properties of both meshes.

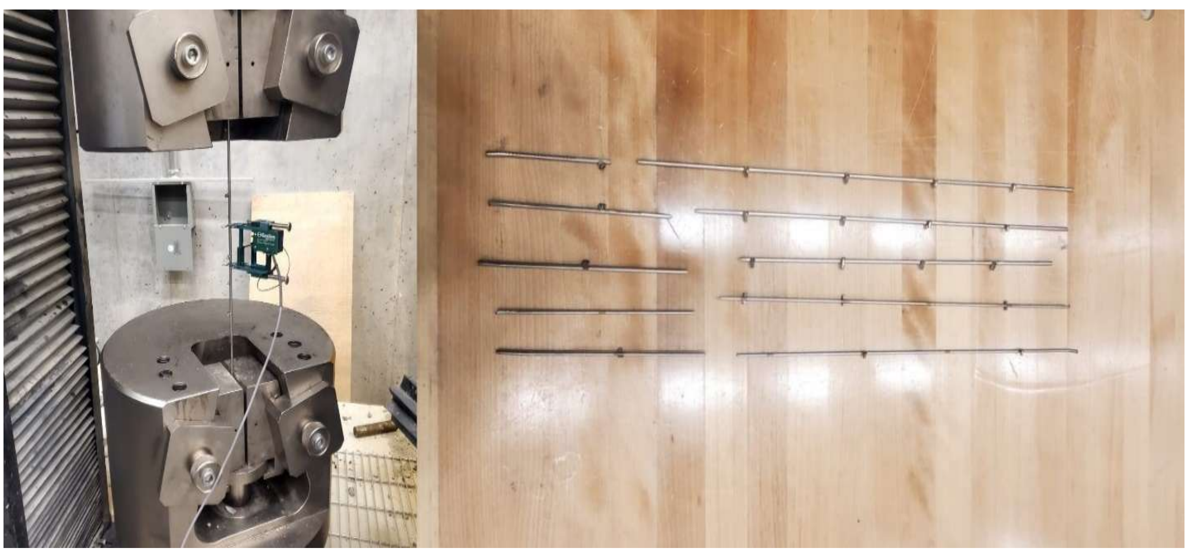

Figure 3.12. Tensile test for a strand of SS304

Table 3.3: Material properties of SS304 mesh

Material Properties	SS304-3.1 Dia.	SS304-4.1 Dia.
Yield Strength (MPa)	510	530
Tensile Strength (MPa)	702	788
Elastic Modulus (MPa)	195, 073	227, 053
Ductility (%)	45	42
Toughness (MPa)	270	288

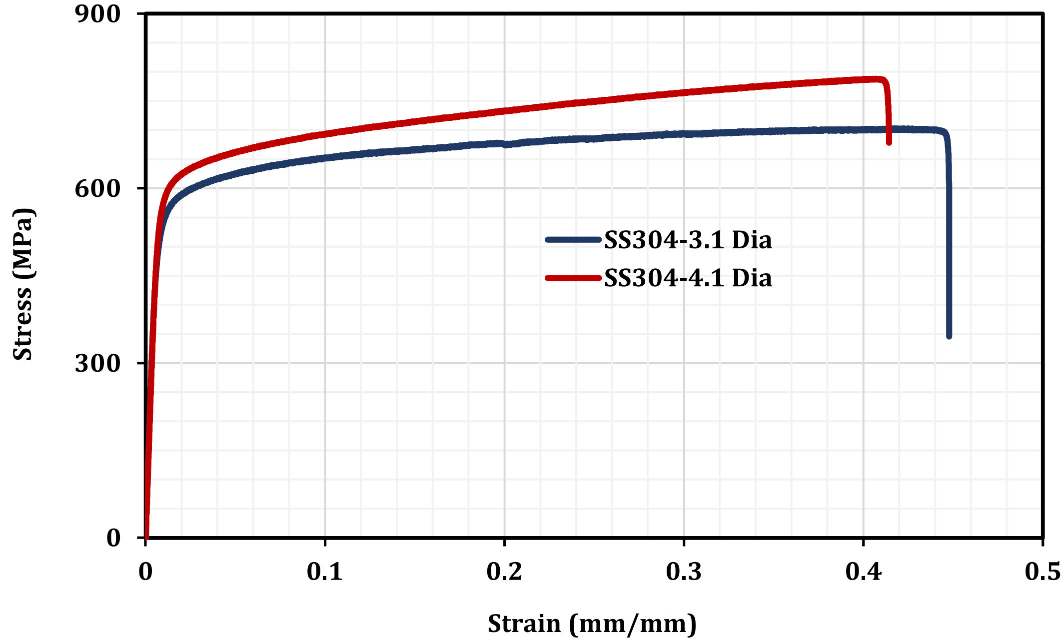

Figure 3.13. Stress-strain curve for SS304 mesh

3.4 Test Setup, Instrumentation and Loading Protocol

3.4.1 Shock Tube Facility

The equipment used for testing the walls is a shock tube situated in the Structural Engineering Laboratory of the University of Ottawa. The shock tube is a blast simulator built and designed to test the response of structural components when exposed to blast loads. The device can generate varying blast pressures and is a suitable alternative to real-life explosives. It consists of three components: An extendable driver section, a double diaphragm spool section, and an expansion chamber section with a square end opening of *2032mm by 2032mm* that accommodates test specimens. The driver length can be varied from *305mm to 5185mm*. The double diaphragm spool section connects the driver section to the expansion chamber, i.e., the driver-spool section and spool-expansion section. Aluminum foils are installed into the driver-spool and spool-expansion sections; they provide pressure balance between the driver and spool sections. The foils have a square dimension of 813 mm by 813 mm. They have nominal strength of *34 kPa, 90 kPa, and 172 kPa* and corresponding thicknesses of 0.127 mm, 0.203 mm, and 0.356 mm. The intended driver pressure governs the number of foils installed. The working mechanism of the shock tube involves filling the driver and spool section simultaneously with air from an air compressor regulated by a firing station control box and measured by static pressure gauges until their desired pressures are achieved (the air pressure in the spool section is usually half of that in the driver section). Then, a gradual release of air from the spool section regulated by the control box creates a pressure gradient force between the driver-spool interface. Then, the compressed air from the driver section causes the aluminum foils installed in the driver-spool diaphragm and those installed in the spool-expansion diaphragm to rupture simultaneously. The compressed air travels at supersonic velocity through the entire length of the expansion chamber until the pressure hits the test specimen mounted at the opening of the shock tube. To ensure full interaction between the blast and the specimens, any existing gaps between the shock tube opening and test samples are sealed with wooden frames. Also, four pressure relief vents exist on each side of the square opening to allow the blast pressure to dissipate quickly. A blast/explosion results from this operation, with the specimen either resisting/deflecting excessively or failing completely, which happens in milliseconds. Figure 3.14 shows the details of the Shock Tube.

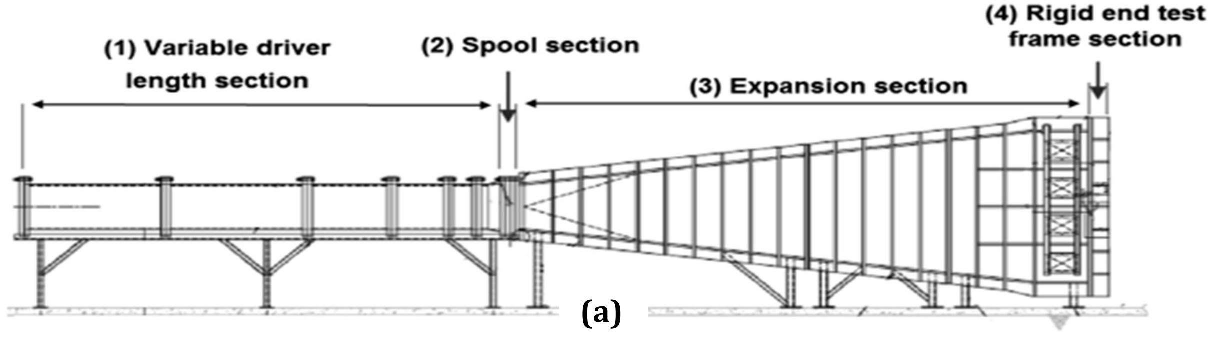

(a)

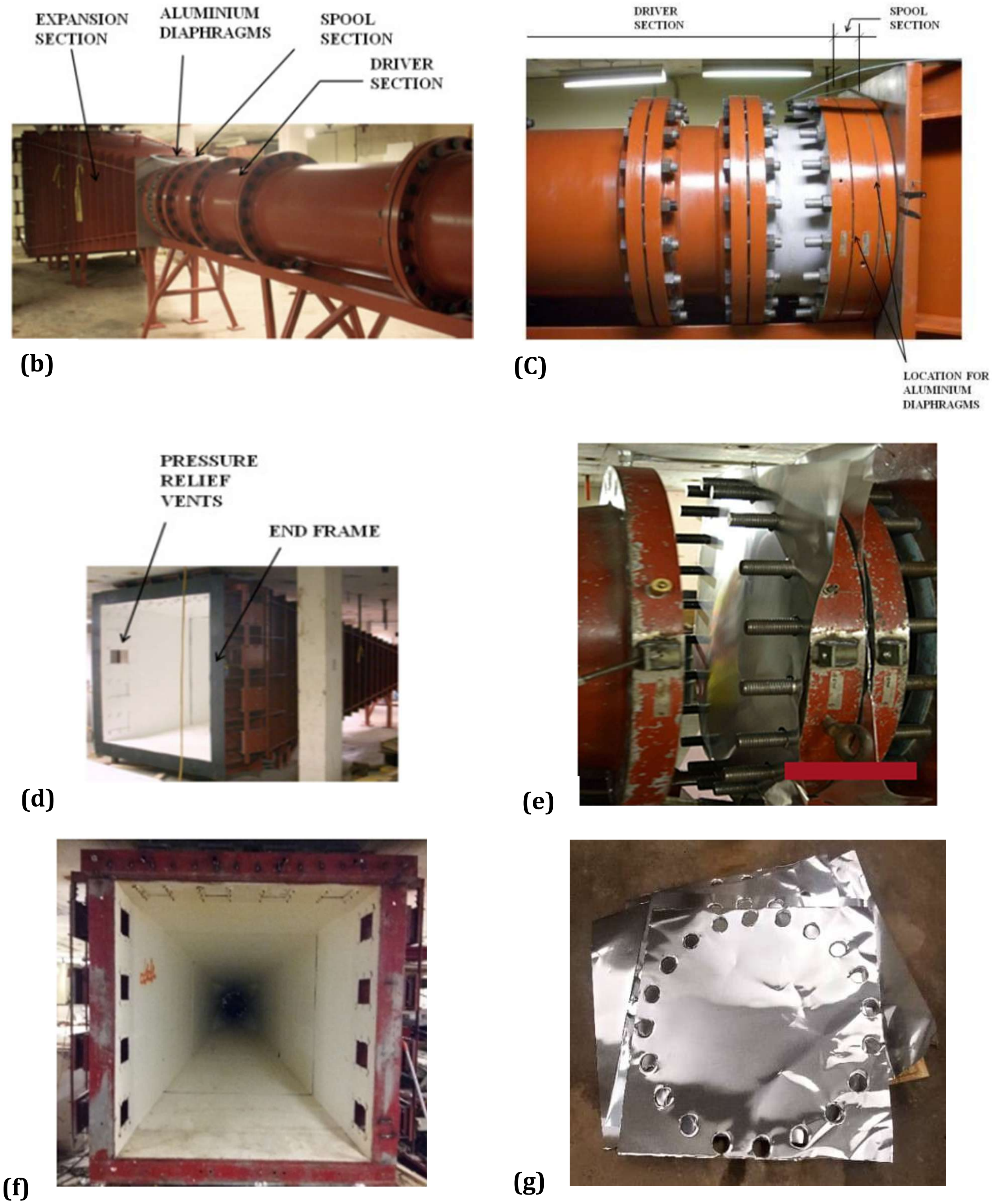

Figure 3.14. (a) Schematic diagram of the shock tube (b) Shock tube rear view (c) Spool-diaphragm section (d) Expansion chamber with square end opening (e) Diaphragm with aluminum foils (f) End opening with vents (g) Aluminum foils

3.4.2 Instrumentation and Data Acquisition

The shock tube is equipped with pressure transducers to measure reflected overpressures at the end of the tube and in the driver and spool sections. Two pressure transducers are placed close to the test samples to record reflected pressures. Each wall was instrumented with a Linear Variable Displacement Transducer (LVDT) to measure horizontal deflections. All transducers were connected to a Data Acquisition system (DAS), which was connected to a computer to record and monitor the test remotely. Two high-speed video cameras and camera tracking software were used to record the deflected shape of the test walls. The cameras record at a rate of 2000 frames per second (fps) and act as backup devices for displacement measurement. Figures 3.15, 3.16, and 3.17 show the instrumentation and the test setup. Table 3.4 shows the shock tube blast properties and their equivalent TNT values.

3.4.3 Test Arrangement and Loading Protocol

The test walls were attached to the top and bottom of the shock tube frame around the square test area without restraints along the vertical edges to simulate a one-way action. The walls were fixed to the shock tube by clamping the ends by means of HSS element. The clamping action did not provide significant fixity, and the supports were observed to rotate during testing, creating boundary condition close to a pin-pin connection. Steel plates were also used at the supports to prevent out-of-plane sliding.

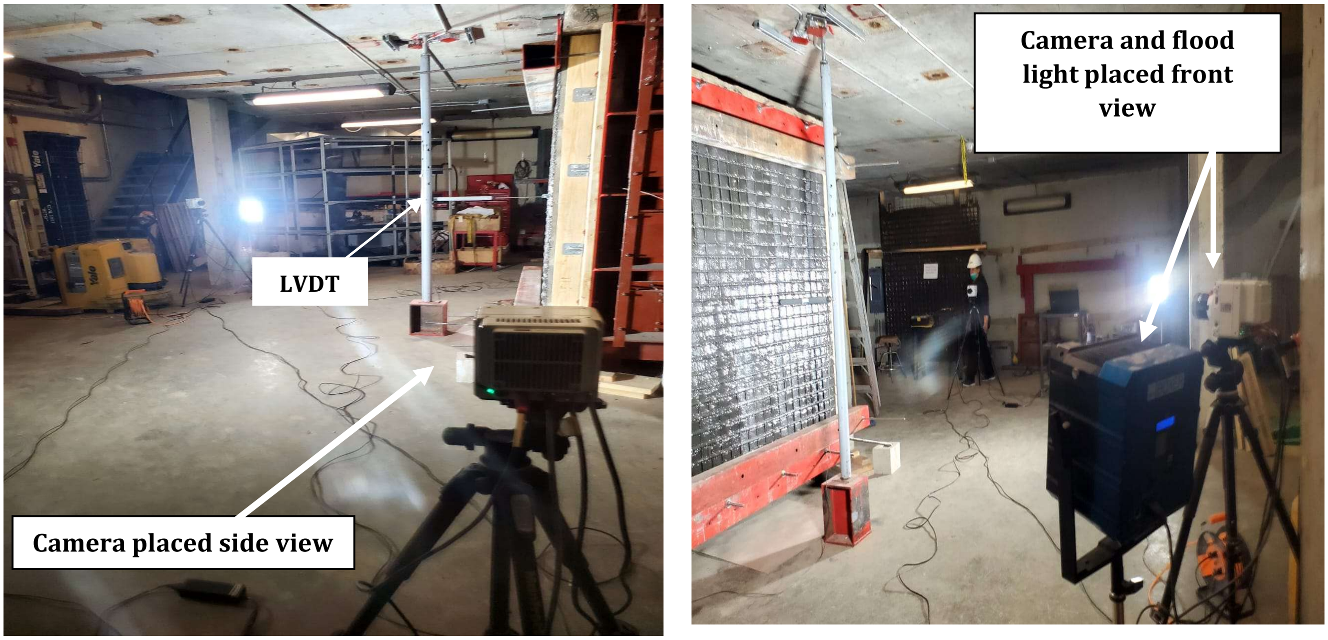

Figure 3.15. Instrumentation set up

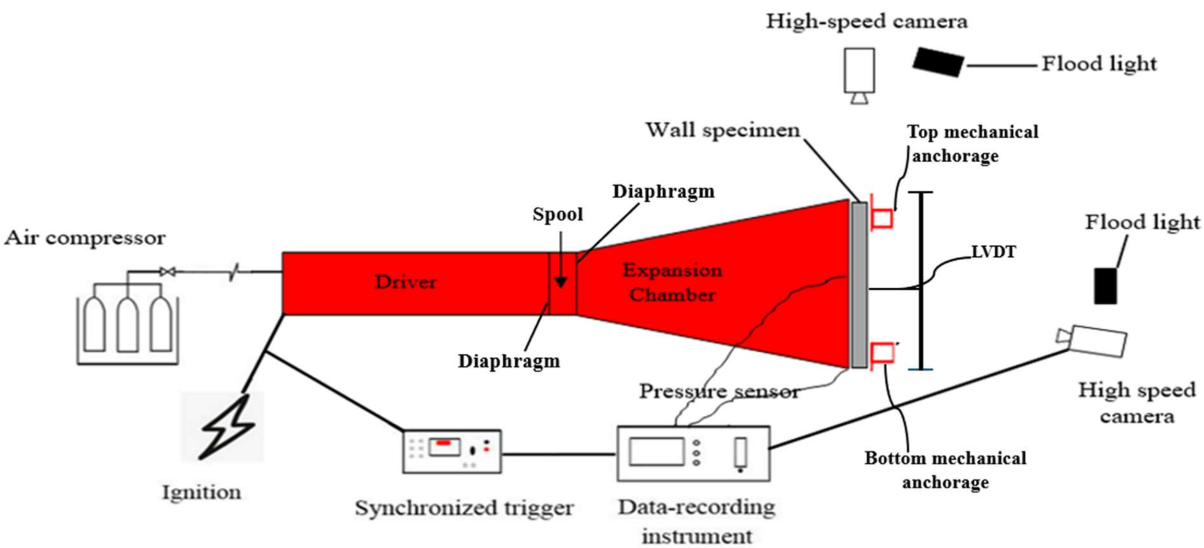

Figure 3.16. Schematic diagram of the shock tube and its instrumentation setup

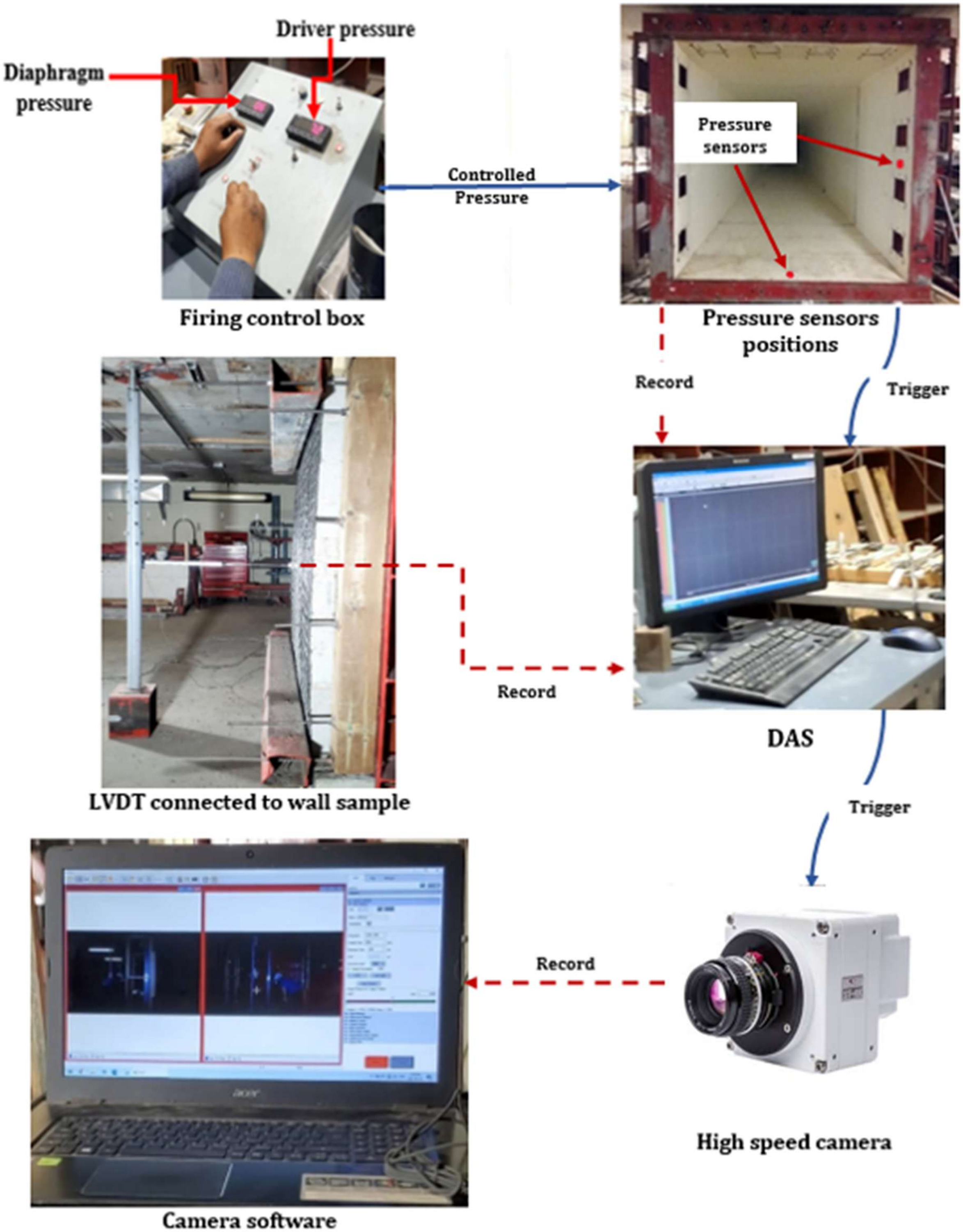

Figure 3.17. Instrumentation and data acquisition setup of the shock tube

CHAPTER 4. EXPERIMENTAL RESULTS

4.1 General

This chapter presents experimental results obtained during the test program. Four CMU walls and two stone walls were retrofitted with reinforced polyurea (SS304/SS304L + XS-350 polyurea) and were subjected to several blast shots. The blast shots increased successively until the failure of the walls was achieved. Data was recorded, and observations were made to assess the performance of each specimen with specific test parameters. The driver pressure (P_D) and driver length (L_D) of the shock tube were used to determine the reflected pressure (P_r) and positive phase duration (t_d) of the blast, respectively. The relationship between the recorded pressure and the positive phase duration is described graphically, and the area under the pressure-time history curve is computed as an impulse (I_r). The response of non-load bearing and load-bearing walls was measured using their maximum mid-height displacements (d_{max}) and residual displacements (d_{res}). These values are presented graphically as displacement-time histories. Also, pictures showing the gradual damage imposed on the walls at different stages of loadings are presented. The test samples are labeled as "Wall" followed by two numbers representing the wall and shot numbers. For instance, Wall-1-1 means the first wall subjected to the first shot.

4.2 URM-1: Non-Load Bearing Control Wall

Wall URM-1 was presented by Ciornei (2012) as a control in an earlier phase of this research program, and it has been adopted as a reference for the non-load-bearing walls in this present research. The wall is an unretrofitted non-load bearing built with the same materials and specifications as the test walls used in this experiment. It was constructed with standard

100mm x 200mm x 400mm hollow concrete masonry unit (CMU) blocks and Type S mortar joints of 10mm thickness. Its surface area was 2000mm x 2000mm, and no axial load was applied. The summary of its test results is given in Table 4.1.

Table 4.1: Summary of test results of control wall URM-1 (Ciornei 2012)

CONTROL	P_D (kPa)	L_D (mm)	P_r (kPa)	I_r (kPa-ms)	t_d (ms)	d_{max} (mm)	d_{res} (mm)	θ_{max} (degrees)
URM-1-1	40	1828.8	6.1	53.1	10	9.1	6.2	0.5
URM-1-2	75.8	1828.8	13.7	150.9	11.4	23.8	12	1.4
URM-1-3	125.5	1828.8	23.4	179.3	13.5	56.5	13.9	3.2
URM-1-4	165.5	1828.8	30.7	265.1	13.9	n/a	n/a	n/a

4.3 URM-3: Load Bearing Control Wall

Ciornei (2012) also tested this second wall earlier and used it as the control Unretrofitted load-bearing wall. The wall was tested under a constant axial load of 122 kN; it has the same construction materials and specifications as the load-bearing walls used in this research. Therefore, it has been adopted as the reference load-bearing wall. The results of its tests are summarized in Table 4.2.

Table 4.2: Test Results of the load-bearing control wall URM-3 (Ciornei 2012)

CONTROL	P_D (kPa)	L_D (mm)	P_r (kPa)	I_r (kPa-ms)	t_d (ms)	d_{max} (mm)	d_{res} (mm)	θ_{max} (degrees)
URM-3-1	34.5	1828.8	6.1	49	9.4	1.1	0.4	0.06
URM-3-2	79.3	1828.8	13.2	121.9	12.7	8.2	1.6	0.47
URM-3-3	121.4	1828.8	24.7	193.3	13.5	16.6	3.2	0.95
URM-3-4	166.9	1828.8	28	271.9	13.6	28.6	5.3	1.64
URM-3-5	212.4	1828.8	37.7	309.2	13.7	45	8.7	2.58
URM-3-6	248.2	1828.8	39	290.8	12.9	41.7	8.7	2.39
URM-3-7	288.2	1828.8	51	414.6	14.5	N/A	N/A	N/A

4.4 Wall-1

Wall-1 was constructed as a stone masonry non-load bearing wall adopting an uncoursed laying pattern with no gaps between it and its support frames to initiate quick arching action during testing. It was retrofitted with reinforced polyurea-3.1 mm. No axial load was applied to it. Four progressively increasing shots were applied (Wall-1-1, Wall-1-2, Wall-1-3, Wall-1-4) until the wall reached its global failure, as shown in Table 4.3. The driver length of the shock tube was kept at 1829mm (6ft) for all shots to determine their load duration in each case.

Table 4.3: Summary of test results of Wall-1

Wall Type	Wall-1	P_D (kPa)	L_D (mm)	P_r (kPa)	I_r (kPa-ms)	t_d (ms)	d_{max} (mm)	d_{res} (mm)	θ_{max} (degrees)
STONE	Wall-1-1	207	1829	43	301	16	16	NA	1
	Wall-1-2	345	1829	57	403	16	26	6	1.5
	Wall-1-3	483	1829	67	542	18	39	14	2.2
	Wall-1-4	621	1829	93	711	24	100	74	5.7

4.4.1 Test Wall-1-1

This marked the commencement of the blast tests. Three aluminum foils were used, two installed in the driver-spool connection and one installed in the spool-expansion section connection. The driver section charged 30psi (207 kPa) of air pressure, and 15psi (103 kPa) pressure was injected into the spool section. The blast load was initiated when the air in the spool section gradually drained from the control box. The pressure gradient created between the driver and the spool caused the compressed air in the driver to rupture the foils (first shot) and impact the test wall attached to the open end of the expansion chamber. The incident pressure recorded was 22 kPa, while the peak reflected pressure generated was 43 kPa after air interaction with the wall. The reflected impulse over a positive phase duration of 16 ms was computed as 301 kPa-ms. A maximum mid-height deflection of 16 mm was recorded, producing 1^0 support rotations with no visible residual displacement or damage. Figures 4.1 and 4.2 depict the pressure and impulse time history curves and the pressure and displacement time history curves for Wall-1-1.

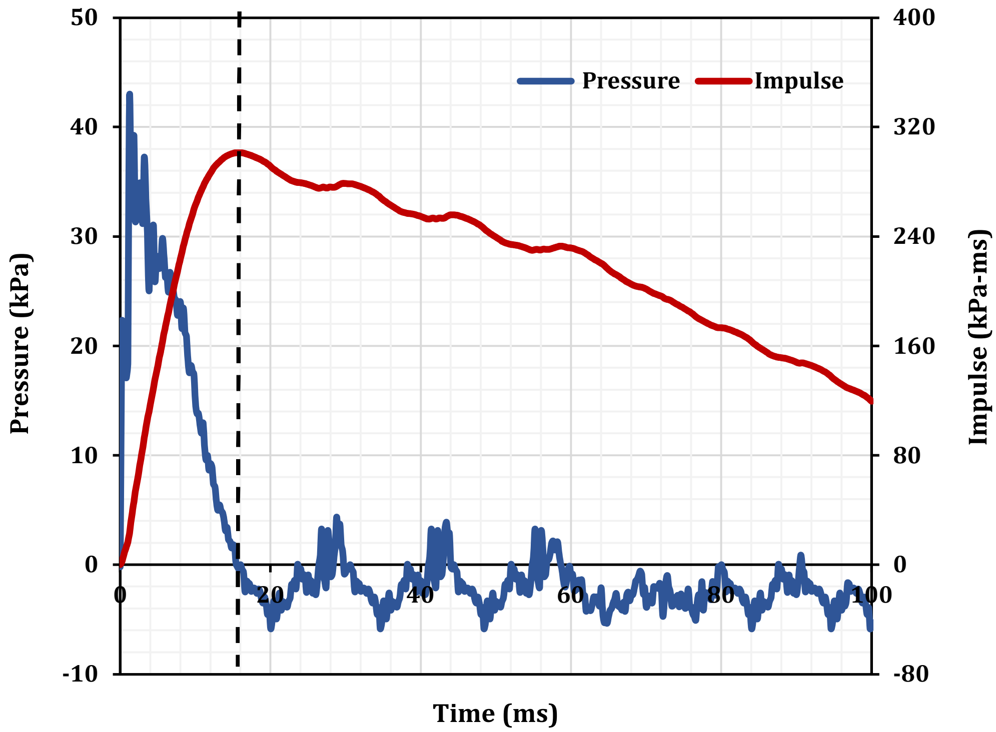

Figure 4.1. Pressure and impulse time history of Wall-1-1

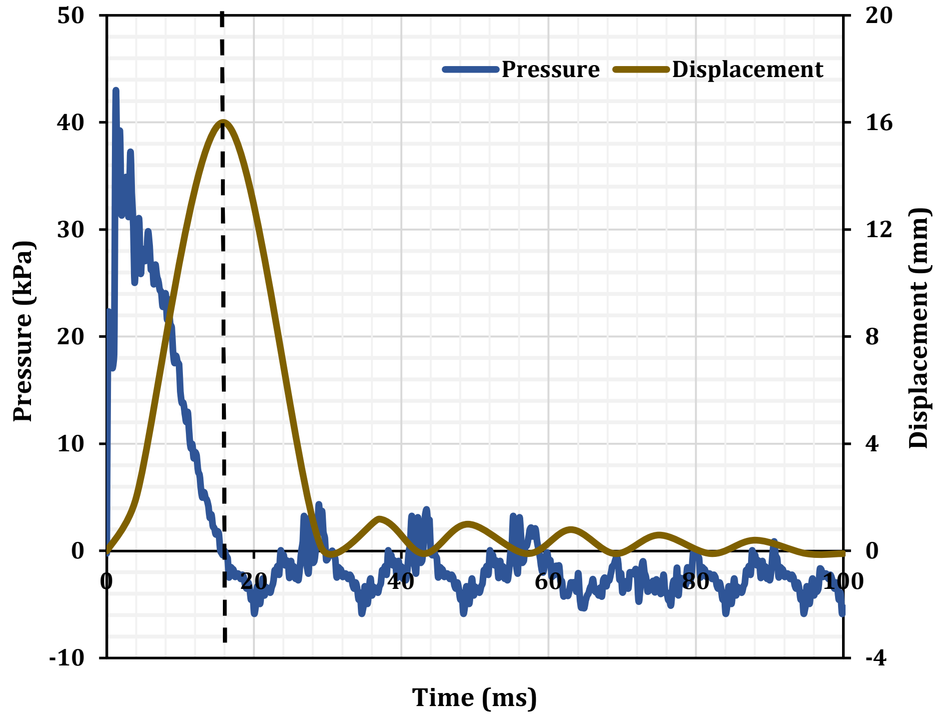

Figure 4.2. Pressure and displacement time history of Wall-1-1

4.4.2 Test Wall-1-2

Four foils were used for the second shot: two installed in the driver-spool diaphragm and two installed in the spool-expansion section diaphragm. 50 psi (345 kPa) of air was pumped into the driver section, and 25 psi (172 kPa) of air was pumped into the spool section. At the release of air into the spool, the foils ruptured with an incident pressure of 28 kPa, resulting in a peak-reflected pressure of 57 kPa within a positive phase duration of 16 ms and a reflected impulse over the positive phase of 403 kPa-ms. A maximum mid-height deflection of 26 mm was recorded, which caused a 1.5^0 rotation at the supports. Although no visible damage was seen, a residual displacement of 6 mm was sustained. Figures 4.3 and 4.4 show the recorded data in pressure and impulse displacement time history curves for Wall-1-2.

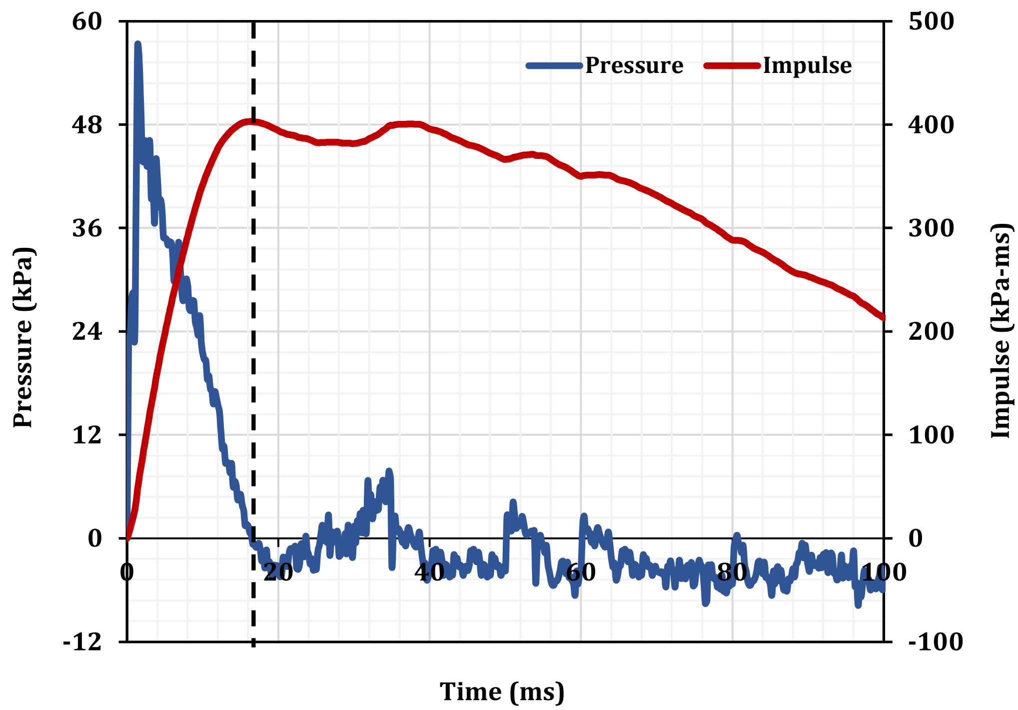

Figure 4.3. Pressure and impulse time history of Wall-1-2

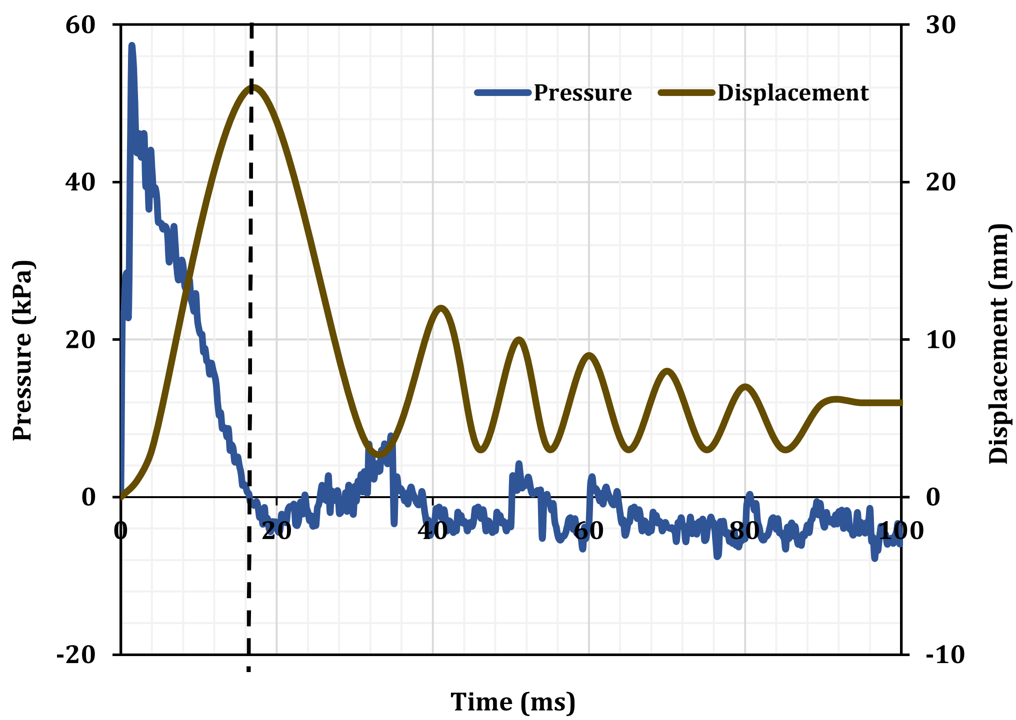

Figure 4.4. Pressure and displacement time history of Wall-1-2

4.4.3 Test Wall-1-3

A total of six foils were installed for the third shot, three in each diaphragm. An air pressure of 70 psi was pumped into the driver section, and 35 psi of air was to fill the spool section. At the release of pressure from the spool, the compressed air from the driver ruptured the foils and rushed towards the expansion section with a generated incident pressure of 34 kPa. It impacted the test wall with a peak-reflected pressure of 67 kPa within a positive phase duration of 18 ms. A reflected impulse over the positive phase of 542 kPa-ms was calculated, a maximum mid-height displacement of 39 mm was measured at 2.20 support rotation, and a residual displacement of 14 mm was sustained. Fine cracks developed along the mid-height and the course's mortar joint below the wall's mid-height. Figures 4.5, 4.6, and 4.7 show the cracks observed and the pressure and impulse displacement time history curves for Wall-1-3, respectively.

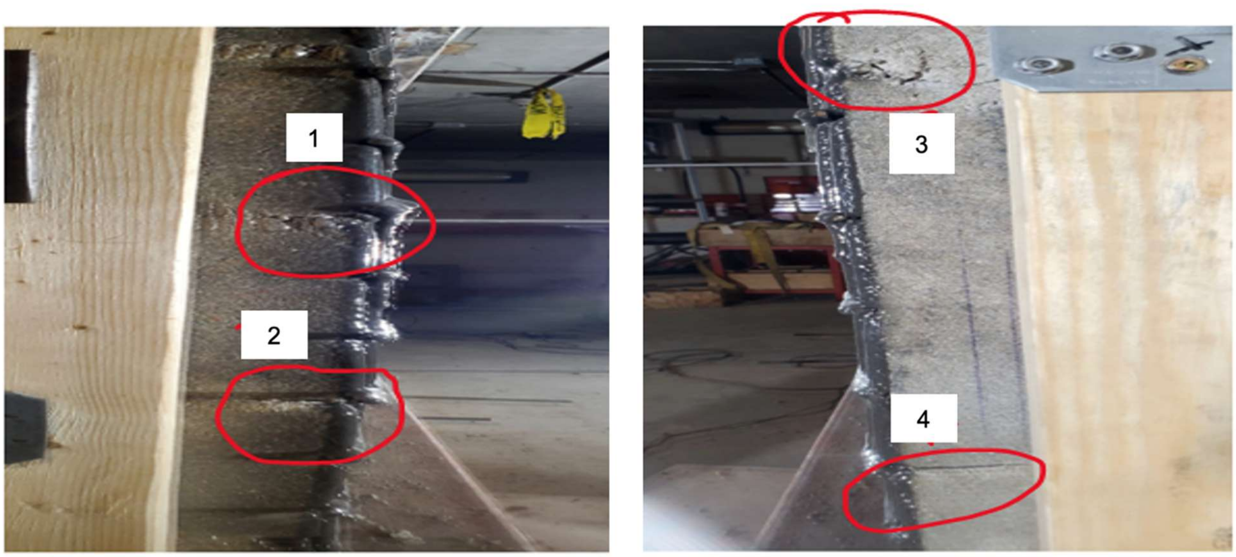

Figure 4.5. Fine cracks were seen on Wall-1-3

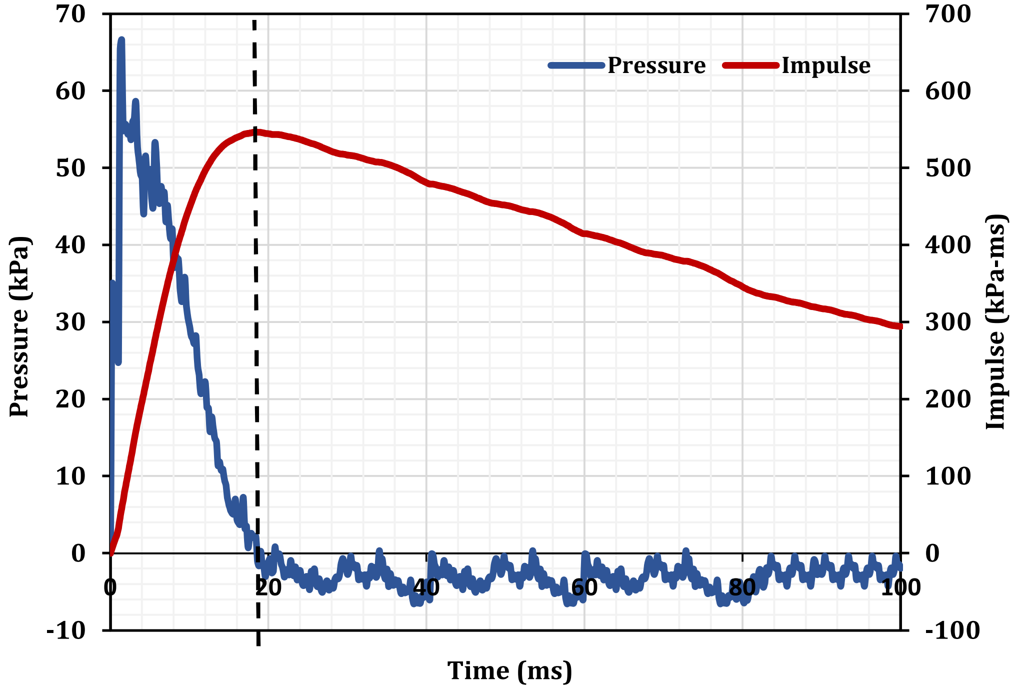

Figure 4.6. Pressure and impulse time history of Wall-1-3

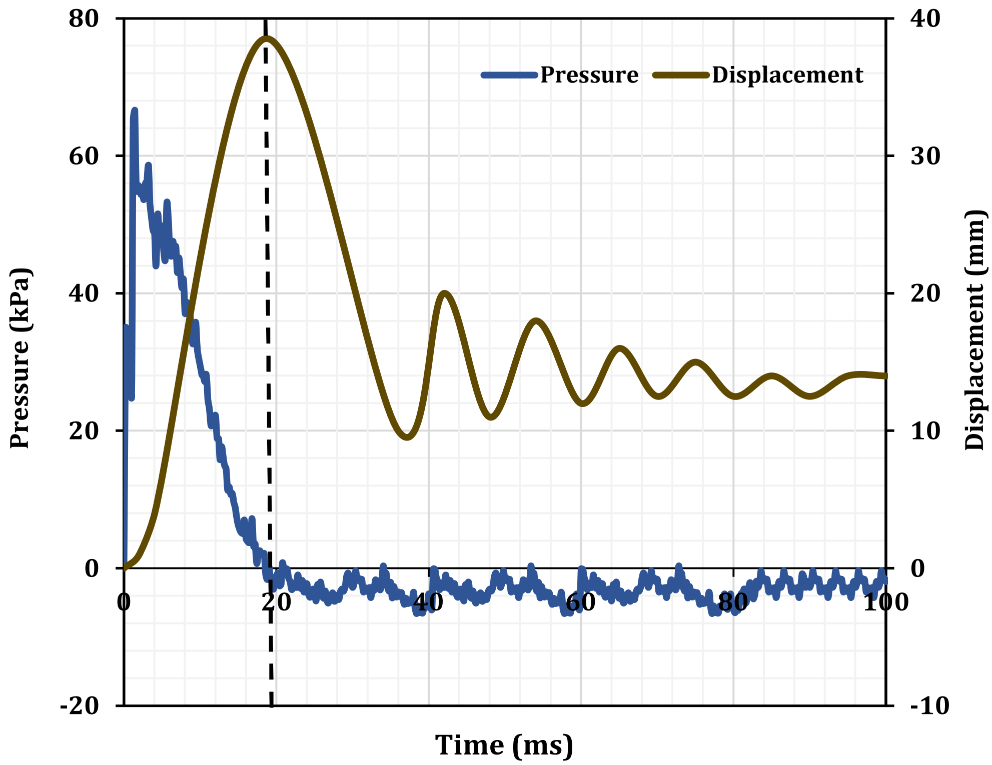

Figure 4.7. Pressure and displacement time history of Wall-1-3

4.4.4 Test Wall-1-4

The fourth shot required eight aluminum foils, four in each diaphragm. Compressed air pressure of 90 psi (621 Pa) was injected into the driver section, while 45 psi (310 kPa) of air was simultaneously pumped into the spool. At the release of the spool pressure, the foils ruptured with an incident pressure of 47 kPa. This resulted in a peak reflected pressure of 93 kPa with a positive phase duration of 24 ms and a reflected impulse over the positive phase of 711 kPa-ms. The maximum mid-height deflection recorded was 100 mm at 5.7^0 support rotation. The wall failed and broke into two halves along its mid-height mortar joint with a residual displacement of 74 mm. There was no fragmentation observed. Figure 4.9 shows the exterior surface of the wall with minor face shell defects and arching action at the mortar joint between the frame and the wall. Recorded data of the pressure and impulse time history, displacement time history, and the observed failure mode of Wall-1-4 are shown in Figures 4.8, 4.10, and 4.11, respectively.

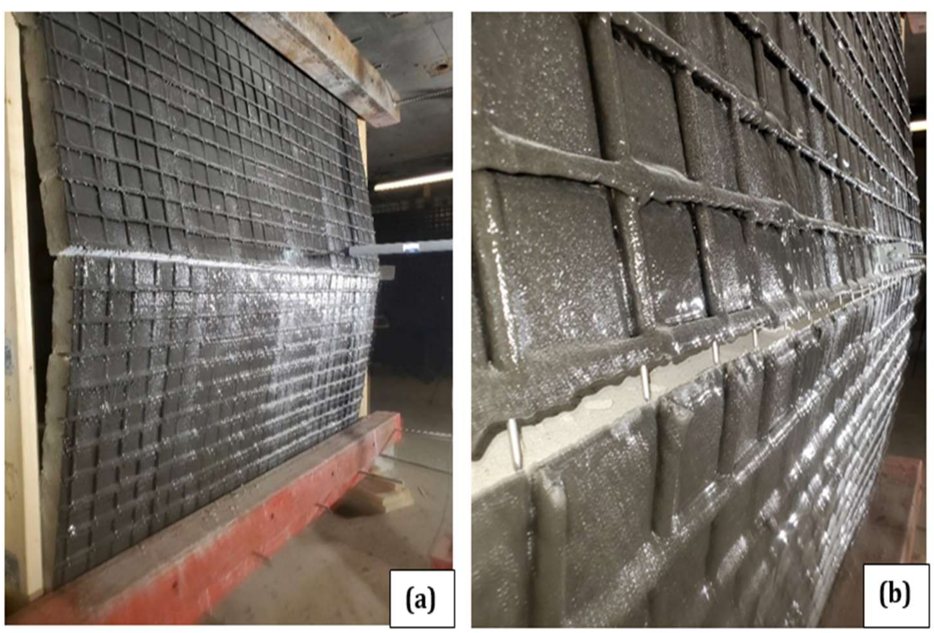

Figure 4.8. (a) Wall-1 split into two equal parts at mid-height after shot 4
(b)Mortar failure and SS304 strands necking point after shot 4

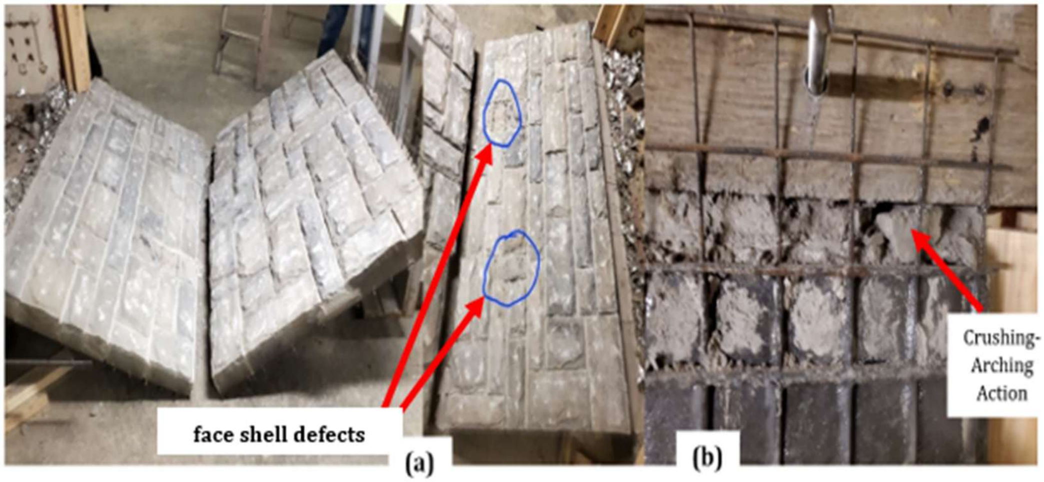

Figure 4.9. (a) The exterior surface of the stone wall has some face shell defects (b) Arching action on Wall-1

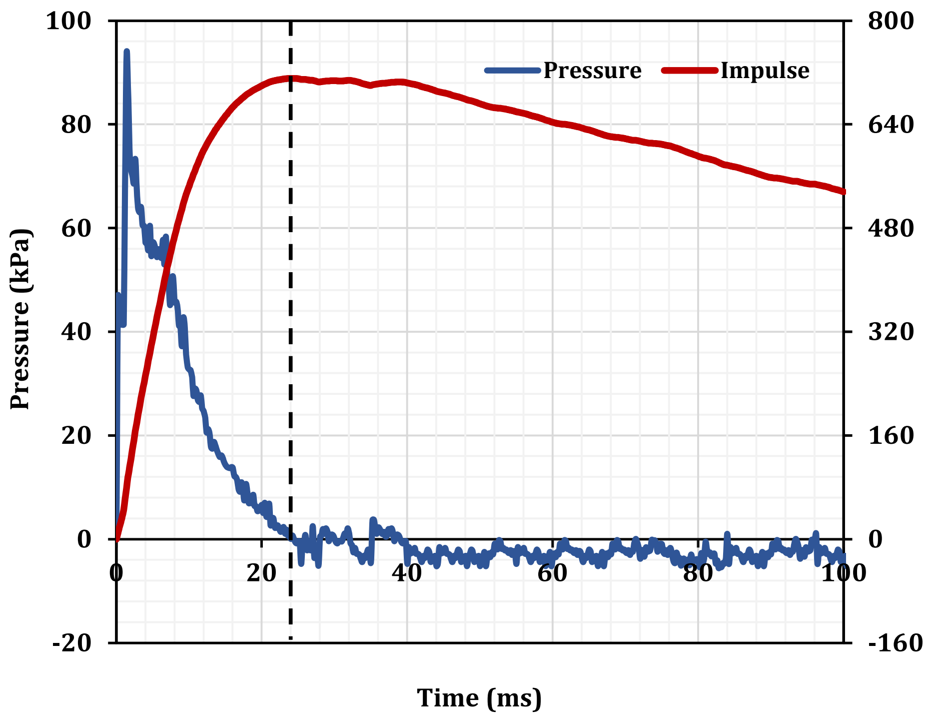

Figure 4.10. Pressure and impulse time history of Wall-1-4

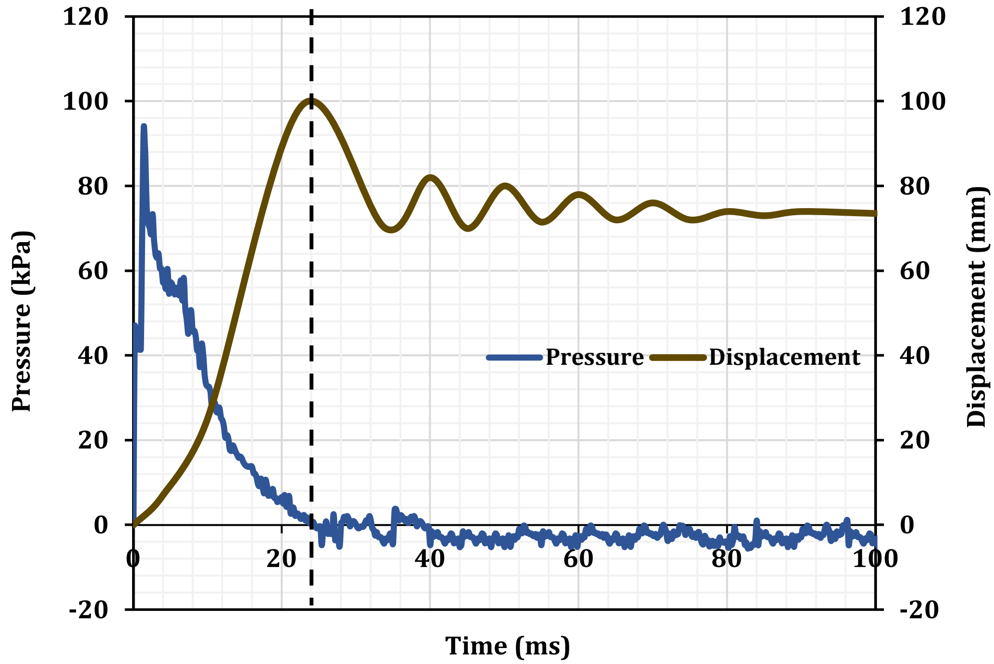

Figure 4.11. Reflected pressure and displacement time history of Wall-1-4

4.5 Wall-2

Wall-2 was constructed as a concrete masonry unit wall using a coursed laying pattern with no gap between it and its supporting frames. This wall is an unreinforced, infill, non-load bearing wall. It was retrofitted with reinforced polyurea-4.1mm, and no axial load was applied. Five test shots were fired on Wall-2 (Wall-2-1, Wall-2-2, Wall-2-3, Wall-2-4, and Wall-2-5) until it reached global failure. The 1829 mm (6ft) driver length was used for the first four shots to determine their loading duration. At the end of the fourth shot, the complete failure of the wall was unachieved, although the pressure loading was almost at the shock tube capacity. As such, an extra shot (fifth shot) was required, and the driver length was adjusted to 3962mm (13ft) to increase the impulse to achieve the wall failure. Table 4.4 shows the summary of test results for Wall-2.

Table 4.4: Summary of test results of Wall-2

Wall type	Wall-2	P_D (kPa)	L_D (mm)	P_r (kPa)	I_r (kPa-ms)	t_d (ms)	d_{max} (mm)	d_{res} (mm)	θ_{max} (degrees)
CMU	Wall-2-1	345	1829	50	419	18	23	6	1.3
	Wall-2-2	483	1829	72	550	18	34	9	2.0
	Wall-2-3	621	1829	74	701	25	56	22	3.2
	Wall-2-4	758	1829	85	793	28	80	30	4.6
	Wall-2-5	710	3962	85	2177	57	203	110	11.5

4.5.1 Wall-2-1

The first shot fired on Wall-2 was generated from a driver pressure of 50 psi (345 kPa) and a spool pressure of 25 psi (172 kPa). At the rupture of the foils, an incident pressure of 25 kPa was released with a resultant reflected pressure of 50 kPa. The reflected impulse of 419 kPa-ms was computed over the positive phase duration of 18 ms. The maximum mid-height deflection of 23 mm was recorded at 1.3^0 support rotations, and a residual displacement of 6 mm was sustained with no visible damage. The wall test setup, pressure, and impulse displacement time histories are seen in Figures 4.12, 4.13, and 4.14, respectively.

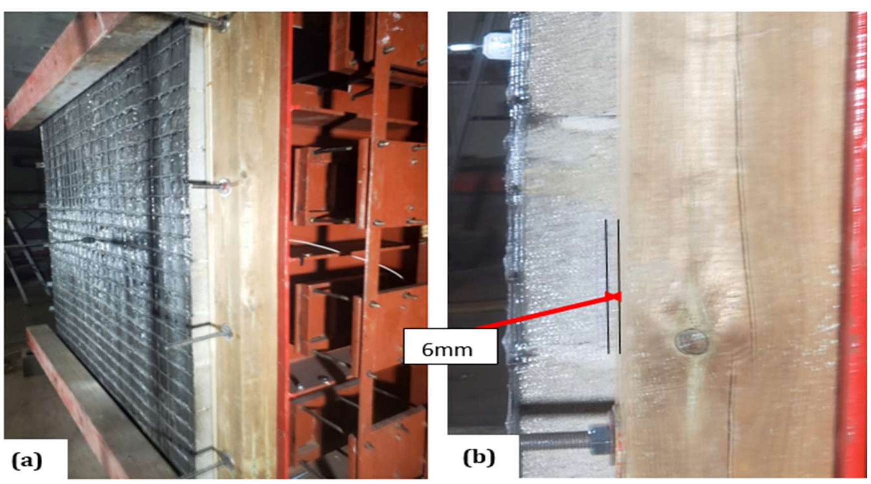

Figure 4.12. (a) Set up of Wall-2 and (b) Residual displacement on Wall-2-1

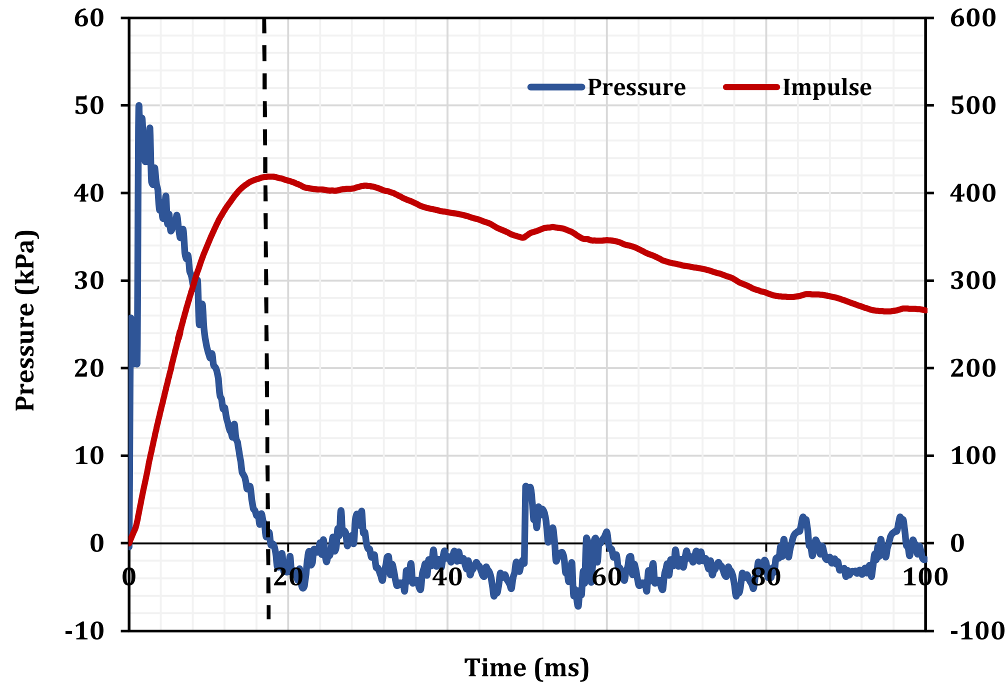

Figure 4.13. Pressure and impulse time history of Wall-2-1

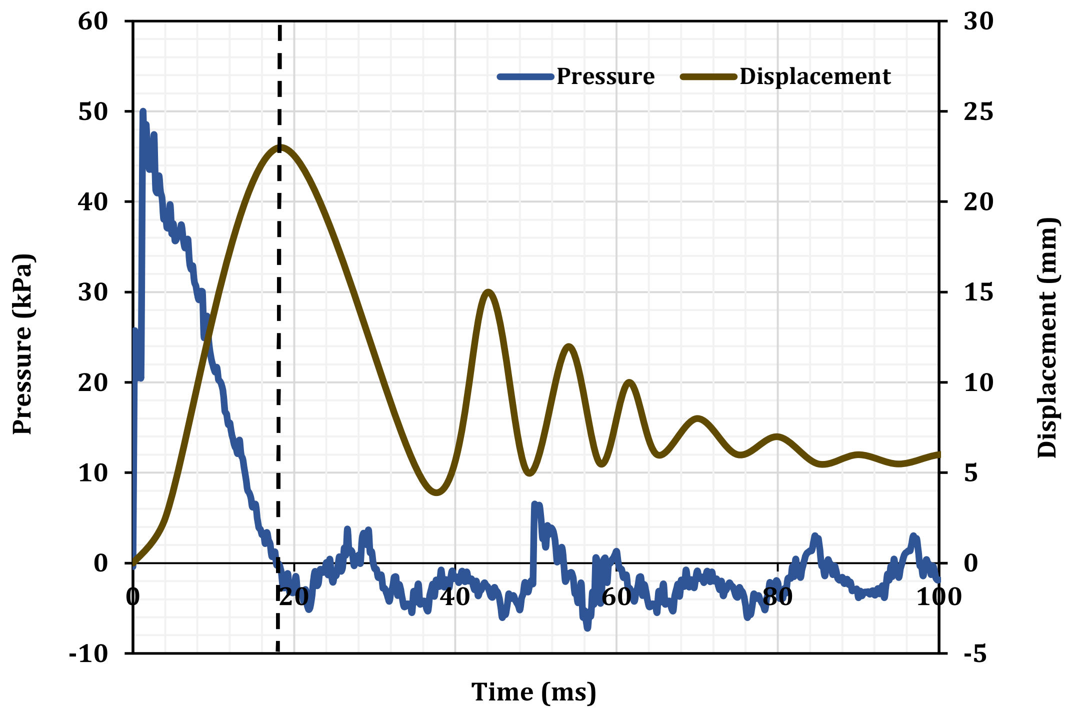

Figure 4.14. Pressure and displacement time history of Wall-2-1

4.5.2 Wall-2-2

Wall-2 was further exposed to a second shot as the driver pressure increased to 70 psi (483 kPa), and the diaphragm pressure was increased to 35 psi (241 kPa). The driver length remained unchanged. An incident pressure of 31 kPa was released, and the peak reflected pressure of 72 kPa and reflected impulse of 550 kPa-ms were generated within a positive phase duration of 18 ms. Also, a maximum mid-height deflection of 34 mm was recorded at 2^0 support rotations, as in Table 4.4 and Figures 4.15 and 4.16. The wall sustained a residual displacement of 9 mm with no visible damage or cracks.

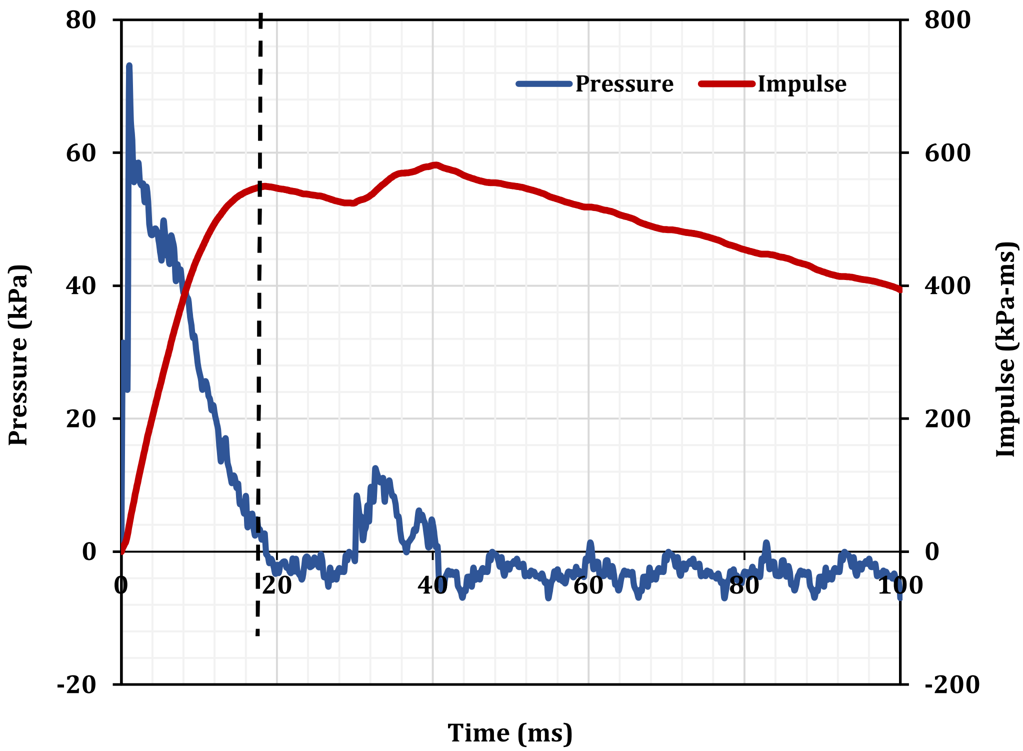

Figure 4.15. Pressure and impulse time history of Wall-2-2

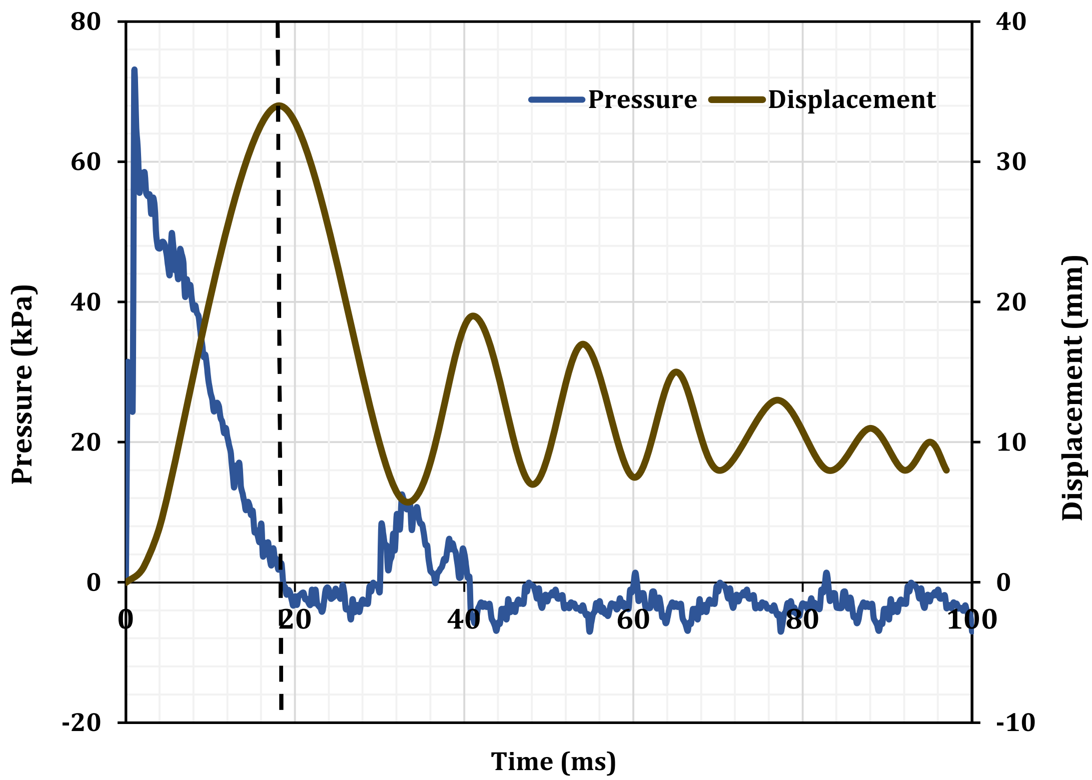

Figure 4.16. Pressure and displacement time history of Wall-2-2

4.5.3 Wall-2-3

The driver pressure applied on Wall-2 was increased for the third shot to 90 psi (621 kPa) with a corresponding increase in spool pressure to 45 psi (310 kPa). The incident pressure was 37 kPa, and the reflected pressure and impulse time history plotted in Figure 4.17 showed their maximum values to be 74 kPa and 701 kPa-ms, respectively, over a positive phase duration of 25 ms. Also, a maximum mid-height deflection of 56 mm was recorded at a support rotation of $3.2^{0,}$ as shown in Figure 4.18. The wall sustained a residual displacement of 22 mm, with cracks observed along the mortar joints of the top four courses of the wall (Figure 4.19).

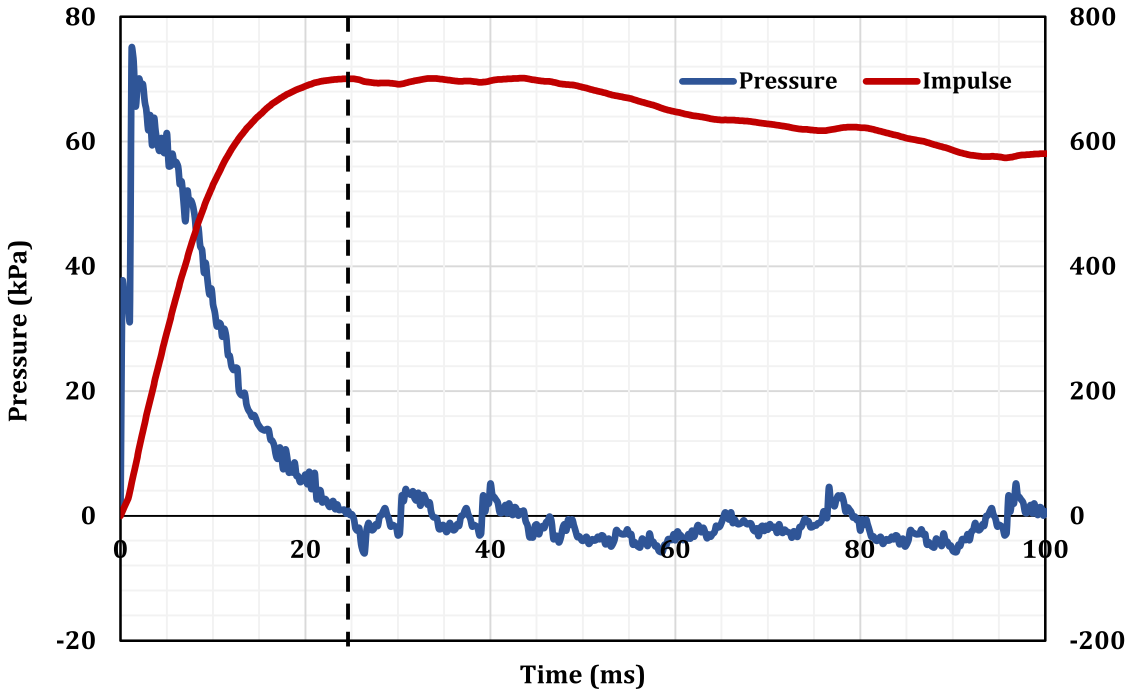

Figure 4.17. Pressure and impulse time history of Wall-2-3

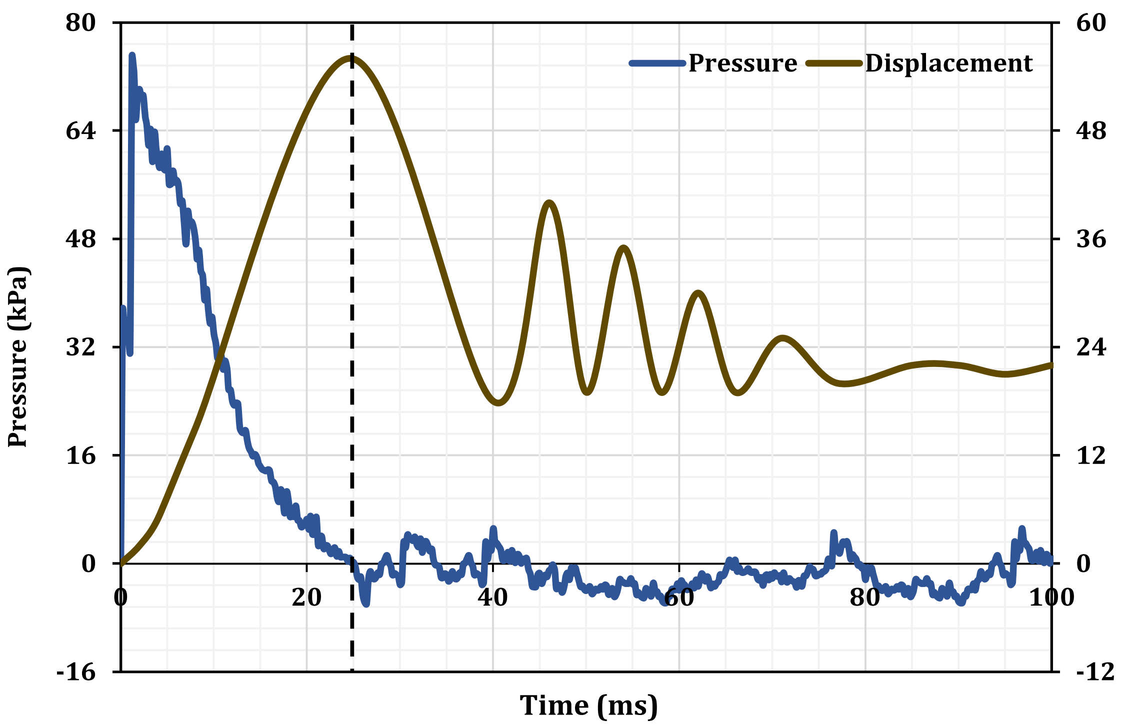

Figure 4.18. Pressure and displacement time history of Wall-2-3

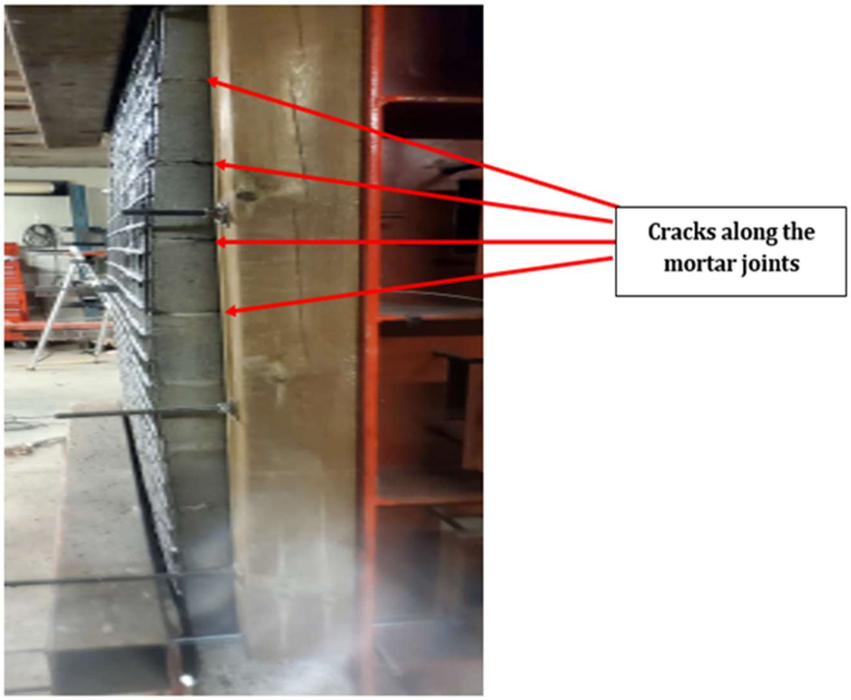

Figure 4.19. Cracks were seen along the mortar joints of Wall-2-3

4.5.4 Wall-2-4

The fourth shot on Wall 2 was carried out with a driver pressure of 110 psi (758 kPa) and a spool pressure of 55 psi (379 kPa), with the driver length unchanged. Eight aluminum foils were used: four foils between the driver-spool interface and four foils between the spool-expansion chamber interface. Upon releasing the pressure, the generated incident pressure was 42 kPa, and the maximum reflected pressure and positive phase impulse were recorded to be 85 kPa and 793 kPa-ms, respectively, over a positive phase duration of 28 ms. The maximum mid-height deflection was measured to be 80 mm (Figure 4.22) at a support rotation of 4.6^0. The wall retained a residual displacement of 30 mm with major face shell cracks seen on the fifth course of the wall, as shown in Figure 4.20. The pressure and impulse time history of Wall-2-4 are plotted in Figure 4.21.

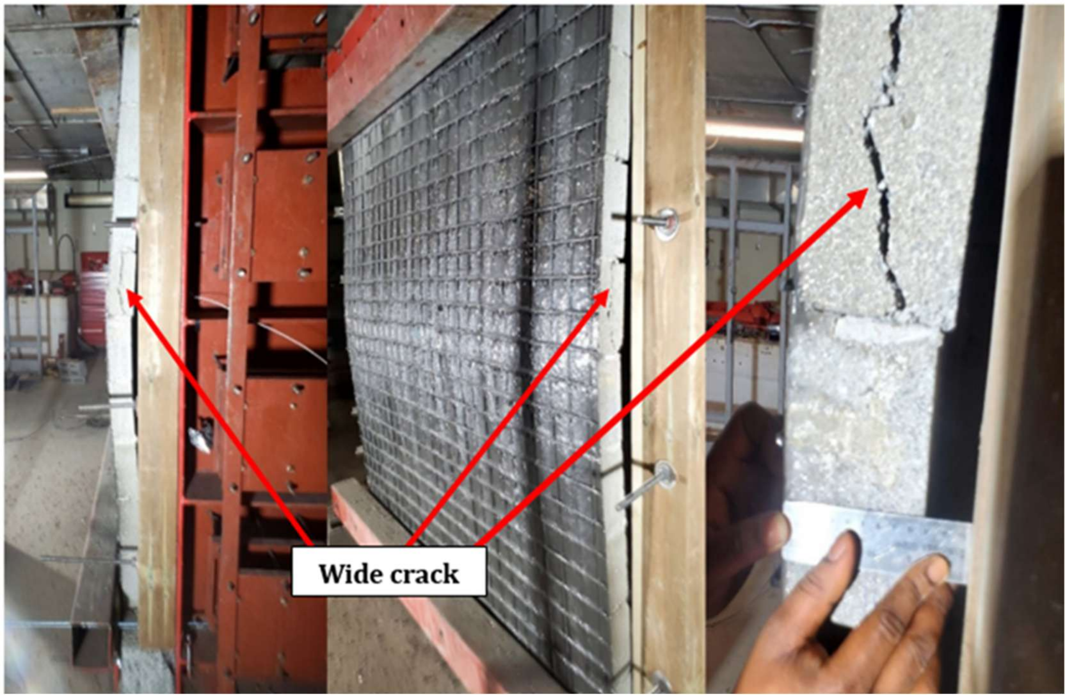

Figure 4.20. Failure in compression due to arching on Wall-2-4

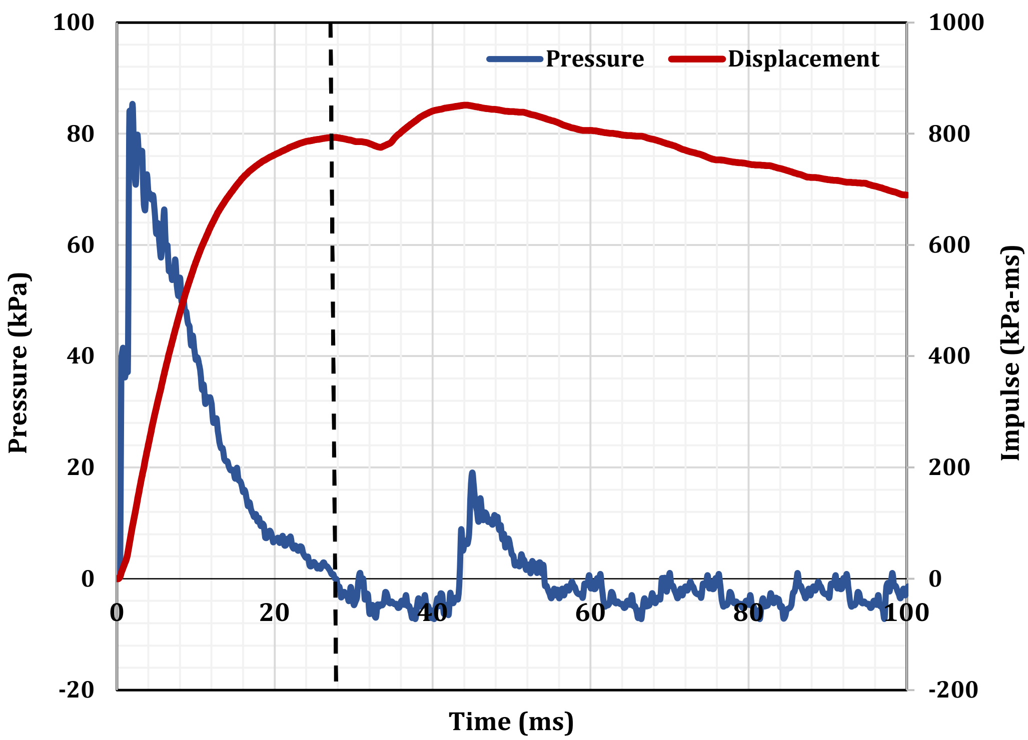

Figure 4.21. Pressure and impulse time history of Wall-2-4

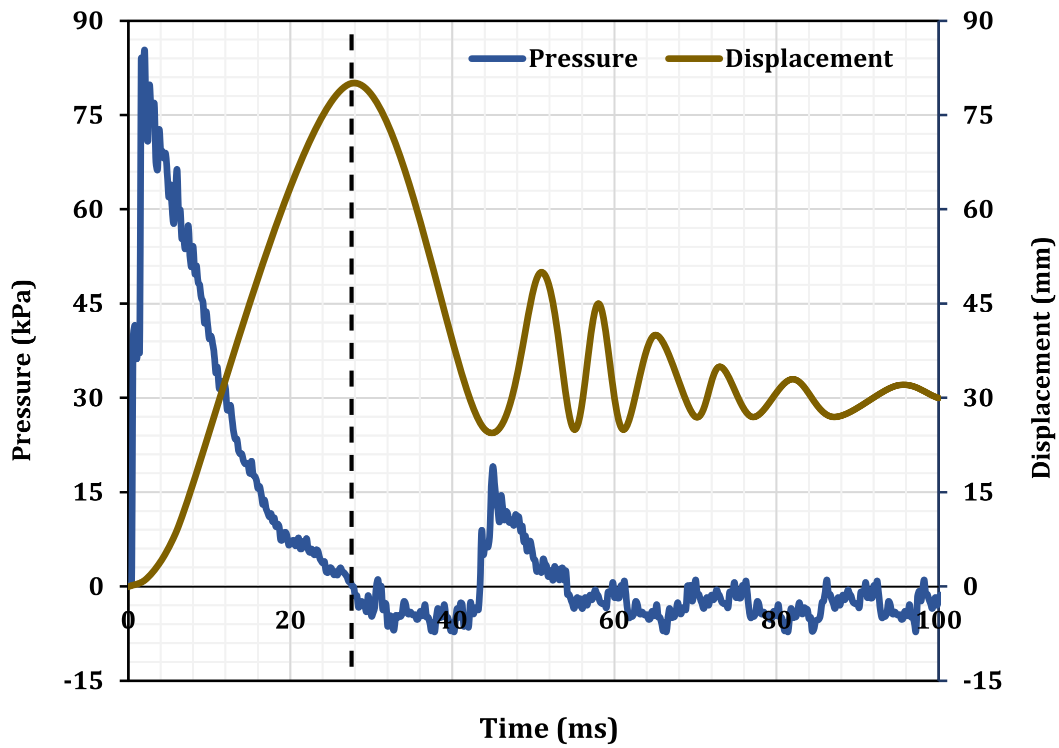

Figure 4.22: Time History of Pressure and Displacement for Wall-2-4

4.5.5 Wall-2-5

The driver length was extended to 3962 mm before the fifth shot was fired on Wall 2 to increase the reflected impulse to fail the wall within the pressure capacity of the shock tube. A total of ten aluminum foils were used: ten aluminum foils at the driver-spool interface and ten foils at the spool-expansion chamber interface. The driver pressure was 103 psi (710 kPa), and the spool pressure was 51.5 (355 kPa). An incident pressure of 43 kPa was released, a maximum reflected pressure of 85 kPa, and a maximum positive phase reflected impulse of 2177 kPa-ms were recorded after impact. The maximum mid-height deflection measured was 203 mm (Figure 4.25) at support rotations of 11.5^{0}, as shown in Table 4.4. The positive phase duration of the blast lasted for 57 ms, and the wall sustained a residual displacement of 110 mm. Visible damages were seen on the wall with major cracks along the wall mid-height, yielded and necked mesh reinforcement, torn polyurea at mid-height, and major face shell cracks on the fifth and sixth courses of the wall (Figure 4.23). The pressure and impulse time history of Wall-2-5 is shown in Figure 4.24.

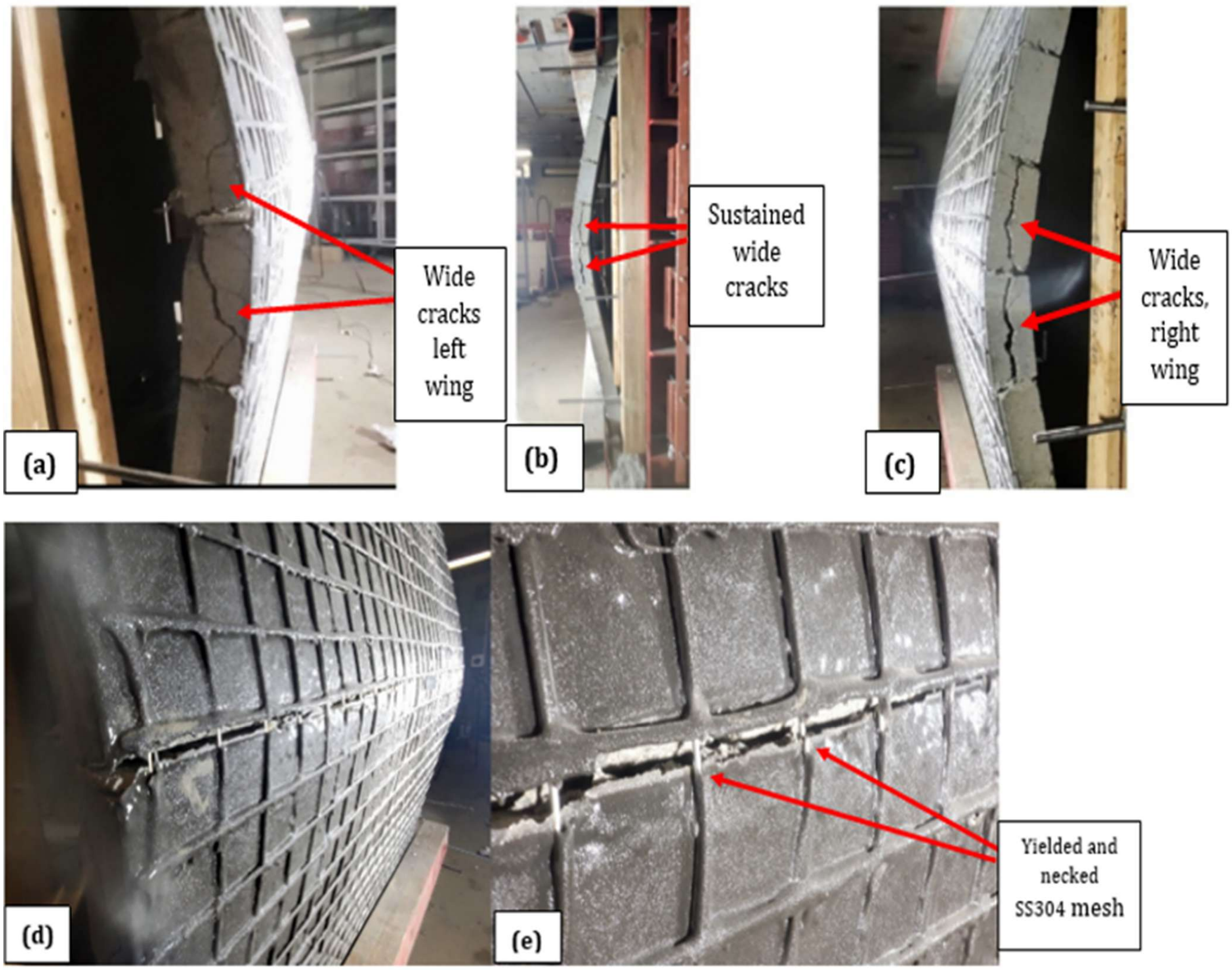

Figure 4.23. Cont'd

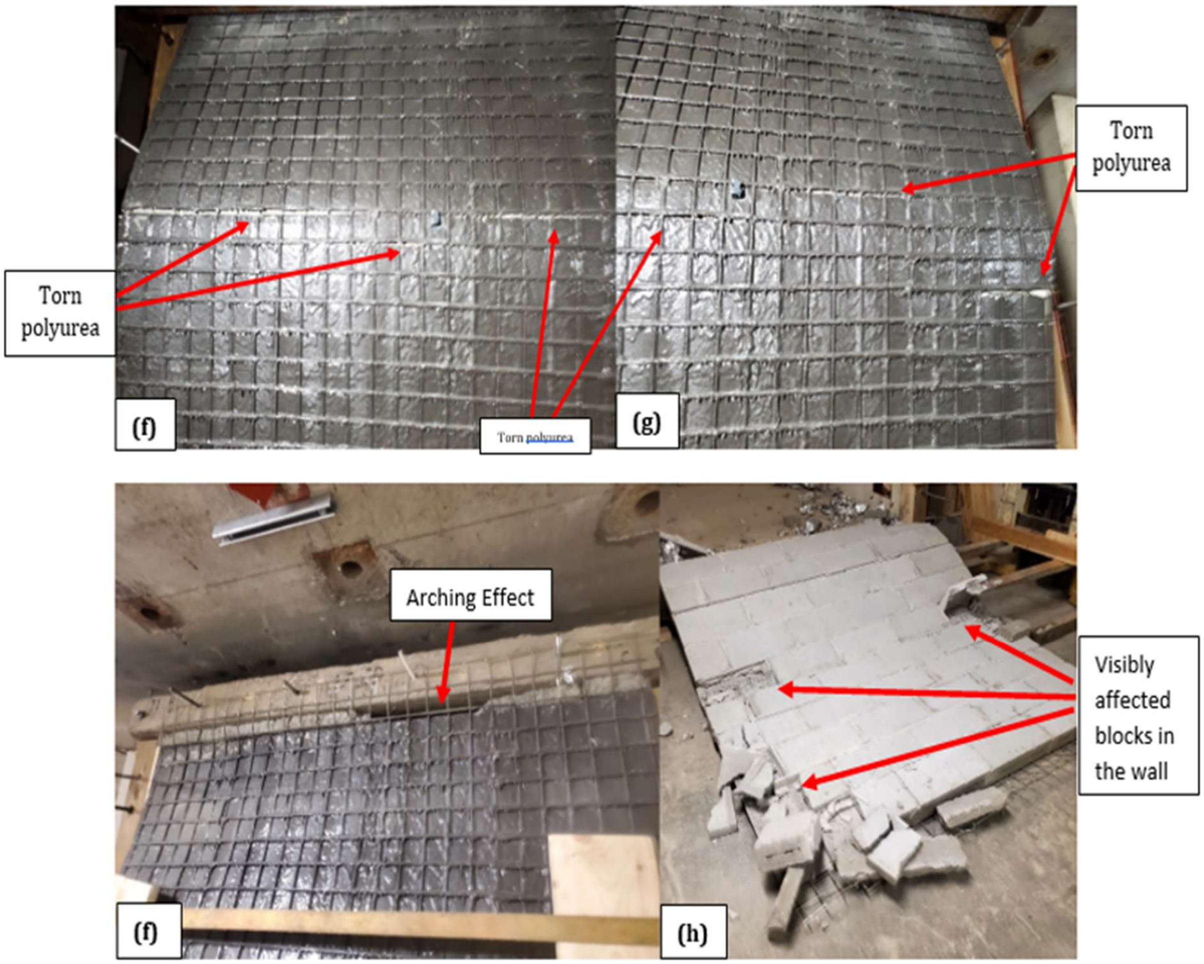

Figure 4.23. Views of failed Wall-2-5

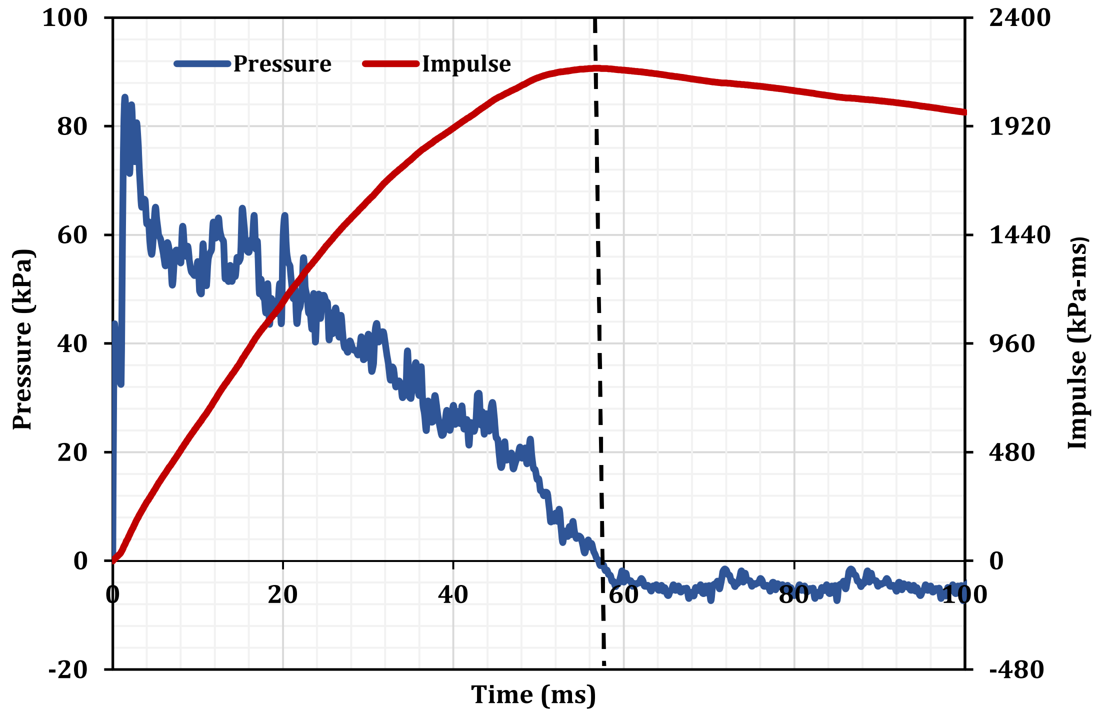

Figure 4.24. Pressure and impulse time history of Wall-2-5

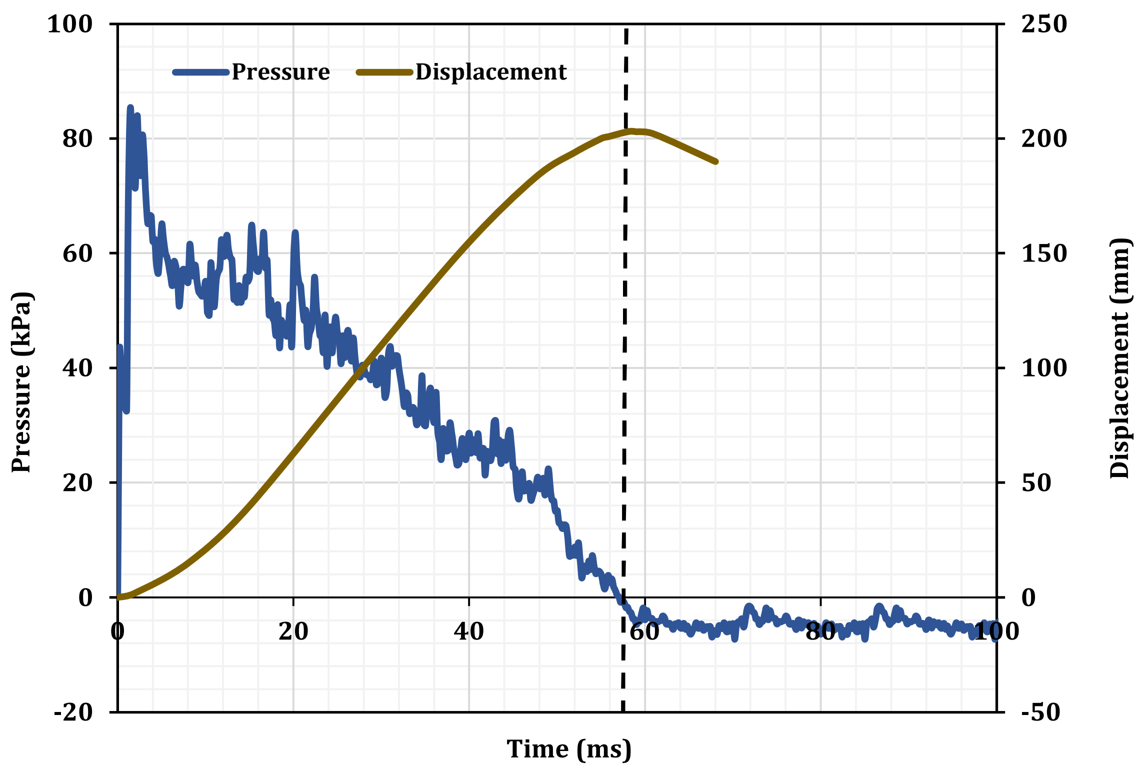

Figure 4.25. Pressure and displacement time history of Wall-2-5

4.6 Wall-3

Wall-3 has a similar configuration as Wall-2 except that its retrofit mesh has smaller diameter strands of 3.1 mm. Five test shots were fired on Wall-3 (Wall-3-1, Wall-3-2, Wall-3-3, Wall-3-4, and Wall-3-5) until it achieved global failure. The driver length of 1829mm (6ft) was used for the first four shots, while its length was extended to 3962mm (13ft) for the final shot (fifth shot) to generate higher impulse and eventually fail the wall. Table 4.5 provides a summary of test results.

Table 4.5: Summary of the test result of Wall-3

Wall Type	Wall-3	P_D (kPa)	l_D (mm)	P_r (kPa)	I_r (kPa-ms)	t_d (ms)	d_{max} (mm)	d_{res} (mm)	θ_{max} (degrees)
CMU	Wall-3-1	345	1829	50	420	18	25	6	1.4
	Wall-3-2	483	1829	67	547	19	39	18	2.2
	Wall-3-3	621	1829	76	714	28	89	25	5.1
	Wall-3-4	758	1829	89	874	30	140	30	8.0
	Wall-3-5	745	3962	88	1479	32	NA	NA	NA

4.6.1 Wall-3-1

The first shot on Wall-3 had a driver pressure of 50 psi (345 kPa) and a spool pressure of 25 psi (172 kPa). At the rupture of the foils, the incident pressure generated was measured to be 26 kPa. This resulted in a maximum reflected pressure of 50 kPa and a maximum positive phase impulse of 420 kPa-ms. The positive phase duration was 18 ms, and a maximum mid-height deflection of 25 mm was measured at 1.4^0 support rotations. A residual displacement of 6 mm was sustained with no visible damage. The reflected pressure, impulse, and displacement time histories are shown in Figures 4.26 and Figure 4.27.

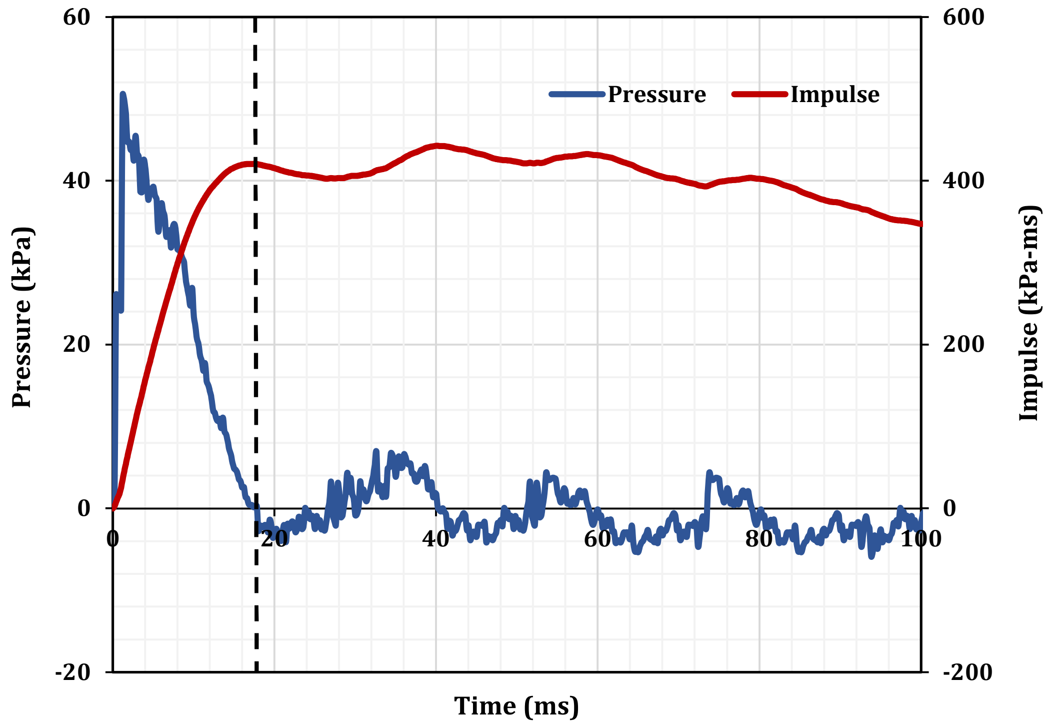

Figure 4.26. Pressure and impulse time history of Wall-3-1

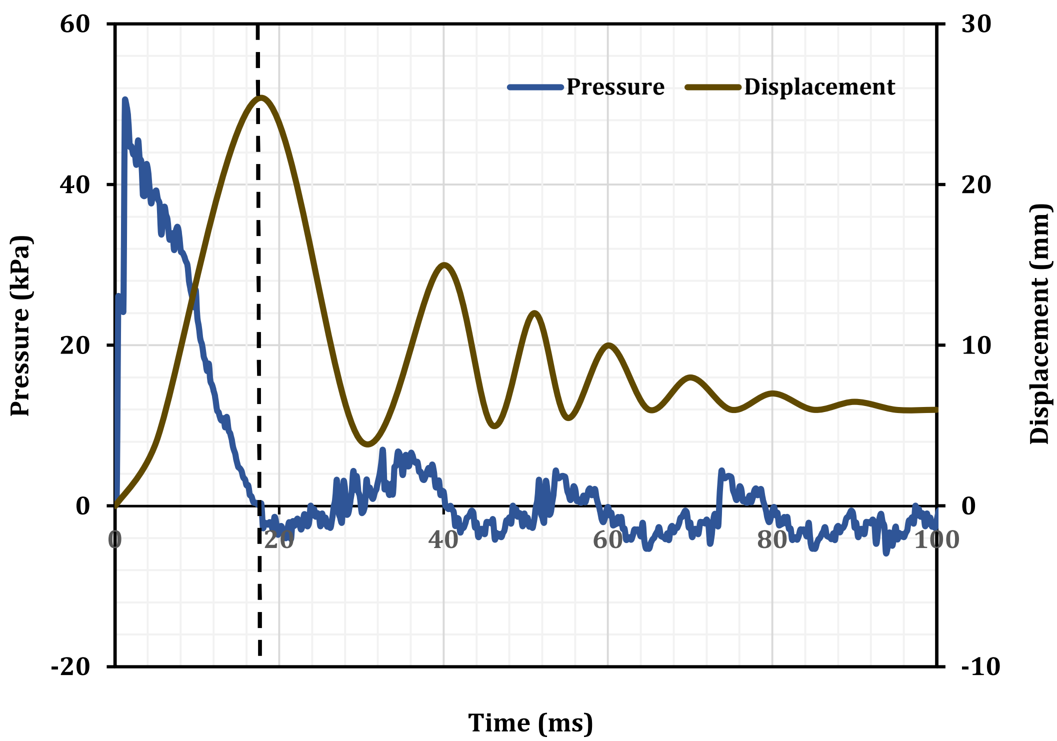

Figure 4.27. Pressure and displacement time history of Wall-3-1

4.6.2 Wall-3-2

The second shot on Wall-3 had its driver pressure increased to 70 psi (483 kPa) and spool pressure to 35 psi (241 kPa). A maximum incident pressure of 31 kPa was produced at the rupture of the foils. The maximum reflected pressure and the maximum positive phase impulse recorded were 67 kPa and 547 kPa-ms, respectively, over a positive phase duration of 19 ms. The maximum mid-height deflection was 39 mm at 2.2^0 support rotations. The wall sustained a residual displacement of 18 mm with visible cracks on its fifth course, as shown in Figure 4.28. The reflected pressure, impulse, and displacement time histories are plotted in Figures 4.29 and 4.30.

Figure 4.28. Medium cracks on the fifth course of wall-3-2

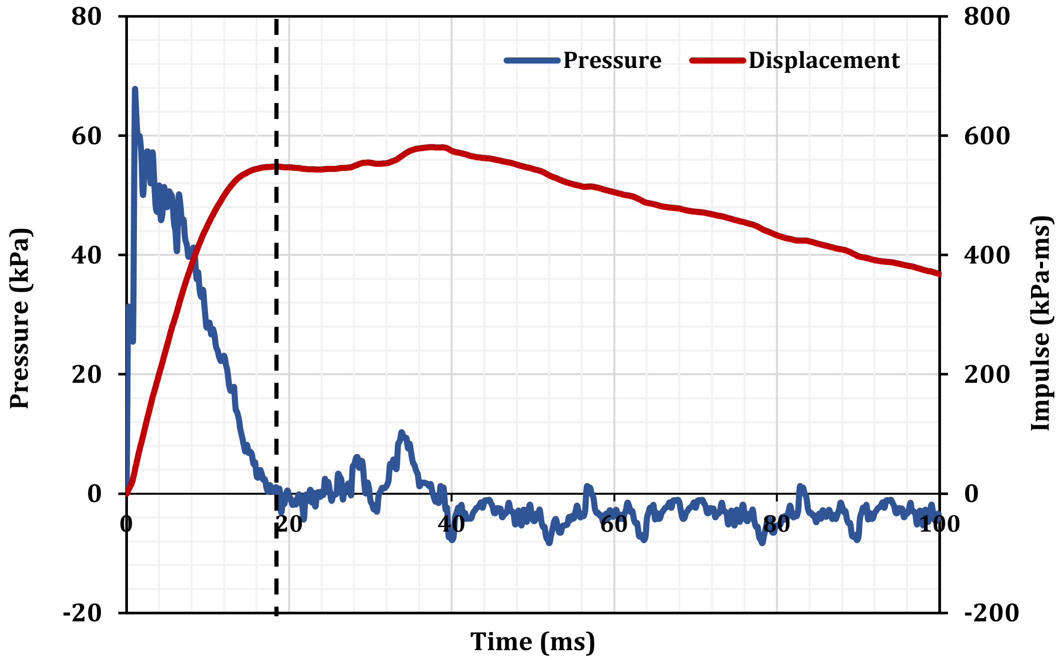

Figure 4.29. Pressure and impulse time history of Wall-3-2

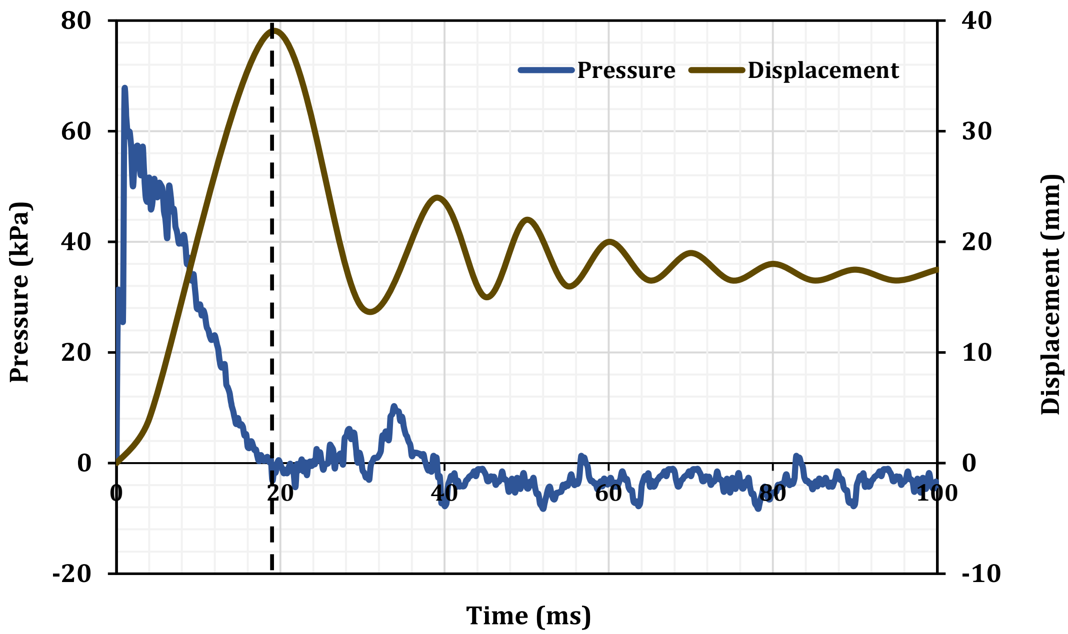

Figure 4.30. Pressure and displacement time history of Wall-3-2

4.6.3 Wall-3-3

The capacity of Wall-3 was further subjected to higher pressure in the third shot. The driver and spool pressures were increased to 90 psi (621 kPa) and 45 psi (310 kPa), respectively. The incident pressure of 42 kPa was fired. The peak reflected pressure and positive phase impulse were 76 kPa and 714 kPa-ms, respectively. The positive phase duration was 28 ms. This shot generated a maximum wall mid-height deflection of 89 mm when the support rotations were 5.1^0. The wall experienced a residual displacement of 25 mm at the end of the test, with wide cracks seen on the fifth course and the reinforced polyurea slightly detached from the wall at the mid-height region, as shown in Figure 4.31. The partial debonding of the reinforced polyurea could be attributed to the inconsistency in the application of the elastomer over the mesh. The pressure, impulse, and displacement time histories are seen in Figures 4.32 and 4.33.

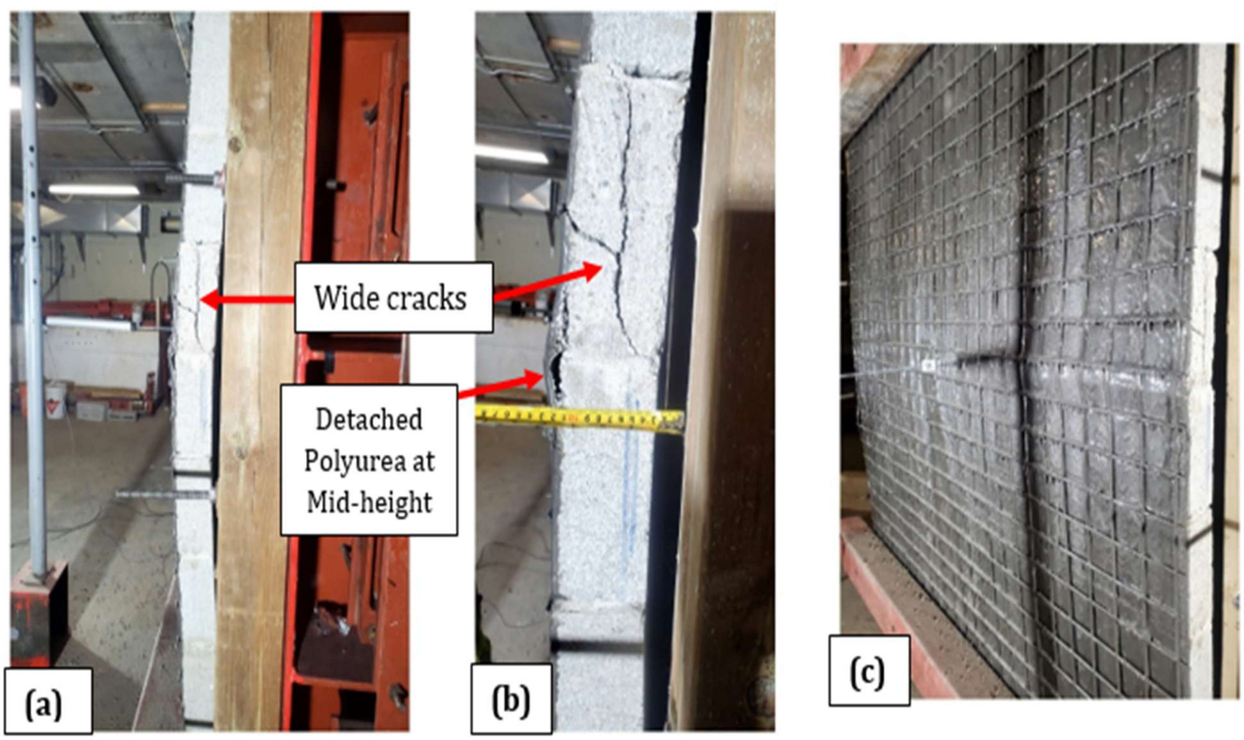

Figure 4.31. Failure in compression due to arching on Wall-3-3

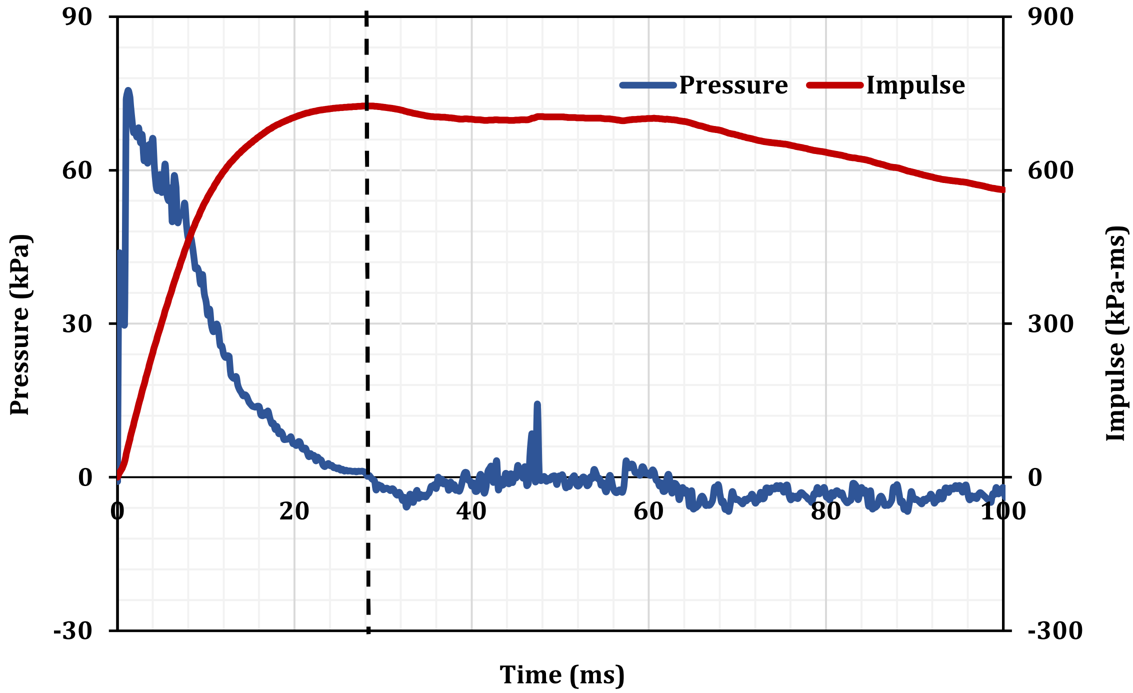

Figure 4.32. Pressure and impulse time history of Wall-3-3

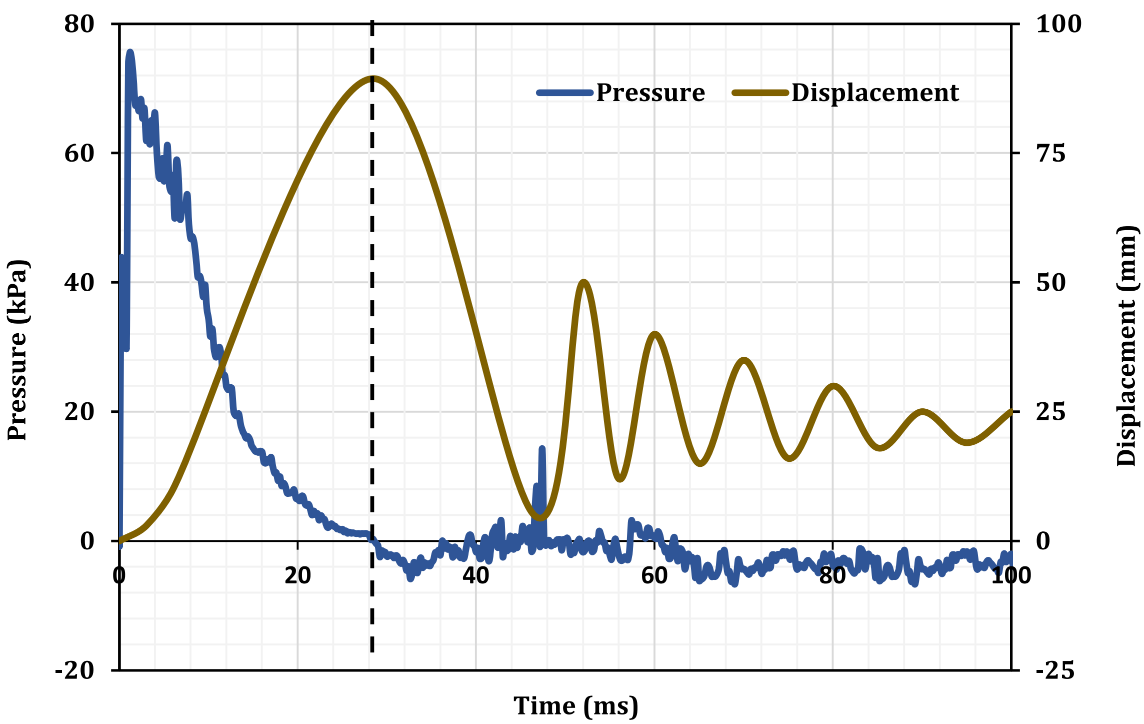

Figure 4.33. Pressure and displacement time history of Wall-3-3

4.6.4 Wall-3-4

The fourth shot on Wall-3 had its pressure further increased. The driver and the spool pressures were raised to 110 psi (758 kPa*)* and 55 psi (379 kPa), respectively. The incident pressure generated was 53 kPa, while its resultant peak reflected pressure and peak positive phase impulse were 89 kPa and 874 kPa-ms, respectively. The duration of the positive phase loading was 30 ms. The peak mid-height deflection was measured to be 140 mm*,* and its corresponding support rotations were 8.0^0. The wall sustained a residual displacement of 30 mm with further widened cracks on its fifth course. Somewhat narrower cracks surfaced on the second and third courses of the wall. The reinforced polyurea tore at some points and debonded partially at mid-height, as shown in Figures 4.34 and 4.35. Figures 4.36 and 4.37 display the wall-3-4 pressure, impulse, and displacement time histories.

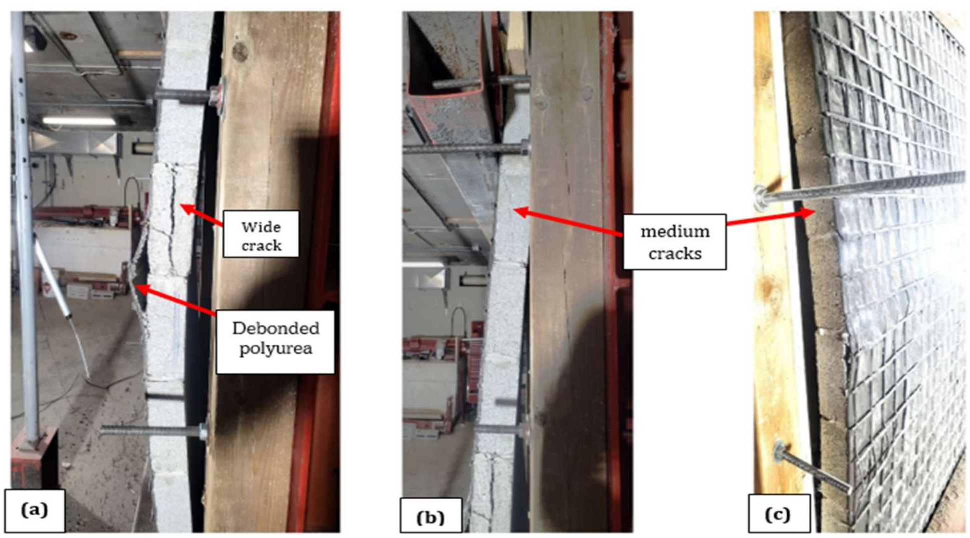

Figure 4.34. Failure in compression due to arching and slight de-bonding of reinforced polyurea on Wall-3-4

Figure 4.35. Torn and Partially debonded reinforced polyurea retrofit on Wall-3-4

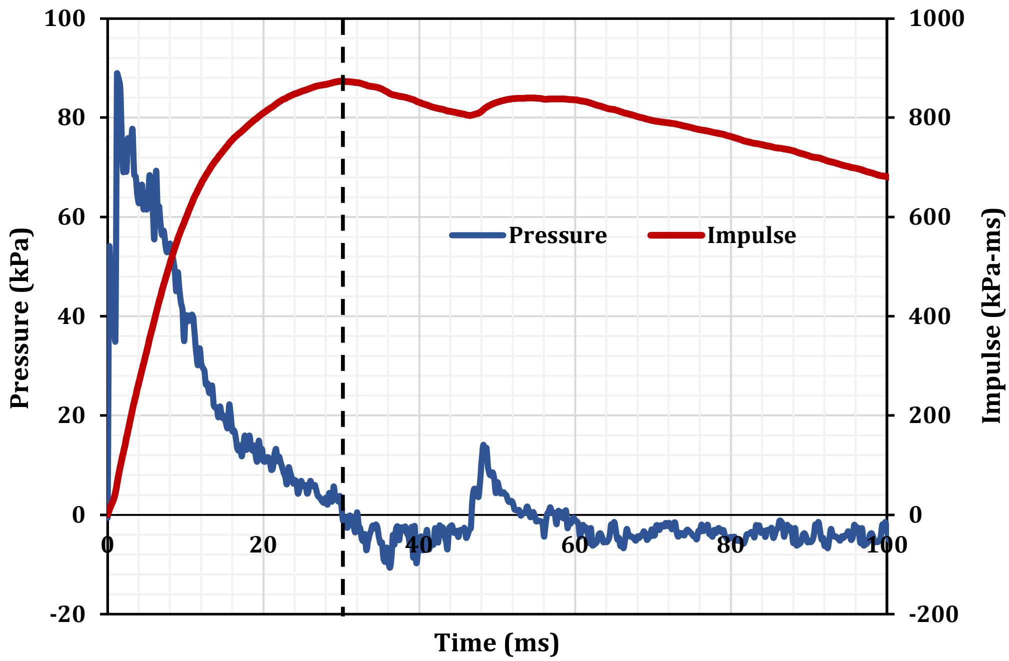

Figure 4.36. Pressure and impulse time history of Wall-3-4

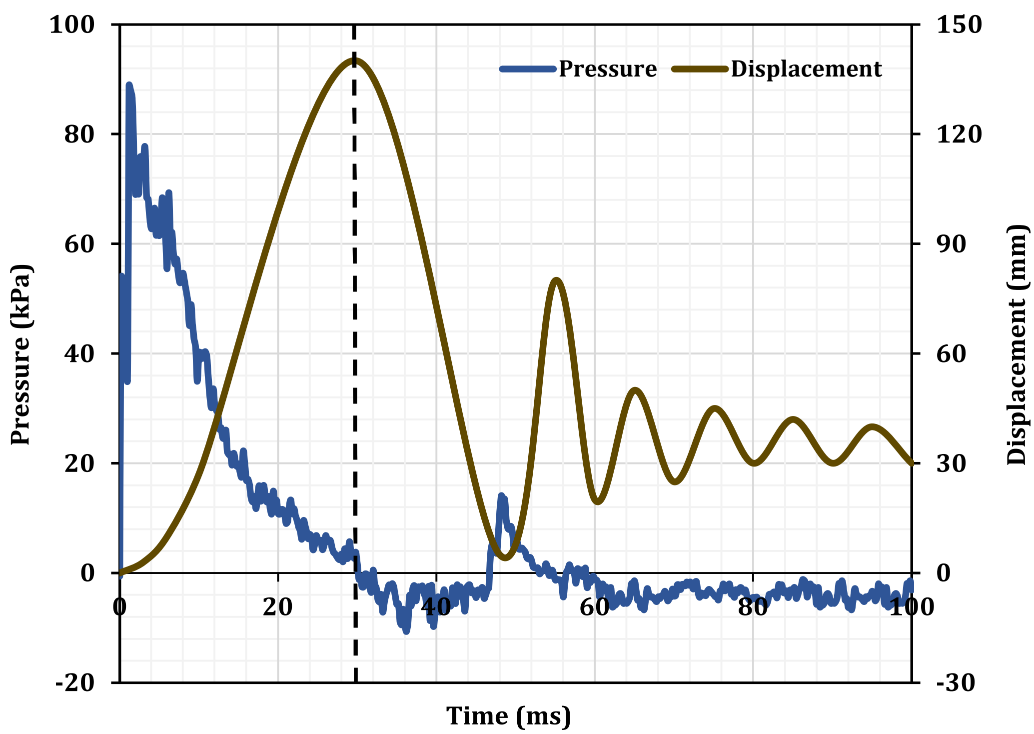

Figure 4.37. Pressure and displacement time history of Wall-3-4

4.5.5 Wall-3-5

The driver length was increased to 3962 mm for the fifth shot to increase the impulse. The driver and spool pressures were 108 psi (745 kPa) and 54 psi (372 kPa), respectively. However, the wall could not survive this shot as it collapsed (Figure 4.38). A maximum reflected pressure and positive phase reflected impulse of 88 kPa and 1479 kPa-ms were recorded over a positive phase duration of 32 ms. The pressure, impulse, and displacement time histories of Wall-3-5 are shown in Figures 4.39 and 4.40.

Figure 4.38. The collapse of Wall-3-5 with the release of debris

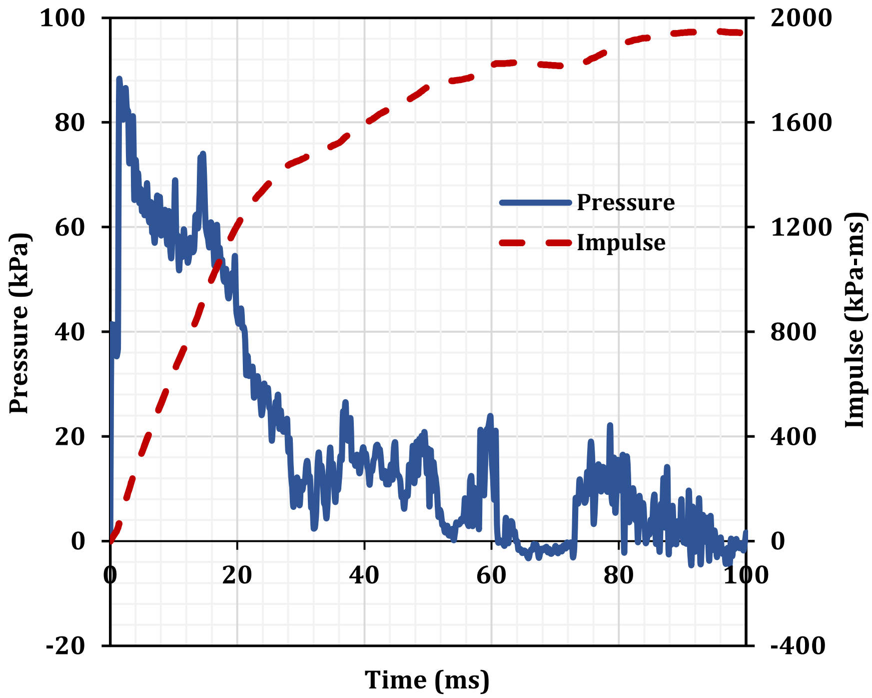

Figure 4.39. Pressure and impulse time history of Wall-3-5

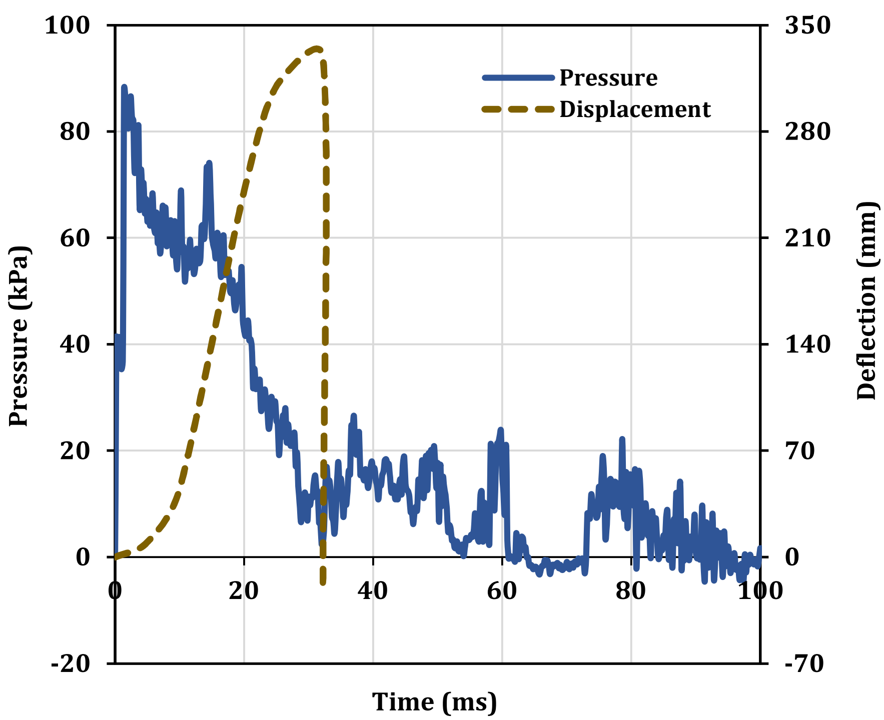

Figure 4.40. Pressure and displacement time history of Wall-3-5

4.7 Wall-4

Wall-4 was constructed as a stone masonry wall, with its blocks laid in an uncoursed pattern that had tight contact with its support frames. The wall was designed as a load-bearing wall by applying an axial load of 120kN from two hydraulic jacks mounted on its top concrete support. The wall was retrofitted with reinforced polyurea-4.1mm. Five blast shots were fired on wall-4 (Wall-4-1, Wall-4-2, Wall-4-3, Wall-4-4, and Wall-4-5) until global failure was attained. The summary of loading parameters is given in Table 4.6. The driver length of 1829 mm (6ft) was kept constant for the first four shots but extended to 3962 mm (13ft) to attain a higher impulse capable of total failure.

Table 4.6: Summary of test results of Wall-4

Wall Type	Wall-4	P_D (kPa)	l_D (mm)	P_r (kPa)	I_r (kPa-ms)	t_d (ms)	d_{max} (mm)	d_{res} (mm)	θ_{max} (degrees)
STONE	Wall-4-1	345	1829	49	432	18	17	3	1
	Wall-4-2	483	1829	66	560	19	22	6	1.3
	Wall-4-3	621	1829	74	695	22	32	10	1.8
	Wall-4-4	758	1829	82	808	24	38	14	2.2
	Wall-4-5	724	3962	110	2488	60	197	170	11

4.7.1 Wall-4-1

The first shot on Wall-4 required a driver pressure of 50 psi (345 kPa) and a spool pressure of 25 psi (172 kPa). At the rupture of the diaphragm foils, an incident pressure of 29 kPa was released, which resulted in a Peak reflected pressure of 49 kPa and a reflected peak impulse of 432 kPa-ms. The positive phase duration was measured to be 18 ms. A maximum mid-height deflection of 17 mm occurred at 1^0 support rotations and dropped to a residual displacement of 3 mm with no visible damage. The pressure, impulse, and displacement time histories are shown in Figures 4.41 and 4.42.

4.7.2 Wall-4-2

The driver and spool pressures were raised to 70 psi (483 kPa) and 35 psi (241 kPa) for the second shot on Wall-4. An incident pressure of 28 kPa was released, while a peak reflected pressure of 66 kPa and a reflected impulse of 560 kPa-ms were generated. The maximum mid-height deflection of 22 mm was recorded, corresponding to support rotations 1.3^0. The positive phase duration was measured as 19 ms. After the impact, it left a residual displacement of 6 mm without any visible cracks. The pressure, impulse, and displacement time histories are plotted in Figures 4.43 and 4.44.

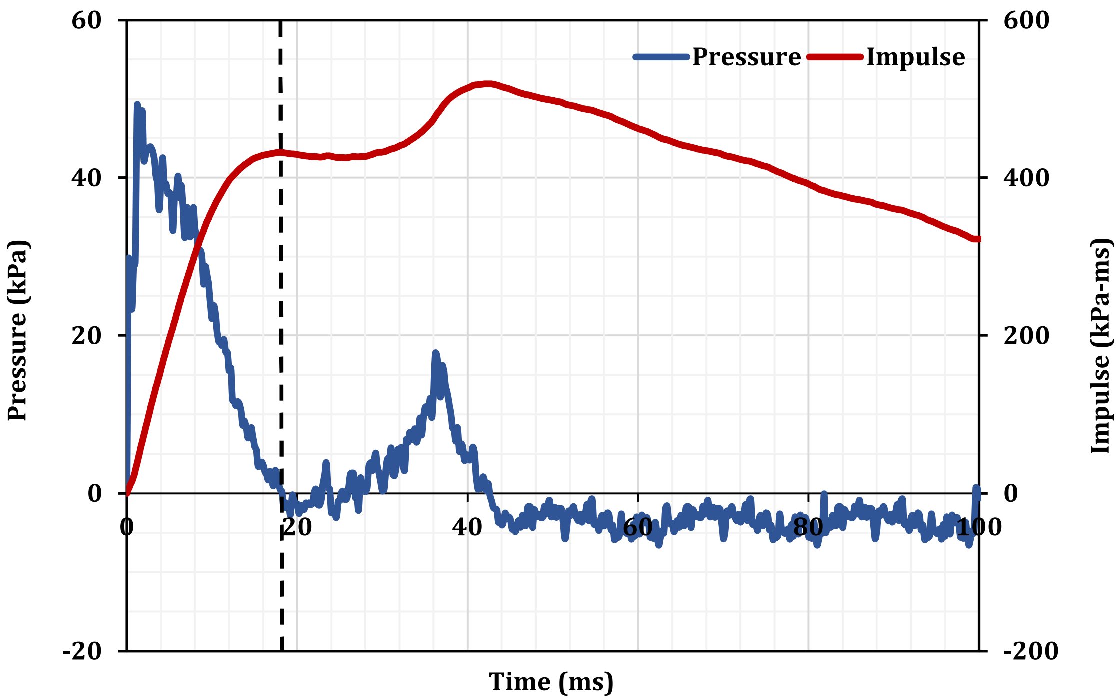

Figure 4.41. Pressure and impulse time history of Wall-4-1

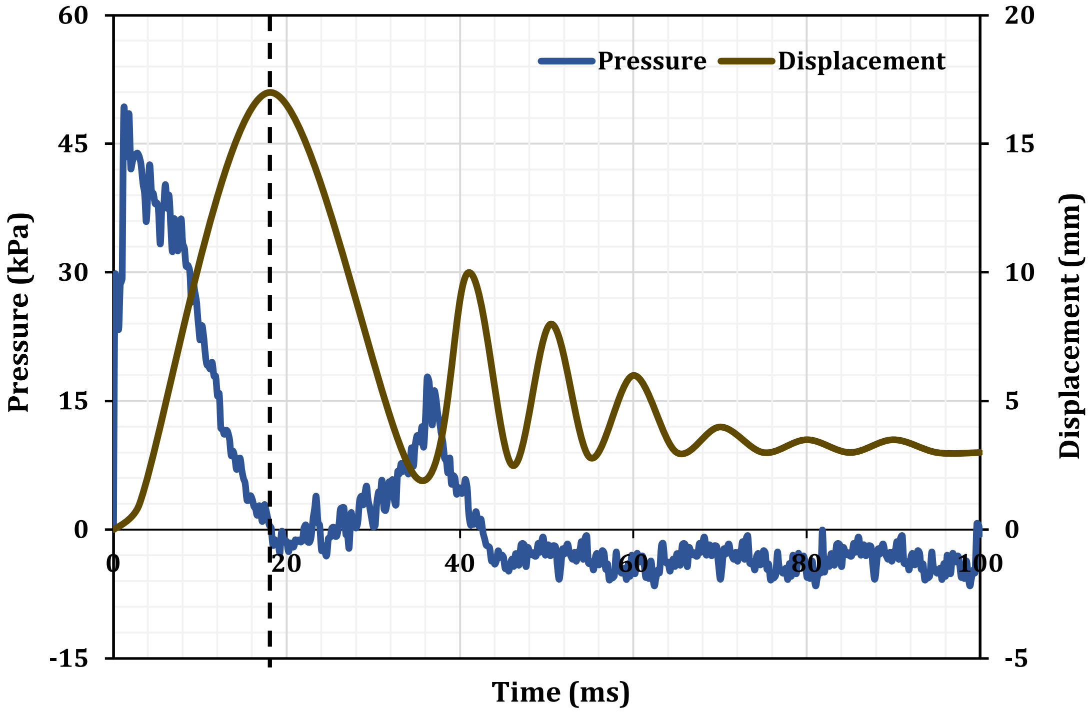

Figure 4.42 Pressure and displacement time history of Wall-4-1

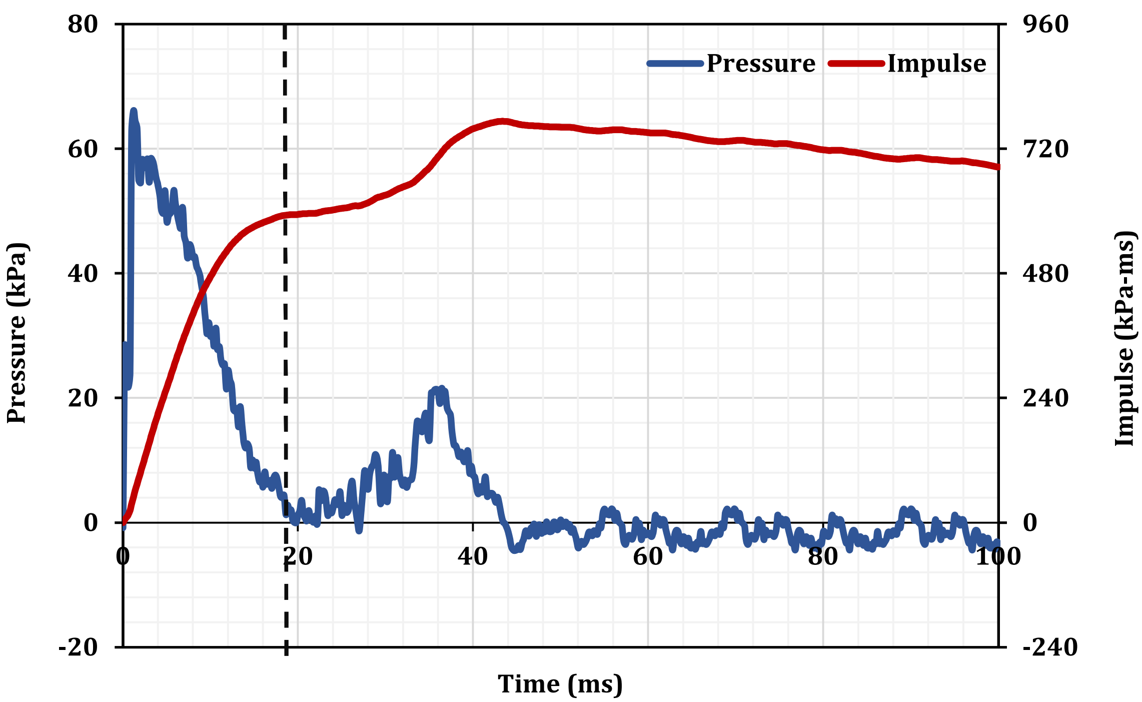

Figure 4.43. Pressure and impulse time history of Wall-4-2

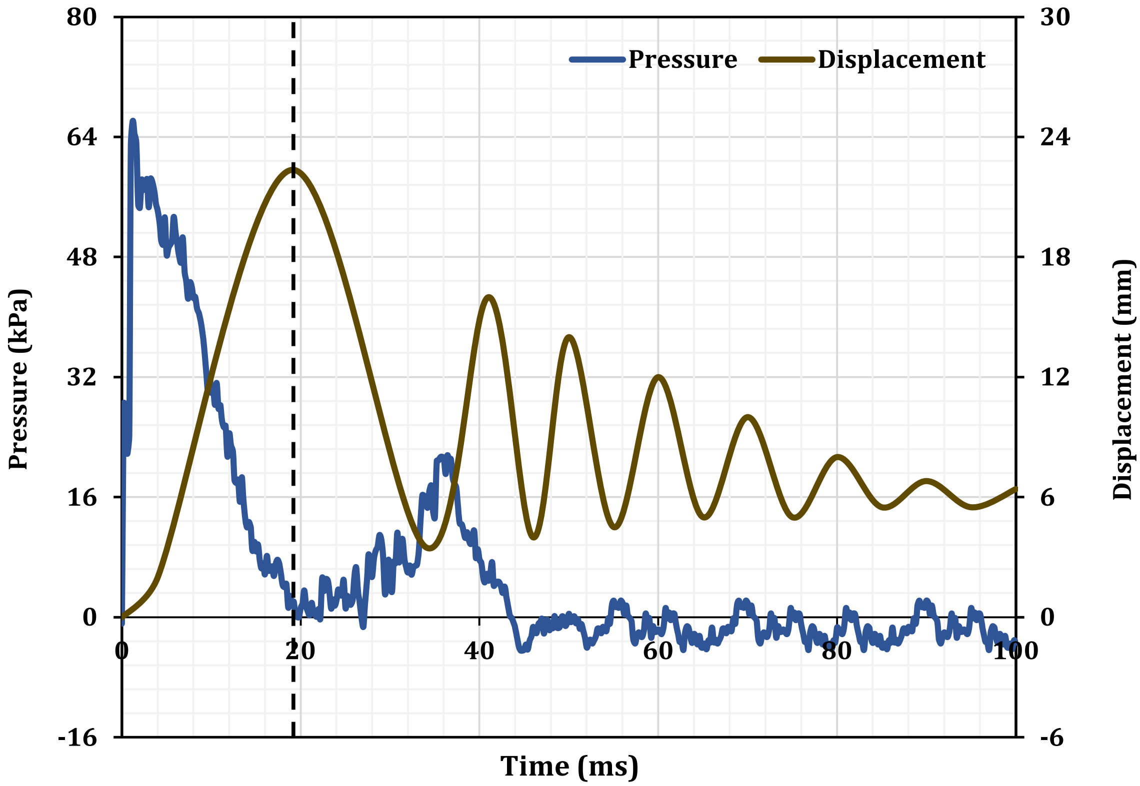

Figure 4.44. Pressure and displacement time history of Wall-4-2

4.7.3 Wall-4-3

For the third shot on Wall-4, the driver pressure was further increased to 90 psi (621 kPa), and the diaphragm pressure was concurrently increased to 45 psi (310 kPa). The incident pressure released was 37 kPa, while a peak reflected pressure of 74 kPa and a reflected impulse of 695 kPa-ms were generated over a positive phase duration of 22 ms. Wall-4-3 experienced a maximum mid-height deflection of 32 mm, corresponding to support rotations 1.8^0. The residual displacement was 10 mm, and no visible damage was observed on the wall. Its pressure, impulse, and displacement time histories can be seen in Figures 4.45 and 4.46.

4.7.4 Wall-4-4

The fourth shot on Wall-4 had a driver pressure of 110 psi (758 kPa) with a corresponding spool pressure of 55 psi (379 kPa). An incident pressure of 42 kPa was released with a peak reflected pressure of 82 kPa and a reflected impulse of 808 kPa-ms. The positive phase duration was 24 ms, and a maximum mid-height deflection of 38 mm was recorded with corresponding support rotations 2.2^{0}. A residual displacement of 14 mm was measured, with some cracks observed along its fifth course. Figures 4.47 and 4.48 display the pressure, impulse, and displacement time histories recorded for Wall-4-4.

4.7.5 Wall-4-5

In the fifth shot, the driver length was extended to 3962 mm to increase impulse as the shock tube pressure capacity was reached during the previous shot. A driver pressure of 105 psi (724 kPa) and a spool pressure of 53 psi (362 kPa) were pumped into the two sections, respectively. An incident pressure of 53 kPa was released after the foils ruptured. This resulted in a reflected pressure of 110 kPa and a reflected impulse of 2488 kPa-ms. A maximum mid-height deflection of 197 mm occurred at a support rotation $13^{0,}$ as indicated in Table 4.6. The positive phase duration of the blast pressure was 60 ms, and the residual displacement was measured to be 170 mm. The wall failed at its mid-height without fragmentation, as shown in Figures 4.49 to 4.51. The wall's pressure, impulse, and displacement time histories are shown in Figures 4.52 and 4.53.

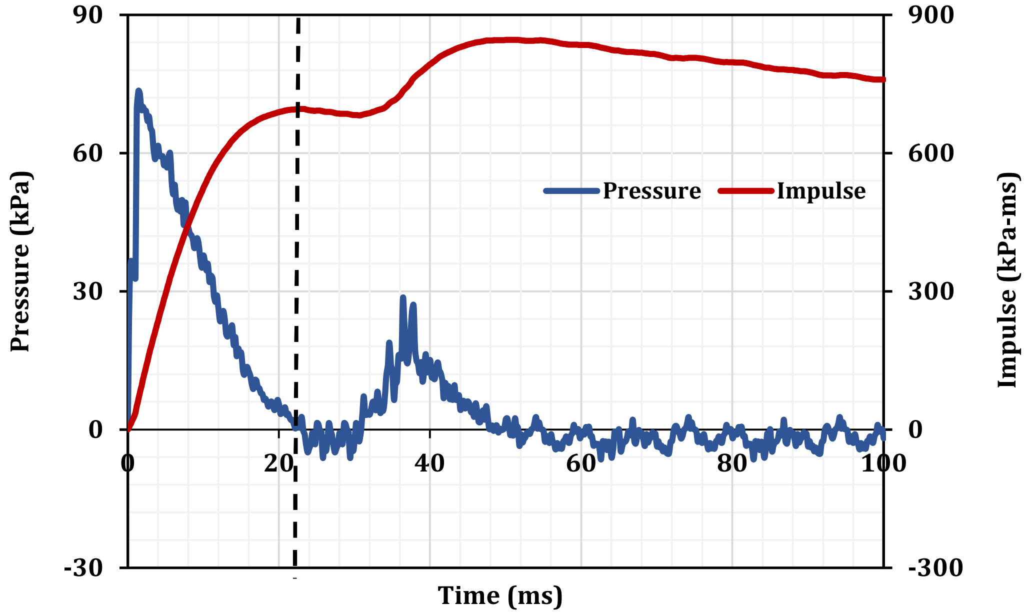

Figure 4.45. Pressure and impulse time history of Wall-4-3

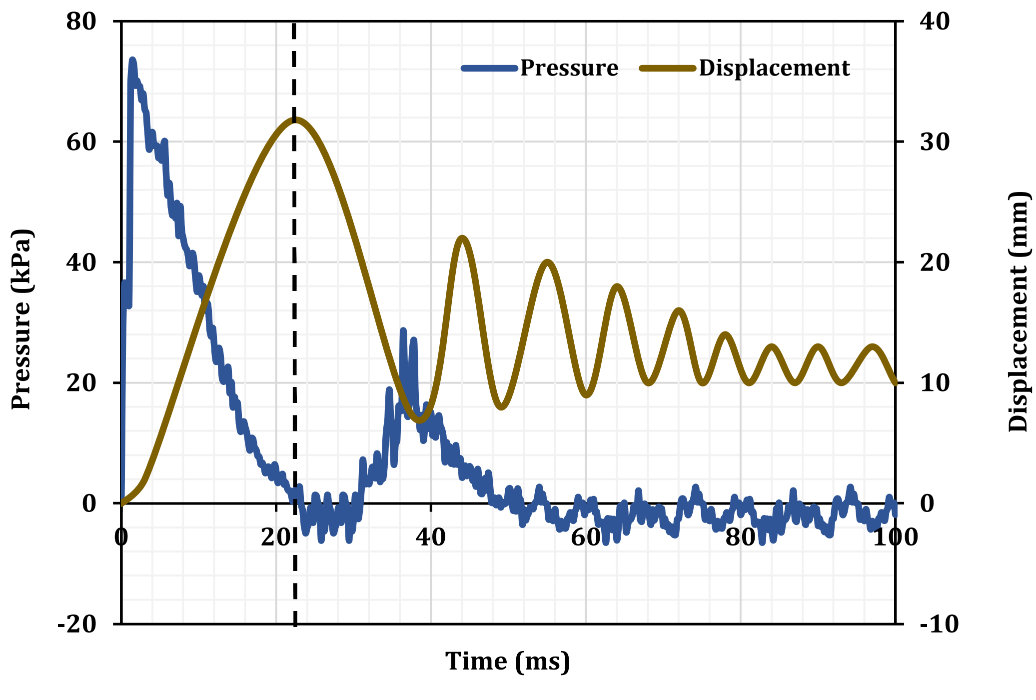

Figure 4.46. Pressure and displacement time history of Wall-4-3

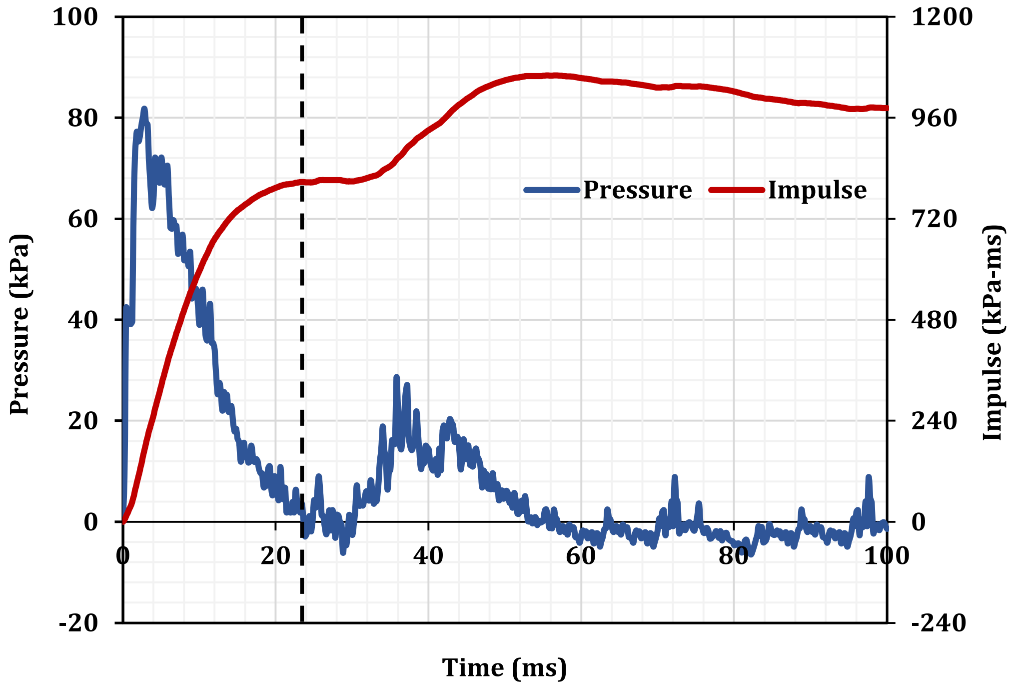

Figure 4.47. Pressure and impulse time history of Wall-4-4

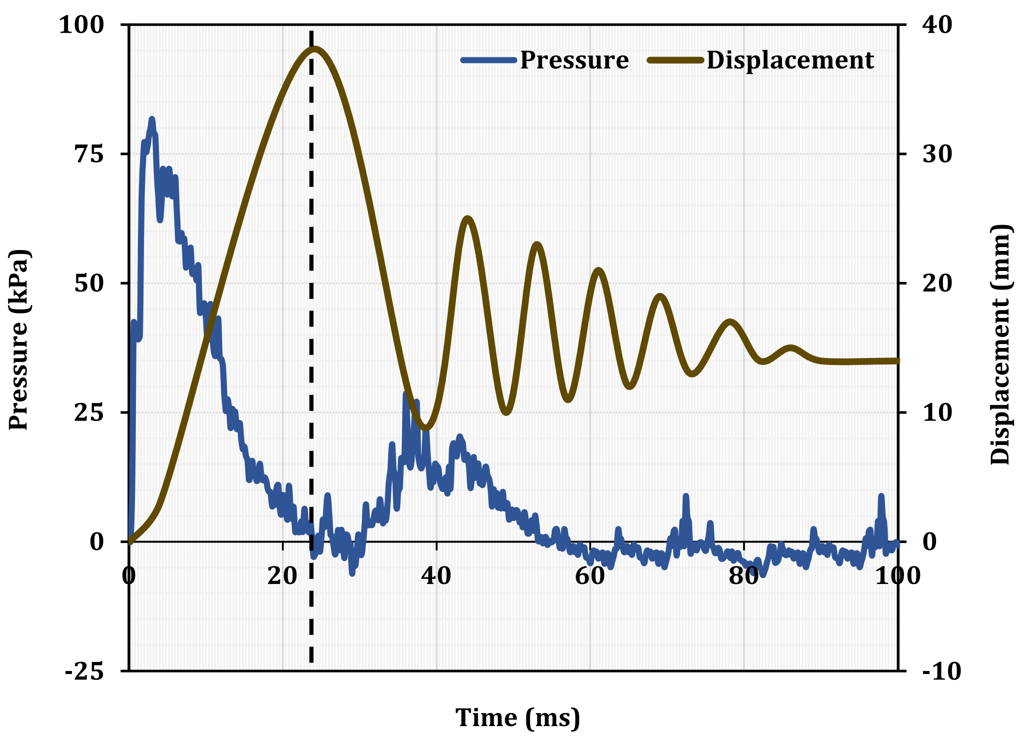

Figure 4.48. Pressure and displacement time history of Wall-4-4

Figure 4.49. Wall-4 split into two halves after shot 5 with no release of debris

Figure 4.50. Yielded and necked SS304 strands

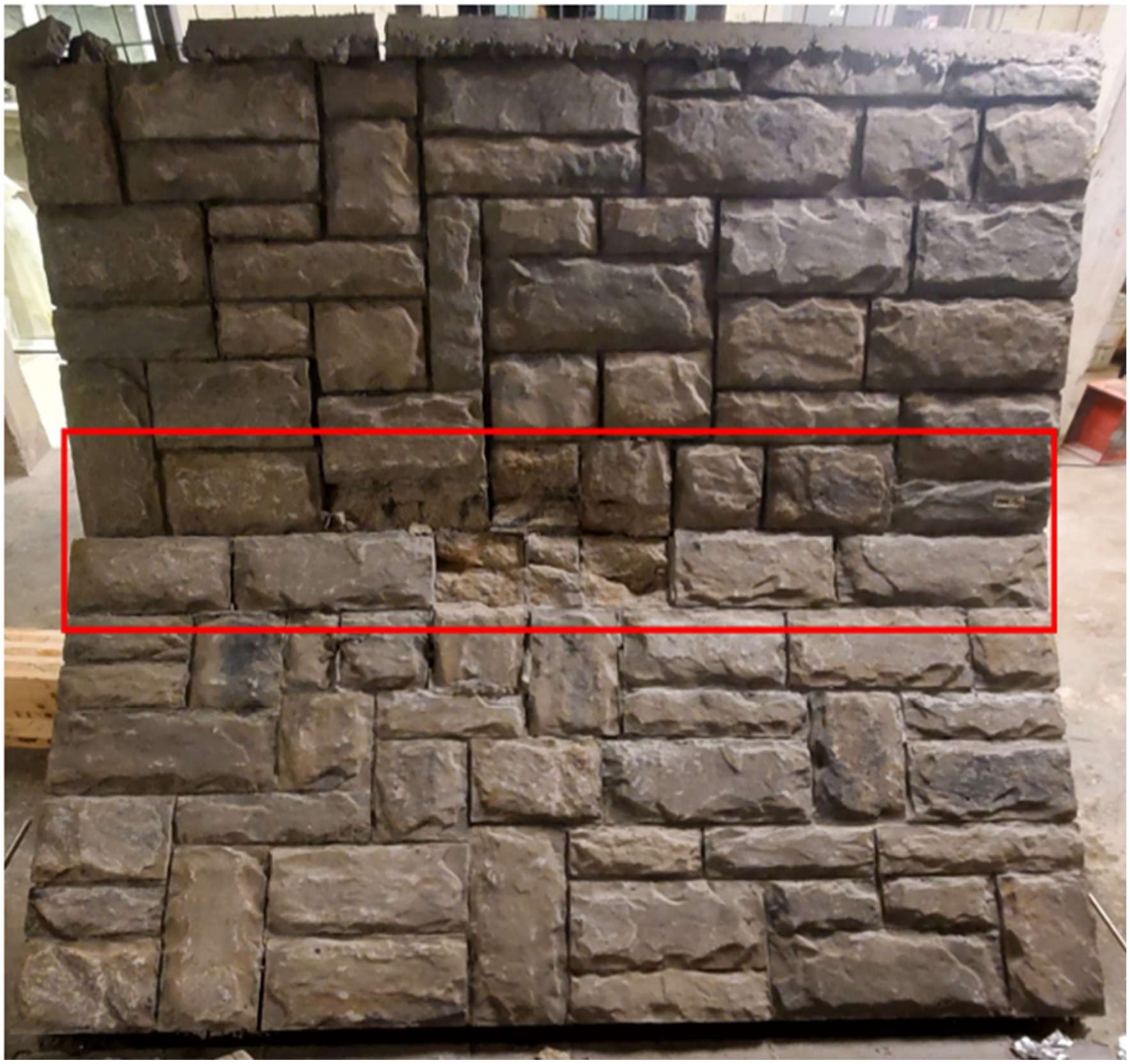

Figure 4.51. The exterior face of the failed Wall-4-5

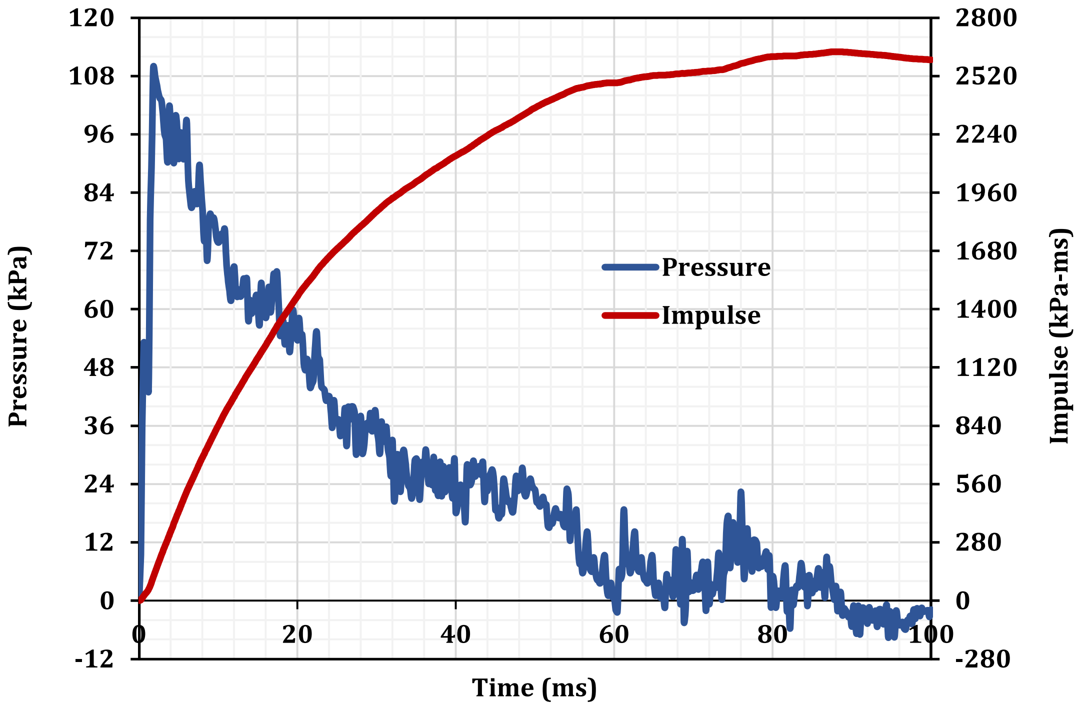

Figure 4.52. Pressure and impulse time history of Wall-4-5

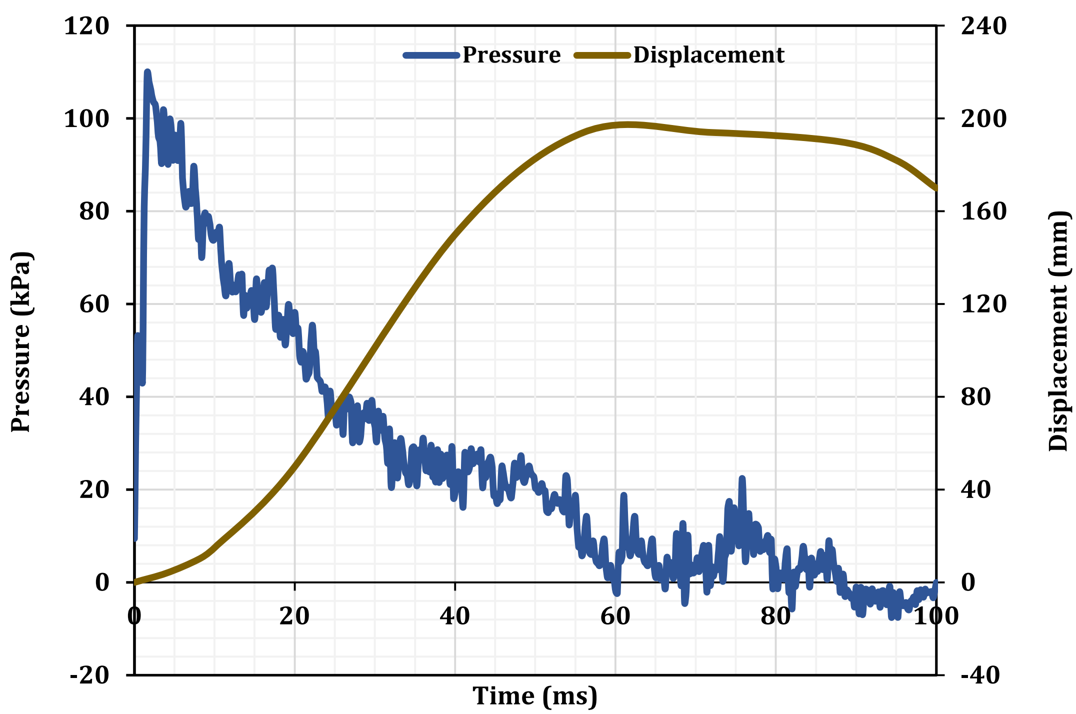

Figure 4.53. Pressure and displacement time history of Wall-4-5

4.8 Wall-5

Wall-5 was constructed with CMU blocks laid in a coursed pattern and tightly connected to its supports. The wall was designed as a load-bearing wall as an axial load of 120kN was applied over its top concrete beam with two hydraulic jacks. It was retrofitted with reinforced polyurea-3.1mm. Three test shots were fired on the wall-5 (Wall-5-1, Wall-5-2, Wall-5-3) until it reached global failure. The loading parameters and the displacement responses obtained are summarized in Table 4.7. The 1829 mm (6ft) driver length was used for all three shots.

Table 4.7: Summary of test results of Wall-5

Wall Type	Wall-5	P_D (kPa)	l_D (mm)	P_r (kPa)	I_r (kPa-ms)	t_d (ms)	d_{max} (mm)	d_{res} (mm)	θ_{max} (degrees)
CMU	Wall-5-1	345	1829	51	420	18	23	6	1.3
	Wall-5-2	483	1829	73	578	21	47	22	2.7
	Wall-5-3	621	1829	103	1030	27	108	95	6.2

4.8.1 Wall-5-1

The first shot on Wall 5 had a driver pressure of 50 psi (345 kPa) and a spool pressure of 25 psi (172 kPa). This resulted in an incident pressure of 25 kPa and a reflected pressure of 51 kPa. A reflected impulse of 420 kPa-ms was measured over a positive phase duration of 18 ms. The maximum mid-height deflection was 23 mm and corresponded to 1.3^0 support rotations. Its residual displacement response was 6 mm with no visible damage. The pressure, impulse, and displacement time histories are shown in Figures 4.54 and 4.55.

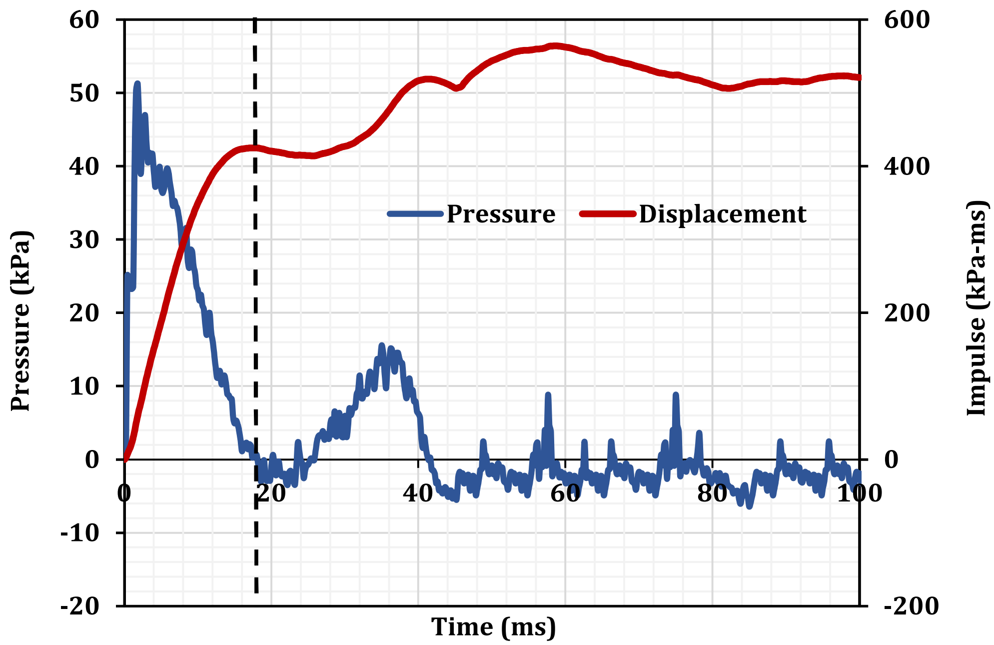

Figure 4.54. Pressure and impulse time history of Wall-5-1

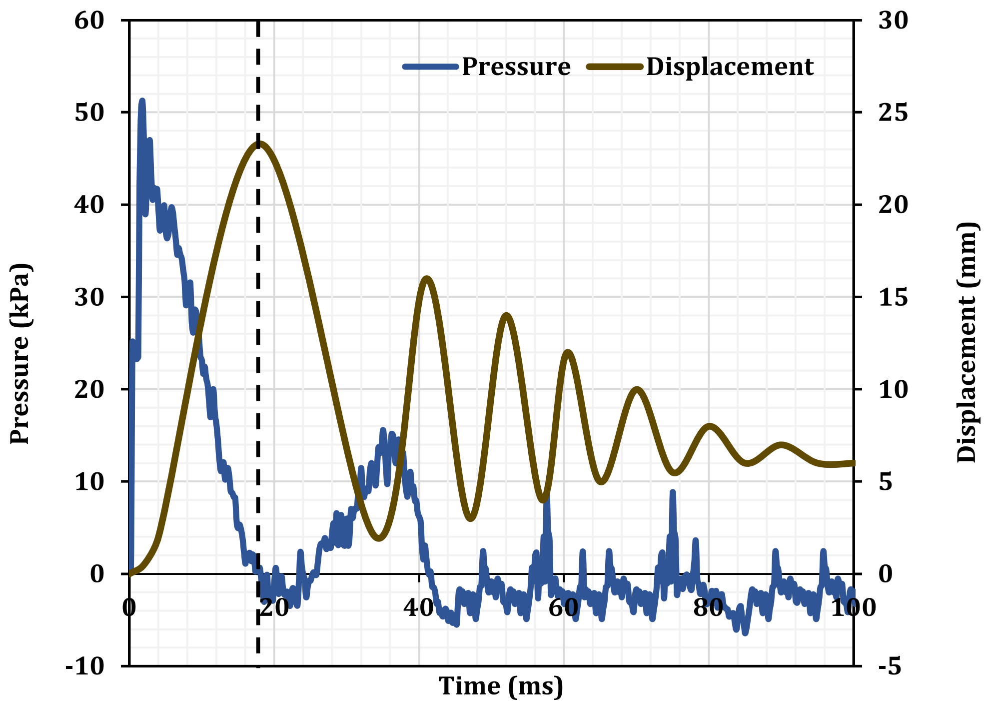

Figure 4.55. Pressure and displacement time history of Wall-5-1

4.7.2 Wall-5-2

In the second shot on Wall-5, the driver pressure was increased to 70 psi (483 kPa), and correspondingly, the spool pressure was increased to 35 psi (241 kPa). An incident pressure of 35 kPa was generated with a peak reflected pressure of 73 kPa and an impulse of 578 kPa-ms. The maximum wall mid-height deflection was measured at 47 mm with corresponding support rotations of 2.7^0. The positive phase duration of blast pressure was 21 ms. The residual displacement of the wall was 22 mm, with visible cracks seen along the sixth course of the wall, as shown in Figure 4.56. The pressure, impulse, and displacement time histories are plotted in Figures 4.57 and 4.58.

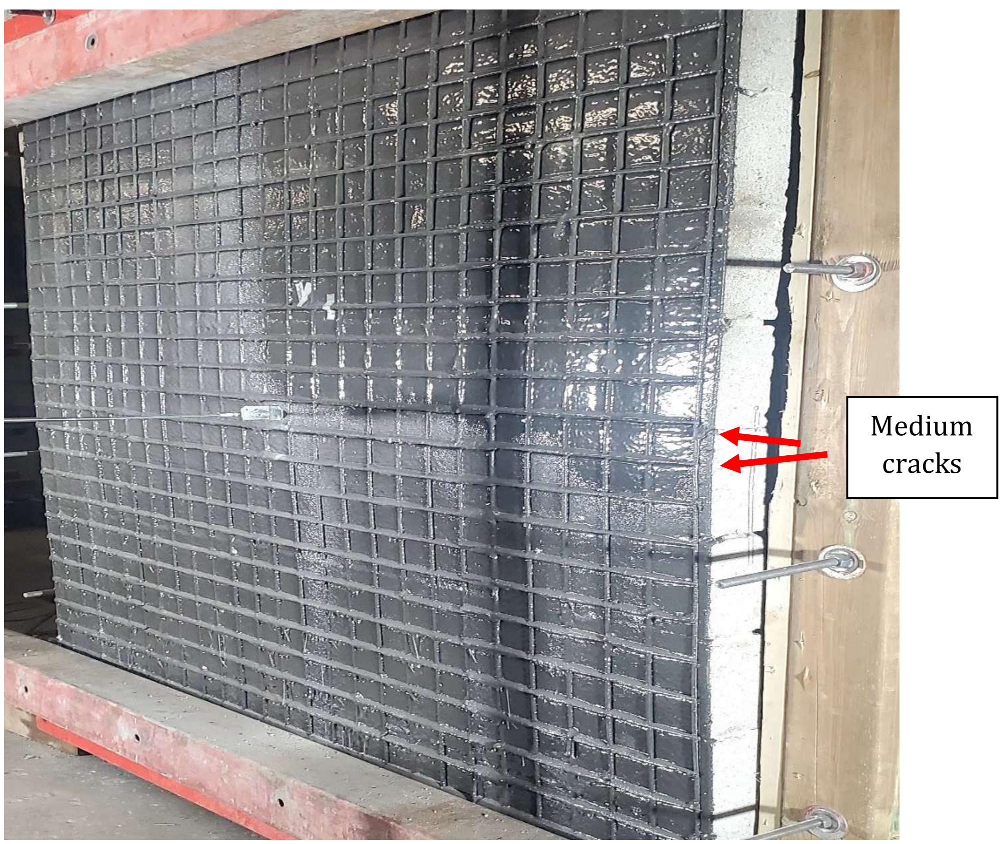

Figure 4.56. Cracks seen on the sixth course of Wall-5-2

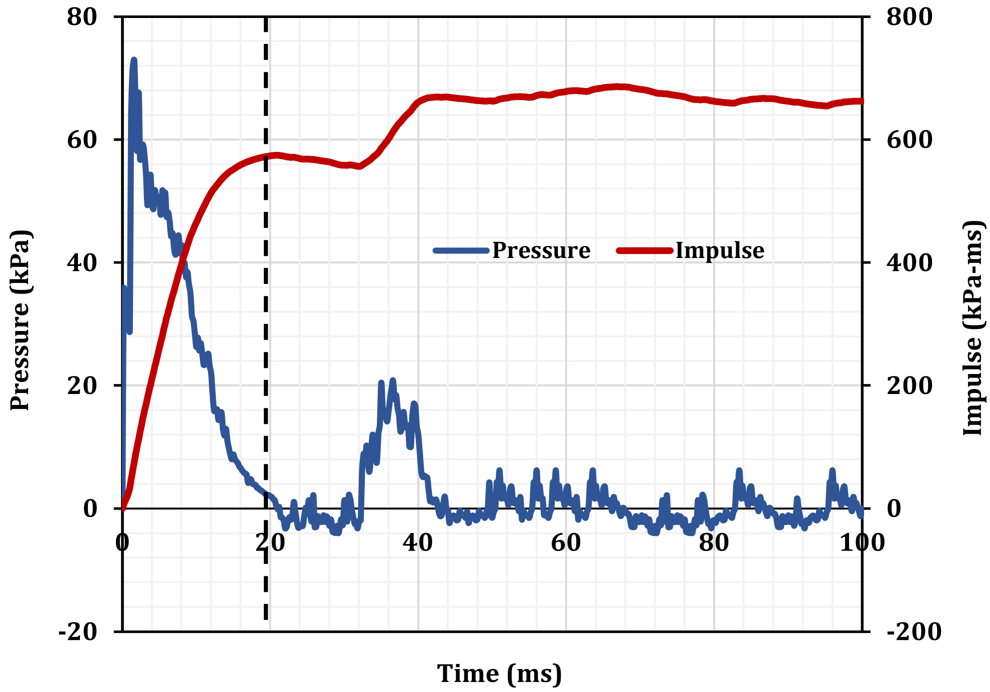

Figure 4.57. Pressure and impulse time history of Wall-5-2

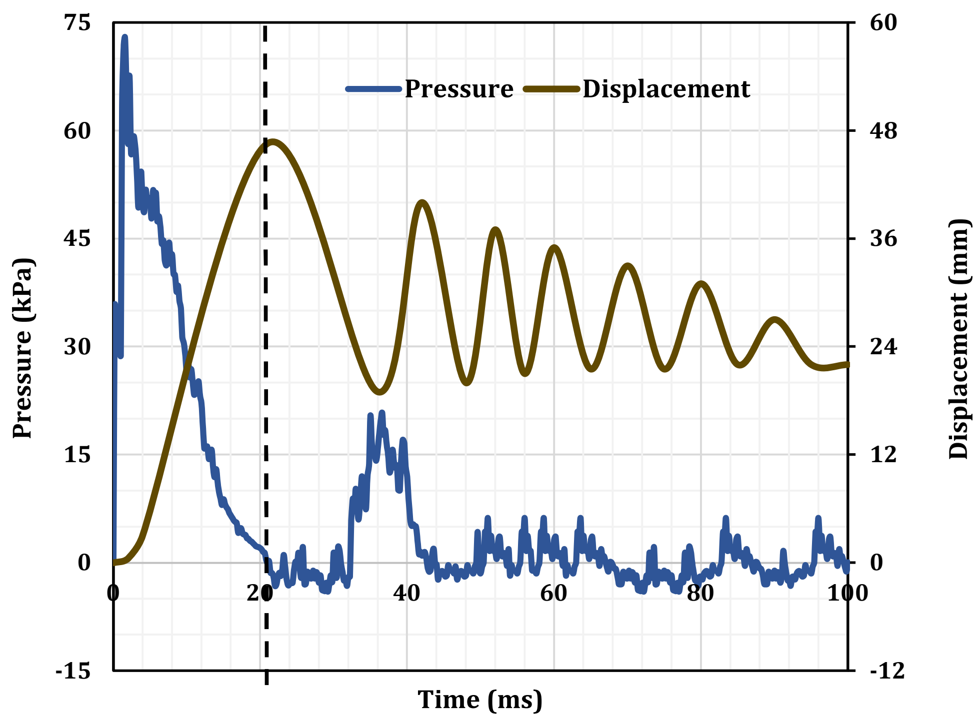

Figure 4.58. Pressure and displacement time history of Wall-5-2

4.8.3 Wall-5-3

For the third shot on Wall-5, the driver pressure was further increased to 90 psi (621 kPa), and that of the spool section was increased to 45 psi (310 kPa). As the foils ruptured, an incident pressure of 64 kPa was fired, and a peak reflected pressure of 103 kPa was generated at impact with the wall. The reflected impulse over the positive phase duration of 27 ms was 1030 kPa-ms. The maximum mid-height deflection of the wall was 108 mm, and the corresponding support rotations were 6.2^0. The residual displacement was measured to be 95 mm with the wall split into two halves; the mesh yielded at its mid-height, and no fragmentation was observed as the reinforced polyurea held the wall in place, as presented in Figures 4.59 and 4.60. Its reflected pressure, impulse, and displacement time histories can be seen in Figures 4.61 and 4.62.

Figure 4.59. Failure of Wall-5-3

Figure 4.60. The exterior surface of Wall-5 after failure

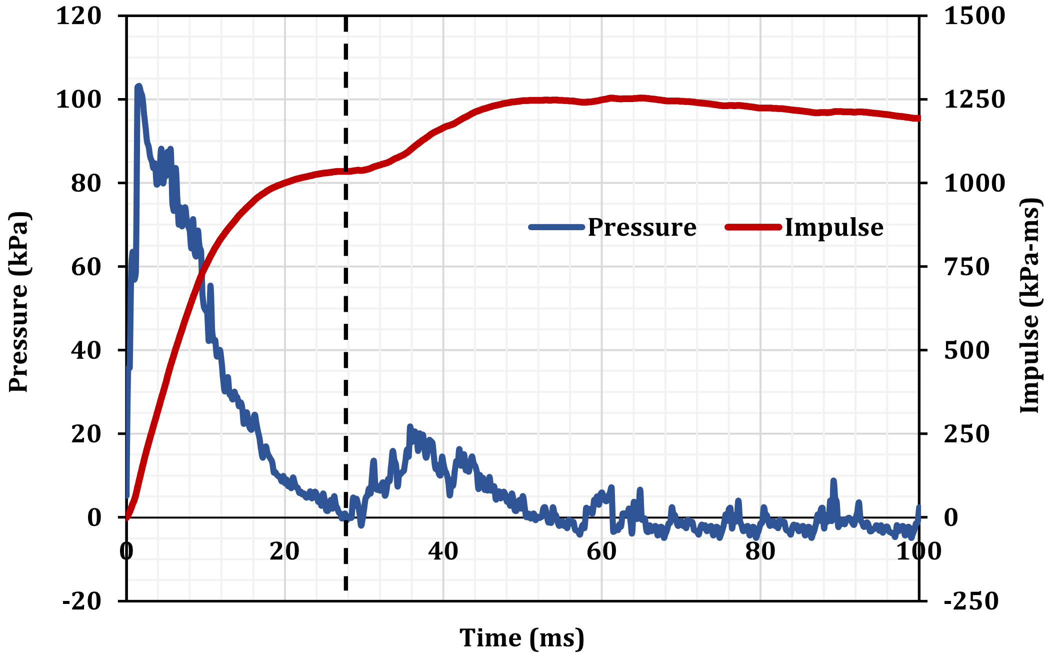

Figure 4.61. Pressure and impulse time history of Wall-5-3

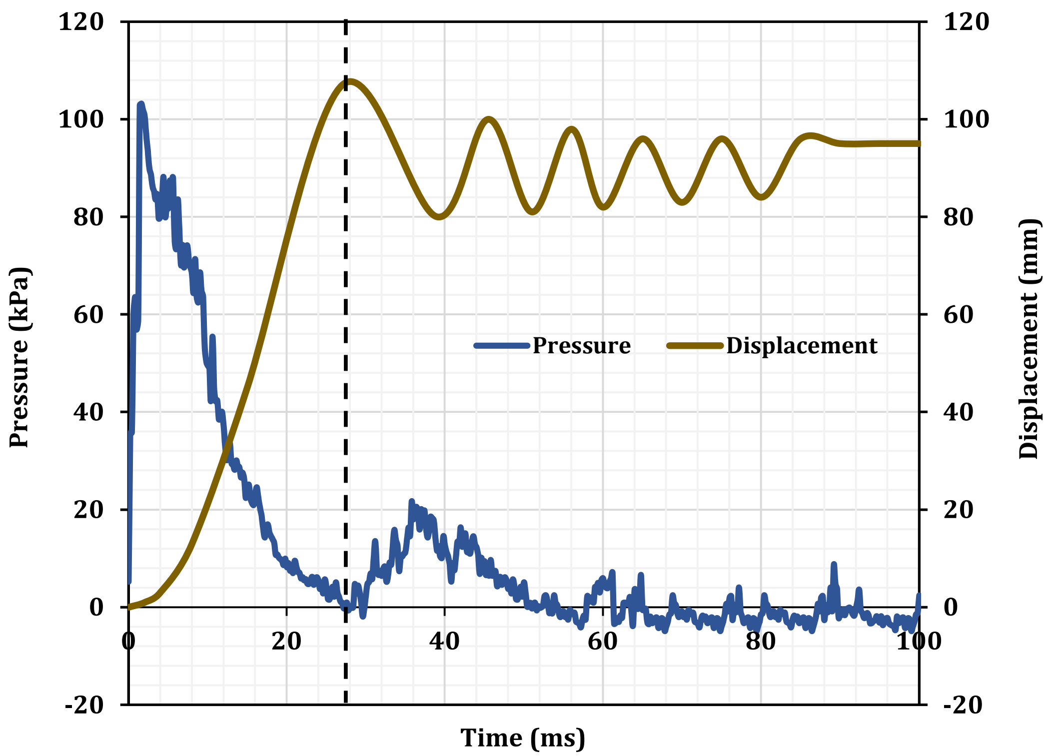

Figure 4.62. Pressure and displacement time history of Wall-5-3

4.9 Wall-6

Wall-6 is a load-bearing CMU wall. It was subjected to an axial compressive force of 180 kN utilizing two hydraulic jacks. Five progressively increasing blast shots were fired on it (Wall-6-1, Wall-6-2, Wall-6-3, and Wall-6-4 and Wall-6-5) until global failure was reached. The loading parameters and the measured mid-height deflections are tabulated in Table 4.8. A constant driver length of 1829mm (6ft) was used for the first four shots, while the last shot, which required higher impulse beyond the pressure capacity of the shock tube, had the driver length extended to 3962.4mm (13ft).

Table 4.8: Summary of test results of Wall-6

Wall Type	Wall-6	P_D (kPa)	l_D (mm)	P_r (kPa)	I_r (kPa-ms)	t_d (ms)	d_{max} (mm)	d_{res} (mm)	θ_{max} (degrees)
CMU	Wall-6-1	345	1829	52	451	20	17	0	1
	Wall-6-2	483	1829	67	631	23	26	4	1.5
	Wall-6-3	621	1829	86	764	27	44	27	2.5
	Wall-6-4	758	1829	120	1067	29	76	40	4.3
	Wall-6-5	696	3962	125	2420	62	185	120	10.8

4.9.1 Wall-6-1

For the first shot on Wall-6, the shock tube was set to a driver pressure of 50 psi (345 kPa) and a spool pressure of 25 psi (172 kPa). It generated an incident pressure of 29 kPa and a peak reflected pressure of 52 kPa. A reflected impulse of 451 kPa-ms was computed over a positive phase duration of 20 ms. The maximum mid-height deflection was measured at 17 mm, corresponding to 1^0 support rotations. No residual displacement or visible damage was sustained. The pressure, impulse, and displacement time histories are illustrated in Figures 4.63 and 4.64.

4.9.2 Wall-6-2

The second shot on Wall-6 was applied concurrently with increased driver and spool pressures to 70 psi (483 kPa) and 35 psi (241 kPa). The resulting peak incident and reflected pressures were 37 kPa and 67 kPa, respectively. A reflected impulse of 631 kPa-ms was recorded over a positive phase duration of 23 ms. The wall developed a maximum mid-height deflection of 26 mm when the support rotations were 1.5^0. The residual deflection at the end of the test was measured to be 4 mm with no visible cracks. The pressure, impulse, and displacement time histories are given in Figures 4.65 and 4.66.

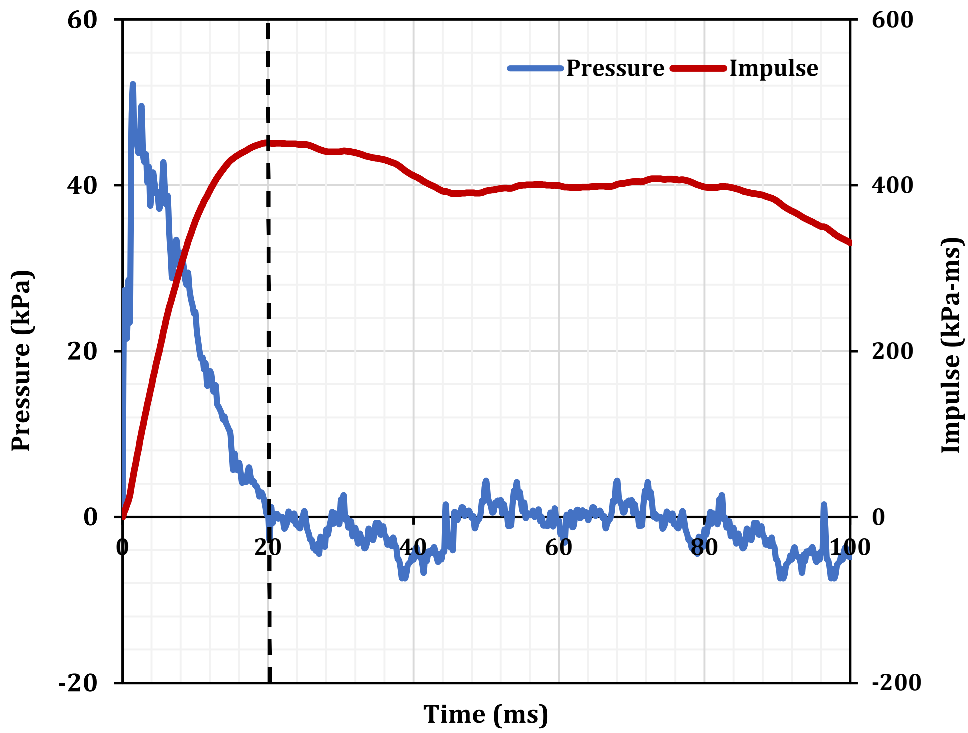

Figure 4.63. Pressure and impulse time history of Wall-6-1

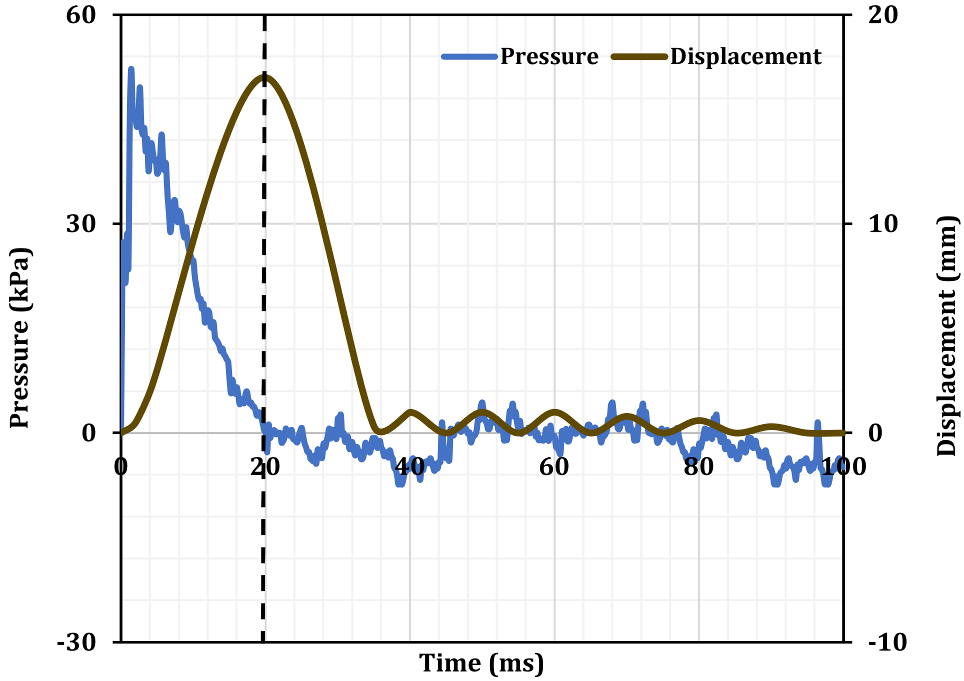

Figure 4.64. Pressure and displacement time history of Wall-6-1

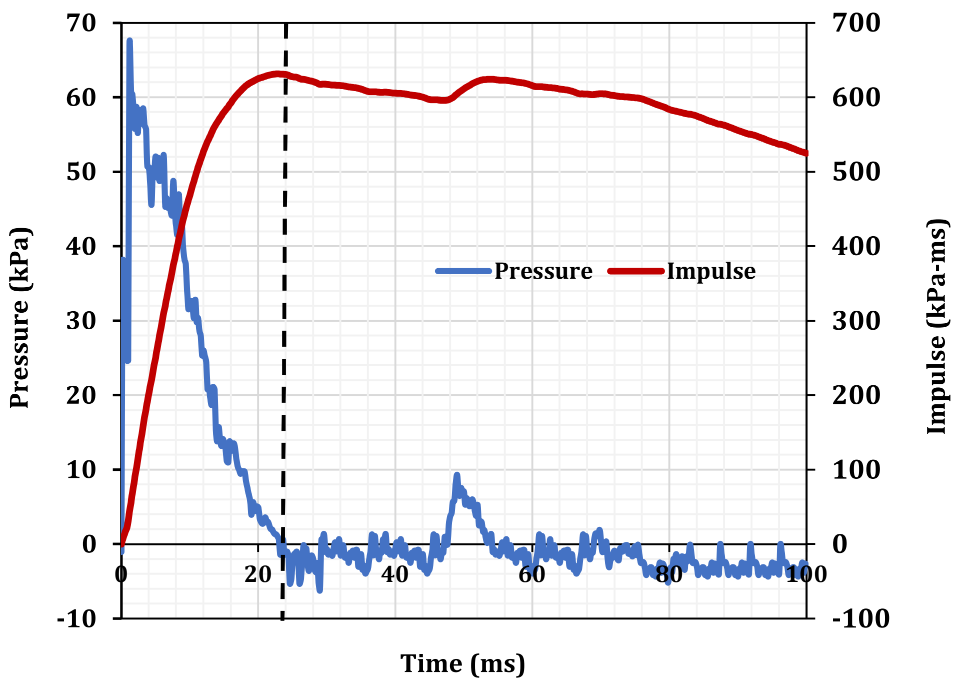

Figure 4.65. Pressure and impulse time history of Wall-6-2

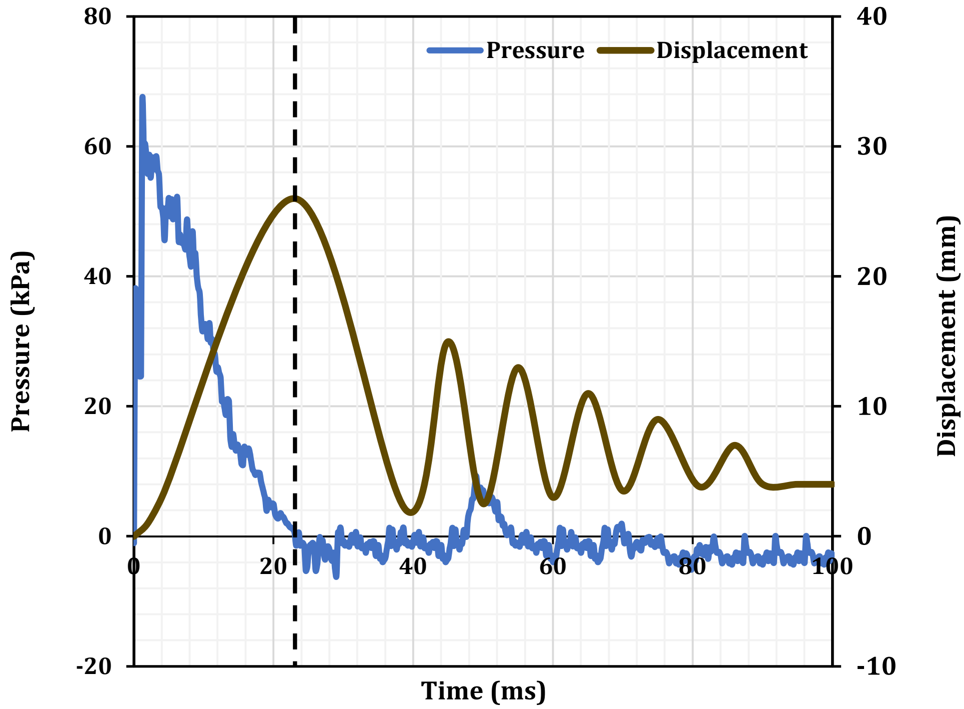

Figure 4.66. Pressure and displacement time history of Wall-6-2

4.9.3 Wall-6-3

In executing the third shot, the driver pressure was further raised to 90 psi (621 kPa) and that of the spool to 45 psi (310 kPa). The release of the pressures produced a peak incident pressure of 42 kPa and a peak reflected pressure of 86 kPa. Its positive phase duration was 27 ms with a resultant impulse of 764 kPa-ms. The maximum mid-height deflection of the wall was measured to be 44 mm at a support rotation of 2.5^0. The residual deflection at the end of the test was 27 mm with visible fine cracks, as shown in Figure 4.67. The recorded pressure, impulse, and displacement time histories are plotted in Figures 4.68 and 4.69.

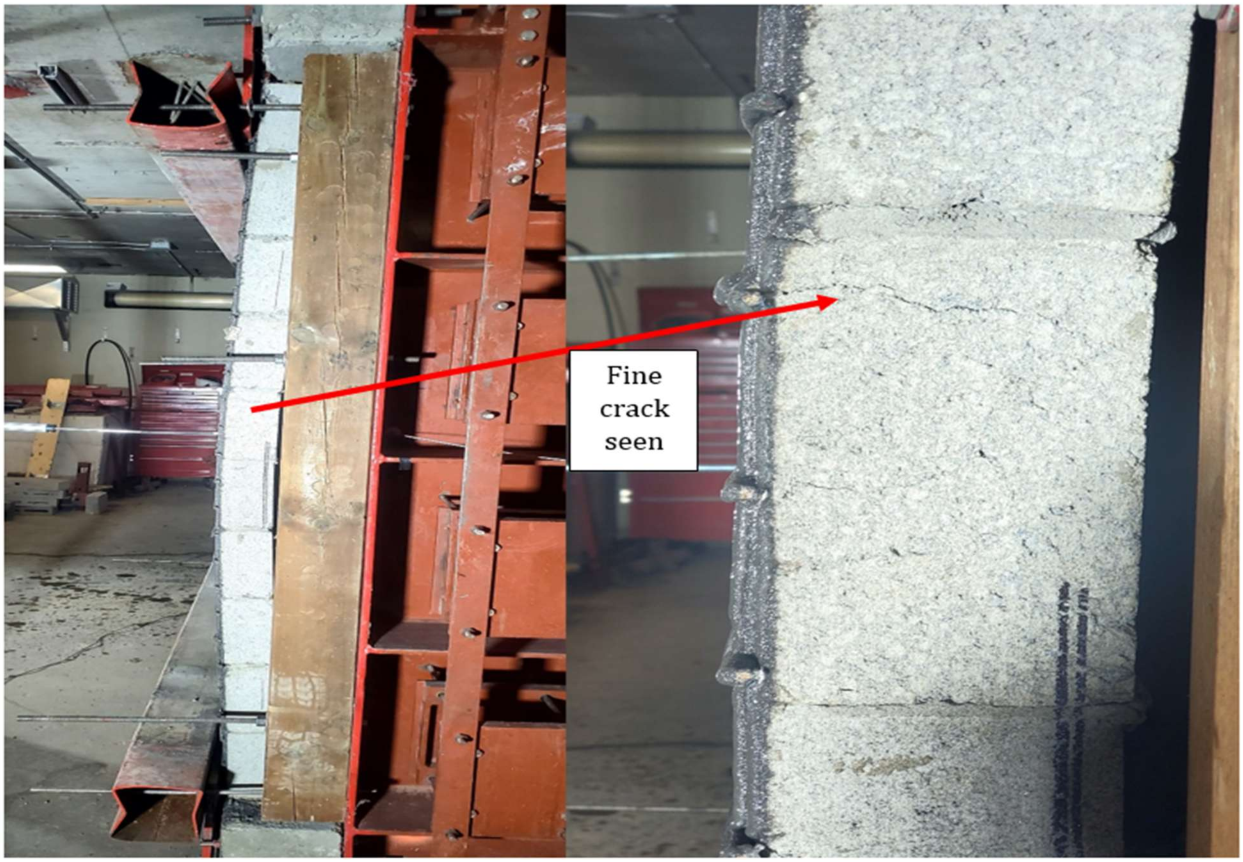

Figure 4.67. A fine crack was seen on the fifth course of Wall-6 after shot 3

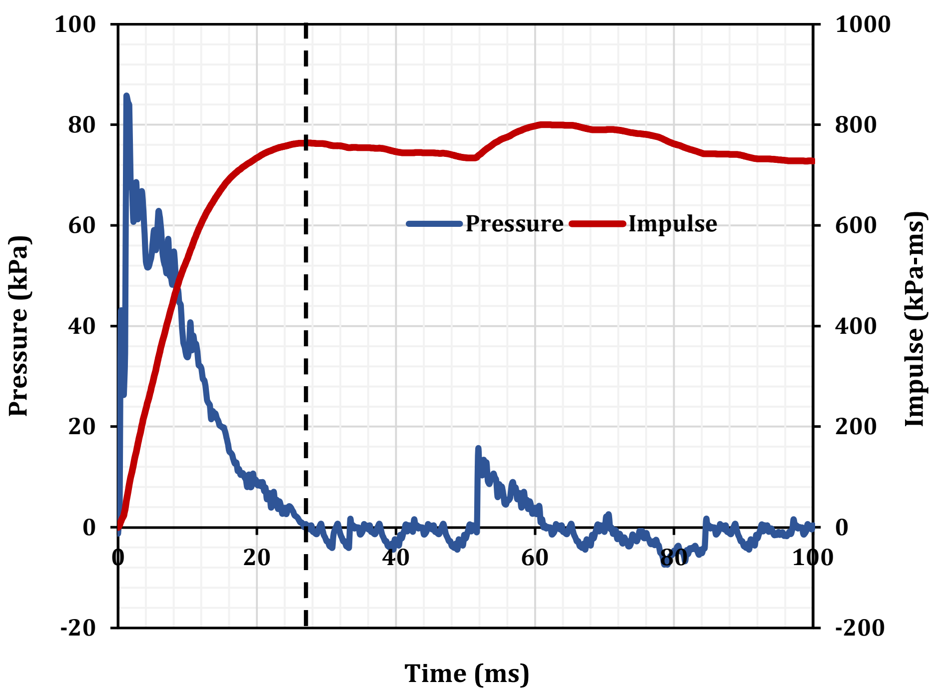

Figure 4.68. Pressure and impulse time history of Wall-6-3

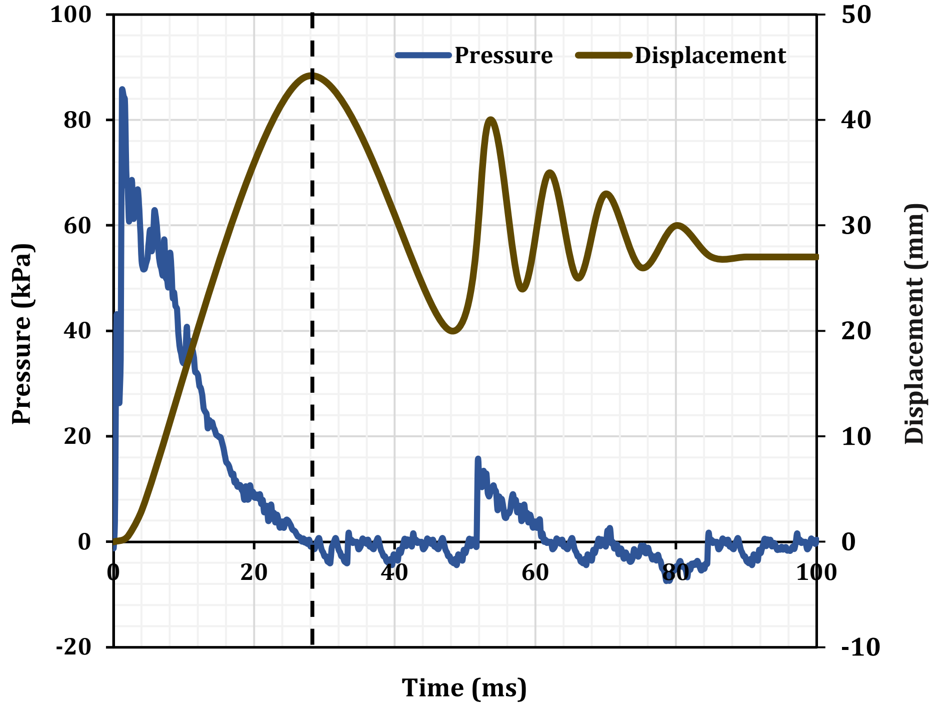

Figure 4.69. Pressure and displacement time history of Wall-6-3

4.9.4 Wall-6-4

The driver pressure was 110 psi (758.4 kPa), and the spool pressure was 55 psi (379.2 kPa) to generate the fourth shot. An incident pressure of 50 kPa and a peak reflected pressure of 120 kPa were recorded. The positive phase duration and the reflected impulse read 29 ms and 1067 kPa-ms, respectively. The maximum wall mid-height deflection was 76 mm at support rotations of 4.3^0. The residual displacement at the end of the test was recorded to be 40 mm, with a wide crack observed on its fifth course and torn polyurea, as shown in Figure 4.70. Figures 4.71 and 4.72 displayed its pressure, impulse, and displacement time histories.

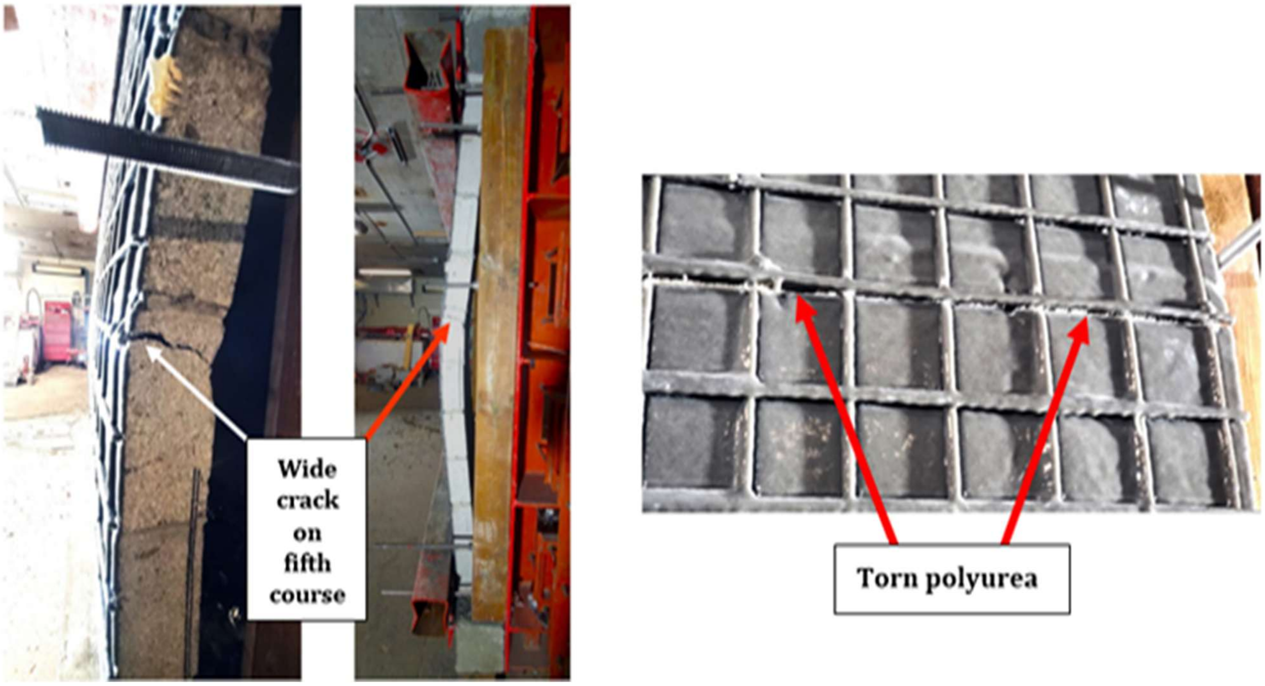

Figure 4.70. Torn polyurea and wider cracks are seen on the fifth course of Wall-6-4

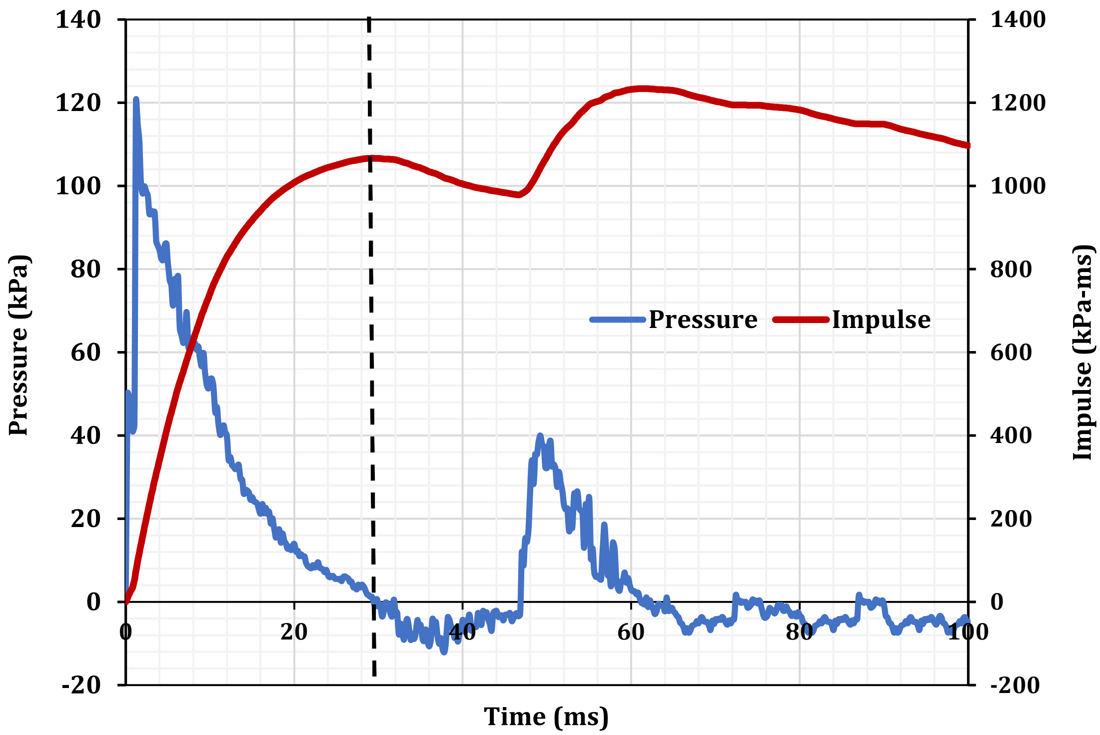

Figure 4.71. Pressure and impulse time history of Wall-6-4

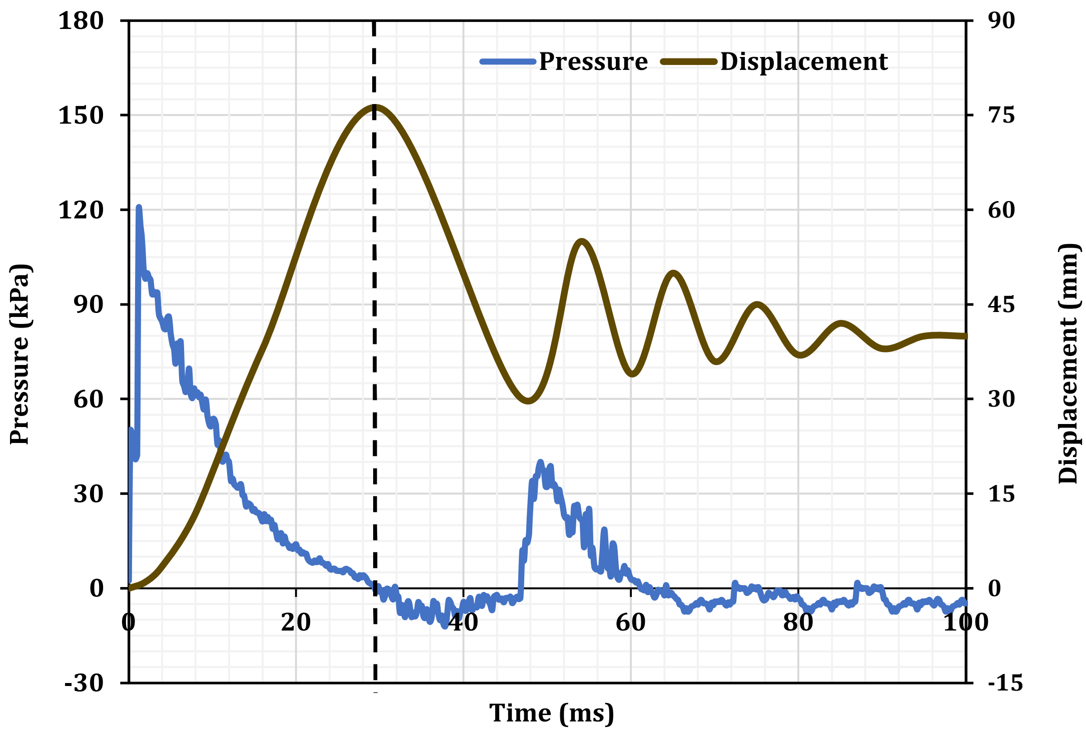

Figure 4.72. Pressure and displacement time history of Wall-6-4

4.9.5 Wall-6-5

The fifth shot caused the wall to fail. At this stage of pressure load, the shock tube capacity had been reached, and the driver length needed to be extended to 3962 mm for higher impulse. This final shot's driver and spool pressures were 101 psi (696 kPa) and 51 psi (348 kPa). The incident and peak reflected pressures recorded were 65 kPa and 125 kPa, respectively. The positive phase lasted for 62 ms, generating an impulse of 2420 kPa-ms. The maximum wall mid-height deflection was measured to be 185 mm at a support rotation of 10.8^{0}. The residual deflection of the wall at the end of the test was 120 mm. The wall developed failure planes at three locations along its height: the fifth course, the sixth course, and the mortar joint between the sixth and the seventh course (Figure 4.73). There was no release of debris at failure. The pressure, impulse, and displacement time histories of Wall-

6-5 are shown in Figures 4.74 and 4.75. Table 4.9 summarizes the loading parameters and recorded deformations for all six walls tested.

Figure 4.73. Failed Wall-6-5

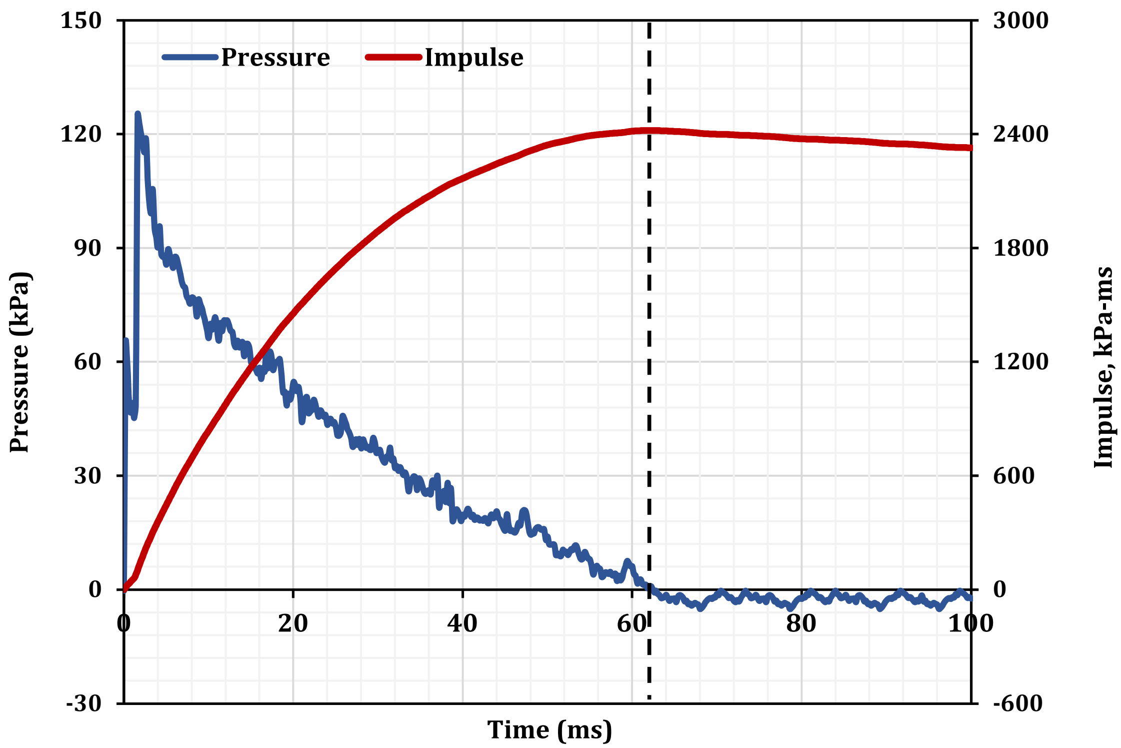

Figure 4.74. Pressure and impulse time history of Wall-6-5

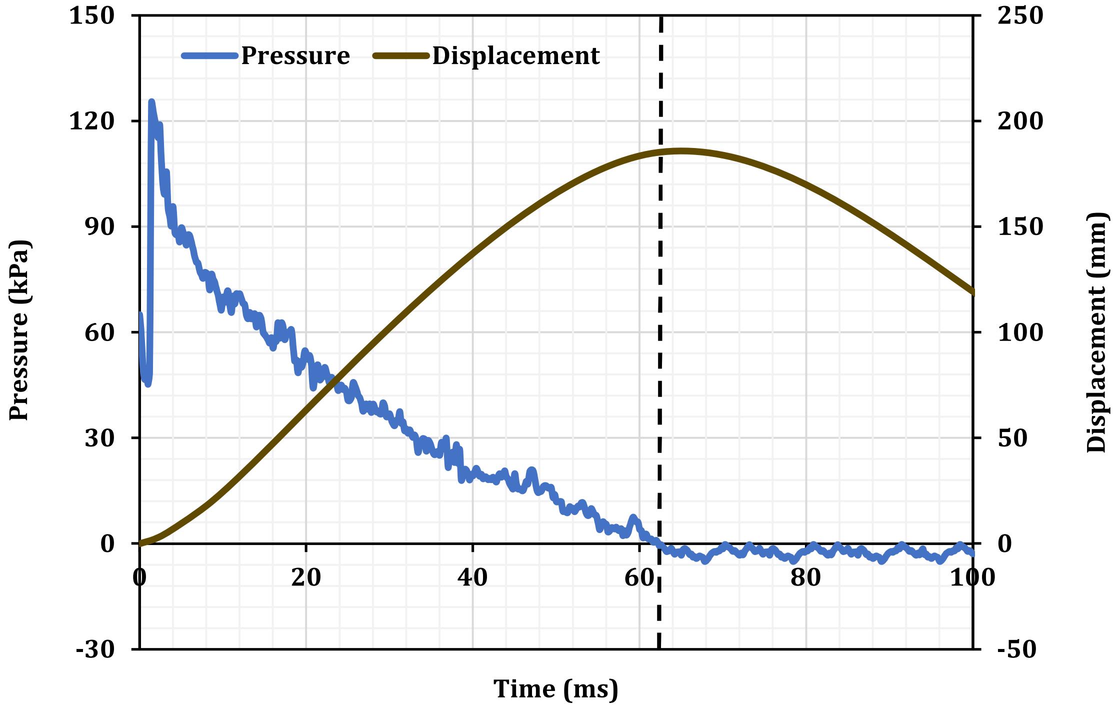

Figure 4.75. Pressure and displacement time history of Wall-6-5

Table 4.9: Summary of the experimental results

Samples	Wall Type	Mesh Size (mm)	Axial Load (kN)	P_r (kPa)	I_r (kPa-ms)	d_{max} (mm)	d_{res} (mm)	Θ_{max} (degrees)
Wall-1-1	STONE	3.1	-	43	301	16	NA	1
Wall-1-2				57	403	26	6	1.5
Wall-1-3				67	542	39	14	2.2
Wall-1-4				93	711	100	74	5.7
Wall-2-1	CMU	4.1	-	50	419	23	6	1.3
Wall-2-2				72	550	34	9	2.0
Wall-2-3				74	701	56	22	3.2
Wall-2-4				85	793	80	30	4.6
Wall-2-5				85	2177	203	110	11.5
Wall-3-1	CMU	3.1	-	50	420	25	6	1.4
Wall-3-2				67	547	39	18	2.2
Wall-3-3				76	714	89	25	5.1
Wall-3-4				89	874	140	30	8.0
Wall-3-5				88	1479	NA	NA	NA
Wall-4-1	STONE	4.1	120	49	432	17	3	1
Wall-4-2				66	560	22	6	1.3
Wall-4-3				74	695	32	10	1.8
Wall-4-4				82	808	38	14	2.2
Wall-4-5				110	2488	197	170	11.1
Wall-5-1	CMU	3.1	120	51	420	23	6	1.3
Wall-5-2				73	578	47	22	2.7
Wall-5-3				103	1030	108	95	6.2
Wall-6-1	CMU	4.1	180	52	451	17	0	1
Wall-6-2				67	631	26	4	1.5
Wall-6-3				86	764	44	27	2.5
Wall-6-4				120	1067	76	40	4.3
Wall-6-5				125	2420	185	120	10.8

CHAPTER 5. EXPERIMENTAL RESULTS DISCUSSION

5.1 General

This chapter presents the effects of test parameters considered in the experimental phase of the current research project. The parameters studied include the effects of wire mesh reinforcement area, axial load simulating load-bearing walls, and the type of masonry used in the wall construction (CMU versus stone). The effects of these parameters are discussed with due consideration given to the level of blast loading (reflected pressure and impulse), the wall performance exhibited by mid-height deflections, and the observed failure patterns. The results are compared with those obtained from the control walls (URM-1, URM-3) and the polyurea retrofit system tested by Ciornei, 2012 (URM-2).

The chapter is divided into the following sections:

- Effect of wire mesh reinforcement area
- Effect of masonry type
- Effect of axial load application

5.2 Effect of wire mesh reinforcement area

5.2.1 Non-Load Bearing CMU Walls

The performance of the control wall, URM-1, and the two non-load bearing CMU retrofitted walls (Wall-2, Wall-3) are discussed under this subsection. URM-1 was not retrofitted and was tested by Ciornei (2012) in an earlier phase of this research program. The wall was exposed to four blast shots (Table 4.1) and had cracks formed along its mortar joint for each shot. It attained a maximum displacement of 56.5 mm before its catastrophic collapse from its last shot. Its failure was brittle, with many fragments and flying debris released. Its crack formation was instant from the mortar joint of the mid-height to its other joints; no cracks or damage was seen on the block units until the collapse. Before collapse, the wall absorbed up to a blast load of 23.4 kPa reflected pressure and 179.3 kPa-ms impulse and suffered global failure at a reflected pressure of 30.7 and impulse of 265.1kPa (Ciornei 2012).

Wall-2 was strengthened with reinforced polyurea-4.1 mm. It was subjected to five blast shots and failed at its fifth shot after it had absorbed a blast load of 85 kPa reflected pressure and 2177 kPa-ms impulse. It attained a maximum mid-height displacement of 203 mm and failed in a non-catastrophic ductile manner with no fragments and flying debris released (Figure 4.23).

Wall-3 was retrofitted with reinforced polyurea-3.1mm. It was also exposed to five successive blast shots like Wall-2. Upon its fourth shot, it absorbed a maximum blast load of 89kPa reflected pressure and 874kPa-ms impulse, which caused a maximum mid-height displacement of 140 mm. It failed globally when the last shot was fired with a blast capacity of 88 kPa reflected pressure and 1479 kPa-ms impulse and a devastating release of heavy fragments (Figure 4.38).

5.2.2 Performance and Response Comparison

(a) Blast capacity

The composite nature of the reinforced polyurea formed with Wall-2 and Wall-3 significantly improved their blast resistance when compared with URM-1. Both retrofitted walls were able to absorb far higher blast capacity than those of the control. The maximum reflected pressure and impulse on Wall-2 were 263% and 1114%, significantly greater than the blast-resistant capacity of URM-1 before its global failure. Similarly, the peak reflected pressure and reflected impulse of Wall-3 were increased by 280% and 387% over those of the reference wall at their penultimate shots before both failed.

(b) Out of plane capacity

The ductility of the reinforced polyurea impacted both retrofitted walls (Wall-2 and Wall-3) with increased out-of-plane capacity by more than 259% and 148%, respectively, over the control wall. URM-1 failed in a brittle manner, releasing flying debris at a much lower blast load. At the same time, Wall-2 and Wall-3 maintained a ductile manner of failure even at higher blast energies as their stainless-steel mesh yielded, strain-hardened, and necked, and the block units were held in place by the bonding force of the polyurea.

(c) Stiffness and strength

Wall-2 and Wall-3 retrofits had higher stiffness and strength than URM-1. The blast loads that failed URM-1 would have negligible impacts on the retrofitted walls. Of the two strengthened walls, Wall-2 absorbed a higher energy (85 kPa, 2177 kPa-ms) without any fragmentation, whereas Wall-3 failed at a lower blast load (88 kPa, 1479 kPa-ms). The maximum mid-height displacement of Wall-2 was reduced by 59% over that of Wall-3 under the same blast load of P_r = 75 kPa and I_r = 714 kPa-ms. Wall-2 higher energy absorption before its failure is an indication of higher strength, which can be attributed to the larger reinforcement area of its retrofit.

The summary of the comparison of non-load-bearing CMU walls is shown in Figure 5.1.

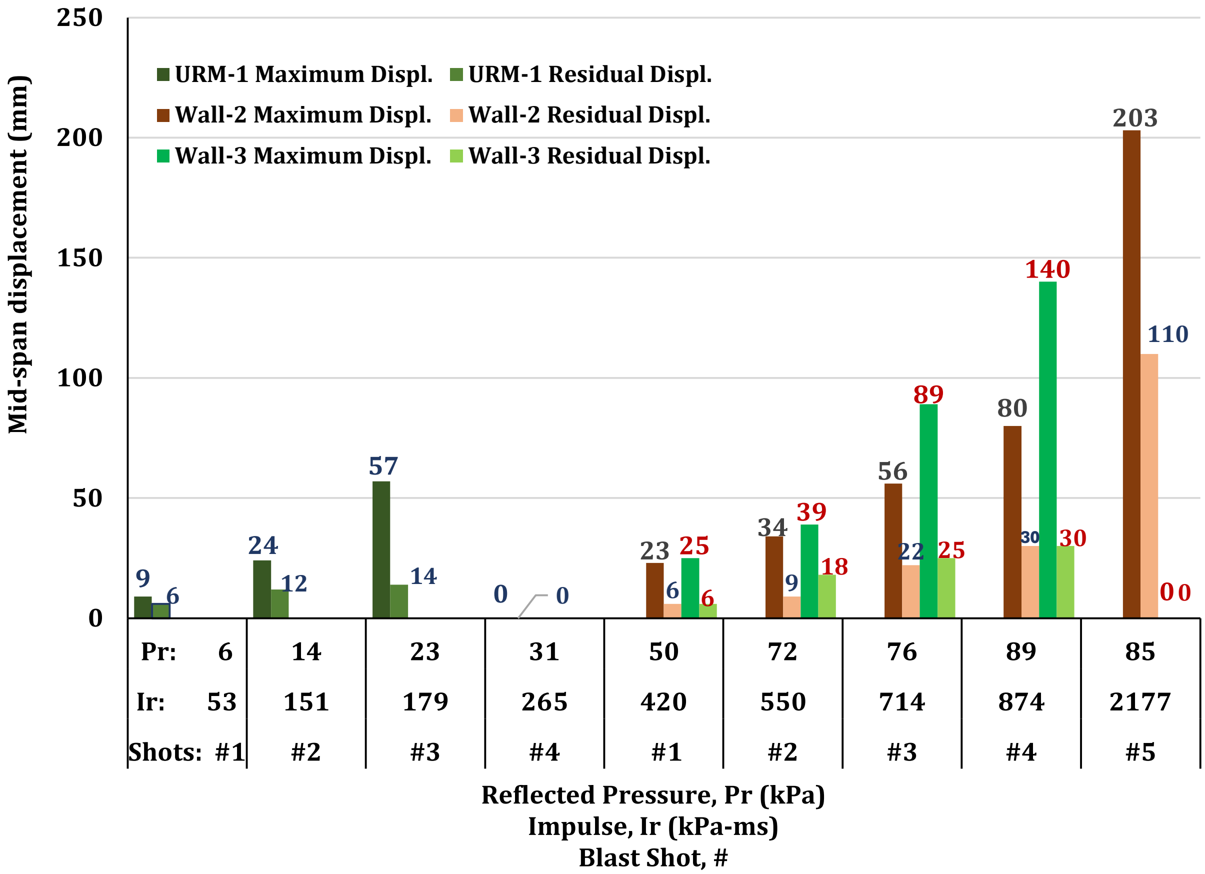

Figure 5.1. Displacements of non-load bearing CMU walls under varying blast loads

5.2.3 Load Bearing CMU Walls

The control-load bearing wall, URM-3, also built without any retrofit, was tested under a constant axial load of approximately 120 kN applied with the aid of two hydraulic jacks placed on the top support of the wall. It was exposed to seven blast shots and had cracks formed along its mortar joints during the second shot. It reached a maximum mid-height displacement of 45 mm on its fifth shot and eventually collapsed on the seventh. The progression of wall damage showed hinge formation at its mid-height with an immediate split of the mid-mortar joint followed by the disintegration of other joints and block units. Its mode of failure was brittle, with significant fragmentation and flying debris. It was observed that URM-3 exhibited higher arching compression than the companion

Unretrofitted infill wall (URM-1), as well as superior performance in terms of blast strength and stiffness. Before its collapse, URM-3 resisted a maximum reflected pressure of 38 kPa and a positive phase impulse of 309 kPa-ms. It also exhibited reduced maximum mid-height deflections than URM-1. The tight contact with its supports and the axial load application triggered quick arching action in URM-3 and introduced higher compressive resistance than its non-load-bearing counterpart. The wall collapsed at a reflected pressure and impulse of 51kPa and 415 kPa-ms, respectively (Ciornei 2012).

Wall-5 was retrofitted with reinforced polyurea-3.1 mm. It was subjected to an axial load of 120 kN distributed over its length by its top support. It resisted up to three blast shots and failed on the third shot with a maximum blast impact of 103 kPa reflected pressure and 1030 kPa-ms impulse. At failure, it attained a maximum mid-height displacement of 108 mm with no disintegration of the wall or release of flying debris.

Wall-6 was retrofitted with reinforced polyurea-4.1mm and subjected to an axial load of 180 kN. The wall could resist up to five progressively increasing shock waves up to a maximum blast capacity of 125 kPa reflected pressure and 2420 kPa-ms reflected impulse. Its maximum mid-height displacement was 185 mm at failure, with no fragmentation and no flying debris released.

5.2.4 Performance and Response Comparison

(a) Blast capacity: Pressure-Impulse Load

All blast shots imposed on Wall-5 and Wall-6 were of higher magnitude than those fired on URM-3. Both retrofitted walls had significantly higher blast capacity than the control wall: Wall-5 absorbed over 171 % of reflected pressure and 233 % impulse more than URM-3;

also, Wall-6 resisted reflected pressure and reflected impulse of over 229% and 683 %, respectively, more than the control wall.

(b) Out of plane of capacity

Both retrofitted walls exhibited far better out-of-plane capacity than the URM-3. Wall-5 and Wall-6 could flex up to 140% and 311% at higher blast loads above the control, as seen from their mid-height displacement response. Although the axial load increased the compressive resistance of the walls to shock waves, URM-3 still failed in a brittle manner by collapsing, while the reinforced walls failed in ductile manners, with their walls held intact (Figures 4.59 and 4.73).

(c) Stiffness and strength

The two retrofitted walls are of higher stiffness and strength than URM-3, as the failing shot of URM-3 was their commencing shot; the reinforced walls only responded elastically.

Wall-6 is superior to Wall-5 as it absorbed higher blast loads before it attained permanent deformation. At similar loadings of reflected pressure and impulse (52 kPa, 451 kPa-ms; 67 kPa, 631 kPa-ms; and 120 kPa, 1067 kPa-ms), the maximum mid-height displacements of Wall-6 were 35%, 81%, and 42% lesser than those of Wall-5 an indication of its higher strength.

In summary, the enhanced capacities of the retrofitted walls over URM-3 can be attributed to the reinforced polyurea, which held the walls firmly, impacting them with their qualities. Polyurea particularly held the walls together and gave them stability and strength. Also, the mesh transferred its strength and tensile properties to the walls and transformed them into flexural walls capable of resisting blast loads. The summary of the comparison of load-bearing CMU walls is shown in Figure 5.2.

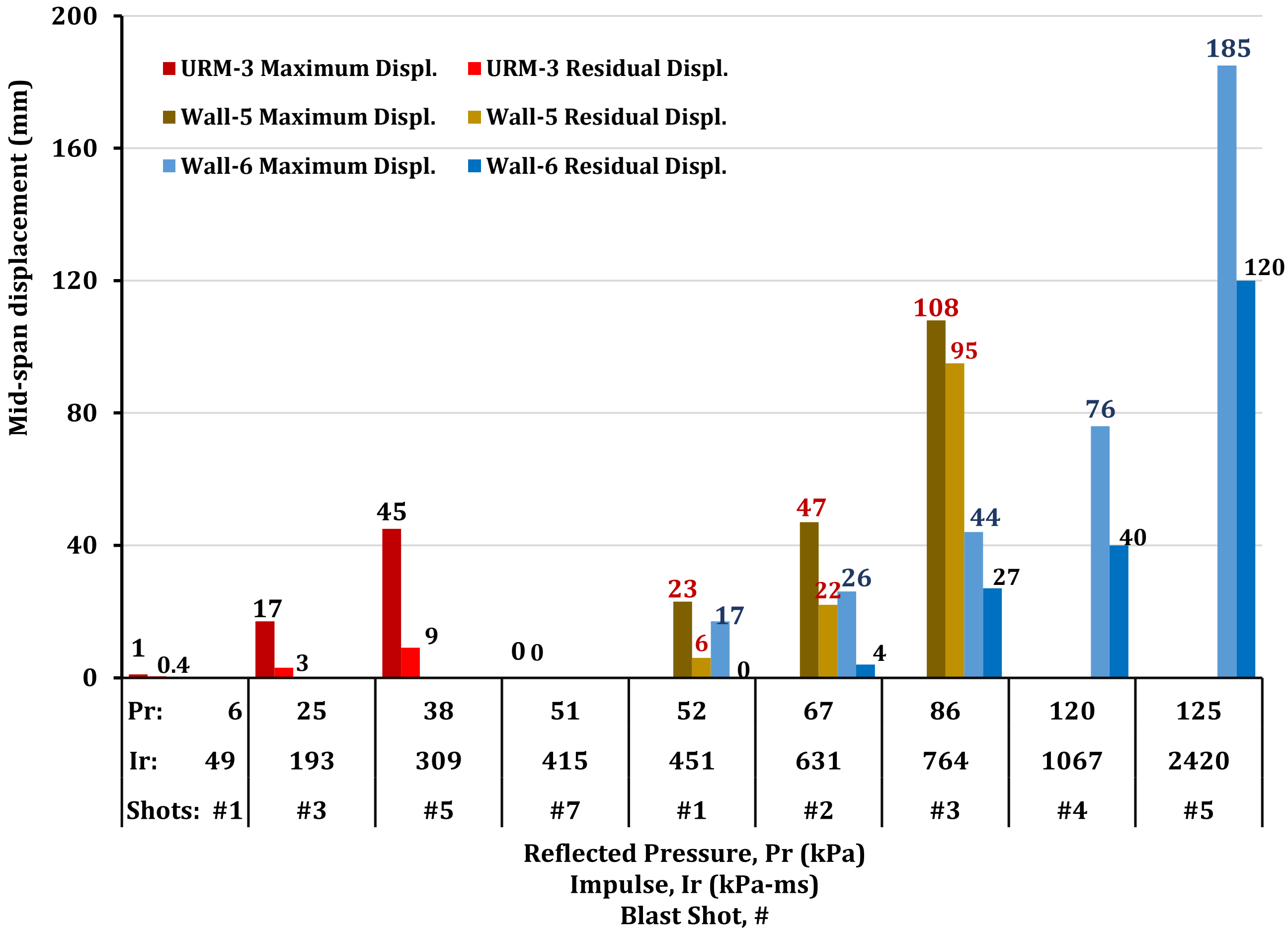

Figure 5.2. Displacements of load-bearing CMU walls under varying blast loads

5.2.5 Polyurea Retrofitted vs Reinforced Polyurea Retrofitted Walls

Another control wall, URM-2, tested by Ciornei (2012), was retrofitted with only polyurea of 3mm thickness as an infill panel without any reinforcement/mesh or axial load applied. It has a similar configuration to Wall-2 and Wall-3 except for the difference in the polyurea thickness and reinforcement in the latter two walls.

The three walls were subjected to equivalent blast shots. Their performance is compared regarding out-of-plane deflections and blast capacities (Figure 5.3). When the walls were subjected to a blast shot of 46 kPa-434 kPa-ms, URM-2 exhibited the largest displacement of 69 mm with no visible damage, whereas Wall-2 and Wall-3 had close range displacements of

23 mm and 25 mm, respectively, with no damage. At a higher level of fired shock wave (84 kPa-597 kPa-ms), an extensive tear of the polyurea was observed in the middle of URM-2, accompanied by the crushing of the fifth mortar joint on the blast face (compression face) with a maximum displacement of 159 mm. In comparison, a maximum displacement of 39 mm was observed in Wall-3, with visible cracks on its fifth course. Wall-2, with a higher percentage of reinforcement, developed the least displacement of 34 mm with no visible damage or cracks. The walls were further exposed to an increased blast shot of 78 kPa reflected pressure and 723 kPa-ms impulse. This shot resulted in the global failure of URM-2 with a maximum displacement of 254 mm and extensive polyurea tearing. Also, a maximum displacement of 89 mm was observed in Wall-3, and wide face-shell cracks were seen along the fifth course; additionally, the reinforced polyurea debonded partially at its mid-height. Wall-2 had the lowest displacement of 56 mm with cracks sustained along the mortar joints of the top courses of its wall; its retrofit did not de-bond.

With an extension of the driver length to 3962 mm, the impulse significantly increased to 1479 kPa-ms and above to reach the failure loads of Wall-2 and Wall-3 which was far beyond the failure load of URM-2. Wall-3 collapsed dangerously with fragmentation and flying debris after its exposure to the dynamic force (Figure 4.38). However, Wall-2 could resist the load while developing a maximum mid-height deflection of 203 mm and no fragmentation and flying debris released. Wall-2 was stable, but observed damages were major cracks along its mid-height, yielded and necked mesh, torn polyurea, and major face shell cracks on the fifth and sixth course of masonry (Figure 4.23).

In summary, Wall-2 and Wall-3 at the blast shots (46 kPa, 434 kPa-ms) developed a reduced mid-height response of approximately 200% over URM-2. For a higher blast load (84 kPa, 597 kPa-ms), Wall-2 and Wall-3 deflections were 368% and 308%, respectively, reduced to that of URM-2. Further, at the shot (78 kPa, 723 kPa-ms) at which URM-2 failed, Wall-2 and Wall-3 had reduced displacements of 354% and 185%, correspondingly. The reinforced polyurea walls had superior performances over URM-2 majorly because of their mesh. The resilient structural capacities of Wall-2 could be traced to its retrofit type and the continuous higher arching force it provided.

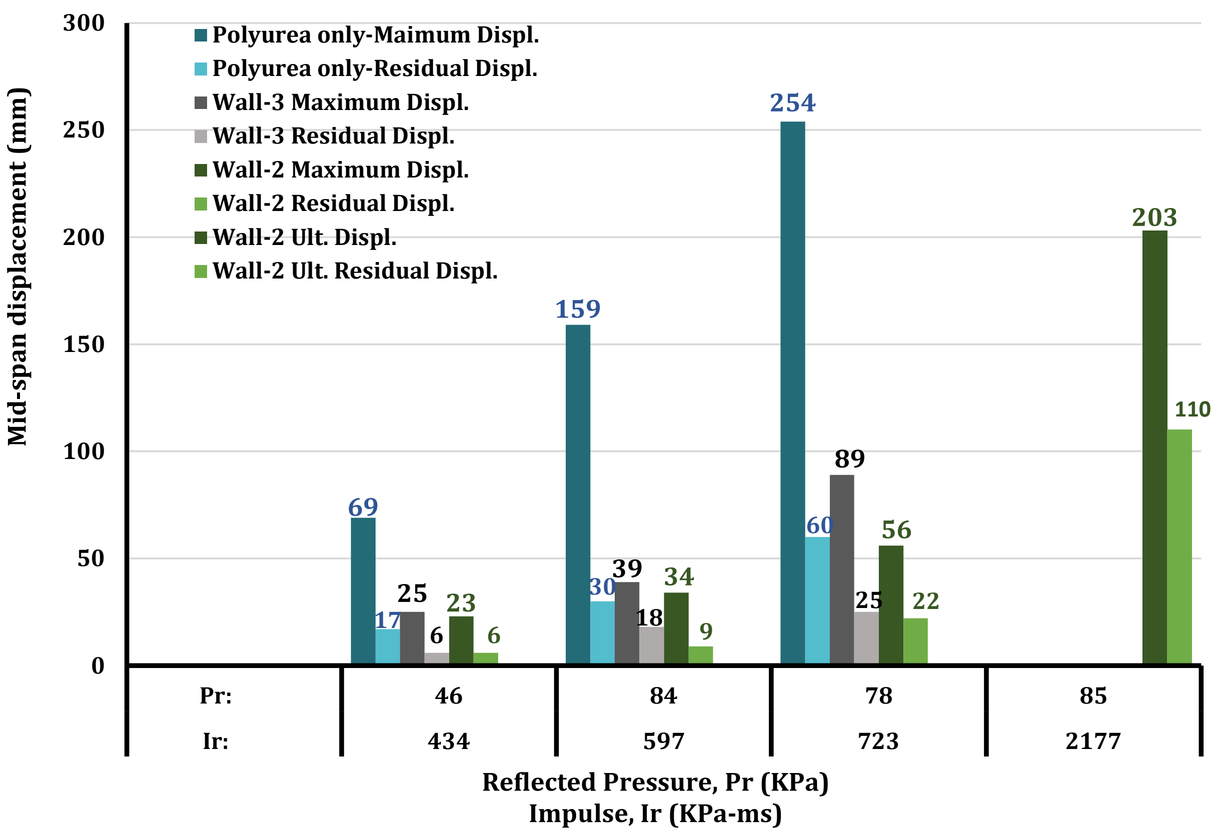

Figure 5.3. Non-load bearing CMU walls: Polyurea only vs reinforced polyurea responses at equivalent blast loads

5.3 The effects of masonry type

This section compares the performance of CMU and stone masonry walls strengthened with reinforced polyurea. It considers both load-bearing and non-load bearing (infill) walls.

5.3.1 Stone vs CMU: Load-bearing walls with large reinforcement area

Wall-4 is a stone wall with an initial axial load of 120 kN, while Wall-6 is a CMU wall with an applied axial load of 180 kN. Both were retrofitted with reinforced polyurea having 4.1mm mesh. They both resisted the highest blast loads in the experiment, bringing the shock tube nearly to its pressure capacity. The walls absorbed high blast capacities of over 100 kPa reflected pressure and 2400 kPa-ms impulse and showed similar responses of ductile failure with no disintegration of the block units or release of flying debris. Figure 5.4 compares the walls at similar intensity of blast loads in terms of out-of-plane deflections. Their high energy absorb capacity and strength were provided by the type of retrofit applied to them.

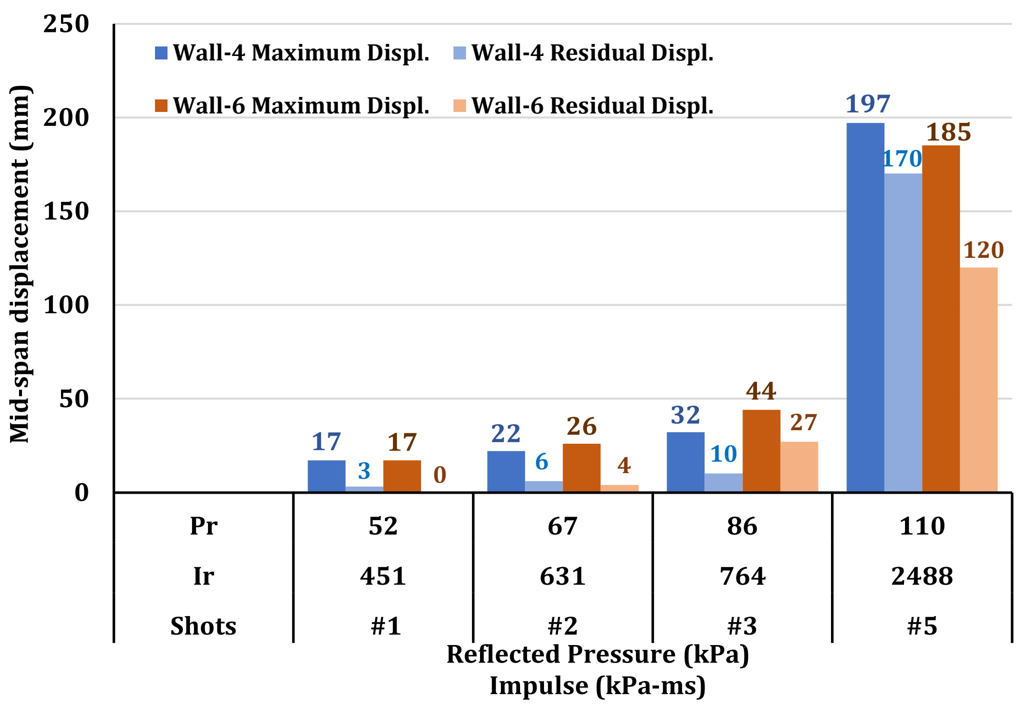

Figure 5.4. Responses of load-bearing walls of stone vs. CMU retrofitted with reinforced polyurea-4.1mm under similar blast loads

5.3.2 Stone vs. CMU: Non-load bearing walls with small reinforcement area

The major difference between Wall-1 and Wall-3 was the type of masonry used. Wall-1 was built with a block-laying pattern of coursed and uncoursed patterns as stone masonry, while Wall-3 was a CMU wall constructed with a mainly coursed pattern. Both walls had the same retrofit system. Their responses were compared in terms of out-of-plane deflections and blast capacities.

Wall-1 was exposed to four blast shots and failed on its fourth shot. Wall-3 was subjected to five blast shots and failed on its fifth shot. Both were subjected to equivalent blast loads and displayed similar responses, as shown in Figure 5.5.

Wall-1 had a ductile failure under a blast shot of 93 kPa reflected pressure and an impulse of 711 kPa-ms with a maximum mid-height displacement of 100mm. The progression of the wall failure showed hinge formation at its supports and mid-height with an immediate split of the mid-mortar joint. The reinforcement yielded at the critical section. Subsequently, the mesh necked, and some strands ruptured, resulting in the wall breaking into two halves; however, the wall did not collapse, and no fragmentation or flying debris was released as it was held in place by the reinforced polyurea.

Wall-3, at a similar level of blast loading, deflected by 89 mm and developed wide cracks on the edge block of its fifth course with its polyurea partially detached at its mid-height. Wall-3 could absorb a further higher blast shot (89 kPa, 874 kPa-ms) beyond Wall-1 and responded with a deflection of 140 mm. At this load level, the cracks on its fifth course widened more, its polyurea tore partially and debonded more, and the steel wires yielded at mid-height, but no fragmentation or flying debris was released. It eventually failed catastrophically when the reflected impulse increased to 1479 kPa-ms at a reflected pressure of 88 kPa.

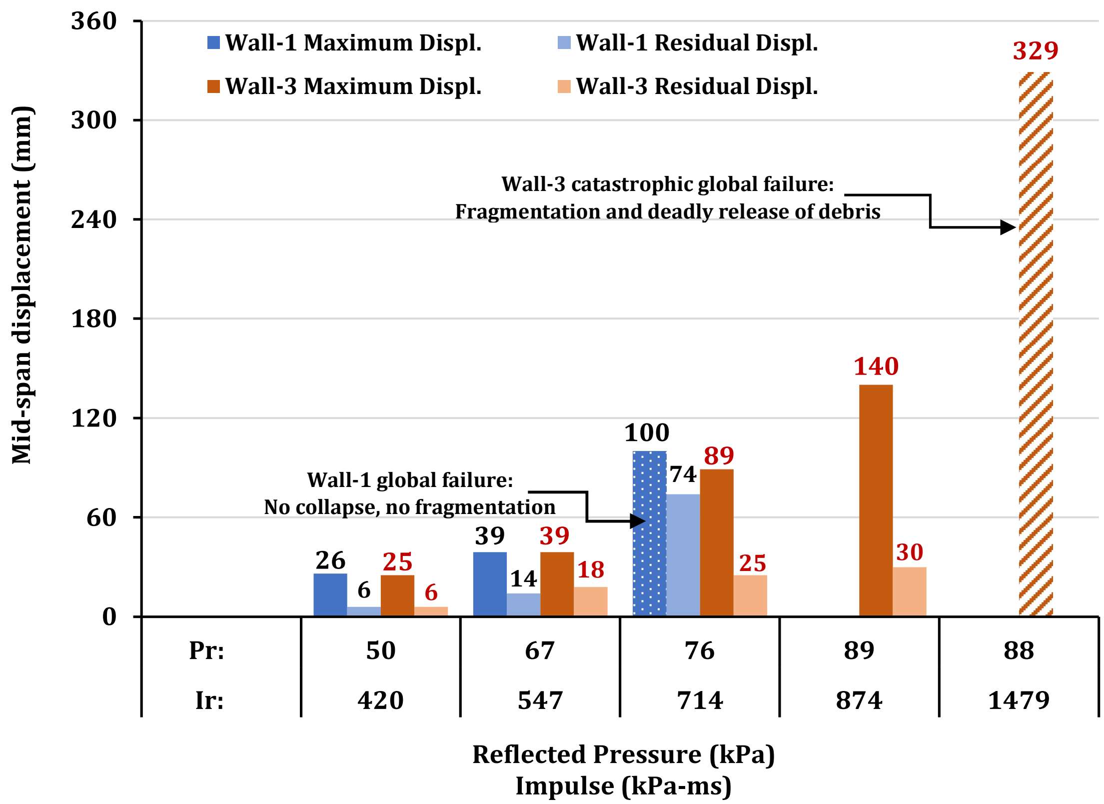

Figure 5.5. Maximum and residual displacement of non-load bearing walls of stone vs CMU

In summary, Wall-3 had a higher out-of-plane blast capacity than the stone Wall-1. The difference in behavior could be attributed to the CMU wall's higher self-weight over the stone wall. Also, the stone wall's block laying pattern likely contributed to its early failure, as it failed along the mortar bed of the part constructed with a coursed pattern (Figures 4.8 and 4.9). Figure 5.5 shows the comparison of the two walls.

5.4 The Effects of Axial Load Application

5.4.1 CMU Walls: Non-Load Bearing vs Load Bearing with Small Reinforcement Area

Wall-3 and Wall-5 are both CMU walls retrofitted with reinforced polyurea-3.1 mm. However, Wall-3 was tested without an axial load, while Wall-5 had a 120 kN axial load applied to it via its top support. Their performances were measured regarding blast capacity and maximum mid-height responses under equivalent blast shots. For the first fired shot (51 kPa, 420 kPa-ms), both walls responded elastically and showed approximately the same mid-height displacements (25mm for Wall-3 and 23mm for Wall-5) with no visible damage. A second higher shot (73 kPa, 578 kPa-ms) was fired, and the walls behaved inelastically with medium cracks seen on the fifth course of Wall-3 and similar cracks observed on the sixth course of Wall-5. Wall-3 and Wall-5 developed mid-height displacements of 39 mm and 47 mm, respectively; Wall-5 deflected more than Wall-3 by 21%. At a third shot (103 kPa, 1030 kPa-ms), Wall-5 was observed to deflect up to 108 mm at mid-height with a residual displacement of 95mm. It broke into two halves in a ductile manner with no fragmentation observed. However, Wall-3 at a further load (89 kPa, 874 kPa-ms) displayed a mid-height displacement of 140 mm with wide cracks observed on the fifth course of CMU. Although Wall-3 did not fail, it was observed to be too weak to take further shots as it suffered cracks and debonded retrofit at mid-height. In conclusion, Wall-5 responded relatively better as the axial load increased its compressive stress, contributing to its higher arching action and out-of-plane resistance than Wall-3.

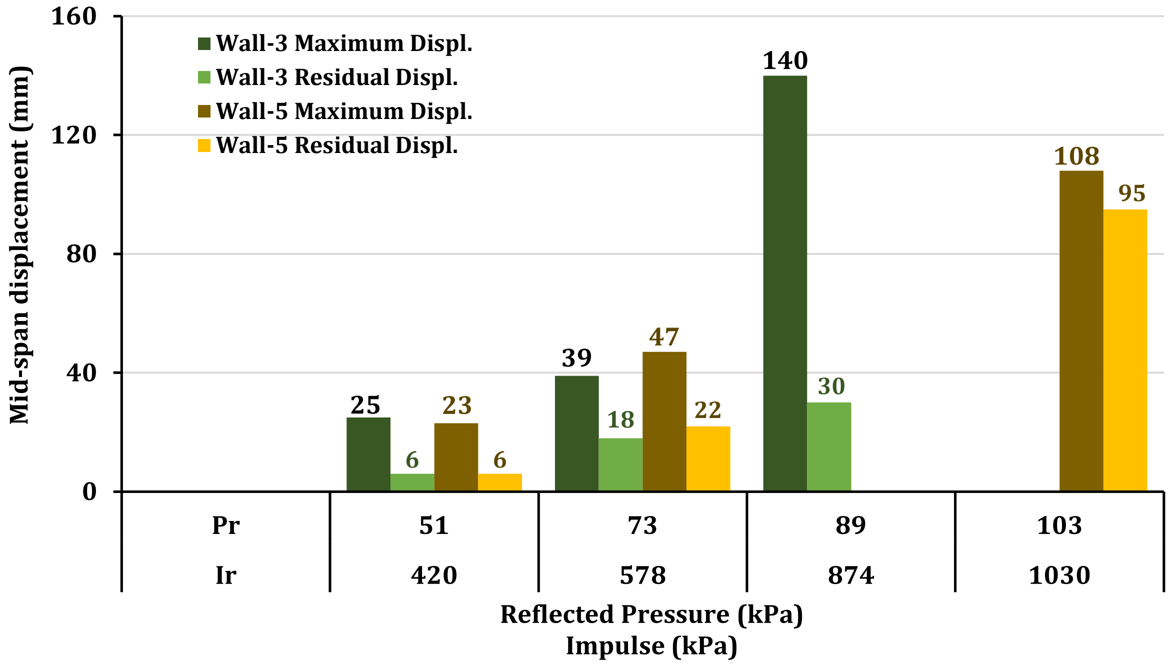

Figure 5.6. Responses of non-load vs. bearing CMU walls retrofitted with reinforced polyurea-3.1mm under similar blast loads

5.4.2 CMU Walls: Non-Load Bearing vs Load Bearing with Large Reinforcement Area

Wall-2 and Wall-6 were retrofitted with reinforced polyurea-4.1mm, except for the axial load of 180 kN applied on Wall-6. They were subjected to equivalent blast loads, but their final shots differed slightly. Their responses regarding out-of-plane capacity, damage assessment, and blast load resistance are compared. At a blast load of 52 kPa -451 kPa-ms, both walls behaved elastically with mid-height displacements of 23mm (Wall-2) and 17mm (Wall-6), and no visible damage was seen on both. At an increased blast shot of 74 kPa-701 kPa-ms, Wall-2 behaved inelastically with a mid-height displacement of 56 mm and fine cracks in the mortar joints along the four top courses, while Wall-6 maintained elastic response deflecting 26 mm. Both walls responded inelastically when the load was further increased to 85 kPa-793 kPa-ms. Visible face shell cracks were seen on the fifth course of Wall-2 as it deflected by 80 mm, while Wall-6 developed a mid-height deflection of 44 mm with fine cracks along its fifth course. The impulse for their final shots increased as the driver length doubled. Both walls failed in a ductile manner, and no collapse or fragment occurred. However, widened face shell cracks were seen on the fifth and sixth courses of Wall-2, while Wall-6 had three splits: one on the fifth course, the other on the sixth course, and along the mortar joint of the sixth and seventh courses. The maximum mid-height displacement of Wall-2 was 203 mm, whereas that of Wall-6 was 185 mm. Their residual displacements were 110 mm (Wall-2) and 120 mm (Wall-6). In summary, Wall-6 showed increased strength due to the applied axial load and developed a 10 % lesser mid-height response at failure.

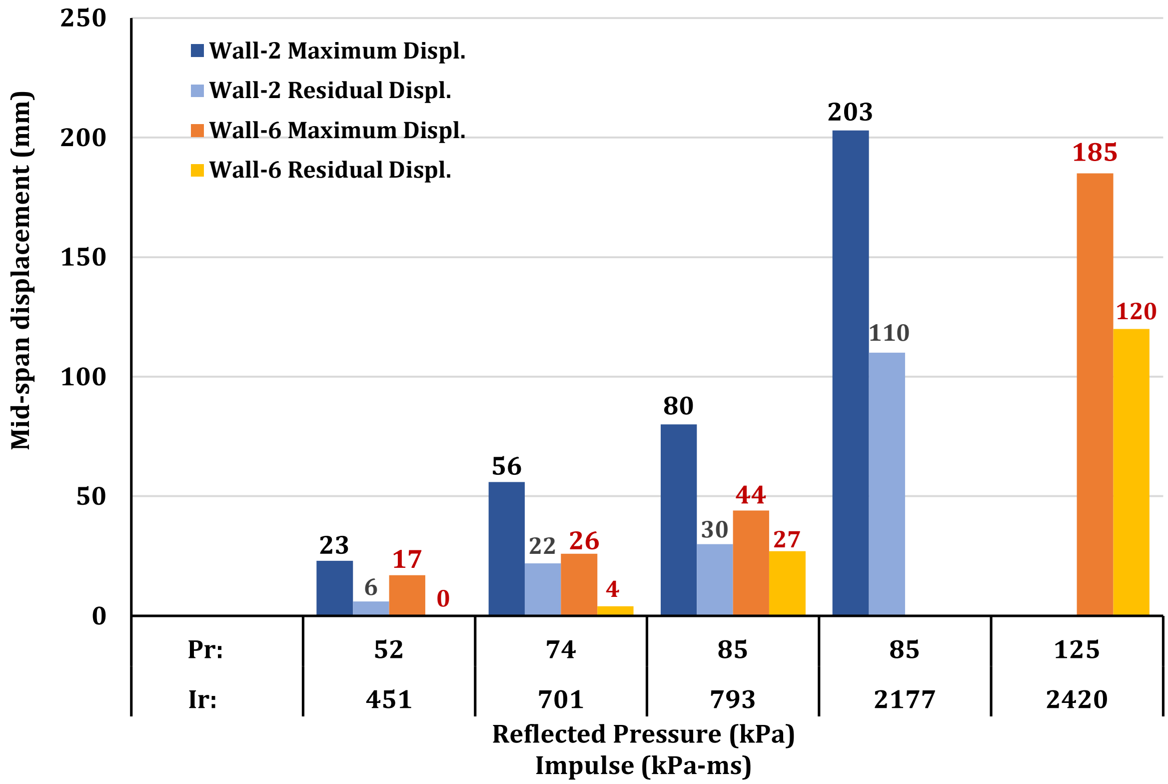

Figure 5.7. Responses of non-load vs. bearing CMU walls retrofitted with reinforced polyurea-4.1mm under similar blast loads

5.4.3 Stone Walls: Non-Load Bearing vs Load Bearing

Wall-1 is a non-load bearing wall retrofitted with reinforced polyurea-3.1mm, whereas Wall-4 is a load-bearing wall with an axial load of 120kN retrofitted with reinforced polyurea-4.1mm. Both walls were exposed to equivalent blast shots: at the blast shot (49 kPa-432 kPa-ms), Wall-1 responded with a maximum mid-height displacement of 26 mm while Wall-4 response was 17 mm; at a higher blast capacity (66 kPa-560 kPa-ms), Wall-1 and Wall-4 displacements were 39 mm and 22 mm respectively; with a further increase of the shock wave to shot (93 kPa-711 kPa-ms), wall-1 failed with a peak mid-height displacement of 100 mm, however Wall-4 had a maximum mid-height response of 32 mm (68% reduction to that of Wall-1) within its elastic limit. Two more intense shots (82 kPa-808 kPa-ms) and (110 kPa-2488 kPa-ms) were fired on Wall-4 before it eventually failed. Although both walls failed in a ductile manner without fragmentation, Wall-4 had significantly higher blast resistance capacity than Wall-1, which can be attributed to its combined effects of a higher percentage of reinforcement and axial load.

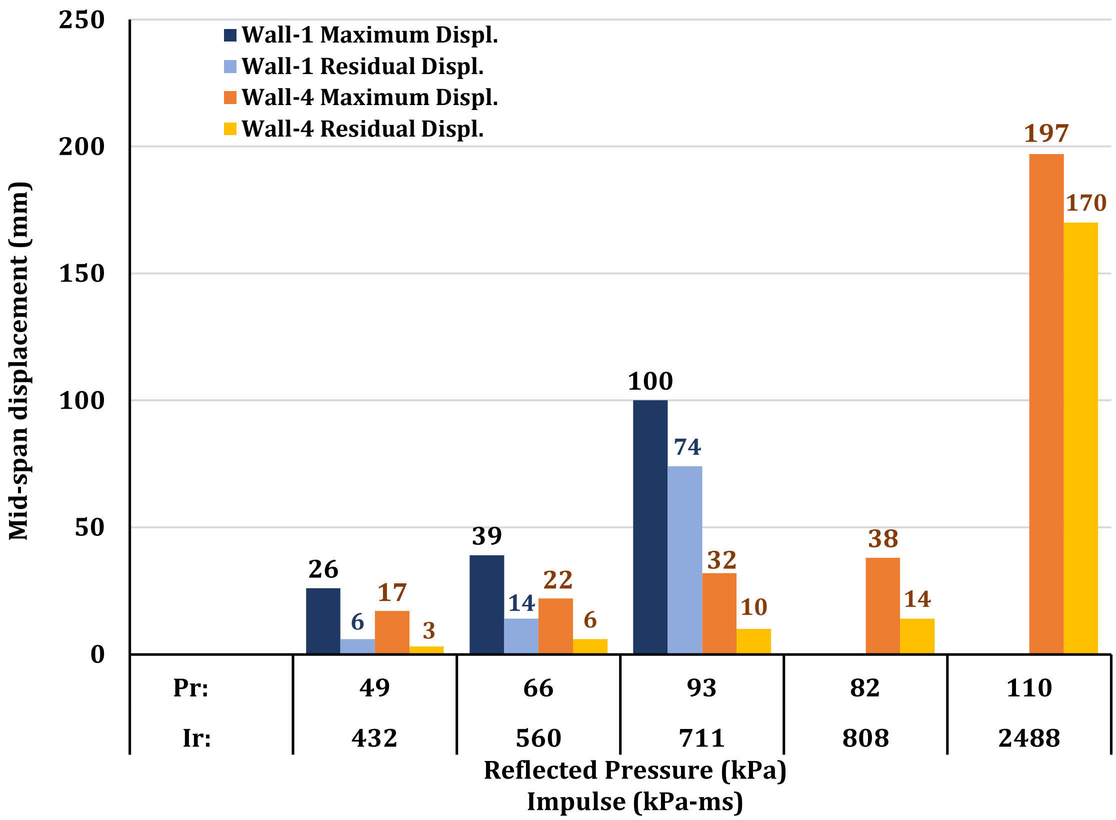

Figure 5.8. Displacements of non-load vs. bearing stone walls under equivalent blast loads

5.5 Summary of the Effects of Test Parameters

5.5.1 Effect of Axial Load

The effect of axial load on the walls was observed to increase their strength. The increased coupling axial force at the critical mid-height level due to initial compression increased the flexural capacity of the walls. Initial axial compression reduced cracking and increased the stiffness of the load-bearing walls, given reduced maximum mid-height deflections under high blast loads. The axial load also contributed to the P-Δ effect and amplified the residual wall deflection.

5.5.2 Block Laying/Effect of Masonry Type

The block-laying patterns influenced the responses of walls. The stone wall built with an uncoursed pattern had an improved blast resistance. The course laying pattern should be avoided for stone walls as their uneven surfaces make them fail quickly along their mortar joints under blast loads. The CMU walls had excellent responses under the course pattern.

5.5.3 Effect of Reinforced Polyurea Retrofit

Two retrofit types were understudied: reinforced polyurea-3.1 mm and reinforced polyurea-4.1 mm, and their performances were investigated. Generally, the retrofits held the walls together, increased their compressive force, and made them more stable for blasting loads than an unretrofitted URM wall. Particularly, all the walls retrofitted with reinforced polyurea-4.1 mm had proven higher strength, blast resistance capacity, and out-of-plane capacity than their counterparts. It was observed that increasing the thickness of the polyurea and the mesh's reinforcement area enhanced the retrofit's performance against blast loads.

5.5.4 Effect of Retrofit Type

Reinforced polyurea presents a better approach for protecting masonry units relative to unreinforced polyurea application due to its increased strength and stiffness, which significantly enhances structural resistance to high blast loads. Unlike the use of polyurea alone as a retrofit technique, which is effective for fragment control under relatively low blast loads, reinforced polyurea offers higher load resistance with reduced deflection. A thickness of 6mm, which is recommended by the supplier, is particularly effective for ensuring sufficient bond between the steel and the masonry while also ensuring fragment control.

CHAPTER 6. ANALYTICAL RESEARCH

6.1 General

This chapter describes the analytical research conducted to generate further data on the performance of reinforced polyurea retrofitted blast-resistant masonry walls. It consists of sections stating and showing steps for developing the resistance functions of all the walls considered in this experimental research, followed by Single-Degree-of-Freedom (SDOF) analyses of the test walls. The SDOF analyses were conducted using the software "RC-Blast," and the results were validated against those obtained experimentally. The analyses were then expanded to carry out an analytical parametric investigation to extend the test variables beyond those considered in the test program. More specifically, the effects of the percentage of reinforcement in polyurea, wall thickness, wall aspect ratio, and axial load were investigated. The results provided much-needed data to formulate a design procedure for the implemented retrofit technique. The design procedure is described for use in practice.

6.2 Development of Resistance Functions

The resistance function for the masonry walls describes force-displacement relationships, including the effects of the reinforced polyurea retrofit technique implemented. It provides wall stiffness during different stages of loading for use in the subsequent SDOF dynamic analysis of walls. The approach followed in this research project was initially developed by Moradi et al. (2008). The walls were all one-way elements. Several assumptions were made before the computation of the resistance functions. Accordingly, the failure surface of the walls was assumed to take place at mid-height of the walls, initiating through the formation of a wide horizontal flexural crack. The supports were assumed to be pinned-pinned, and the tensile capacity of mortar joins was negligible. The blast pressure on the walls was assumed to be uniform.

Different resistance functions were developed for different walls with different properties. Microsoft Excel Sheets were used to program the construction of the resistance functions, details of which are discussed in the following sections.

6.2.1 Resistance Function for Un-retrofitted Non-Loading Bearing CMU and Stone Wall with Arching Action

Non-load-bearing walls do not have flexural resistance because of the lack of tension elements in the walls, like reinforcement. When the tensile resistance of mortar is neglected, the flexural resistance becomes negligible. However, arching action in walls enclosed in structural framing elements provides a force couple that results in considerable flexural resistance. As the lateral blast load increases, the wall's mid-height deflection increases, creating tensile stresses on the tension side of the wall. URM walls are weak in tension, and cracks initiate along the mid-mortar joint of the wall. As the cracks grow due to increased loading, the wall pushes against the rigid supports (top and bottom), exerting arching forces until either the wall fails in compression or stability failure occurs. The equation that governs the lateral resistance of a URM wall with arching was stated in the review of Chapter 2 relative to Figure 2.11. The governing equation (Eq. 6.1), developed by Moradi et al. (2008), is given below:

$$p = -\frac{8}{h^2}\left[\mathbf{P}\left(\frac{t-a}{2}\right) + \frac{W_i}{2}\left(\frac{t-a}{2} - \frac{\Delta}{2}\right) - \left(\mathbf{P} + V_T + \frac{W_i}{2}\right)\left(\frac{t}{6} + \frac{y}{3} + \frac{t-a}{2} - \Delta\right)\right] \tag{6.1}$$

Where p is the uniformly distributed force on the wall, h is the height of the wall, $\mathbf{P}$ is the initially applied axial load, which is zero as the wall is a non-load bearing wall, W_i is the weight of the wall, t is the wall thickness, a is the width of the arching area, V_T is the arching force, y is the length of crack progression towards the neutral axis, and Δ is the displacement. Before the onset of the crack, the wall is dominated by the compressive force resulting from self-weight, in which case the arching force and crack length are equal to zero. Thus Eq. 6.1 reduces to Eq. 6.2 when written for displacement Δ.

$$\Delta = \frac{\left(\mathrm{P}+\frac{W_i}{2}\right)\left(\frac{t}{6}\right)-\frac{ph^2}{8}}{\mathrm{P}+\frac{W_i}{4}} \tag{6.2}$$

At this initial stage, the wall deflects due to flexure elastically, and its displacement can be calculated using the Euler-Bernoulli beam theory for simply supported one-way members:

$$\Delta = \frac{5ph^4}{384E_C I} \tag{6.3}$$

Equating Eqs. 6.2 and 6.3 results in Eq. 6.4, from which the blast load that would result in maximum flexural resistance could be determined.

$$p = \frac{\left(\mathbf{P}+\frac{W_i}{2}\right)\left(\frac{t}{6}\right)}{\left(\frac{5h^4}{384E_C I}\right)\left(\mathbf{P}+\frac{W_i}{4}\right)+\frac{h^2}{8}}, \tag{6.4}$$

Substituting the value of Eq. 6.4 in Eq. 6.3 gives its equivalent flexural displacement. However, at the onset of cracking, the arching force, V_T, and the crack length, y, are initiated, and the mid-height displacement is calculated using Eq. 6.5

$$\Delta = \beta\Delta_{cr} \tag{6.5}$$

And

$$\Delta_{cr} = \frac{(5-4\alpha)ph^4}{384E_C I} \tag{6.6}$$

Δ_{cr} is the mid-height displacement at crack initiation, α is the % fixity at the support of the wall ($\alpha = 0\%$ for simply supported ends, 50% for partially fixed ends), $E_C I$ is the wall's rigidity. Also,

$$\beta = \frac{\Phi_{crG}}{\Phi_{cr}} = \frac{R_{crG}t^2}{R_{cr}(t-y)^2} \tag{6.7}$$

$$R_{crG} \cong R_{cr} = \mathrm{P} + V_T + \frac{W_i}{2}, \tag{6.8}$$

$\mathbf{P} = 0$; however, V_T *has an axial effect on the wall*

Φ_{crG}, Φ_{cr} are the curvature at the central section of the wall as the cracks grow and at crack onset. As the mid-crack grows, Δ is calculated using Eq. 6.5 and "*p*" is subsequently calculated using Eq. (6.1).

Summary of the steps leading to the development of the static resistance function

a) At crack initiation, y = 0, and V_T = 0; Δ_{cr} is calculated using Eq. 6.6

b) Set Eq. 6.2 equal to Eq. 6.6 and solve for *p* as the applied flexural lateral force.

c) As the mid-crack grows, the crack length, y, increases incrementally.

d) For every change in y, the associated Δ is calculated using Eq. 6.5

e) The value of Eq. 6.5 is input along with other known parameters into Eq. 6.1 to compute the corresponding lateral force, *p,*

f) The resistance function in Figure 6.1 was plotted for a typical Unretrofitted URM wall with geometric dimensions of 100 mm by 2000 mm by 2000 mm dimensions with the material properties recorded during the experimental research phase using the values obtained from Eqs. 6.1 and 6.5.

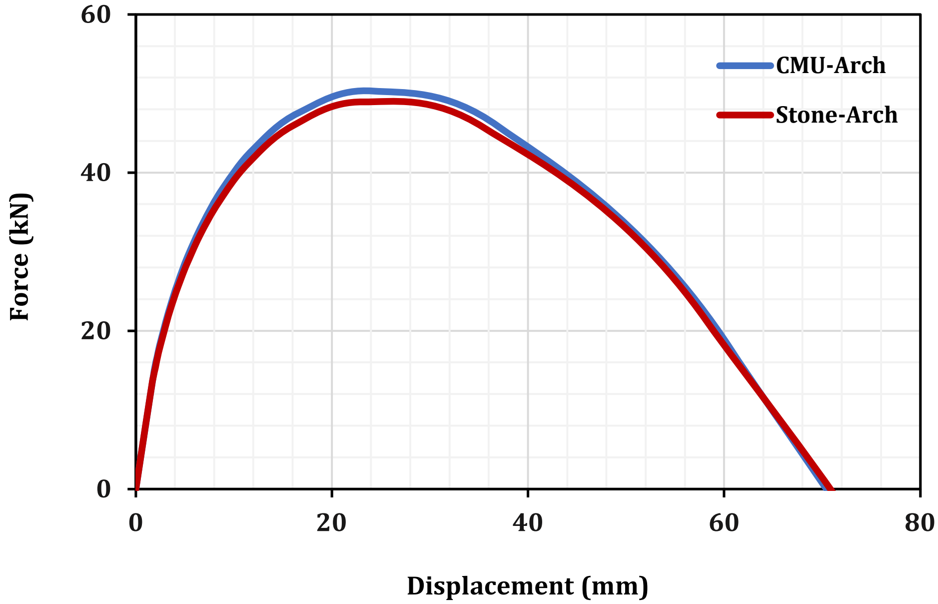

Figure 6.1. Resistance functions for unretrofitted, non-load bearing CMU and stone walls with arching action only

6.2.2 Resistance Function for Non-Loading Bearing CMU and Stone Walls with Reinforced Polyurea Retrofit and Arching Action

This section presents the steps in developing the resistance function for non-load bearing walls without the initial applied axial load but with the reinforced polyurea layer on the wall tension side. The reinforced polyurea membrane is assumed to be fully bonded to the wall. The membrane covers the entire tension side of the wall. A parameter needed in this bonded polyurea analysis is the tributary length of the membrane-affected region crossing the crack opening at the mid-height of the wall. The tributary length was assumed to be approximately half of the CMU block height on each side of the crack opening (Dinan et al. 2003). The governing equation proposed by Moradi et al. (2008) is given in Eq. 6.9. The resulting resistance functions are plotted in Figures 6.2 and 6.3 for CMU and stone walls, respectively, with 3.1 mm and 4.1 mm diameter wires used in the mesh reinforcement.

$$p = -\frac{8}{h^2}\left[\frac{W_i}{2}\left(\frac{t-a}{2} - \frac{\Delta}{2}\right) - \left(T + V_T + \frac{W_i}{2}\right)\left(\frac{t}{6} + \frac{y}{3} + \frac{t-a}{2} - \Delta\right) - T\left(\frac{a}{2} + \Delta\right)\right] \qquad (6.9)$$

T in Eq. 6.9 is the reinforced membrane force, consisting of $T_p + T_{ss}$. T_p is the polyurea membrane force, and T_{ss} is the SS304 mesh tensile force. Other parameters remain, as discussed in Section 6.2.1.

$$T_P = \frac{4E_r t_r t}{lh}\Delta \tag{6.10}$$

$$T_{ss} = \frac{4E_{ss} tA}{lh}\Delta \tag{6.11}$$

The summary of steps that lead to the development of static resistance functions for non-load-bearing walls is similar to that given in Section 6.2.1, where

$$R_{crG} \cong R_{cr} = \mathrm{P} + T + V_T + \frac{W_i}{2}, \tag{6.12}$$

$\mathbf{P} = 0$ and V_T Is the arching force.

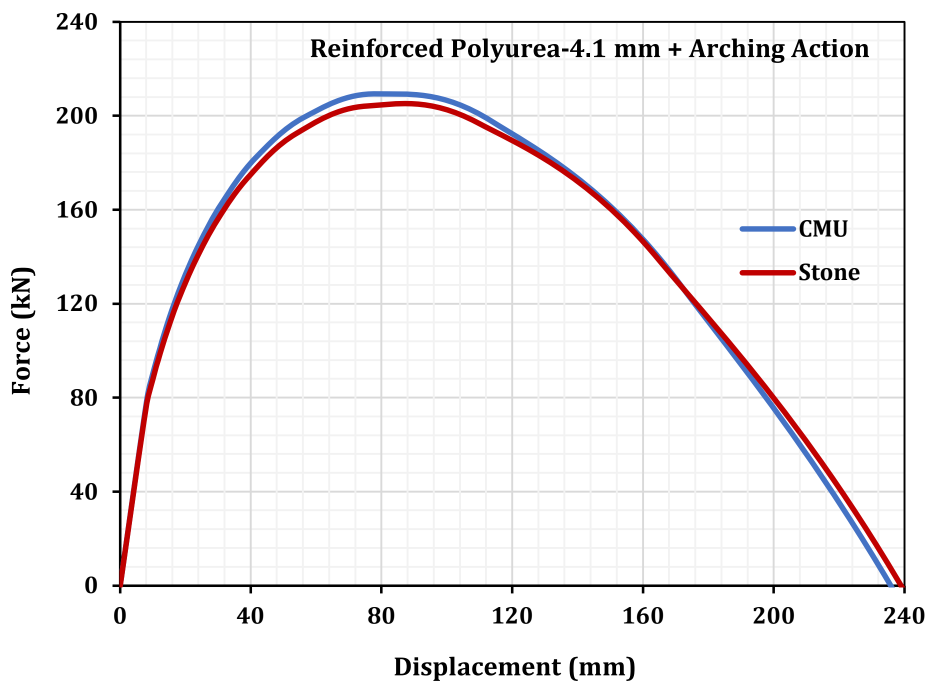

Figure 6.2. Resistance functions for non-load bearing CMU and stone walls retrofitted with reinforced polyurea-4.1 mm and arching action

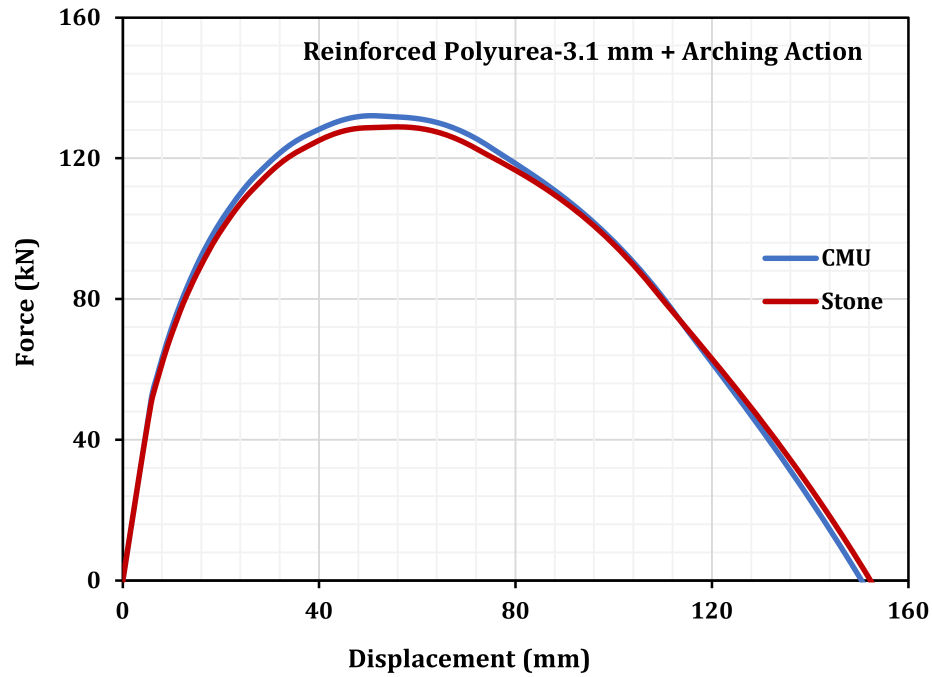

Figure 6.3. Resistance functions for non-load bearing CMU and stone walls retrofitted with reinforced polyurea-3.1 mm and arching action

6.2.3 Resistance Functions for Un-Retrofitted Load Bearing CMU and Stone Walls with Arching Actions

The governing resistance function expression for load-bearing URM walls is the same as Eq. 6.1 used in Section 6.2.1 for non-load bearing walls, except this time the initial axial force **P**, is not zero, increasing the compressive force of the wall. The equation is given below. It generated the resistance functions in Figures 6.4 and 6.5 for CMU and stone masonry walls. The resistance functions are plotted separately for CMU and stone walls in Figure 6.6. and 6.7, respectively, under two different levels of initial axial forces applied in the experimental program.

$$p = -\frac{8}{h^2}\left[\mathbf{P}\left(\frac{t-a}{2}\right) + \frac{W_i}{2}\left(\frac{t-a}{2} - \frac{\Delta}{2}\right) - \left(\mathbf{P} + V_T + \frac{W_i}{2}\right)\left(\frac{t}{6} + \frac{y}{3} + \frac{t-a}{2} - \Delta\right)\right] \tag{6.13}$$

The summary of the steps leading to the development of the resistance functions is similar to that given in Section 6.2.1, with V_T being zero at crack initiation(y=0) and

$$R_{crG} \cong R_{cr} = P + V_T + \frac{W_i}{2}\ ,\ \mathbf{P} \neq 0 \tag{6.14}$$

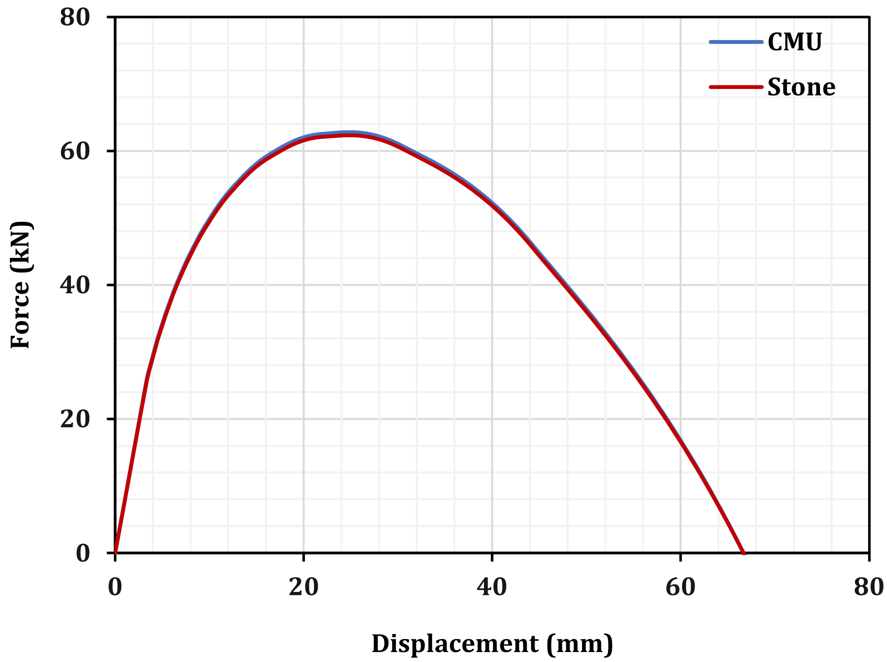

Figure 6.4. Resistance functions for unretrofitted CMU and stone walls with an initial axial force of 120 kN

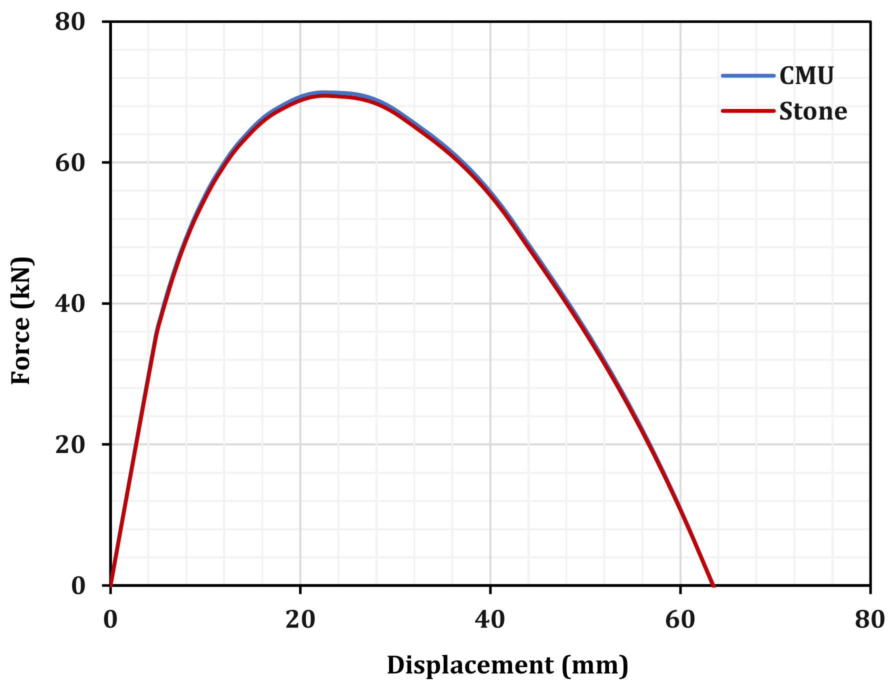

Figure 6.5. Resistance functions for unretrofitted load-bearing CMU and stone walls with an initial axial force of 180 kN

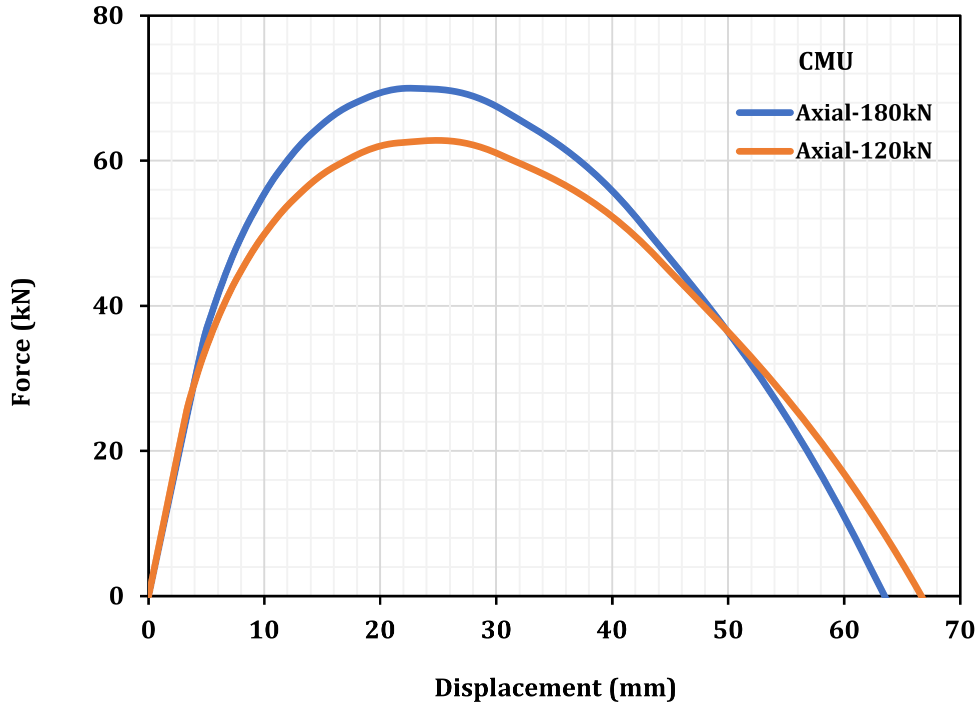

Figure 6.6. Resistance functions for unretrofitted load-bearing CMU walls subjected to initial axial loads of 120kN and 180kN

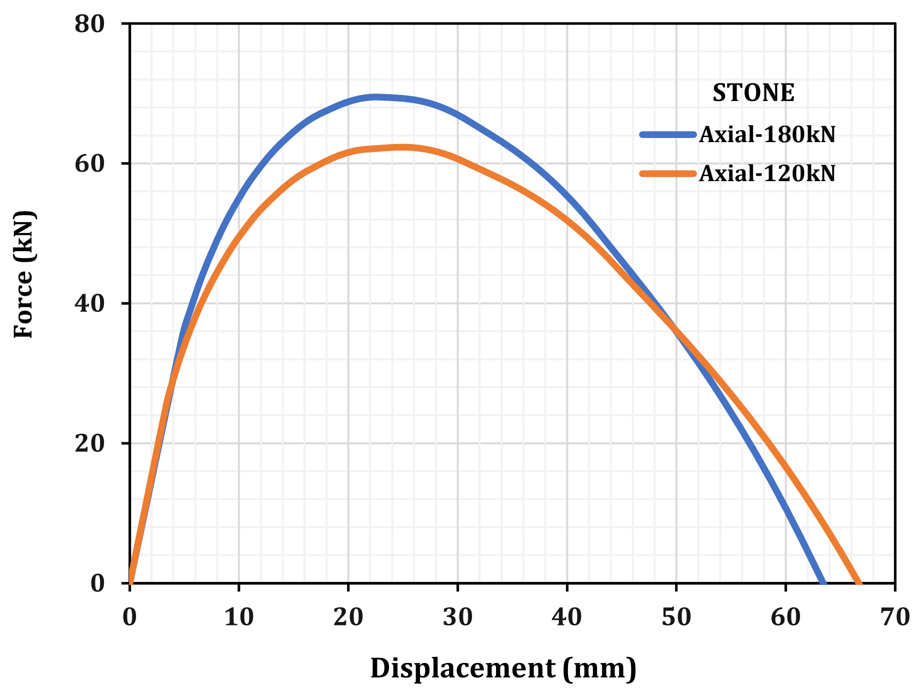

Figure 6.7. Resistance functions for unretrofitted load-bearing stone walls subjected to initial axial loads of 120kN and 180kN

6.2.4 Resistance Functions for Retrofitted Load Bearing CMU and Stone Wall with Arching Action

Resistance functions for load-bearing walls with initial axial compression and subsequent arching forces can be constructed using the governing equation proposed by Moradi et al. (2008), given in Eq. 6.14. In this case, axial forces are applied to the walls due to reinforced polyurea, T, arching action, V_T, and axial loading, P. The resulting resistance functions are plotted in Figures 6.6 through 6.9.

$$p = -\frac{8}{h^2}\left[\mathbf{P}\left(\frac{t-a}{2}\right) + \frac{W_i}{2}\left(\frac{t-a}{2} - \frac{\Delta}{2}\right) - \left(\mathbf{P} + T + V_T + \frac{W_i}{2}\right)\left(\frac{t}{6} + \frac{y}{3} + \frac{t-a}{2} - \Delta\right) - T\left(\frac{a}{2} + \Delta\right)\right] \tag{6.14}$$

The summary of the steps leading to the development of the static resistance functions remains the same as indicated in the previous sections for walls with and without initial axial load and with and without the reinforced polyurea.

$$R_{crG} \cong R_{cr} = P + T + V_T + \frac{W_i}{2} \tag{6.15}$$

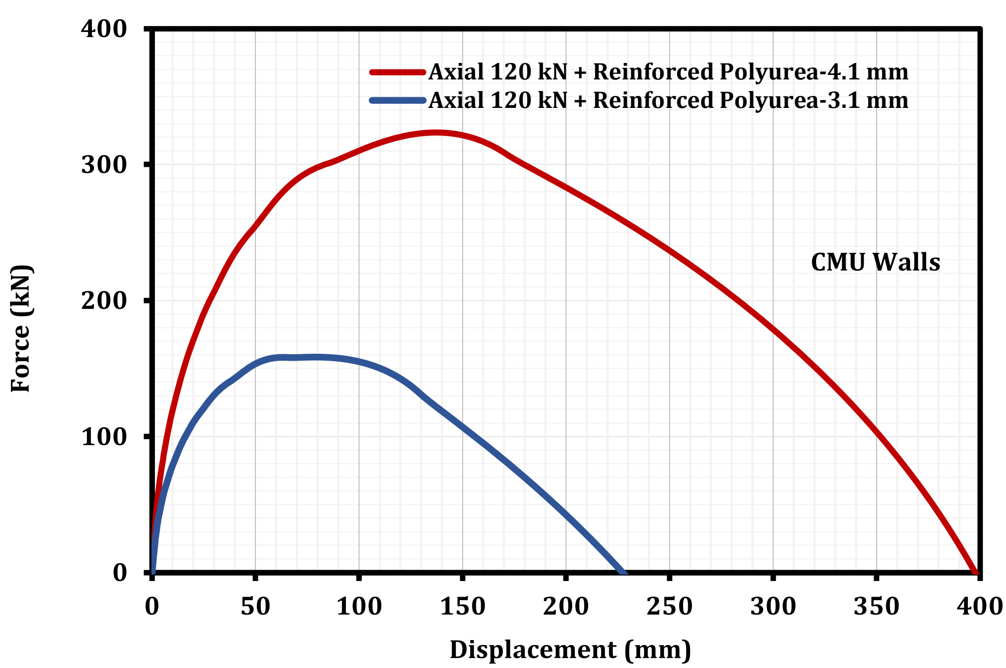

Figure 6.8. Resistance functions for load-bearing CMU walls retrofitted with reinforced polyurea and subjected to an initial axial load of 120kN

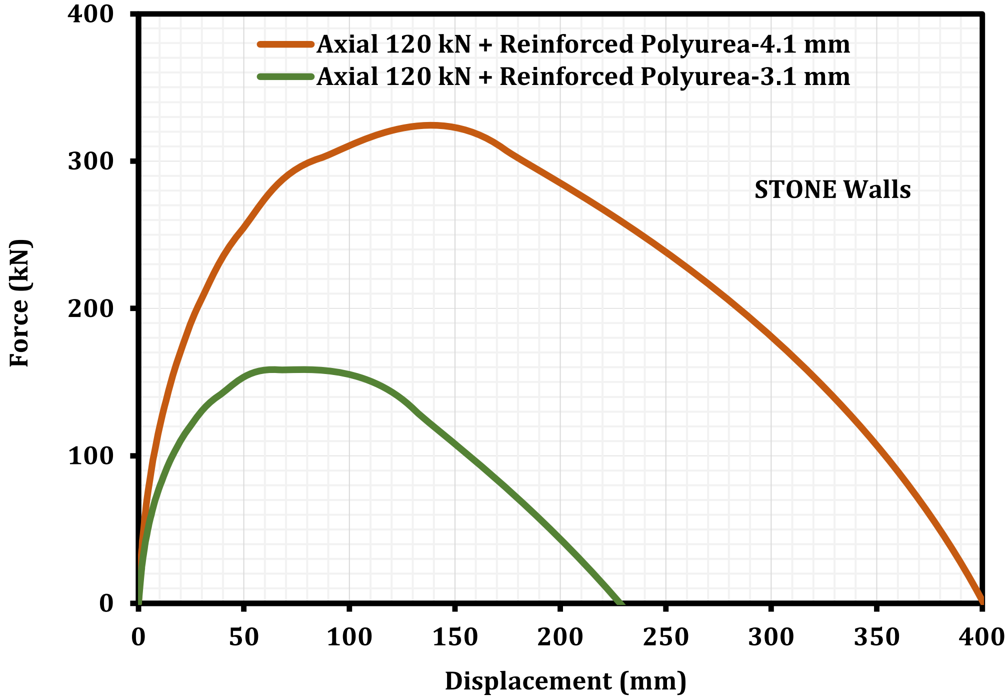

Figure 6.9. Resistance functions for load-bearing stone masonry walls retrofitted with reinforced polyurea and subjected to an initial axial load of 120 kN

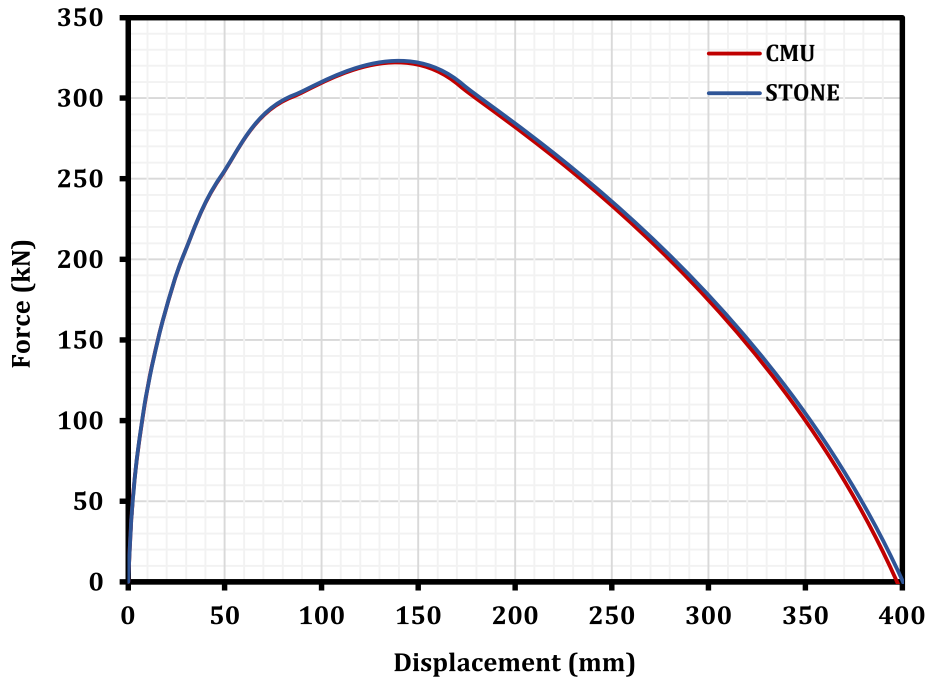

Figure 6.10. Resistance functions for load-bearing CMU and stone walls subjected to an initial axial load of 120 kN and retrofitted with reinforced polyurea- 4.1 mm

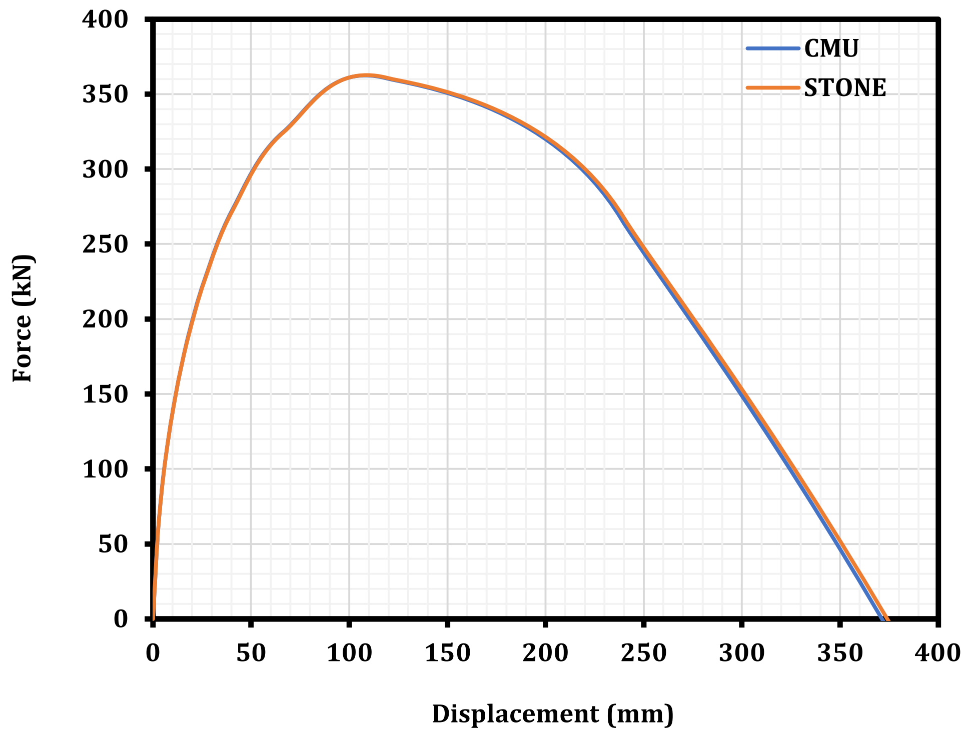

Figure 6.11. Resistance functions for load-bearing CMU and stone walls subjected to an initial axial load of 180 kN and retrofitted with reinforced polyurea-4.1 mm

6.3 Single Degree of Freedom (SDOF) Analysis

SDOF dynamic analysis is a commonly used analysis technique in blast engineering. Blast-induced shock waves with short durations (in the order of milliseconds) excite single structural and non-structural elements with short fundamental periods. Therefore, most analyses are conducted on single elements with distributed mass and a specific stiffness, subjected to uniformly distributed blast pressures. These elements can be transformed into a single spring-lumped-mass model and a concentrated time-varying force. The resulting model can be analyzed as a SDOF system to compute wall deflections. The SDOF analysis is often conducted using available computer software. SBEDS (USACE 2009) and RC-Blast (Jacques 2014, Jacques et al. 2013) are examples of commonly used SDOF blast analysis software.

The RC-Blast software developed at the University of Ottawa was used to conduct a single-degree-of-freedom dynamic analysis of the URM walls tested. Section 2.9.1 and Figure 2.10 provide background information on the mass-spring model used. The general equation of motion for a SDOF system subjected to forced vibration is reproduced below.

$$M_e\ddot{Z}(t) + C_e\dot{Z}(t) + K_eZ(t) = F_e(t) \tag{6.1}$$

Where M_e = equivalent mass of the SDOF; C_e = equivalent damping coefficient of the SDOF; K_e = equivalent stiffness of the SDOF; and F_e (t) = equivalent load-time history applied to the SDOF. The mid-height deflection of a CMU wall can be used as the unknown parameter to solve the problem. The effect of damping for blast loading is usually considered to be negligible. This reduces the equation of motion to Eq. 6.2.

$$M_e\ddot{Z}(t) + K_eZ(t) = F_e(t) \tag{6.2}$$

The equivalent mass M_e, the equivalent stiffness K_e and the equivalent force F_e can be computed by applying transformation factors, K_M, K_K, and K_L, respectively.

$$K_MM_h\ddot{Z}(t) + K_KKZ(t) = K_LF(t) \tag{6.3}$$

The K_K and K_L values are equal since the spring stiffness is the force required to cause unit deflection and is directly proportional to the load. Substituting $K_K = K_L$ in Eq. 6.3 and dividing all terms by K_L.

$$\frac{K_M}{K_L}M_h\ddot{Z}(t) + KZ(t) = F(t) \tag{6.4}$$

$$K_{LM}\ (Z)\ M_h\ddot{Z}(t) + R\ (Z(t)) = AP_r(t) \tag{6.5}$$

K_M/K_L is defined as the load-mass factors $K_{LM}(Z)$ a function of displacement. Load-mass factors are readily available and can be used in the software to convert the uniformly distributed mass of the wall and the uniformly distributed blast loads to a lumped mass and a concentrated force, as shown in Figure 2.10, to conduct the SDOF analysis. The input parameters needed in RC-Blast Software for the analysis include the mass quantities, the resistance function, R(Z), (from which wall strength and stiffness are obtained), and the blast load in the form of blast pressure versus time relationship. The wall mass for the two types of wall samples, CMU and stone, were computed to be 829kg and 785kg, respectively. The spray-on polyurea mass was approximately 26 kg. The wire mesh reinforcement masses for the larger and smaller wires were 12kg and 7 kg, respectively. The effects of high strain rates on material stress-strain relationships were introduced by specifying dynamic increase factors (DIF). The values specified were 1.2 for the masonry, 1.2 for the steel yield strength, and 1.1 for the ultimate rupturing strength of steel. It uses the triangular (idealized) pressure-duration forcing function for the blast load where, $P_r(t)$, is the time-varied applied pressure distribution with a maximum positive phase duration, t_d, from the experiment is used. The surface area, A, of the wall (tributary area) impacted by the blast load was 4 m^2. The load mass factors (K_{LM}) were specified to vary three times as the resistance function changed from elastic to inelastic range with three discrete values assigned as 0.78, 0.72, and 0.66 (UFC 3-340-02, 2008).

The RC Blast software numerically solves the equation of motion given in Eq. 6.1 using the Average Acceleration Method (AAM). AAM is a Newmark's Beta (β) Method that uses the forcing function in the form of acceleration to calculate the average variation between two-time instants. It has two notable parameters α and β which are used to define the variation of acceleration over a time step. α=1/2 ensures second-order accuracy and $\beta = 1/4$ makes the algorithm implicit and equivalent to the trapezoidal rule. The AAM is unconditionally stable as it converges for all time increments, which makes it suitable for the shorter time steps required to describe the responses of the wall-retrofit systems.

6.3.1 SDOF Analysis of Walls Retrofitted with Reinforced Polyurea

The summary of the maximum dynamic mid-height displacements obtained from the SDOF analysis is given in Table 6.1. These displacements are compared with those recorded from the experiments, and their statistical information in terms of mean error and the coefficient of variation is also presented. The positive sign indicates the analytical displacement is greater than its corresponding experimental result and vice versa. Figure 6.12 to Figure 6.37 show the displacement-time history curves of the analytical and experimental with their corresponding pressure-time history graphs. Figure 6.38 to Figure 4.42 show bar chart representation of the displacements from SDOF models and the test wall samples.

Table 6.1 addresses the statistical relationship between the analytical and experimental results. The sample mean error (%) and the coefficients of variation (CV) for both sets of results are given to determine the degree of data variation (or dispersion). The ratio of the CV for experimental results to that of the SDOF results showed an average value of 1. This implies that the data variation of both methods is very close in dispersion.

The statistical data revealed an overall average percentage error of 2.6 between the analytical and experimental results, indicative of the SDOF analysis being an acceptable analytical procedure for predicting the response of retrofitted URM walls.

6.3.2 Variations Between Experimental and SDOF Results and Possible Sources of Errors

The experimental results are compared with those generated by SDOF analysis in Figures 6.12 through 6.43 and show reasonably good agreement. Some discrepancies exist between the two sets of results especially as they relate to the initial stiffness. It was observed that the maximum deflection agreed very well, while the initial stiffness of the analysis results indicated softer response. This is attributed to the fact that the period of the walls is affected by the limited damage that was introduced to the wall during prior shots as mortar joints experienced cracking, elongating the period of the walls during the tests, which was not accounted for in the analysis. A longer period resulted in lower dynamic increase factors, resulting in responses with slightly lower deflections during the ascending branches of the displacement response. Furthermore, the analytical approach employed may have resulted in resistance functions that could be approximated because of the variations in material characteristics, including the variation in the polyurea thickness that was sprayed on the walls. Nevertheless, the agreement was found to be sufficiently accurate to suggest that the SDOF analysis could be used for design purposes.

Table 6.1: Summary of SDOF models vs Experimental results

Sample Descriptions			Blast properties			Maximum mid-height displacements (mm) & Statistical data							
			P_r (kPa)	I_r (kPa-ms)	t_d (ms)	EXP. d_{max} (mm)	SDOF d_{max} (mm)	ERROR (mm)	ERROR (%)	MEAN ERROR (%)	CV, d_{EXP} (%)	CV, d_{SDOF} (%)	$\frac{CV, d_{SDOF}}{CV, d_{EXP}}$
NON-LOAD BEARING WALLS	STONE SS304-3.1mm	Wall-1-1	43	301	16	16	17	1	6				
		Wall-1-2	57	403	16	26	25	-1	-4				
		Wall-1-3	67	542	18	39	37	-2	-5				
		Wall-1-4	93	711	24	100	101	1	1	**4**	0.8	0.8	**1**
	CMU SS304-4.1mm	Wall-2-1	50	419	18	23	20	-3	-13				
		Wall-2-2	72	550	18	34	32	-2	-6				
		Wall-2-3	74	701	25	56	50	-6	-11				
		Wall-2-4	85	793	28	80	72	-8	-10				
		Wall-2-5	85	2177	57	203	201	-2	-1	**8**	0.9	0.9	**1**
	CMU SS304-3.1mm	Wall-3-1	50	420	18	25	24	-1	-4				
		Wall-3-2	67	547	19	39	39	0	0				
		Wall-3-3	**76**	714	28	89	85	-4	-4				
		Wall-3-4	89	874	30	140	132	-8	-6	**4**	0.7	0.7	**1**
		Wall-3-5	88	1479	32	Global Failure							
LOAD BEARING WALLS	STONE SS304-4.1mm	Wall-4-1	49	432	18	17	14	-3	-18				
		Wall-4-2	66	560	19	22	22	0	0				
		Wall-4-3	74	695	22	32	31	-1	-3				
		Wall-4-4	82	808	24	38	38	0	0				
		Wall-4-5	110	2488	60	197	200	3	2	**4**	1.2	1.2	**1**
	CMU SS304-3.1mm	Wall-5-1	51	420	18	23	21	-2	-9				
		Wall-5-2	73	578	21	47	42	-5	-11				
		Wall-5-3	103	1030	27	108	108	0	0	**6**	0.7	0.8	**1**
	CMU SS304-4.1mm	Wall-6-1	52	451	20	17	15	-2	-12				
		Wall-6-2	67	631	23	26	24	-2	-8				
		Wall-6-3	86	764	27	44	41	-3	-7				
		Wall-6-4	120	1067	29	76	75	-1	-1				
		Wall-6-5	125	2420	62	185	186	1	1	**6**	1	1	**1**
MEAN ERROR (%) = 2.6%												**AVG**	**1**

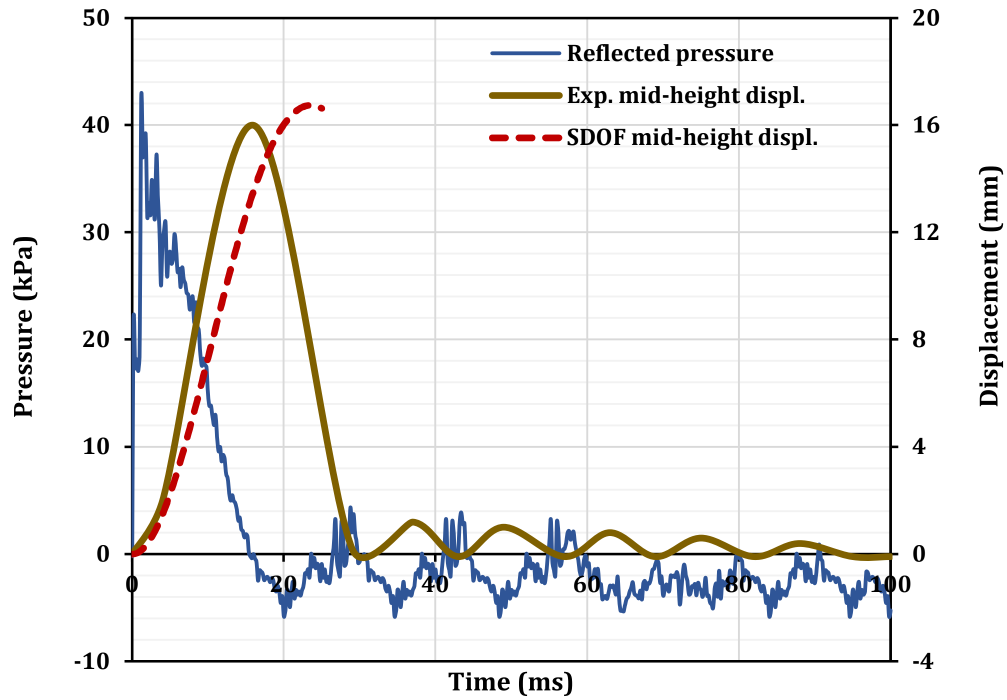

Figure 6.12. Pressure and displacement time history of Wall-1-1

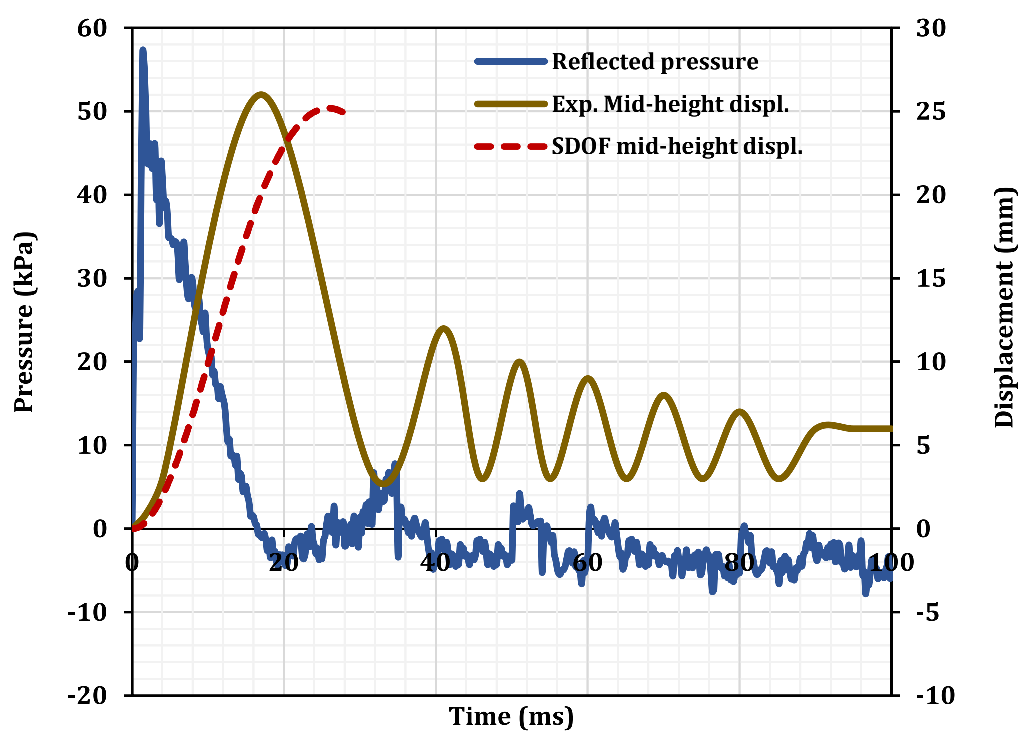

Figure 6.13. Pressure and displacement time history of Wall-1-2

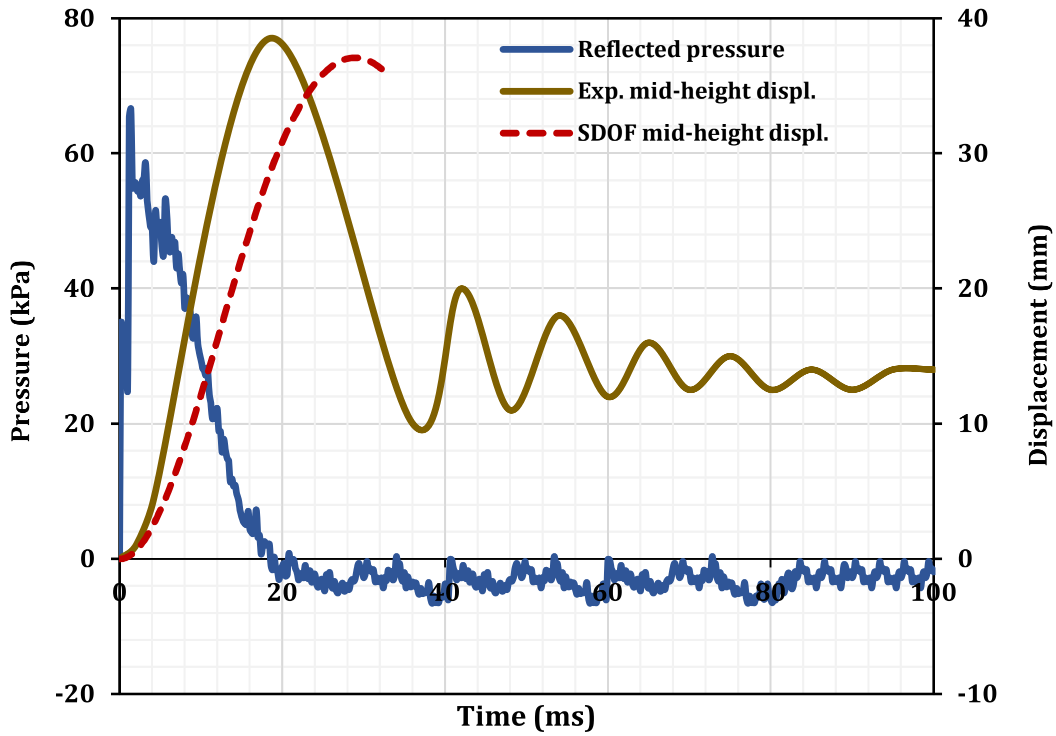

Figure 6.14. Pressure and displacement time history of Wall-1-3

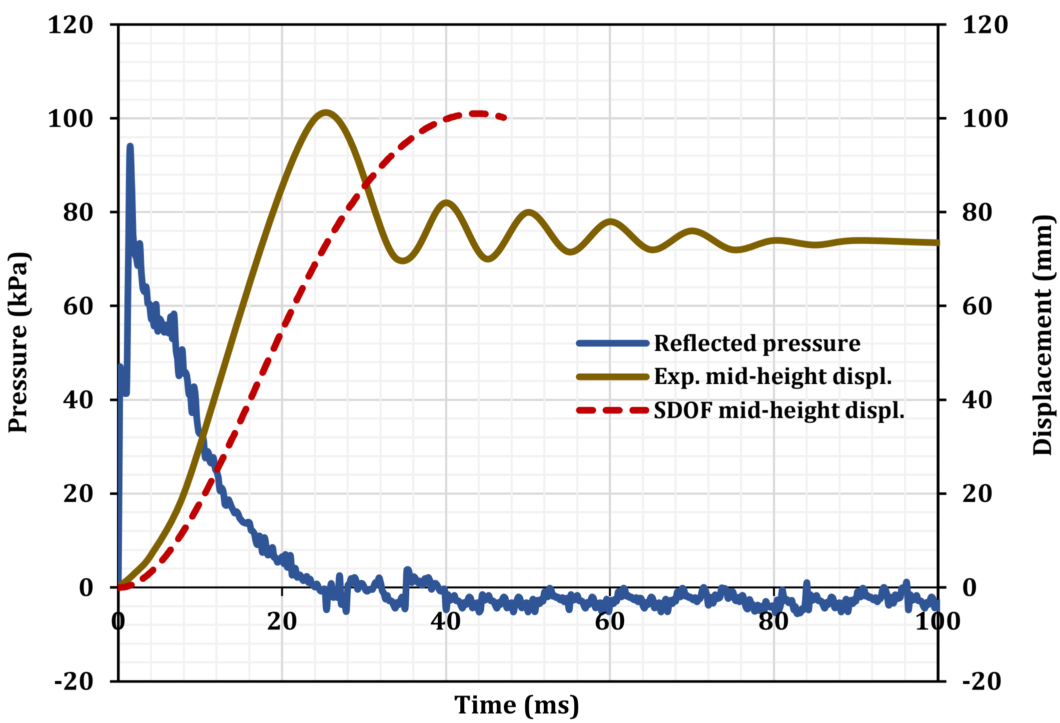

Figure 6.15. Pressure and displacement time history of Wall-1-4

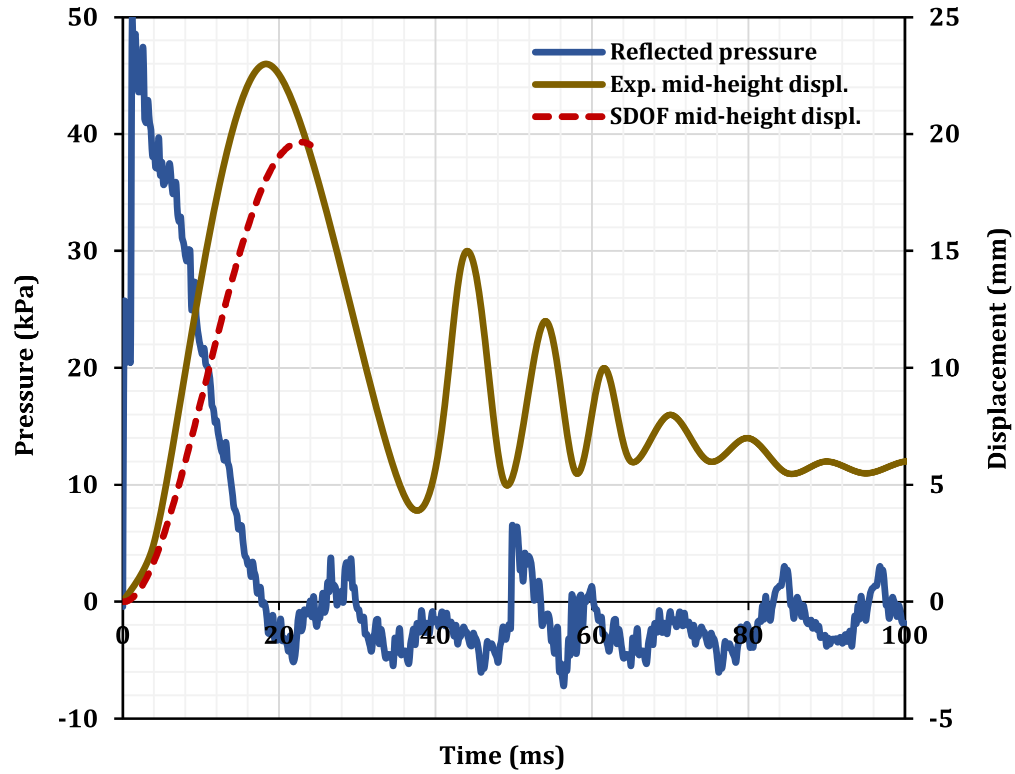

Figure 6.16. Pressure and displacement time history of Wall-2-1

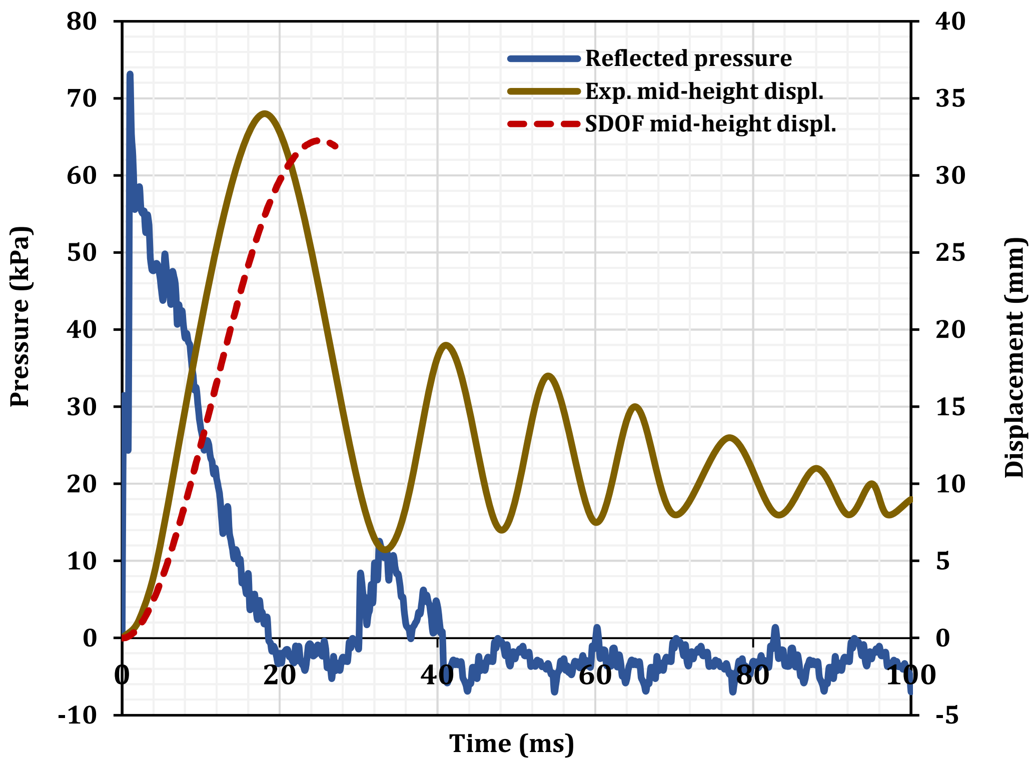

Figure 6.17. Pressure and displacement time history of Wall-2-2

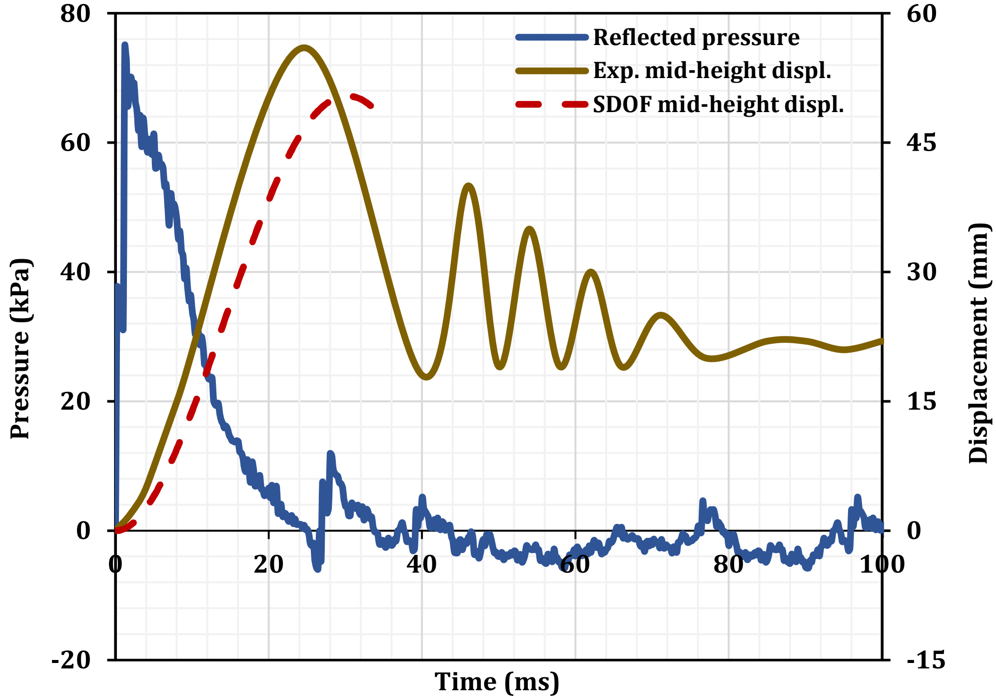

Figure 6.18. Pressure and displacement time history of Wall-2-3

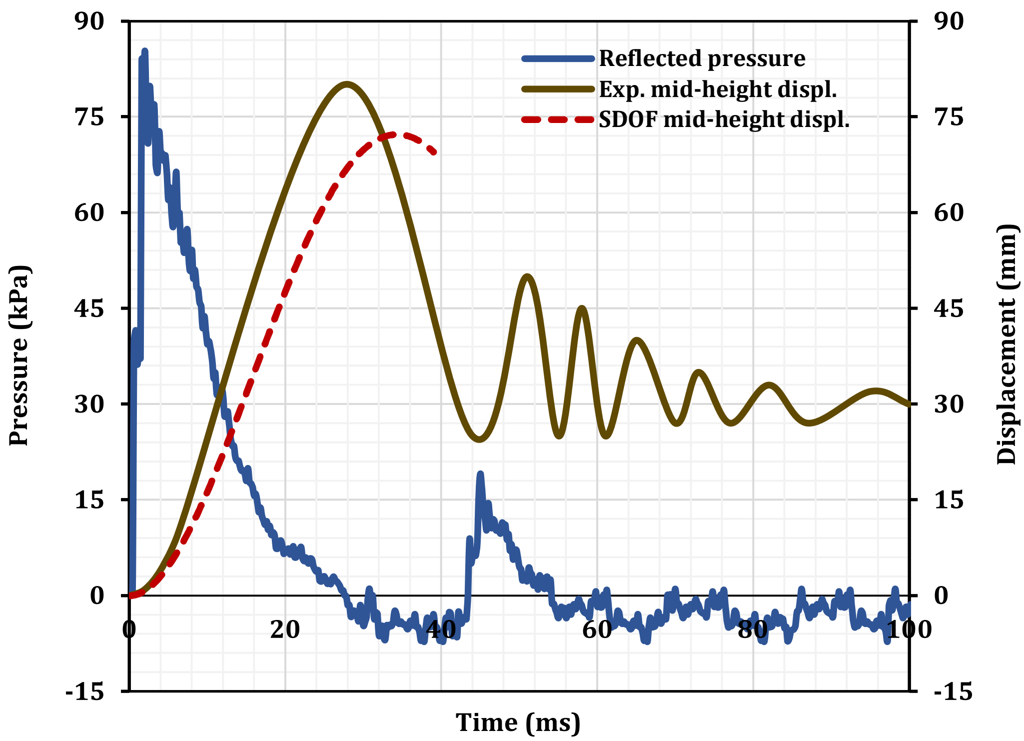

Figure 6.19. Pressure and displacement time history of Wall-2-4

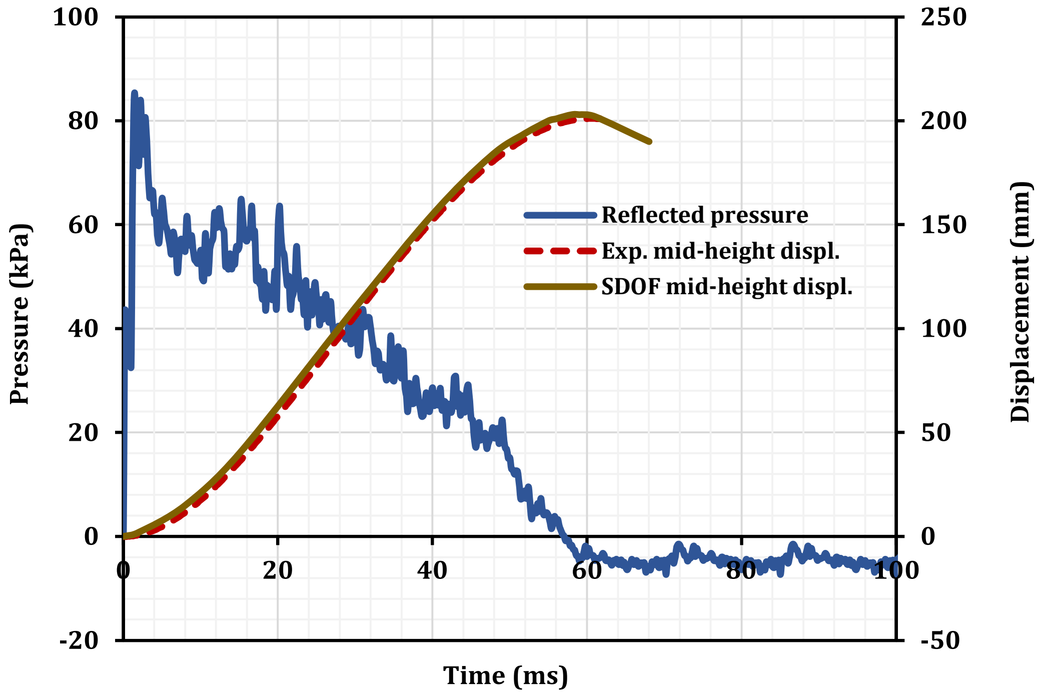

Figure 6.20. Pressure and displacement time history of Wall-2-5

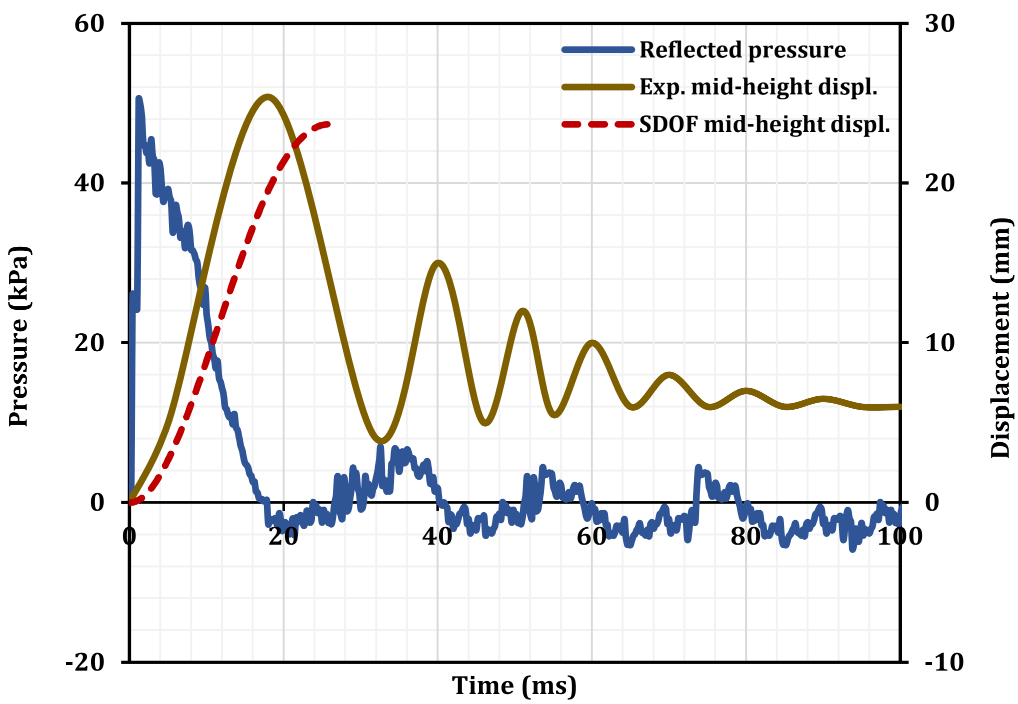

Figure 6.21. Pressure and displacement time history of Wall-3-1

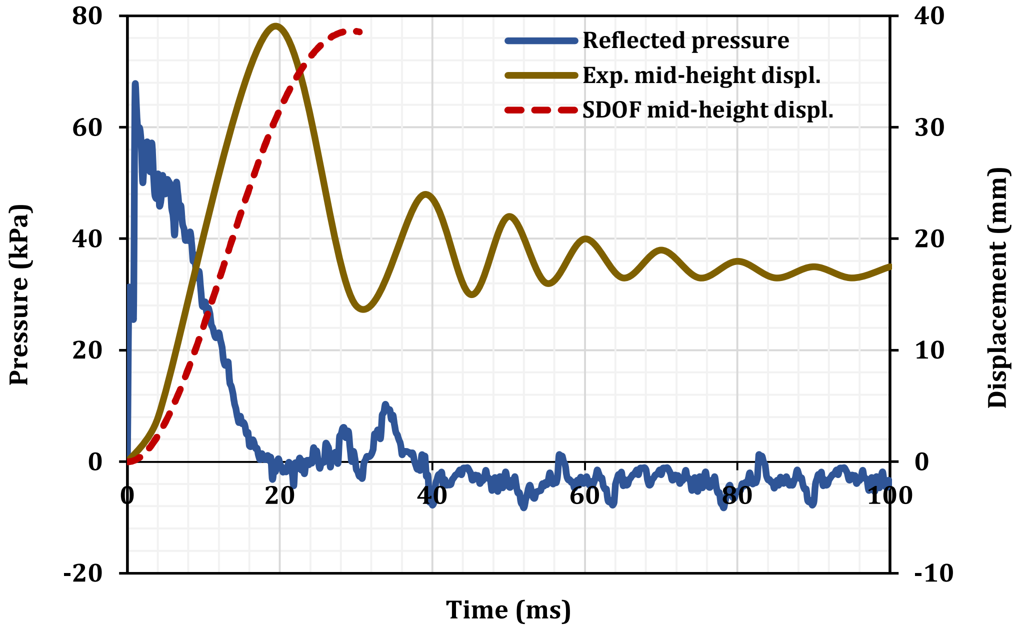

Figure 6.22. Pressure and displacement time history of Wall 3-2

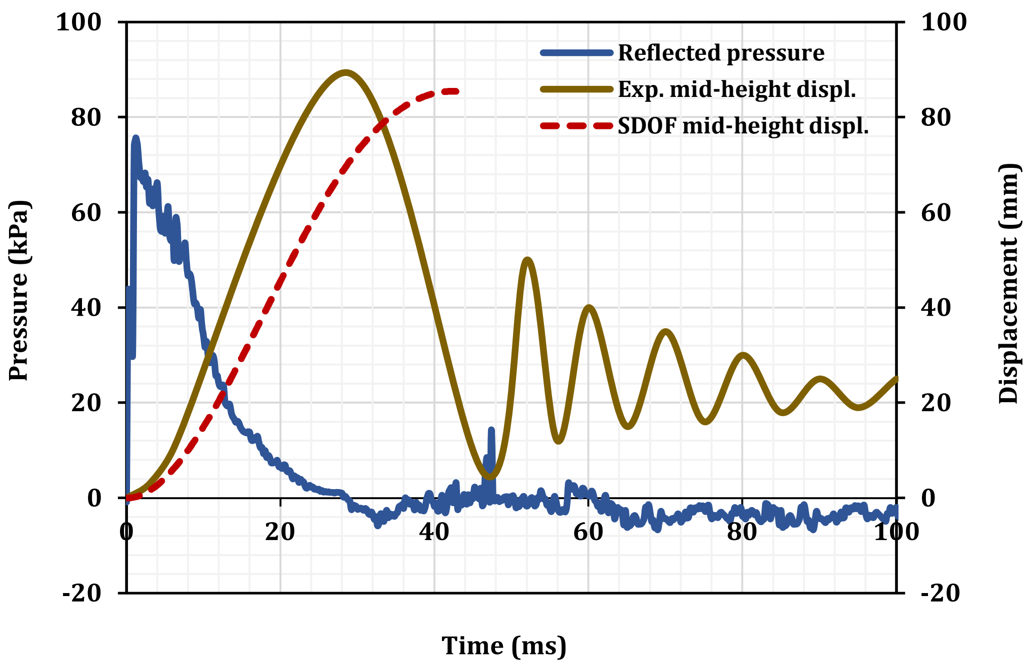

Figure 6.23. Pressure and displacement time history of Wall 3-3

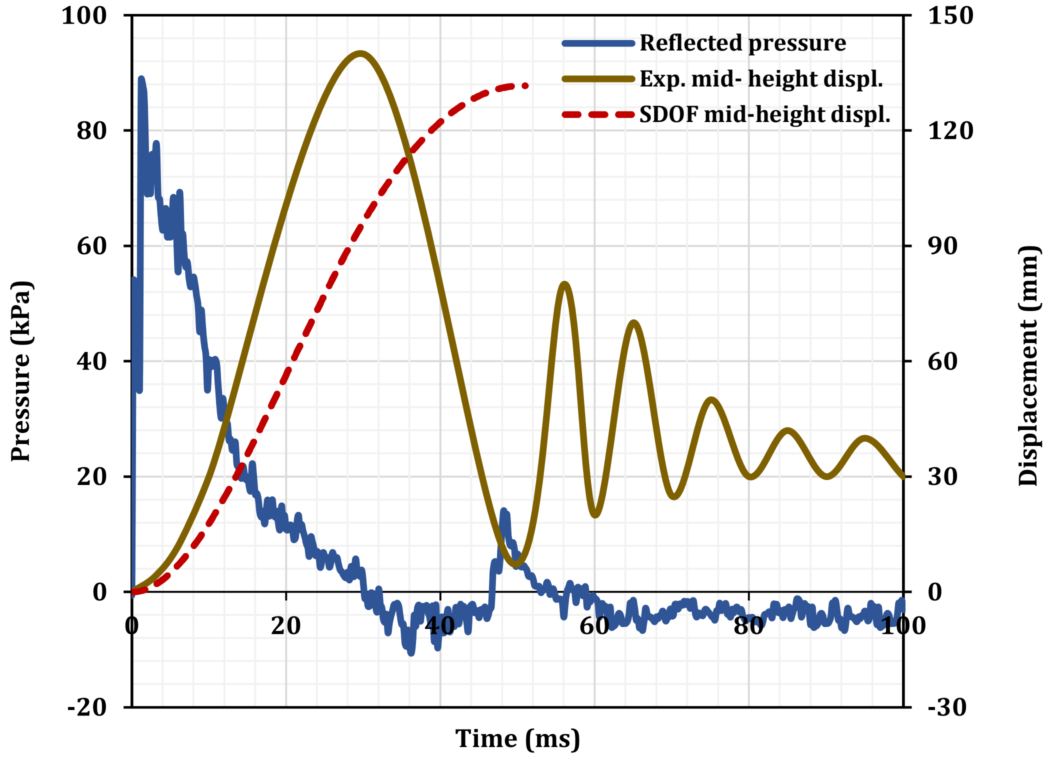

Figure 6.24. Pressure and displacement time history of Wall 3-4

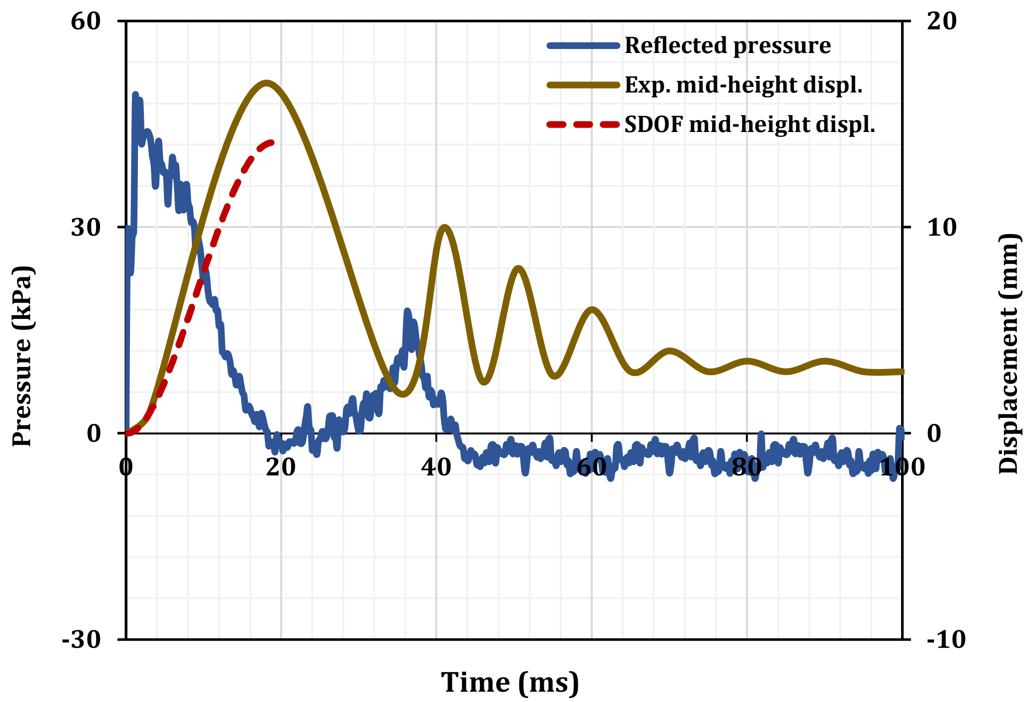

Figure 6.25. Pressure and displacement time history of Wall 4-1

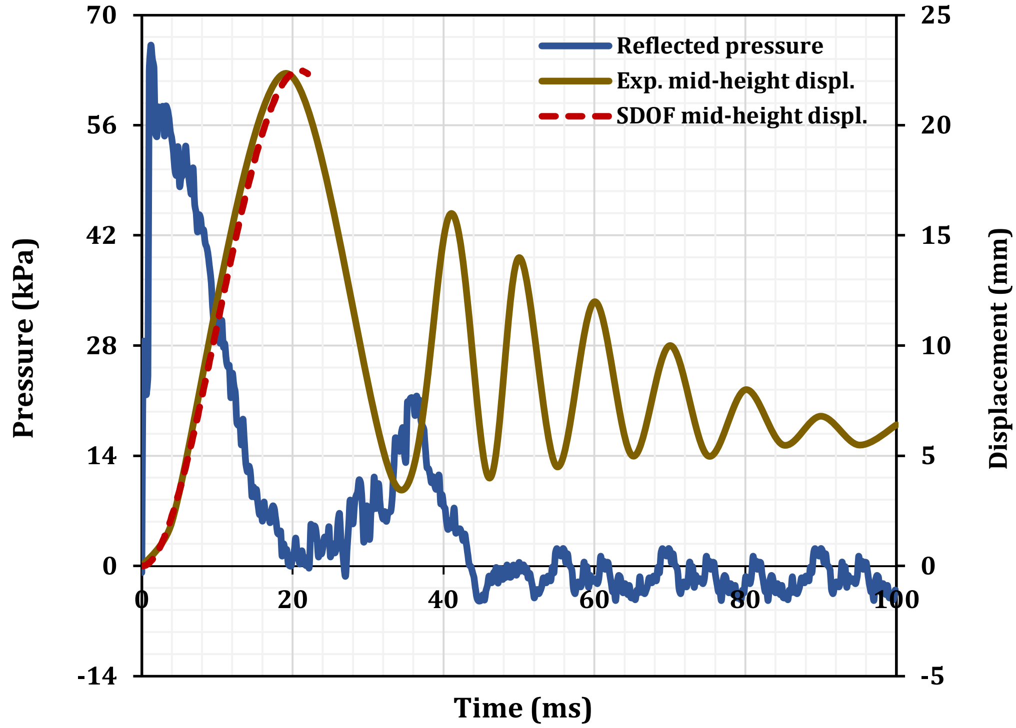

Figure 6.26. Pressure and displacement time history of Wall 4-2

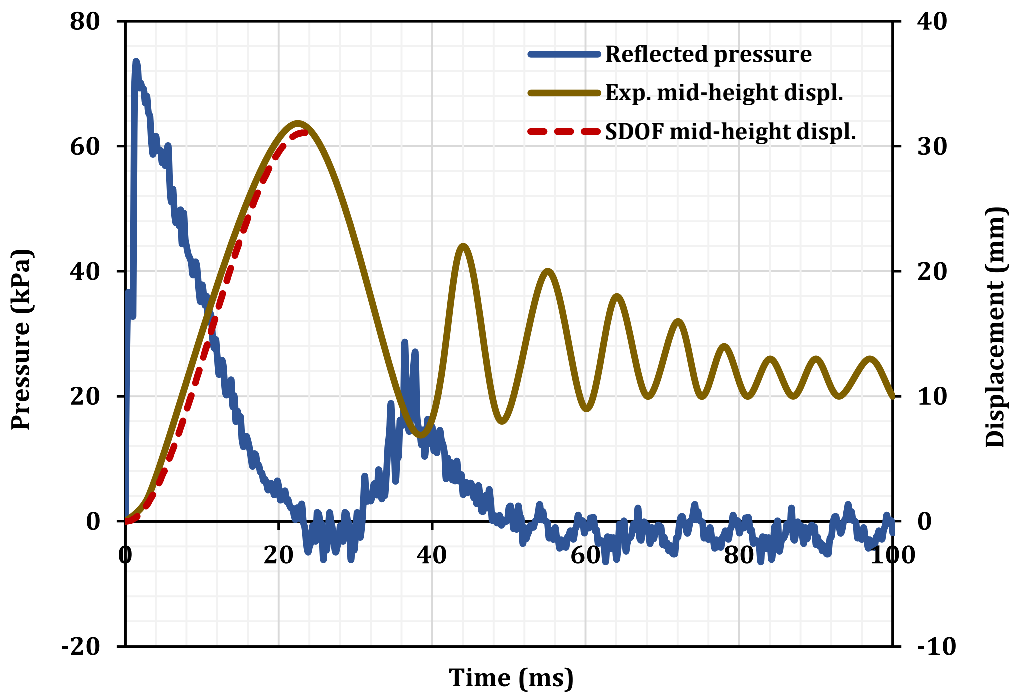

Figure 6.27. Pressure and displacement time history of Wall 4-3

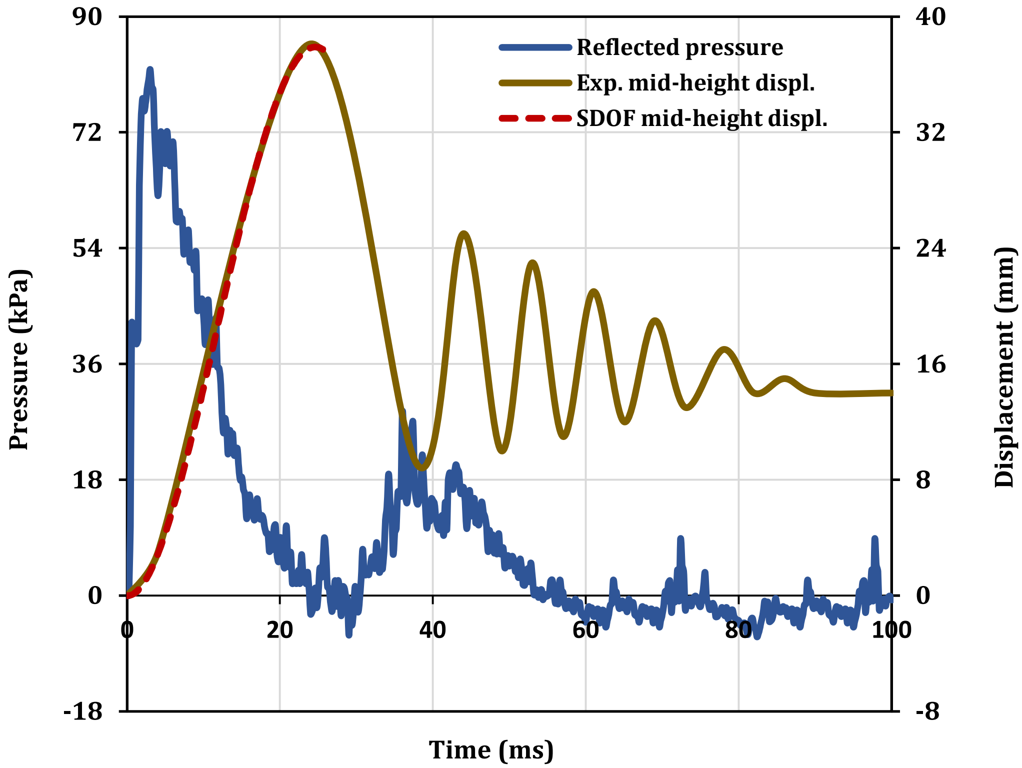

Figure 6.28. Pressure and displacement time history of Wall 4-4

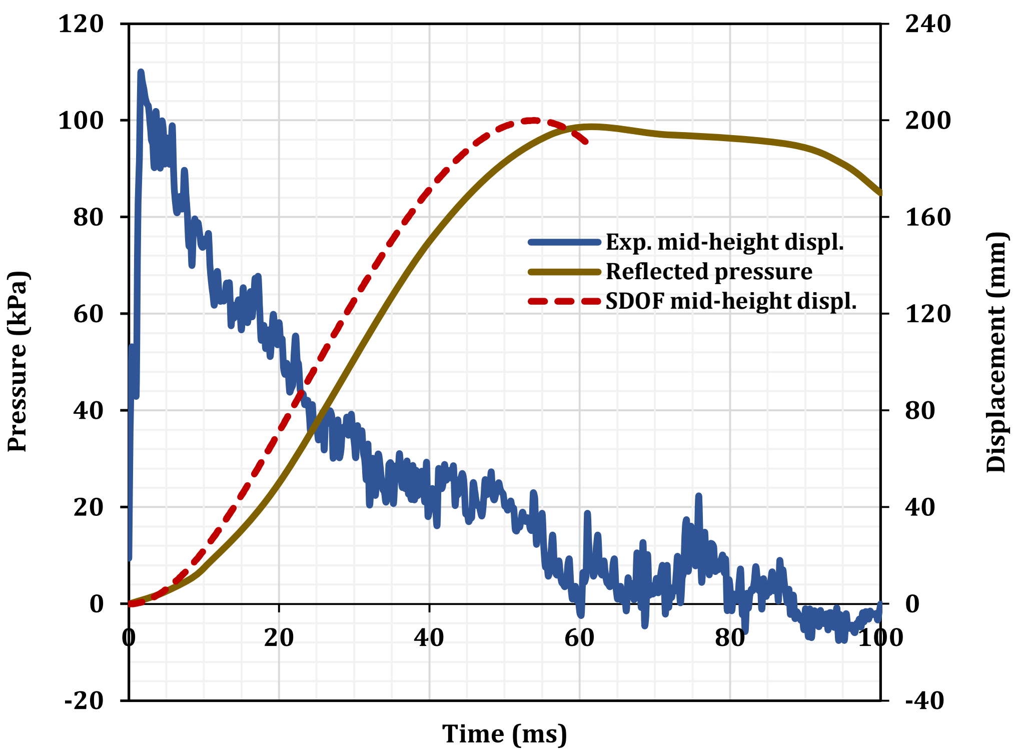

Figure 6.29. Pressure and displacement time history of Wall 4-5

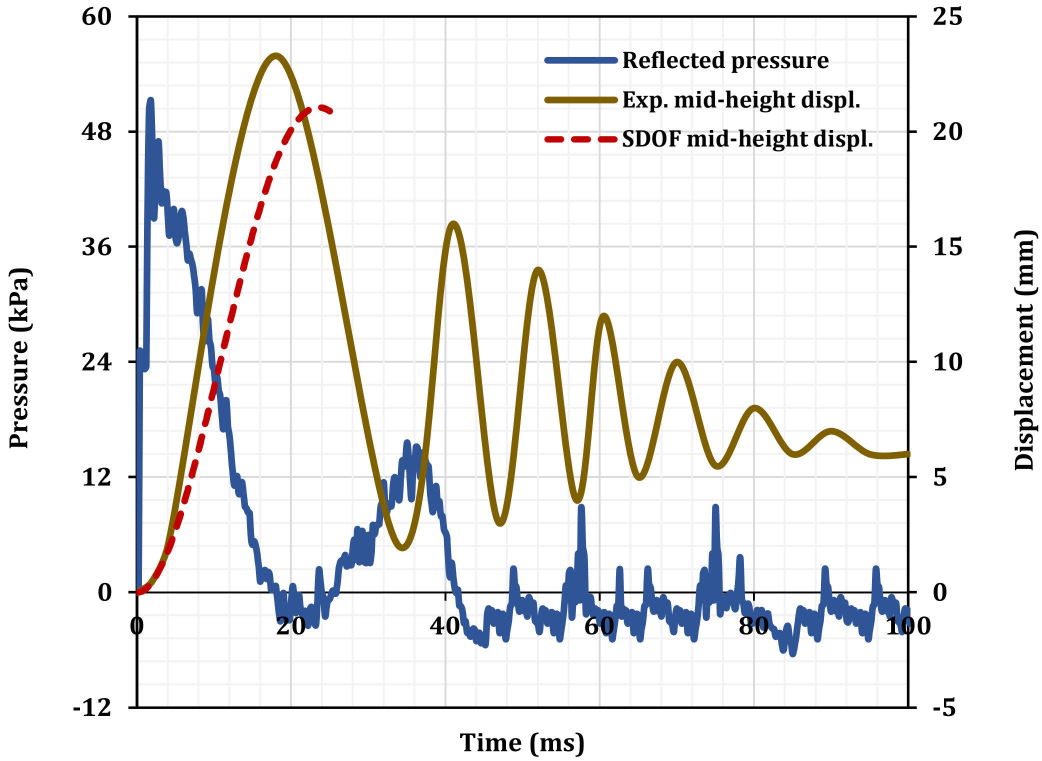

Figure 6.30. Pressure and displacement time history of Wall 5-1

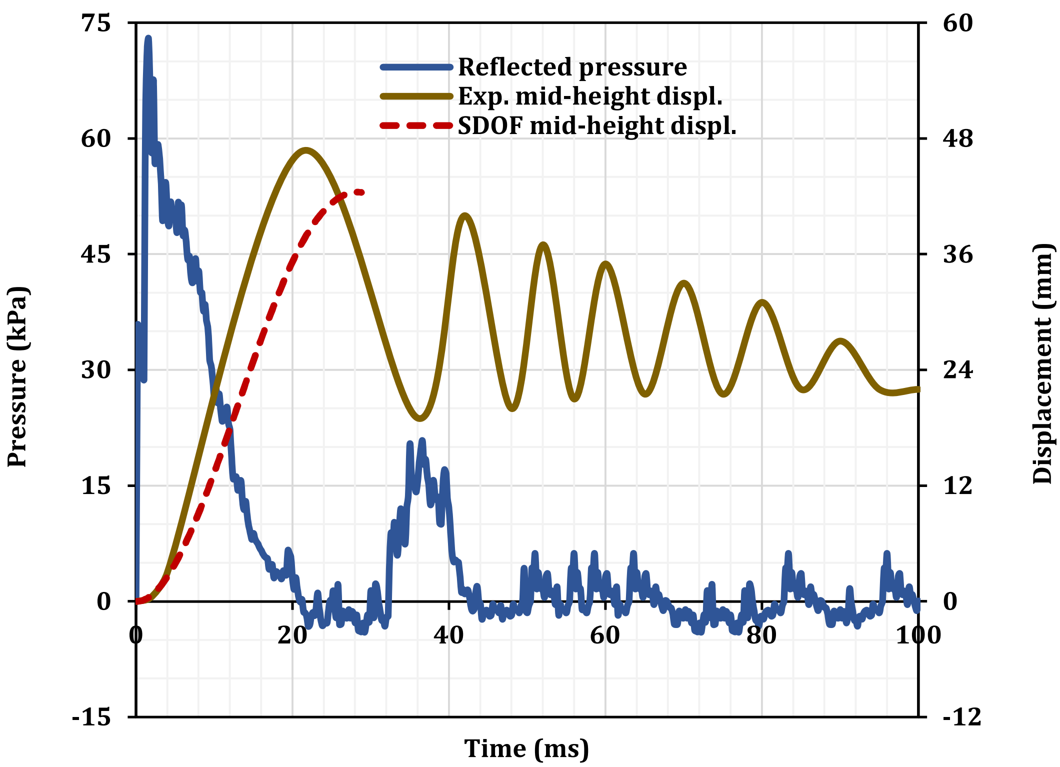

Figure 6.31. Pressure and displacement time history of Wall 5-2

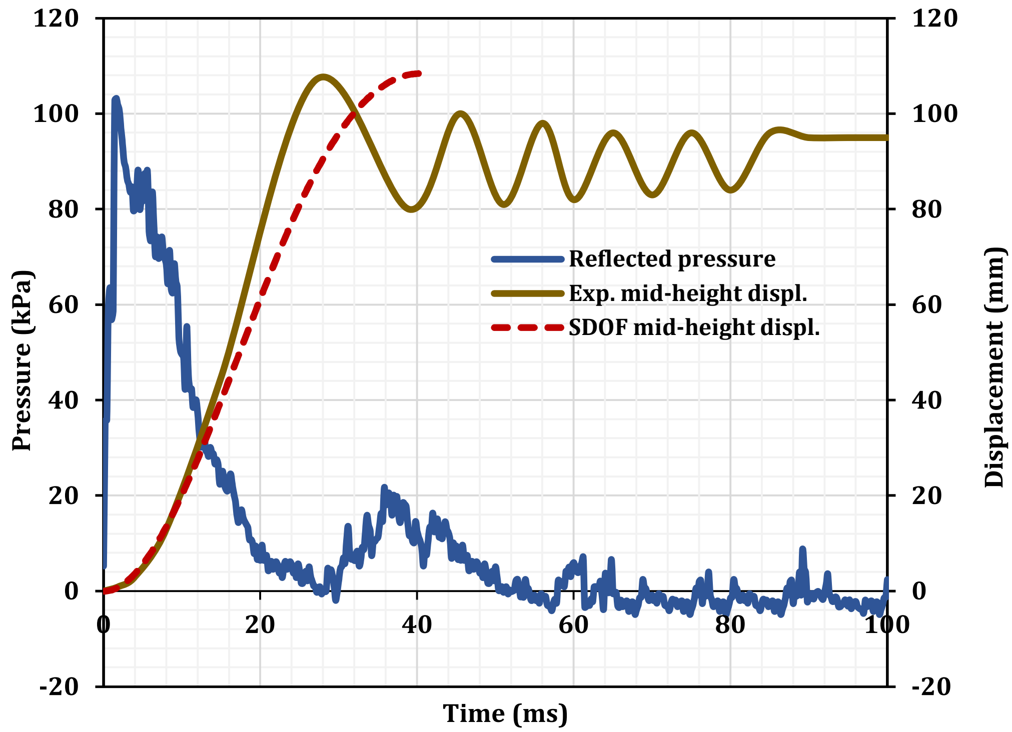

Figure 6.32. Pressure and displacement time history of Wall 5-3

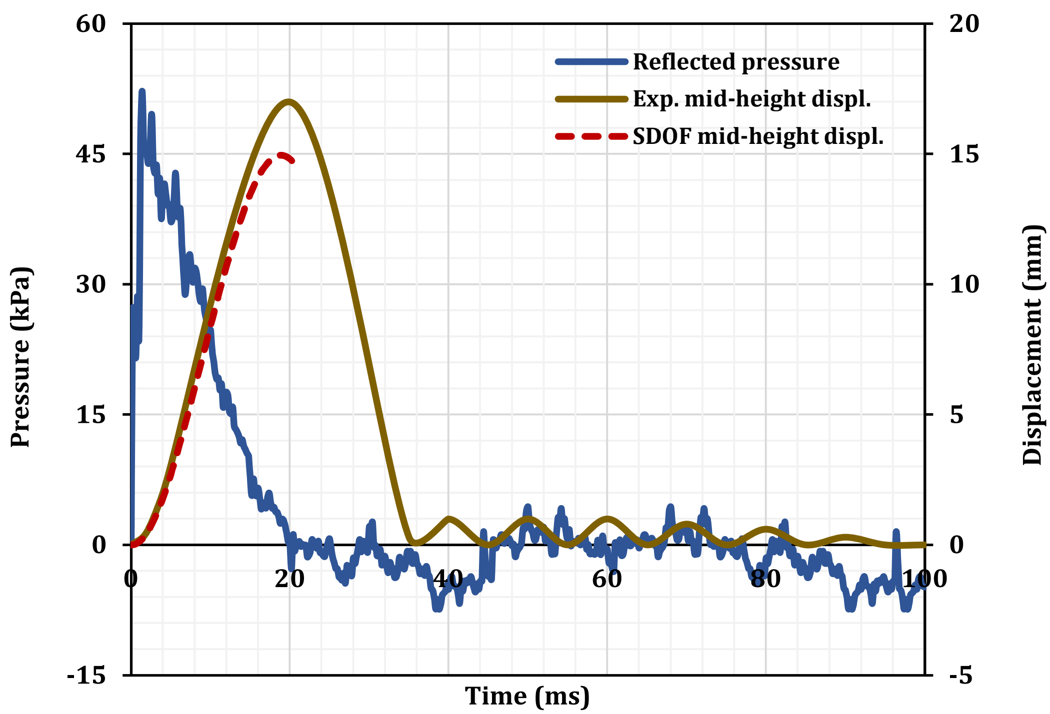

Figure 6.33. Pressure and displacement time history of Wall 6-1

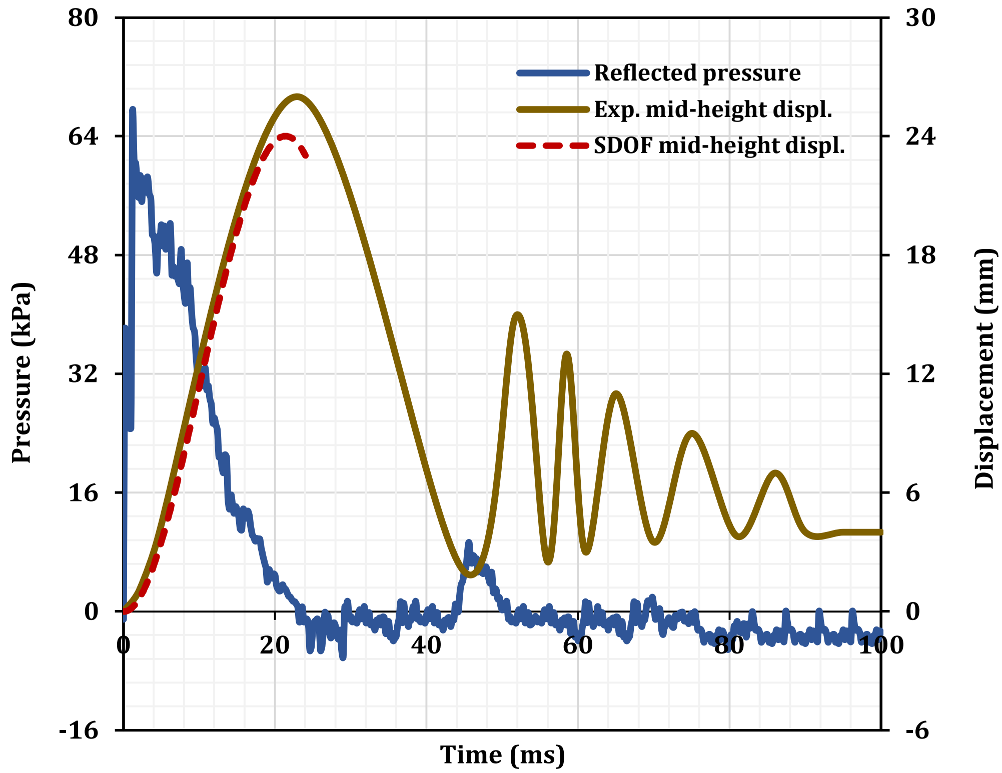

Figure 6.34. Pressure and displacement time history of Wall 6-2

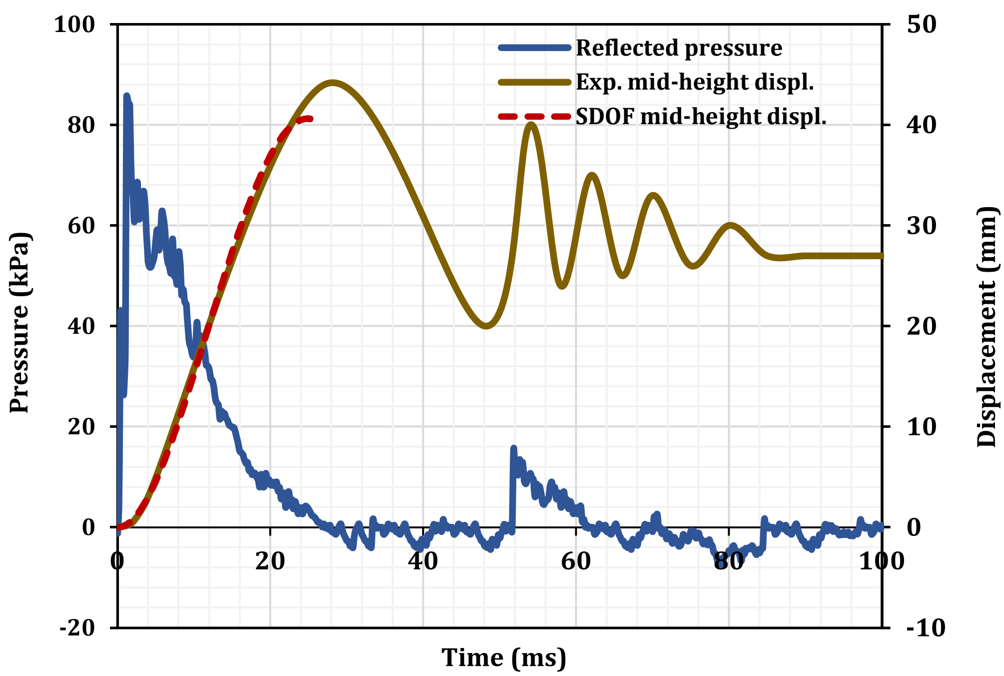

Figure 6.35. Pressure and displacement time history of Wall 6-3

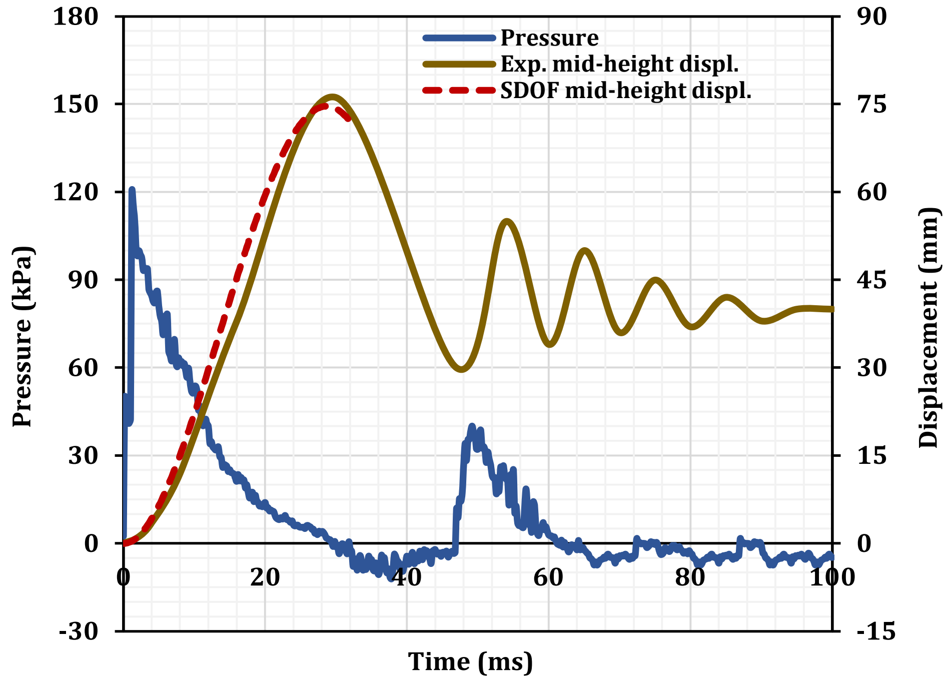

Figure 6.36. Pressure and displacement time history of Wall 6-4

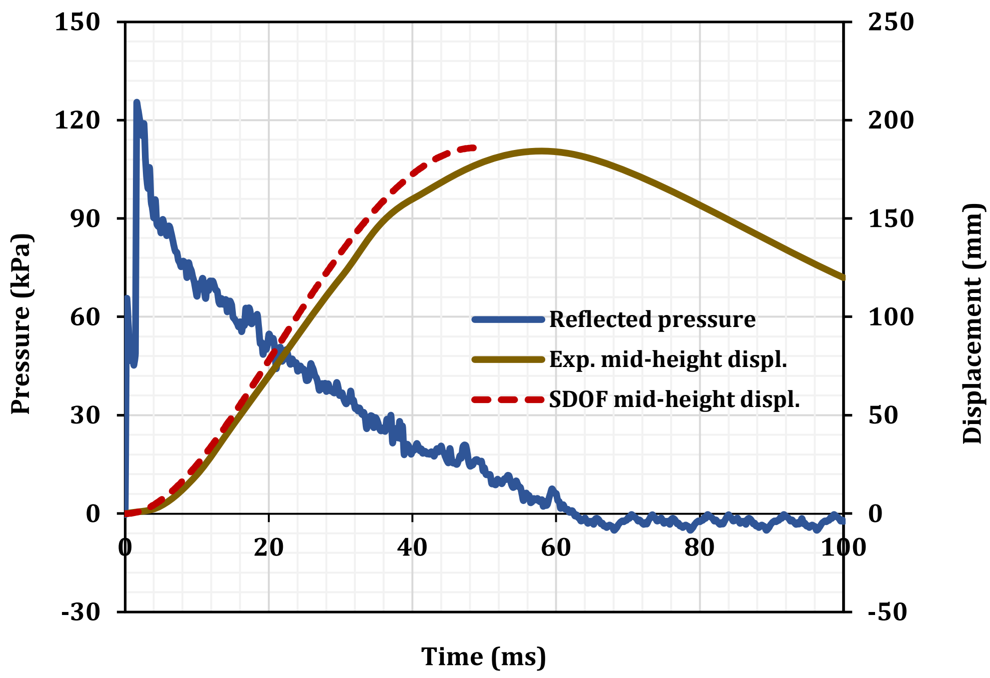

Figure 6.37. Pressure and displacement time history of Wall 6-5

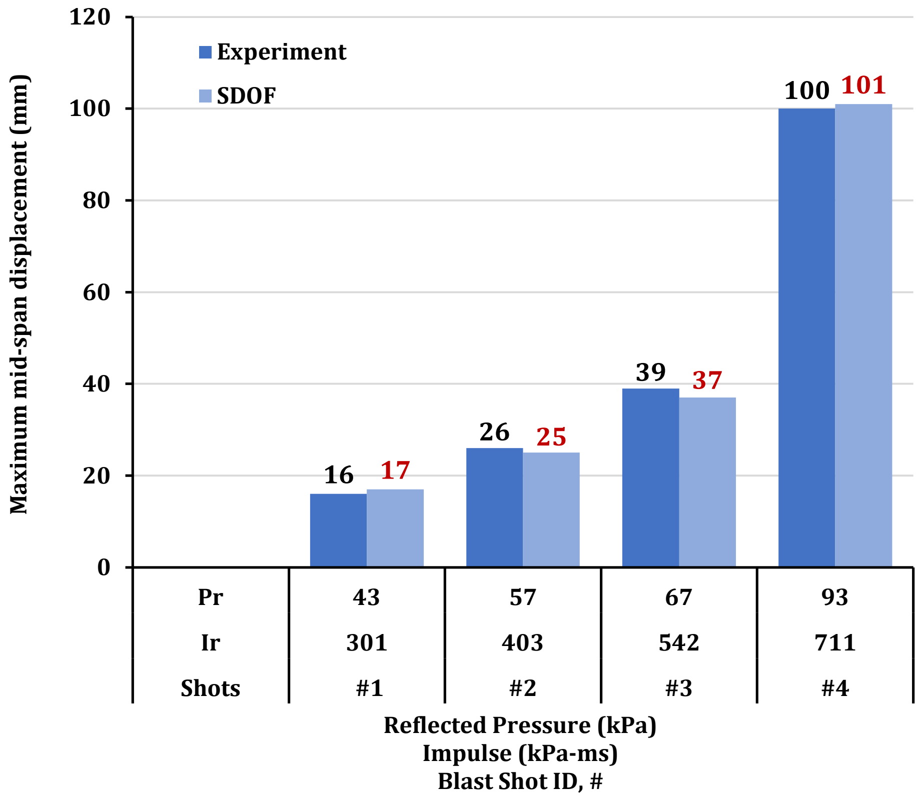

Figure 6.38. Experiment vs SDOF of wall-1

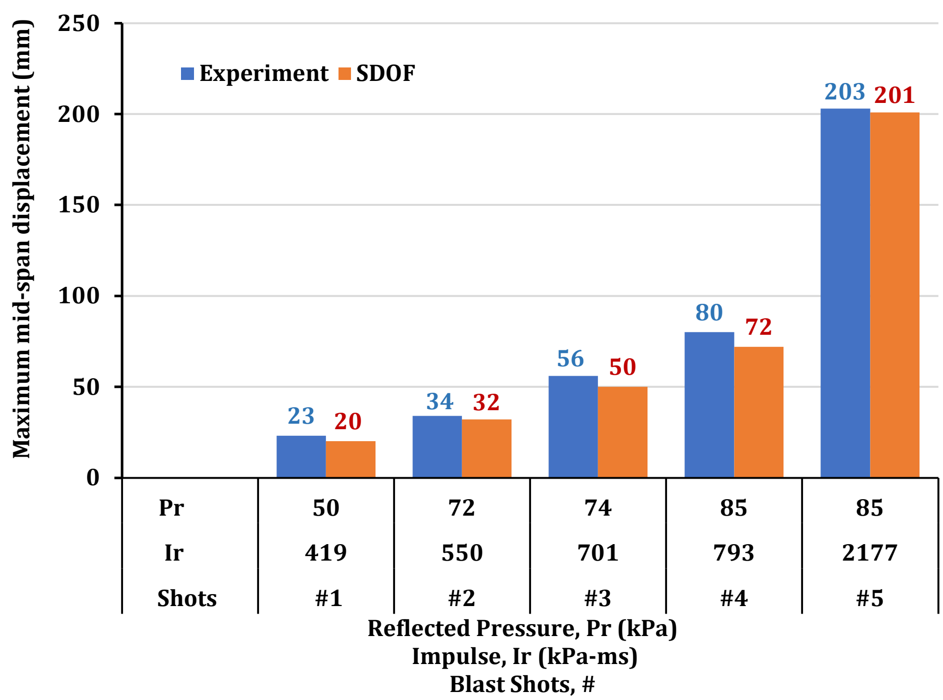

Figure 6.39. Experiment vs SDOF of wall-2

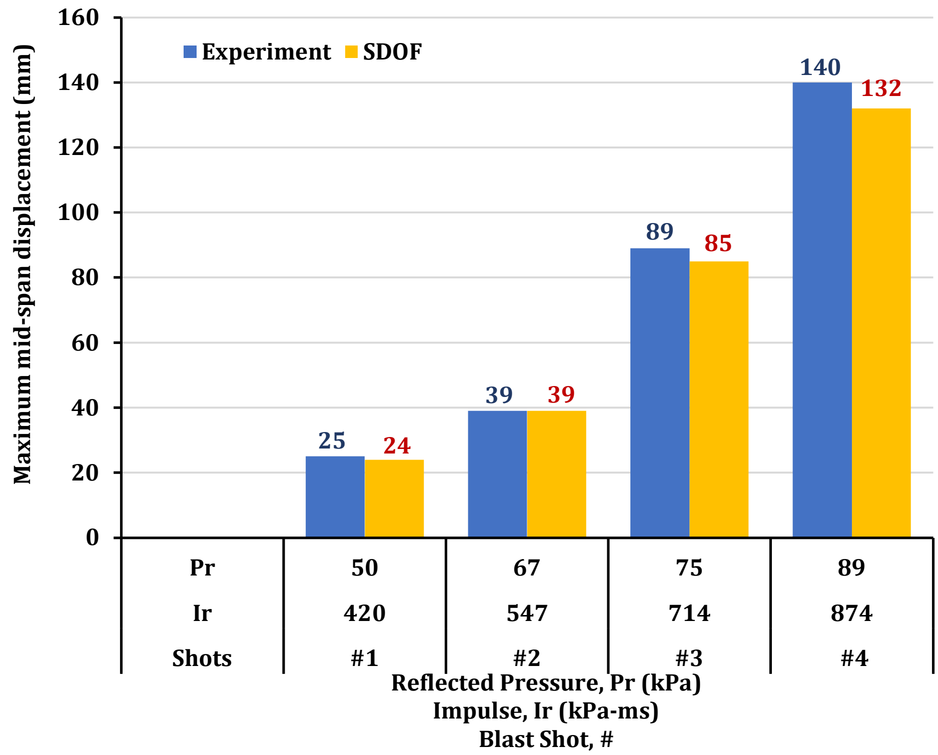

Figure 6.40. Experiment vs SDOF of wall-3

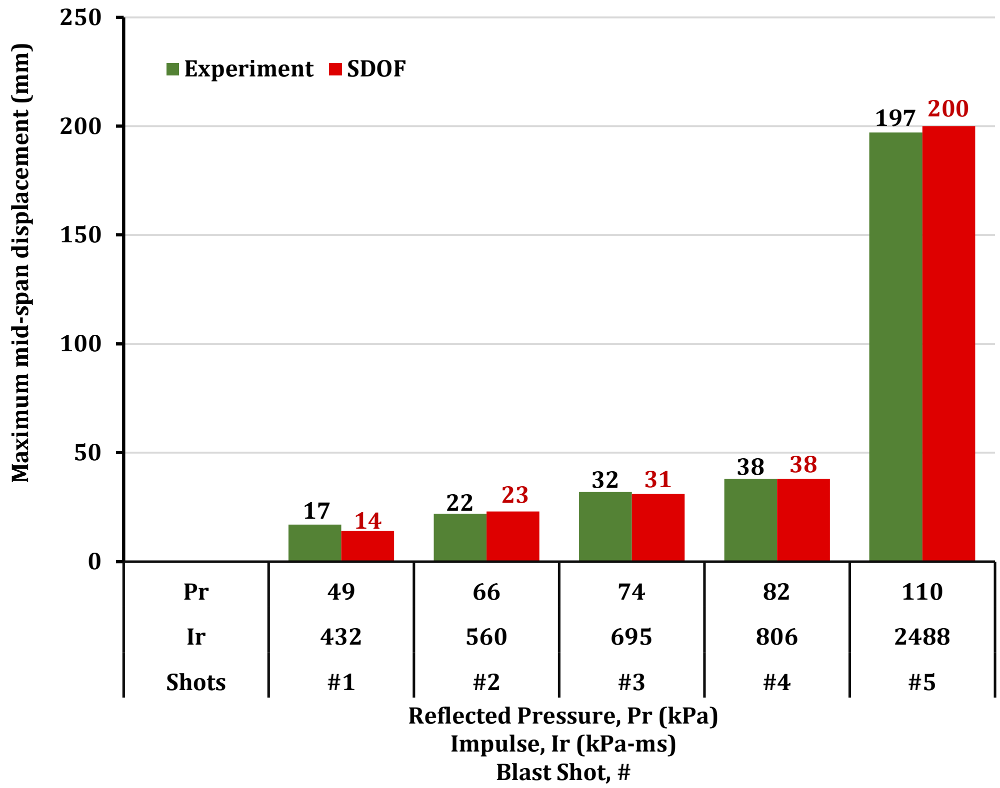

Figure 6.41. Experiment vs SDOF of wall-4

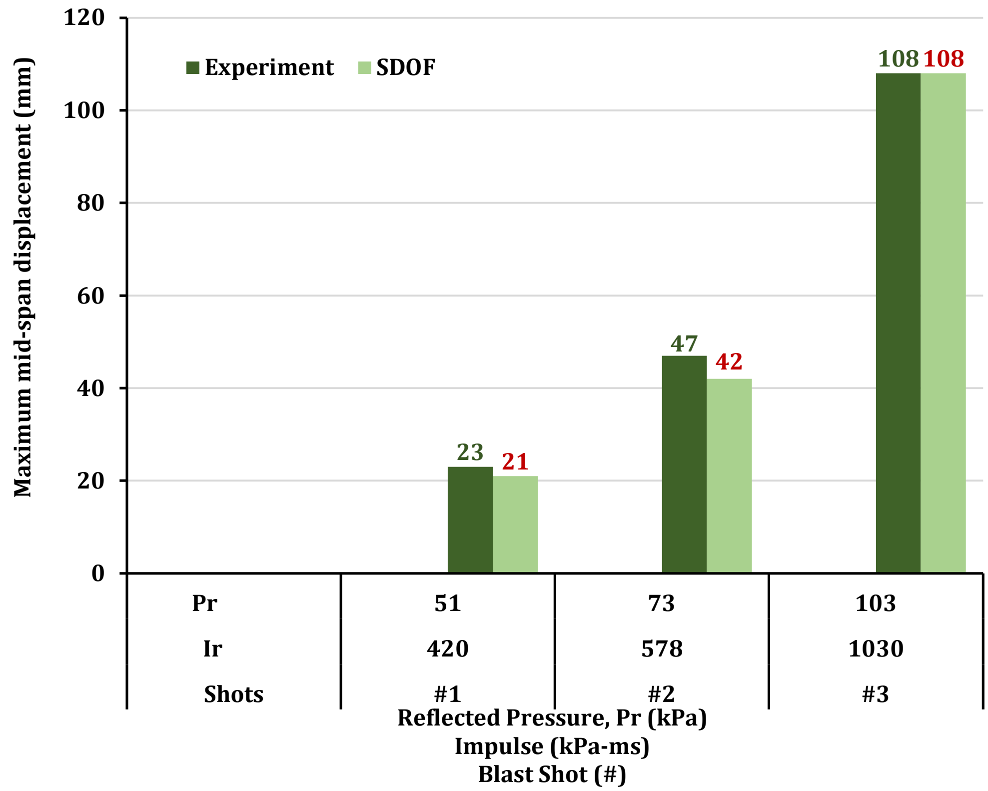

Figure 6.42. Experiment vs SDOF of wall-5

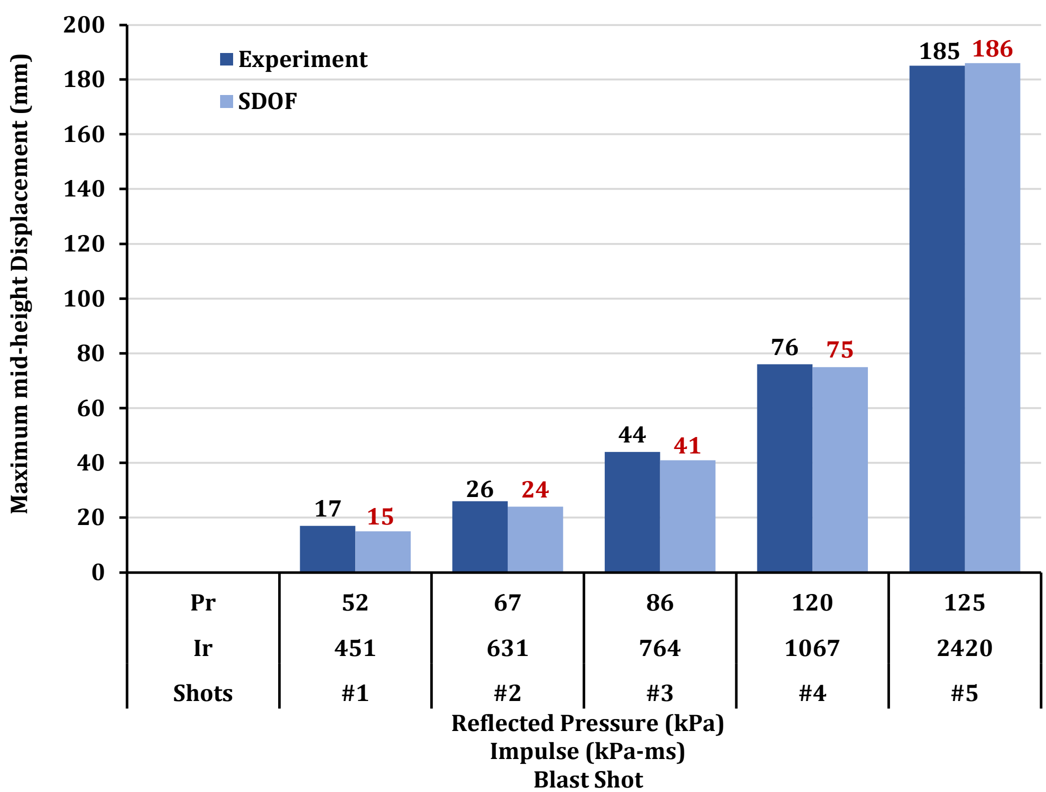

Figure 6.43. Experiment vs SDOF of wall-6

6.4 Parametric Study

An analytical parametric investigation was carried out to expand the experimental observations to walls with properties beyond those tested. The analytical parameters considered included increased percentage of wire mesh reinforcement, increased wall thickness, higher initial axial loads, and different wall aspect ratios. The analysis included the computation of resistance functions, defining strength and stiffness of the walls, and non-linear SDOF dynamic analysis to establish maximum mid-heigh deflections. The results are presented in the proceeding sections.

6.4.1 Increase in Stainless Steel Percentage

A case study of three 140 mm thick CMU walls with 2500 mm height and 3000 mm length was considered. The walls were retrofitted with reinforced polyurea (6.0 mm thick XS-350 polyurea with a SS304 stainless steel wire mesh having square openings of 76.2mm by 76.2mm). Three different wire sizes were considered for the mesh consisting of 4.1 mm, 5.1 mm, and 6.1 mm diameter wires, resulting in three different percentages of steel. The walls were labeled based on the wire size used as Wall-A, Wall-B, and Wall-C with 4.1 mm, 5.1 mm, and 6.1 mm diameter wires, respectively. They were all subjected to a constant axial load of 120 kN as load-bearing walls. The walls were then subjected to a 6056 kg TNT charge weight (a charge weight equivalent to the explosive capacity of a small moving van/delivery truck) with a standoff distance of 86 m.

The resistance functions of the three retrofitted CMU walls were first developed, as shown in Figure 6.44. Subsequently, the resistance functions were used for SDOF analysis using RC-Blast software. Dynamic response was computed up to the maximum mid-height deflections. The results are summarized in Table 6.2 and plotted in Figure 6.45. Wall-A with the smallest percentage of stainless steel, displayed the largest mid-height displacement, while Wall-C, with the highest percentage of steel, responded with the smallest mid-span deflection, as expected. Using a higher percentage of steel resulted in better crack control, increased stiffness, and higher blast load resistance.

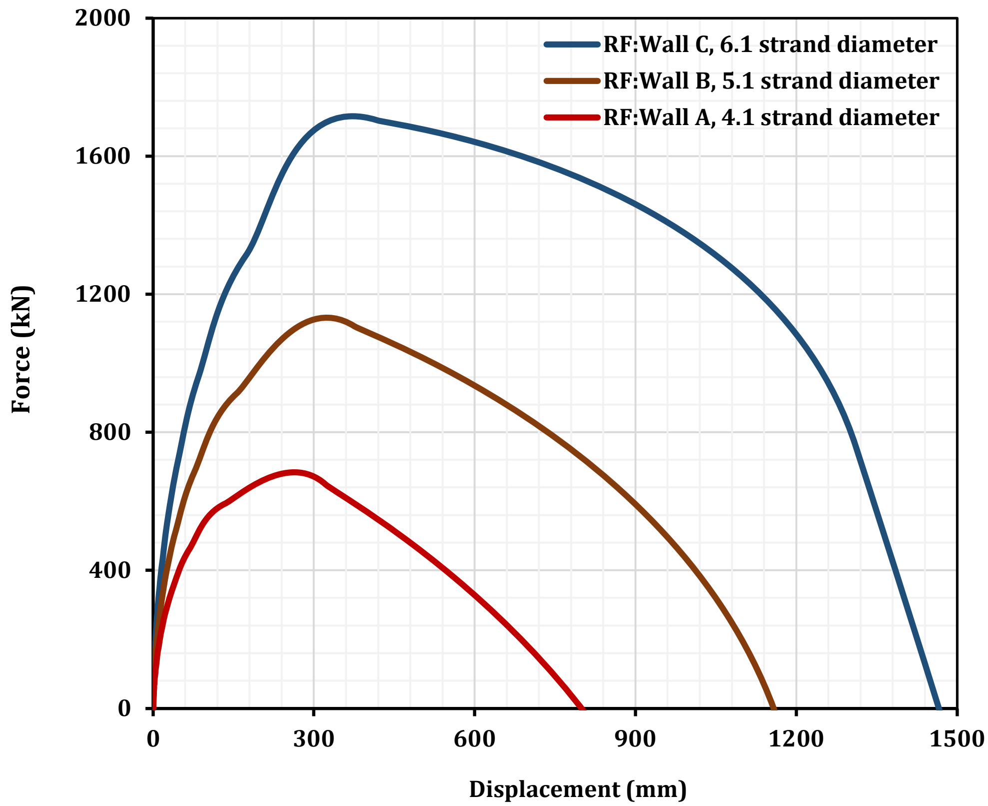

Figure 6.44. Static Resistance Functions of Walls - A, B & C

Table 6.2: Walls with different stainless-steel percentage

Wall sample	**Dynamic mid-height deflections (mm)**		
	Wall A (4.1)	Wall B (5.1)	Wall C (6.1)
Wall A	105		
Wall B		75	
Wall C			53

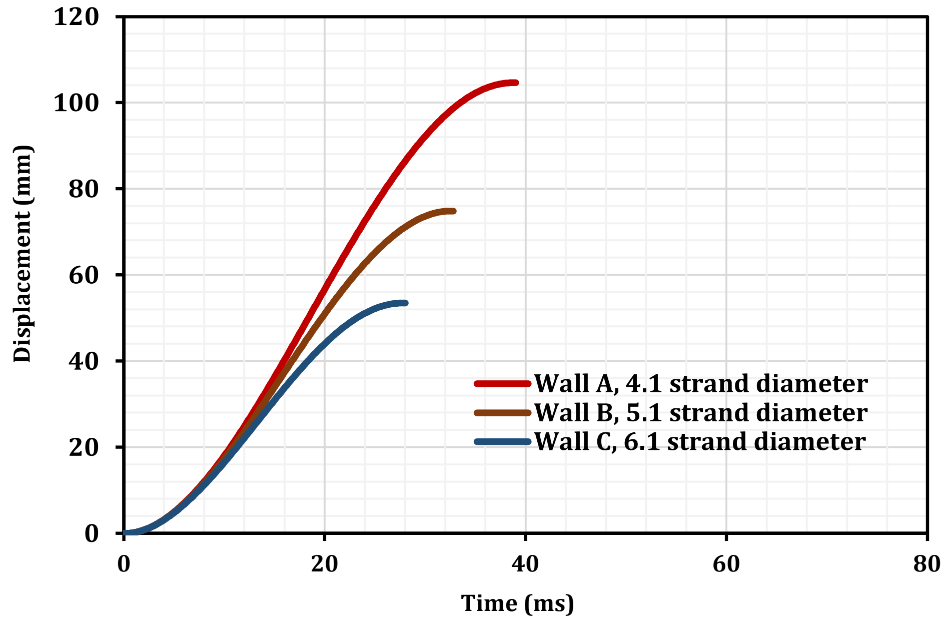

Figure 6.45. Displacement time history of Walls - A, B & C under similar blast load

6.4.2 Varied Wall Thickness

Two walls with two different wall thicknesses but otherwise having the same geometry and retrofit material were analyzed to assess the significance of wall thickness. Both walls had a 2000 mm square surface. The *first wall* (Wall D) had a thickness of 90 mm, resulting in a mass of 1035 kg. The *second wall* (Wall E) had a 140mm wall thickness, resulting in a mass of 1289 kg. Both walls were retrofitted with reinforced polyurea-4.1 mm (6.0 mm thick XS-350 polyurea, reinforced with SS304 mesh with 4.1mm diameter wires forming 76.2mm by 76.2mm grids). The walls were initially loaded with a vertical axial load of 180kN. The blast load applied consisted of a peak reflected pressure of 101 kPa, and a peak reflected impulse of 1863 kPa-ms with a positive phase duration of 37 ms, equivalent to 5080 kg TNT charge weight at a standoff distance of 86 m. Figures 6.46 and 6.47 show the walls' resistance functions and displacement-time histories for comparison. It was observed that the thicker wall exhibited a mid-height displacement of 24 mm, which was about 66% smaller than that displayed by the thinner wall with a displacement of 70 mm. Increasing the wall thickness would effectively work with the reinforced polyurea to greatly improve the wall out-of-plane capacity and stiffness.

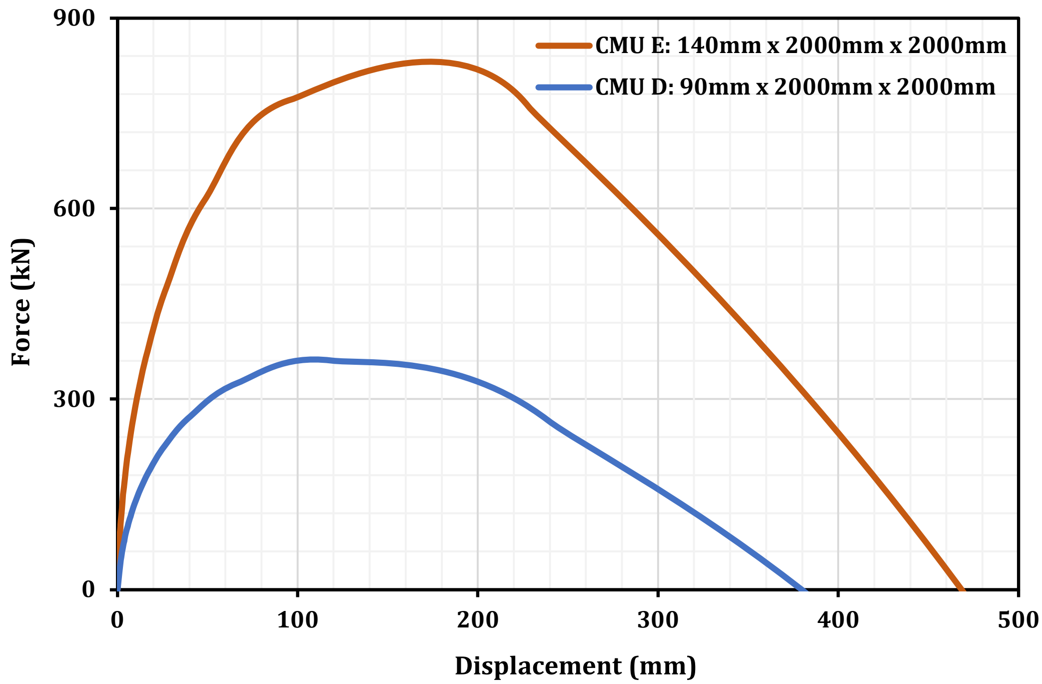

Figure 6.46. Resistant functions of CMU walls with different wall thicknesses under similar blast load

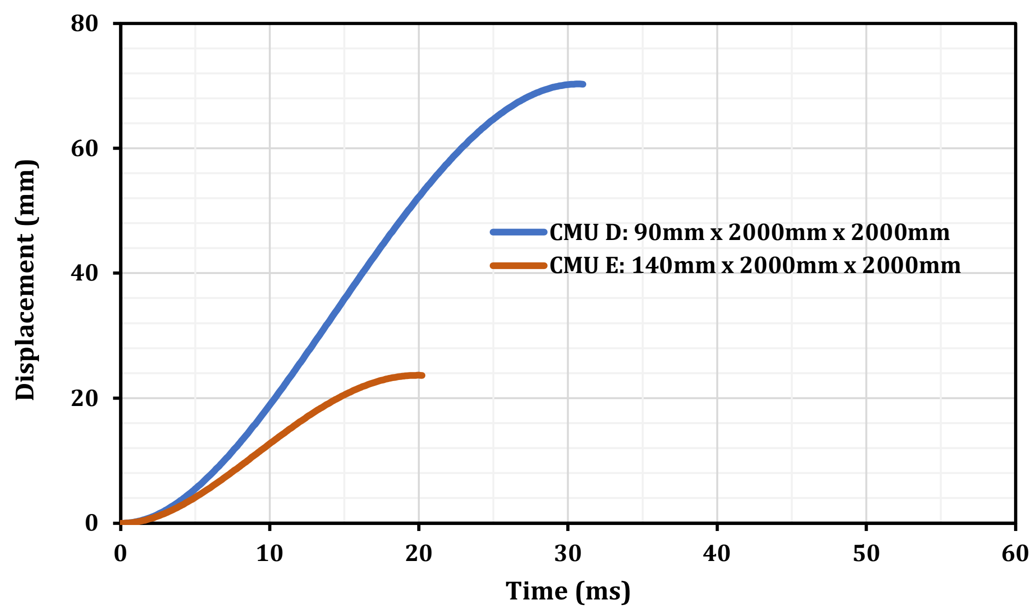

Figure 6.47. Displacement time history of CMU walls with different wall thicknesses under similar blast load

6.4.3 Varied Wall Aspect Ratio

Three walls with the same mass of 2461kg and the same wall thickness of 140 mm but different aspect ratios were modeled and analyzed. The *first wall* had a 3000 mm length and 2500 mm height with an aspect ratio (length-to-height ratio) of 1.2. The *second wall* had a length-to-height ratio of 0.8 with a length of 2500 mm and a height of 3000 mm, and the *third wall* had a length-to-height ratio of 0.6 with a 2143 mm length and a 3500 mm height. All the walls were retrofitted with the same reinforced polyurea-5.1mm (6.0 mm thick XS-350 polyurea, reinforced with SS304 mesh with 5.1mm diameter wires forming 76.2mm by 76.2mm grids). All walls were subjected to an initial axial load of 120kN. They were exposed to a blast load of 6056 kg TNT charge weight with a standoff distance of 86 m, having an average peak reflected pressure of 114 kPa and an average peak reflected impulse of 2003 kPa-ms with a positive phase duration of 35 ms. Their resistance functions and displacement time histories are plotted in Figures 6.48 and 6.49. The results revealed that the *third wall* with the smallest aspect ratio (length-to-height ratio) showed the highest mid-height displacement because of its slenderness. In contrast, the first wall with the largest aspect ratio had the least displacement, having greater stiffness. This implies that the aspect ratio of a wall would influence the percentage of stainless steel to be used in its retrofit membrane, i.e., a wall with a smaller aspect ratio would require a more significant percentage of stainless steel and vice versa to resist a specified design blast load.

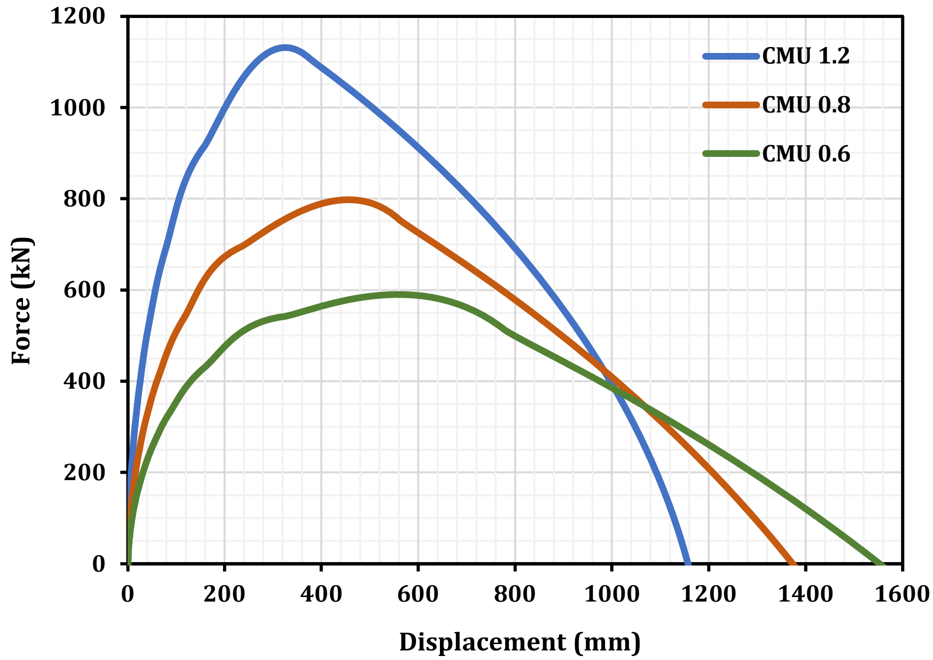

Figure 6.48. Resistant functions of CMU walls of similar surface area with varied aspect ratios subjected to the same blast load.

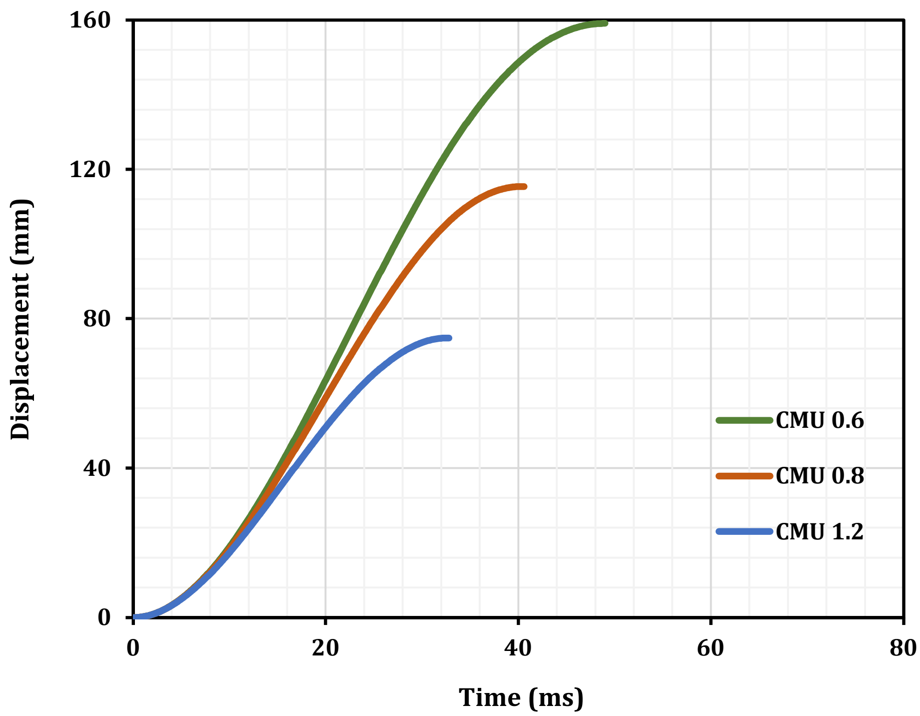

Figure 6.49. Displacement time histories of CMU walls of similar surface area with varied aspect ratios subjected to the same blast load

6.4.4 Varied Axial Loading

Three walls of the same mass of 2461kg and the same aspect ratios were modeled. The *walls* had dimensions of 140 mm thickness, 2500 mm length, and 3000 mm height with an aspect ratio of 0.8. All the walls were retrofitted with the same reinforced polyurea-5.1 mm. The *first wall* was axially loaded with 120 kN, the *second* with 180 kN, and the third with 240 kN. The walls were exposed to a blast load of 6056 kg TNT charge weight with a standoff distance of 86 m, having an average peak reflected pressure of 114 kPa and an average positive phase reflected impulse of 2003 kPa-ms with a positive phase duration of 35 ms. Their resistance functions and displacement-time histories are given in Figures 6.50 and 6.51. The results revealed that the *first wall* with the *smallest axial* loading exhibited the largest mid-height displacement. In contrast, the third wall with the highest axial load had better crack control, increased wall stiffness, and showed the least deflection. This implies that the axial load applications on walls would influence the percentage of stainless steel to be used in the retrofit membrane, i.e., a wall with smaller axial loading would require a more significant percentage of stainless-steel mesh because of the increased flexural force demands under lower axial loads and vice versa for a given blast threat scenario.

6.5 Conclusions of Parametric Study

The analytical parametric study reported in the preceding section demonstrates the significance of primary design parameters. Among the four parameters considered for URM walls (percentage of steel in polyurea, wall thickness, wall aspect ratio, and the level of initial axial load), the wire mesh steel percentage provided in polyurea, and the wall thickness play the most significant roles as they directly affect the wall sectional capacity in flexure by increasing the magnitude of internal force couple. The wall aspect ratio (length-to-height-ratio) in flexural members behaving in one-way mode reflects the effects of two factors, i.e., the effect of wall height as it is directly a function of the flexural moment demands and the period of the wall, which varies with stiffness (height) and mass in terms of their dynamic resistance. The mass was kept constant. However, the change in wall height (L) would affect the moment demand by L^2, whereas the wall period would be affected by $\sqrt{L^3}$ impacting the dynamic increase factor and the deflection response. For the cases considered under the same blast load used, the decrease in wall height, going from an aspect ratio of 0.6 to 1.2, resulted in a factor of approximately 2.0 in both decrease in moment demands and reduction in maximum deflection. However, for different combinations of wall geometry and blast load characteristics, this change in response can be different and, hence, must be considered when performing dynamic analysis for design. Finally, it was shown that the initial wall load increases the stiffness and delay cracking, which also influences arching forces. Most load-bearing masonry walls are exposed to relatively low axial forces compared to their concentric capacity. While these walls behave under combined axial compression and flexure, the level of axial compression is usually below that, corresponding to the balance section axial load; hence, flexure plays a dominant role. For walls that develop arching action, the level of axial compression increases, potentially causing the crushing of the masonry. In the range of initial axial load considered in the parametric study, the effect of the axial load was to increase the flexural capacity and, hence, the wall resistance. An increase in initial vertical load by a factor of 2.0 resulted in an increase of 1.25 in wall resistance. Although this parameter affected the wall dynamic response the least, it is important to consider it in the design for improved accuracy of results and to rule out the possibility of masonry crushing.

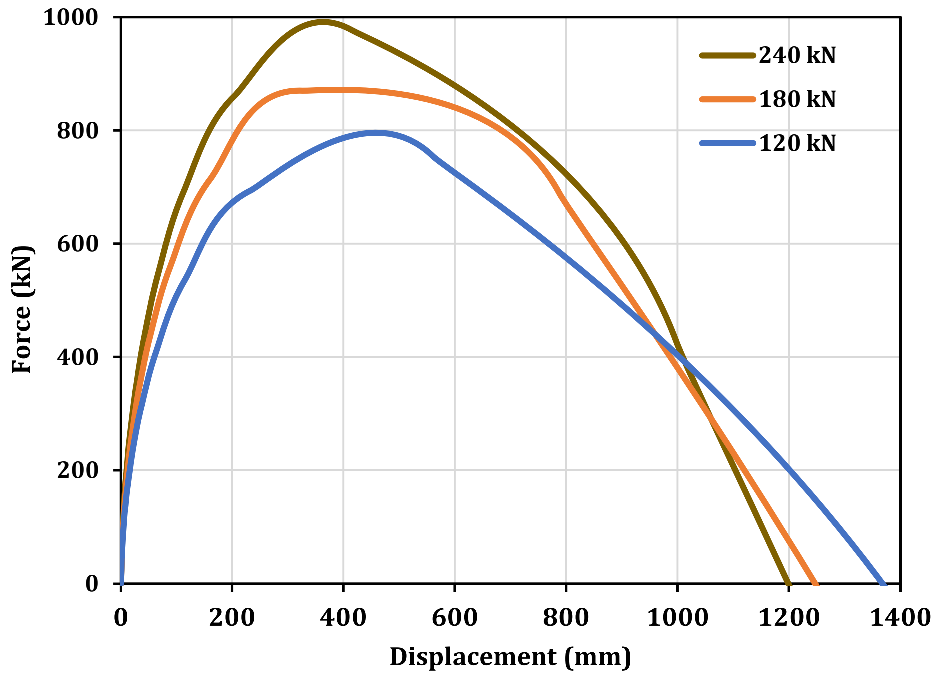

Figure 6.50. Resistant functions of CMU walls of similar surface area with varied axial loading subjected to the same blast load

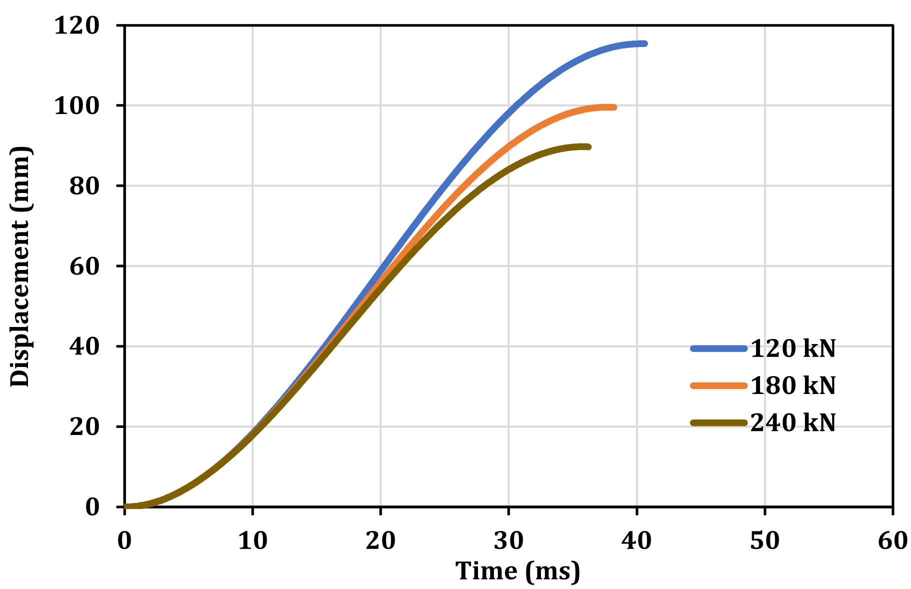

Figure 6.51. Displacement time histories of CMU walls of similar surface area with varied axial loading subjected to the same blast load

6.6 Retrofit Design Procedure

The results of the experimental research presented in Chapters 3, 4, and 5, as well as those generated analytically in the parametric study presented in Chapter 6, provide ample design information to develop a retrofit design procedure for reinforced polyurea to be applied to URM walls. Both stone and CMU masonry walls were considered with and without initial vertical loads (load-bearing and non-load bearing/infill walls). It was observed that reinforced polyurea is an effective blast retrofit (hardening) material, especially when bonded to a wall. Reinforcement in wire mesh increases strength and stiffness, transforming URM walls into reinforced masonry. An important aspect of this externally placed reinforcement is the ability to bond to the masonry surface and form a composite material. This is ensured by a spray-on polyurea, which has the required characteristics to bond the mesh reinforcement. This current experimental research proves that Polyurea also has a very important function. Masonry walls subjected to blast loads pose two types of vulnerabilities: i) those associated with wall failure and ii) those associated with fragmentation and flying projectiles towards occupied areas of the bullet, moving at supersonic velocities. In addition to providing a bond between the mesh reinforcement and the masonry, the polyurea keeps masonry units together under excessive deformations, facilitating continued arching action while controlling fragmentation. These benefits of the material have been observed during the experiments under simulated blast loads, as reported earlier. The flexibility of the polyurea provides the ability to maintain the integrity of masonry at high deformations, combined with the ductility of steel mesh, results in an ideal combination of materials for blast risk mitigation. The polyurea used in the current investigation had a tensile rupturing strain of over 150 %, as illustrated in Figure 3.11.

Another factor in attaining the required inelastic deformability/ductility of the walls is the type of steel used in the mesh. In this current research project, a wire mesh with stainless steel wires was selected because of the inherent ductility of this type of steel. The tensile rupturing strain of the stainless-steel wires was more than 40%, as illustrated in Figure 3.13. Hence, stainless steel reinforced polyurea increases the walls out-of-plane strength, stiffness, and energy absorption capacity.

An important step towards developing a design procedure was validating the SDOF inelastic dynamic analysis procedure for use in design. This required the construction of the resistance function for masonry walls with a polyurea-reinforced hardening material. This was achieved by implementing the approach used by Moradi et al. (2008). The resistance function provided the required stiffness values during inelastic response. The SDOF analysis with the developed resistance functions provided good correlations with the recorded test data in this research experimental phase, as illustrated in Chapter 6. The analytical parametric study expanded the design parameters beyond the scaled test walls and generated additional design data on the effects of design parameters.

The design information generated by the combined experimental and analytical investigations reported in the previous chapters was used to develop the following design procedure for polyurea-reinforced masonry walls as a blast retrofit (hardening) technique.

- <u>Determination of the materials:</u> The XS-350 spray-on polyurea of 6mm thickness and SS304 mesh (with a minimum strand diameter of 4.1mm) should be used. The percentage of mesh reinforcement required can be increased to have a higher internal force couple at the critical section to resist the flexural moment demands obtained from dynamic analysis. The upper limit for reinforcement can be established by considering the crushing of masonry under increased compression due to the combined effects of initial axial load, flexural compression, and arching action.

- Axial load: The design procedure applies to non-load bearing infill and load-bearing walls. When an infill wall is retrofitted, the gap between the wall and the enclosing structural element (e.g., beam, slab) should be filled with high-strength grout to facilitate the early development of the arching forces. However, judgment must be exercised to prevent potentially detrimental effects of the deflection of the top structural element toward the wall. Axial load on load bearing must be applied before dynamic analysis.
- Support Condition: Most URM walls have simple support. However, if there is end restraint for the wall, this should be considered in developing the wall resistance function.
- Development of Resistance Function: Computing the resistance function is an important step towards establishing a dynamic response through dynamic analysis in the design process. The procedure developed by Moradi et al., 2008, can be used to establish the resistance function with the effects of arching action, initial vertical load, and the membrane action while assuming fully bonded reinforced polyurea. Details of the steps are provided in Section 6.2
- SDOF Inelastic Dynamic Analysis: The SDOF dynamic analysis can be conducted through computer software, incorporating the resistance function and the design basis threat as blast pressure-time relationship. All geometric properties, including wall dimensions, support conditions, mass, and time increment for numerical integration, are entered as required data. The output is the displacement-time history

curve, which determines the response of the wall-retrofit system to blast loads. The maximum wall displacement can be used to compute support rotation and/or ductility ratios to establish the level of damage based on the response limits specified in codes and standards. These damage levels are used to assess if the desired level of protection is used in the design. The design standard adopted here is the CSA Standard S850, "Design and Assessment of Buildings Subjected to Blast Loads." Because the retrofitted walls predominantly respond in the flexure mode, Table 6.3, adapted from CSA S850, can establish the wall response relative to the response limits B1 through B4 given in the Table. In the absence of data that relates support rotations to damage levels for reinforced polyurea masonry walls, the wall response can be associated conservatively with damage levels given in Table 6.4. These damage levels lead to levels of protection (LOP) of the building for which the design is performed. Table 6.5 provides LOPs for primary and secondary structural elements and non-structural elements. If the retrofitted masonry wall is a load-bearing wall, it qualifies as a primary structural element, the damage of which can significantly affect the overall building response leading to damage to the other elements. The secondary structural elements are load-carrying elements whose damage does not lead to the damage of the other elements. Infill and non-load bearing walls are "non-structural elements" in the Table.

- <u>Iterative Design Approach:</u> Design for blast loads involves an *iterative design approach*. The member in question (before or after the retrofit) establishes the *resistance function*, which provides strength and stiffness. The resistance function is used in SDOF analysis, from which member response is found. Suppose the response is not adequate for the required LOP. In that case, the characteristics of the reinforced polyurea are changed for a stronger and/or more rigid element so that in subsequent trials, the member remains within the response limits for the desired LOP.

Table 6.3 Response limits for reinforced polyurea masonry wall

Response Limit	B1	B2	B3	B4
Ductility Ratio (μ)	1.0	-	-	-
Support Rotation (θ)	-	2^{o}	2^{o}	2^{o}

Table 6.4 Damage associated with response limits

Component Damage Level	Relationship to Response Limits
Blowout	Response greater than B4.
Hazardous Failure	Response between B3 and B4
Heavy Damage	Response between B2 and B3.
Moderate Damage	Response between B1 and B2.
Superficial Damage	Response is less than B1.

Table 6.5 Building performance levels/levels of protection (LOP)

Building Performance (Level of Protection)	Component Damage		
	Primary Components	Secondary Components	Non-Structural Components
Collapse Prevention (Very Low)	Heavy	Hazardous	Hazardous
Life Safety (Low)	Moderate	Heavy	Heavy
Immediate Occupancy (Medium)	Superficial	Moderate	Moderate
Operational (High)	Superficial	Superficial	Superficial

CHAPTER 7 CONCLUSION

7.1 Summary

Combined experimental and analytical research was conducted to assess the blast response of masonry walls retrofitted with reinforced polyurea. The experimental research consisted of six masonry walls, four built with CMU and the remaining two built with stone masonry. They were retrofitted/hardened with spray-on polyurea and steel mesh. The steel mesh (SS304) had either 4.1 mm or 3.1 mm diameter stainless steel wires with a uniform grid opening size of 76.2 mm by 76.2 mm. The walls were classified into two groups: non-load bearing infill walls and load-bearing walls. Table 3.1 describes the test specimens. They were tested under blast shock waves using a blast simulator (shock tube) at the University of Ottawa to assess their performance. Each wall was subjected to incrementally increasing shock waves under different pressure-impulse combinations as summarized in Tables 4.3 to 4.8. The reflected pressure, reflected impulse, and displacement time histories were recorded during each test and analyzed to assess the effect of test parameters. The test parameters consisted of masonry type, the effect of initial axial load, mesh wire size, and the effectiveness of reinforced polyurea.

Analytical research consisted of the computation of resistance functions, including the effect of arching action and the reinforced polyurea. The resulting stiffness values were used to conduct SDOF dynamic inelastic analyses to validate the procedure. The analyses were extended into an analytical parametric study to generate additional data on the effects of design parameters. The analytical parameters considered included increased percentage of wire mesh reinforcement, increased wall thickness, higher initial axial loads, and different wall aspect ratios. The experimental and analytical observations made resulted in the development of a design procedure for reinforced polyurea hardening of masonry walls.

7.2 Conclusions

The following conclusions were drawn from the research project presented in this thesis:

- Reinforced polyurea, consisting of stainless steel wire mesh with spray-on polyurea, is an effective material for blast hardening of URM walls with CMU or stone masonry units. The reinforced polyurea bonds well with masonry and forms a composite action between the external mesh reinforcement and the masonry wall. The walls hardened with reinforced polyurea develop higher out-of-plane blast resistance and fragment control when compared with unhardened walls. Reinforced polyurea was observed to remain intact and fully bonded to the masonry during blast tests until the yielding of reinforcement occurred at the critical mid-height section, after which the polyurea ruptured.
- Using a higher percentage of steel mesh results in higher crack control, and increased wall stiffness and blast load resistance. An increase in the percentage of steel by a factor of 2.2 has resulted in an increase of a factor of 2.6 in wall resistance and a reduction in maximum wall displacement by a factor of 2.0. The use of a low percentage of steel promotes early yielding at the critical mortar joint at mid-height, followed by early tearing of the polyurea. Hence, an appropriate amount of mesh reinforcement should be provided proportional to the design basis threat (DBT) level considered in the design, up to the wall capacity controlled by the crushing of masonry in compression.

- The wall failure mode can be described as a hinged-arched type collapse, a behavior facilitated by the arching action of the restraining frame and the initial axial load if present. The presence of reinforced polyurea, fully bonded on masonry, develops a concentration of highly localized strains along the bed joints where cracks develop. As such, the polyurea was observed to tear along the critical mid-height mortar joint, with a capacity dependent on the percentage of steel. The use of a higher steel percentage delays failure, with increased wall strength and stiffness, and hence is an important parameter to be considered in design.
- The use of mesh reinforcement in polyurea, as opposed to the polyurea alone considered in an earlier investigation by Ciornei (2012), provides a significantly higher out-of-plane wall strength and stiffness.
- Wire mesh in polyurea should be extended and anchored to the supporting slabs or beams above and below.
- The reinforced polyurea's efficient energy absorption capacity associated with the high elongation capacity of stainless steel used results in ductile response when compared with brittle failure of unhardened walls.
- The type of masonry units used in walls, i.e. CMU versus stone, does not have a significant effect on wall behavior. This is true if an uncoursed pattern of laying is used in stone masonry. The coursed pattern of stone masonry may result in premature failure along the continuous critical mortar joint.
- The effect of initial axial compression on walls (load bearing wall) is to delay cracking and increase the wall strength and stiffness.

- Increased wall thickness and/or wall aspect ratio (height-to-length ratio) result in increased wall capacity due to the increased sectional capacity and increased shear span, respectively.
- Masonry walls hardened with reinforced polyurea can be modeled and analyzed as SDOF elements. Such analyses show good agreement of mid-height deflections when validated against test data under blast loads provided that the resistance functions incorporate the appropriate material models and the effects of arching/axial forces. Hence, SDOF is an effective tool for design purposes. Despite the generally good agreement obtained between the tests and the SDOF analyses, some discrepancy does exist between the two results in a few walls where the failure crack location observed was at a location other than the mid-height section assumed in the analytical model.
- The method of computing the force-deformation relationship of masonry walls, proposed by Moradi et al., (2008), provides a suitable approach in establishing resistance functions of masonry walls retrofitted with reinforced polyurea membrane.
- The hardening methodology developed in the current research project and the proposed design procedure can be used in blast-resistant buildings as façade elements in both existing and new construction.

7.3 Recommendations for Future Research

The following additional experimental and analytical research is recommended to expand the results obtained in the current research project for wider application in practice.

- Additional blast tests using ordinary welded wire mesh (as opposed to the stainless-steel wires used in the current study) of different percentages to assess additional ductility associated with stainless steel.
- Additional blast tests with different wall thicknesses and aspect ratios.
- Blast tests of reinforced polyurea-hardened walls with SS304 mesh oriented at 45^0 or 60^0 to investigate the effectiveness of inclined reinforcement.
- Blast tests of masonry walls with wire mesh used as a catchment system without the polyurea.
- Finite Element Analysis (FEA) of hardened masonry walls with fully bonded reinforced polyurea subjected to blast loads and comparison with the SDOF analysis.

REFERENCES

Abass, B. (2013). Blast Load Effects on Historic Masonry Buildings. Defence Research and Development Canada. DRDC CSS CR 2013-045.

Abou-Zeid, B. M., El-Dakhakhni, W. W., Razaqpur, A. G., Rosen, B.V., & Foo, S. (2011). Response of Arching Unreinforced Concrete Masonry Walls to Blast Loading. Journal of Structural Engineering, 137(10), 1205-1214.

Aghdamy. S., Wu, C., & Griffith, M. (2013). Simulation of Retrofitted Unreinforced Concrete Masonry Units Walls under Blast Loading. International Journal of Protective Structures, 4(1), 21-44. https://doi.org/10.1260/2041-4196.4.1.21

Alameer, A.M. (2020). Performance and Design of Retention Anchors in Blast Resistant Windows (Doctoral dissertation, University of Ottawa).

Al-Bayti, A. (2017). Vulnerability of Reinforced Concrete Columns to External Blast Loading. Ottawa-Carleton Institute for Civil Engineering.

American Society for Testing and Materials. (2012). Standard Guide for Repointing (Tuckpointing) History Masonry, E2260-03, ASTM international, West Conshohocken, PA.

Baer, B.R. (n.d). New Specification for the Design of Structural Stainless Steel. Structure Magazine.

Baddoo N.R., Burgan B.A. (2001). Structural design of stainless steel. SCI Publication P291, The Steel Construction Institute, Ascot.

Bazhenov, V.G., Kibetz, A.I., & Kruszka, L. (2012). Finite Element Analysis of 3-D Problems of Deformation and Failure of Masonry under Explosive Loading. International Journal of Protective Structures, 3(4). https://doi.org/10.1260/2041-4196.3.4.449

Biggs. J.M. (1964). Introduction to Structural Dynamics. New York: McGraw-Hill Book Company

Canadian Standard Association, CSA A165.1 (2004). CSA Standard on Concrete Masonry Units, Series-04, CSA, Mississauga, ON.

Cengiz, O., & Turanli. L. (2004). Comparative Evaluation of Steel Mesh, Steel Fibre and High-Performance Polypropylene Fibre Reinforced Shotcrete in Panel Test. Cement and Concrete Research, 34: 1357-1364.

Ceylan. S. (2014). Comparative evaluation of steel mesh, steel fiber and high-performance polypropylene fiber-reinforced concrete in panel/beam tests. Civil Engineering Department, Middle East Technical University.

Chen. L., Fang. Q., Fan. J., Zhang. Y., Hao. H., & Liu. J. (2014). Responses of Masonry Infill Walls Retrofitted with CFRP, Steel Wire Mesh and Laminated Bars to Blast Loadings. Sage journals: Advances in Structural Engineering, 17(6). https://doi.org/10.1260/1369-4332.17.6.817

Chiquito. M., Castedo. R., Santos. A. P., Lopez. L. M. & Perez-Caldentey. A. (2021). Numerical modelling and experimental validation of the behavior of brick masonry walls subjected to blast loading. International Journal of Impact Engineering, 148, 103760. https://doi.org/10.1016/j.ijimpeng.2020.103760

Chopra. A. K. (2001). Dynamics of Structures, Prentice-Hall, New Jersey.

Ciornei, L. (2012). Performance of polyurea retrofitted unreinforced concrete masonry walls under blast loading (master's thesis, Ottawa-Carleton Institute for Civil Engineering).

Committee on Feasibility of Applying Blast-Mitigating Technologies and Design Methodologies from Military Facilities to Civilian Buildings. Board on Infrastructure and the Constructed Environment; Commission on Engineering and Technical Systems; National Research Council. (1995). Protecting buildings from damage: transfer of blast-effects mitigation technologies from military to civilian applications. National Academy Press, Washington, D.C.

Canadian Standards Association. (2014). Fired masonry brick made from clay or shale (CSA A82:14 (R2023)). Mississauga, ON: CSA Group.

Canadian Standards Association. (2014). CSA Standards on concrete masonry units (CSA A165 SERIES:14 (R2024)). Mississauga, ON: CSA Group.

Canadian Standards Association. (2014). Mortar and grout for unit masonry (CAN/CSA A179-14 (R2024)). Mississauga, ON: CSA Group.

Canadian Standards Association. (2014). Design of masonry structures (CSA A304-14(R2019)). Mississauga, ON: CSA Group.

Canadian Standards Association. (2014). Connectors for masonry (CSA A370:14 (R2023)). Mississauga, ON: CSA Group.

Canadian Standards Association. (2014). Masonry construction for buildings (CSA A371:14 (R2024)). Mississauga, ON: CSA Group.

Canadian Standards Association. (2004). Portable Elevating Work Platforms (CAN/CSA-B354.1-04 (R2016)). Mississauga, ON: CSA Group.

Canadian Standards Association. (2023). Design and assessment of buildings subjected to blast loads (CSA S850:23). Mississauga, ON: CSA Group

Davidson, J. S., Fisher, J. W., Hammons, M. I., Porter, J. R., & Dinan, R. J. (2005). Failure mechanisms of polymer-reinforced concrete masonry walls subjected to blast. Journal of Structural Engineering-ASCE, 131(8), 1194-1205. Retrieved Aug, from Article database.

Davidson, J.S., Moradi, L.G., & Dinan, R.J. (2004). Selection of a Material Model for Simulating Concrete Masonry Walls Subjected to Blast (Accession No. ADA447920). Defense Technical Information Center.

Davidson. S. J., Sudame, S., & Dinan, R. J. (2004). Development of Computational Models and Input Sensitivity Study of Polymer Reinforced Concrete Masonry Walls subjected to Blast. Air Force Research Laboratory Materials and Manufacturing Directorate Airbase Technologies Division, Tyndall AFB, FL 32403-5323.

Davidson, J. S., Porter, J. R., Dinan, R. J., Hammons, M. I., & Connell, J. D. (2004). Explosive testing of polymer retrofit masonry walls. Journal of Performance of Constructed Facilities 18(2), 100-106. Retrieved May, from Article database.

Design Manual for Structural Stainless Steel, 4th Edition-Commentary.

Dinan, R. (2005). Blast Resistant Steel Stud Wall Design. Doctoral Dissertation, University of Missouri, Department of Civil Engineering, Columbia, MO 65211-2200.

Dinan, R., Fisher, J., Hammons, M. I., & Porter, J. R. (2003). Failure mechanisms in unreinforced concrete masonry walls retrofitted with polymer coatings. Air Force Research Lab Tyndall AFB FL.

Dinesh, R., Vasundra, P., & Davidson, D. J. (2020). A Finite Element Analysis Based Study on Effects of Polyurea Coating for Blast Mitigation. IOP Conference Series: Materials Science and Engineering. Doi:10.1088/1757-899X/1128/1/012046

Drysdale, R., & Hamid, A., (2005). Masonry Structures: Behavior and Design. Canadian Edition. Canada Masonry Design Centre, Mississauga, Ontario.

El-Domiaty, K. A., Myers, J. J., & Belarbi, A. (2002). Blast Resistance of Un-Reinforced Masonry Walls Retrofitted with Fiber Reinforced Polymers. Center for Infrastructure Engineering Studies Report 02-28, University of Missouri – Rolla, Rolla, MO.

ElGawady, M. A., Lestuzzi, P., & Badoux, M. (2007). Static Cyclic Response of Masonry Walls Retrofitted with Fiber-Reinforced Polymers. Journal of Composite for Construction © ASCE. DOI: 10.1061/(ASCE)1090-0268(2007)11:1(50)

Felice, G. (2011). Out-of-Plane Seismic Capacity of Masonry Depending on Wall Section Morphology. International Journal of Architectural Heritage,5(4-5),466-482.

Gagnet, E. (2013). Static Resistance Functions for Unbonded Retrofit Unreinforced Concrete Masonry Walls with Plate Connection for Blast Design Applications (MS thesis, Auburn University).

Gagnet, E. M., Hoemann, J. M., & Davidson, J. S. (2017). Assessment of resistance definitions used for blast analysis of unreinforced masonry walls. International Journal of Protective Structures, 8(1), 125-151.

Gardner, L. (2005). The Use of Stainless Steel in Structures. Progress in Structural Engineering and Materials, 7(2),45-55.

Godio, M., Portal, N.W., Flansbjer, M., Magnusson, J., & Byggnevi, M. (2021). Experimental and Numerical Approaches to Investigate the Out-of-Plane Response of Unreinforced Masonry Walls subjected to Free Far-Field Blasts. Engineering Structures 239(112328). DOI: 10.1016/j.engstruct.2021.112328

Hrynyk, T., & Myers, J. J. (2008). Out-of-Plane Behavior of URM Arching Walls with Modern Blast Retrofits: Experimental Results and Analytical Model. Journal of Structural Engineering. DOI: 10.1061/(ASCE)0733-9445(2008)134:10(1589)

Hoemann. J., Davidson. J., Dinan. R., & Bewick. B. (2010). Boundary Condition Behavior and Connection Design for Retrofitted Unreinforced Masonry Walls Subjected to Blast Loads. Proceedings of Structures Congress, May 12-15, Orlando, Florida.

Irshidat, M., Al-Ostaz, A., Cheng, A., & Mullen, C. (2009). Blast Resistance of Unreinforced Masonry (URM) Walls Retrofitted with Nano Reinforced Elastomeric Materials. Structure Congress: Don't Mess with Structural Engineers: Expanding Our Role. https://doi.org/10.1061/41031(341)234

Irshidat, M., Al-Ostaz, A., Cheng, A. H. D., & Mullen, C. (2010). Nanoparticle Reinforced Polymer for Blast Protection of Unreinforced Masonry Wall: Laboratory Blast Load Simulation and Design Models. Journal of Structural Engineering-ASCE, 137(10), 1193-1204. Retrieved Oct, from Article database.

Iqbal, N., Tripathi, M., Parthasarathy, S., Kumar, D., & Roy, P.K. (2016). Polyurea Coatings for Enhanced Blast-Mitigation: A Review. Royal Society of Chemistry, RSC Advances, 6, 109706-109717. DOI: 10.1039/C6RA23866A

Jacques, E., Lloyd, A., & Saatcioglu, M. (2013). Predicting Reinforced Concrete Response to Blast Loads. Canadian Journal of Civil Engineering, 40(5). https://doi.org/10.1139/L2012-014

Johnson, C. F., Slawson, T. R., Cummins, T. K., & Davis, J. L. (2004). Concrete Masonry Unit Walls Retrofitted with Elastomeric Systems for Blast Loads. Engineer Research and Development Center Vicksburg MS.

Johnson, C.F. (2013). Concrete Masonry Wall Retrofit Systems for Blast Protection (Doctoral dissertation, Texas A & M University).

Kiger, S. & Salim, H. (1998). Use and Misuse of Structural Damping in Blast Response Calculations, Concrete and Blast Effects, ACI Special Publication SP-175, 121-130.

Korany Yasser. (2010). Design of Unreinforced Masonry According to the Canadian Standards. Mauerwerk 14, Heft 6.

Knox, K. J., Hammons, M. I., Lewis, T. T., & Porter, J. R. (2000). Polymer materials for structural retrofit. Tyndall AFB: Force Protection Branch, Air Expeditionary Forces Technology Division, Air Force Research Laboratory.

Lefebvre, C. (2009). A Guide to Working with The Federal Heritage Buildings Review Office. Parks Canada.

Lee, J., Li, C., Oh, S., Yang, W., & Yi, W. (2008). Evaluation of Rocking and Toe Crushing Failure of Unreinforced Masonry Walls. Advances in Structural Engineering, 11(5).

Lee, W., & Lin, C. (2001). Impact Properties and Microstructure Evolution of 304L Stainless Steel. Materials Science and Engineering, A308:124-135.

Li, J., & Wu. C. (2007). Experimental Study on Steel Wire Mesh Reinforced Concrete Slabs against Close-in Detonations. Centre for Built Infrastructure Research, School of Civil and Environmental Engineering, University of Technology Sydney, Australia.

Lloyd, A. (2010). Performance of Reinforced Concrete Columns under Shock Tube Induced Shock Wave Loading (master's thesis, University of Ottawa).

Lunn, D.S., & Rizkalla, S.H. (2011). Strengthening of Infill Masonry Walls with FRP Materials. Journal of Composites for Construction, 15(2), 206-214.

McDowell, E. L., McKee, K. E., & Sevin, E. (1956). Arching Action Theory of Masonry Walls. Journal of the Structural Division: Proceedings of the American Society of Civil Engineers, 82(2), 1-8.

Mohammad. A., Zahra. T., Thamboo. J. & Song. M. (2022). Finite element modeling of reinforced masonry walls under axial compression. Engineering Structures, 152, 113594. https://doi.org/10.1016/j.engstruct.2021.113594

Moradi, L.G., Davidson, J.S., & Dinan, R.J. (2008). Resistance of Membrane Retrofit Masonry Walls to Lateral Pressure. Journal of Performance of Constructed Facilities. 22(3). https://doi.org/10.1061/(ASCE)0887-3828(2008)22:3(131)

Moradi, L.G., Davidson, J.S., & Dinan, R.J. (2009). Response of Bonded Membrane Retrofit Concrete Masonry Walls to Dynamic Pressure. Journal of Performance of Constructed Facilities. 23(2). https://doi.org/10.1061/(ASCE)0887-3828(2009)23:2(72)

Moradi, L.G., Dinan, R.J., Bewick, B.T., & Davidson, J.S. (2011). Resistance of Concrete Masonry Walls with Membrane Catcher Systems Subjected to Blast Loading. International Journal of Protective Structures, 2(1), 83-102.

Myers, J.J., Abdeldjelil. B., & Khaled, A. E. (2004). Blast Resistance of FRP Retrofitted Un-Reinforced Masonry (URM) Walls with and without Arching Action. The Masonry Society Journal, 9-26.

National Research Council (NRC). (1995). Protecting Buildings for Bomb Damage: Transfer of Blast-Effects Mitigation Technologies from Military to Civilian Applications. Washington D.C.: National Academy Press.

Ngo, T., Mendis. P., Gupta. A., & Ramsay, J. (2007). Blast Loading and Blast Effects on Structures: An Overview. EJSE Special Issue: Loading on Structures: 76-91.

Noor-E-Khuda. S., Dhanasekar. M., & Thambiratnam. P. D. (2016). An explicit finite element modeling method for masonry walls under out-of-plane loading. Engineering Structures, 113, 103-120. https://doi.org/10.1016/j.engstruct.2016.01.026

Panto, B., Raka, E., Cannizzaro, F., Camata, G., Caddemi, S., Spacone, E., & Calio, I. (2015). Numerical Macro-Modeling of Unreinforced Masonry Structures: A Critical Appraisal. Proceedings of the Fifteenth International Conference on Civil, Structural and Environmental Engineering Computing, Civil-Comp Press, Stirlingshire, Scotland.

Prem, P. B., Maneek, K., & Kaushik, S.K. (2008). Effect of Wire Mesh Orientation on Strength of Beams Retrofitted using Ferrocement Jackets. International Journal of Engineering, 20.

Rosen, B.V. (2013). Modeling History Masonry with Single-Degree-Of-Freedom (DRDC CSS CR 2013-044). Defence Research and Development Canada-CSS.

Salim, H., Dinan, R., & Townsend, P.T. (2005). Analysis and Experimental Evaluation of In-Fill Steel-Stud Wall Systems under Blast Loading. Journal of Structural Engineering, 131(8). https://doi.org/10.1061/(ASCE)0733-9445(2005)131:8(1216)

Salmanpour, A. H., Mojisilovic, N., & Joseph, S. (2012). Deformation Capacity of Structural Masonry: A Review of Theoretical Research. Proceedings, 15th World Conference on Earthquake Engineering, Lisbon, September 24-28, Paper No. WCEE2012-2145.

Sarva, S.S., Deschanel, S., Boyce. M.C., & Chen, W. N. (2007). Stress-Strain Behavior of a Polyurea and a Polyurethane from Low to High Strain Rates. Polymer, 48(8):2208-2213. http://dx.doi.org/10.1016/j.polymer.2007.02.058

Stone, H. & Engebretsen, J. (2001). The Basics of Blast Resistant Design. Proc. 70th Annual Convention, Structural Engineers Association of California. 87-94.

Terrorism through America's History. (2004). American History. <http://americanhistory.about.com/library/fastfacts/blffterrorism.htm>

Thango. G. S., Stavroulakis. G. E., & Drosopoulos. G. A. (2023). Investigation of the Failure Response of Masonry Walls subjected to Blast Loading using Nonlinear Finite Element Analysis. Computation, 11, 165. https://doi.org/10.3390/computation11080165

The Oklahoma City Bombing. (1996). CNN Interactive. <http:www.cnn.com/US/OKC/bombing.html>

Thornburg, D.L. (2004). "Evaluation of Elastomeric Polymer Used for External Reinforcement of Masonry Walls Subjected to Blast," MS Thesis, University of Alabama at Birmingham, Birmingham, AL.

UFC 3-340-02, (2008). "Structures to Resist the Effects of Accidental Explosions." Washington, DC, USA.

Tomazevic, M. (2008). Shear Resistance of Masonry Walls and Eurocode 6: Shear versus Tensile Strength of Masonry. Materials and Structures. DOI: 10.1617/s11527-008-9430-6

Tylek, I., & Kuchta, K (n.d). Mechanical Properties of Structural Stainless Steels. Civil Engineering Technical Transactions.

Vaghani, M., Vasanwala, S. A., & Desai, A.K. (2014). Stainless Steel as a Structural Material: State of Review. Int. Journal of Engineering Research and Applications, 4(3):657-662.

Yi, J., Boyce. M.C., Lee. G.F., & Balizer. E. (2006). Large deformation rate-dependent stress-strain behavior of polyurea and polyurethanes. Polymer, 47(1):319-29.

Youssef. G., & Gupta. V. (2012). Dynamic response of polyurea subjected to nanosecond rise-time stress waves. Mechanics of Time-Dependent Materials, 16(3):317-328. https://doi:10.1007/s11043-011-9164-7

Zapata, B.J., & Weggel, D.C. (2008). Collapse Study of an Unreinforced Masonry Bearing Wall Building subjected to Internal Blast Loading. Journal of Performance of Constructed Facilities, 22(2). DOI: 10.1061/(ASCE)0887-3828(2008)22:2(92)

Zhao. J., W.G. Knauss. W.G., & Ravichandran. G. (2007). Applicability of the Time–Temperature Superposition Principle in Modeling Dynamic Response of a Polyurea. Mech Time-Depend Mater 11:289-308. DOI 10.1007/s11043-008-9048

APPENDIX A. RC-BLAST SDOF ANALYSIS FOR NON-LOAD BEARING RETROFITTED WALLS

A.1 Wall-1

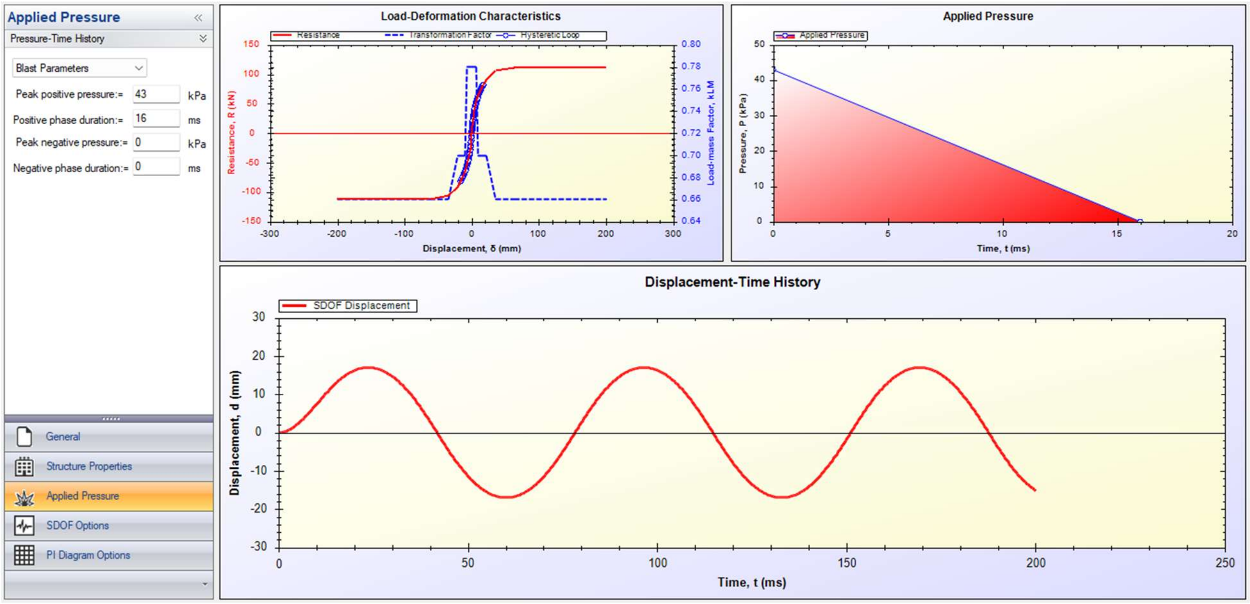

Figure A-1. Wall-1-1 readings

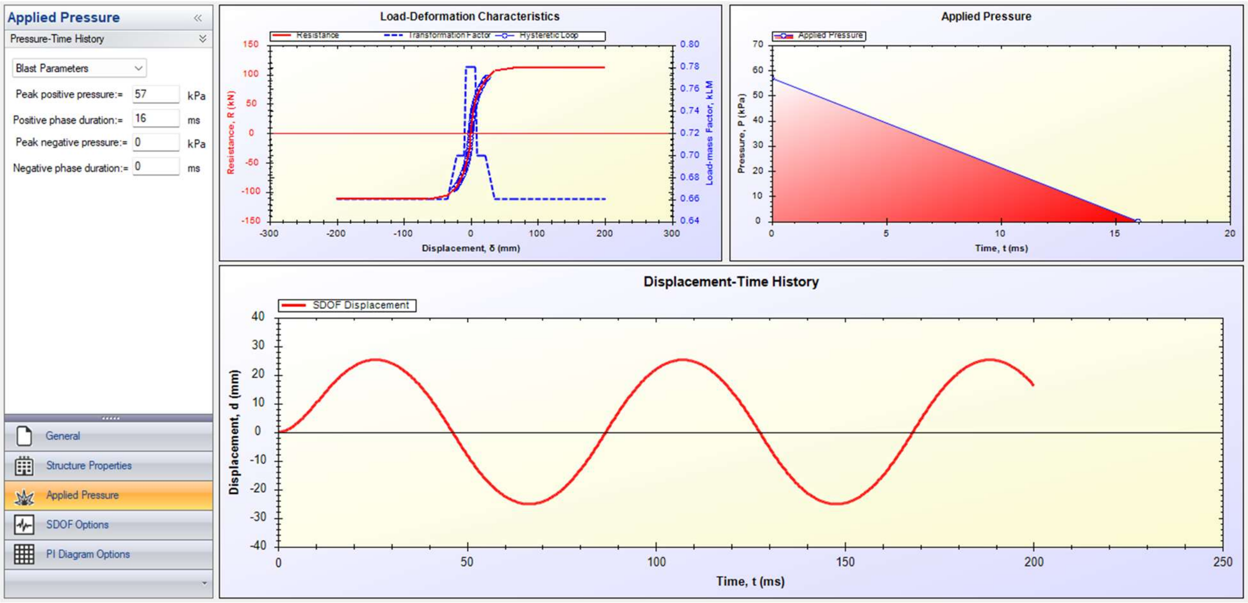

Figure A-2. Wall-1-2 readings

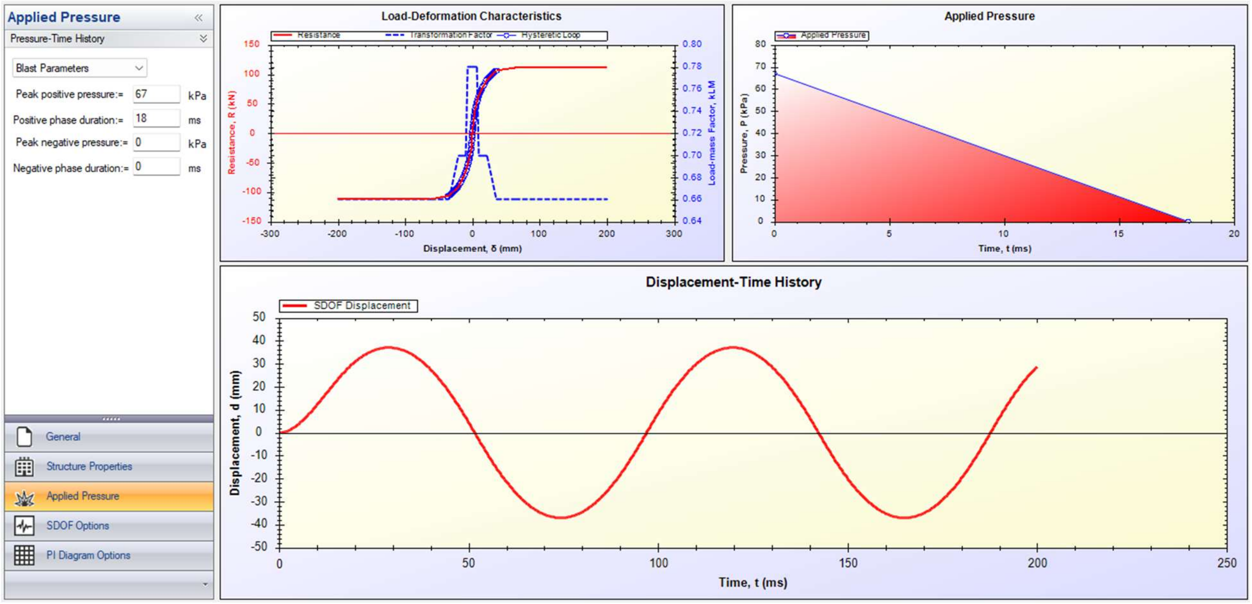

Figure A-3. Wall-1-3 readings

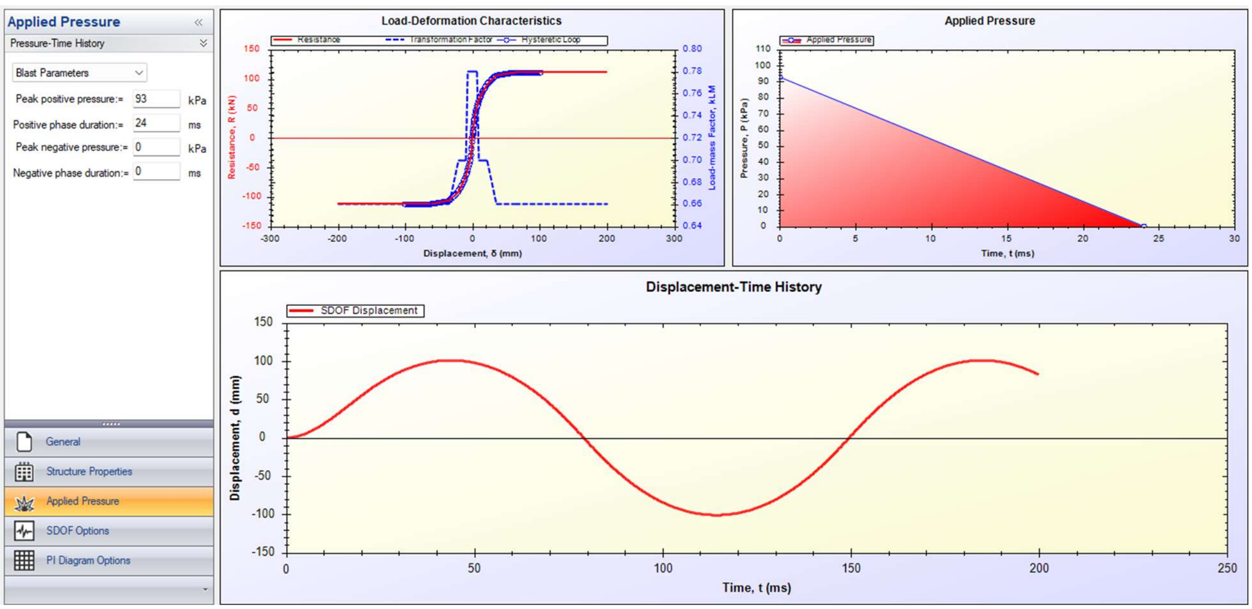

Figure A-4. Wall-1-4 readings

A.2 Wall-2

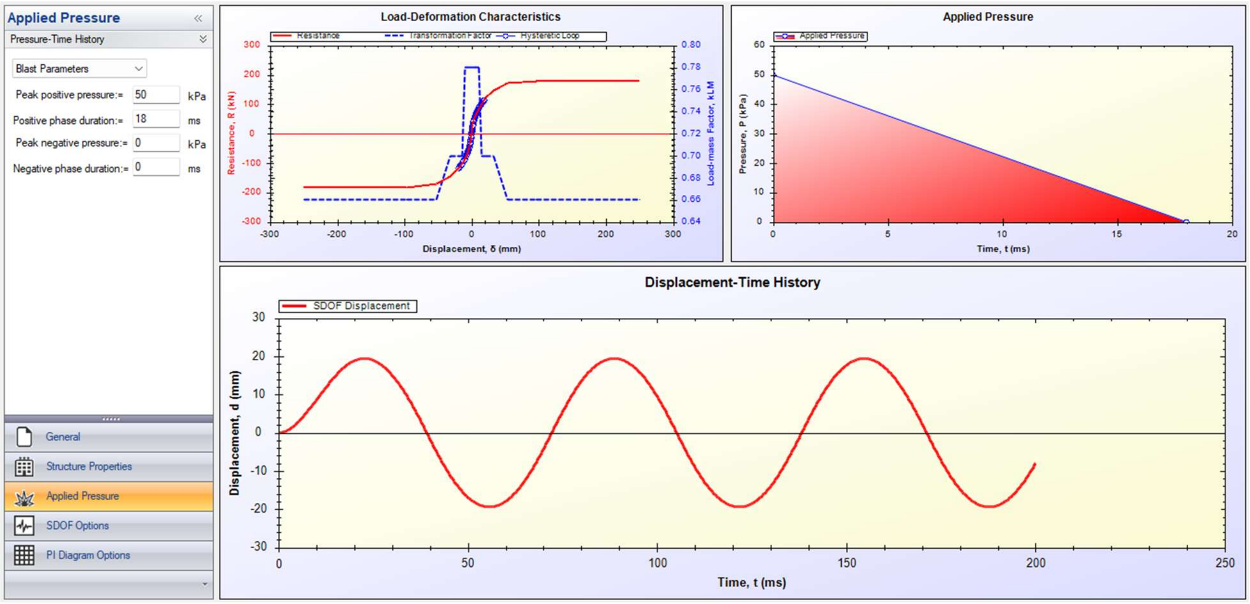

Figure A-5. Wall-2-1 readings

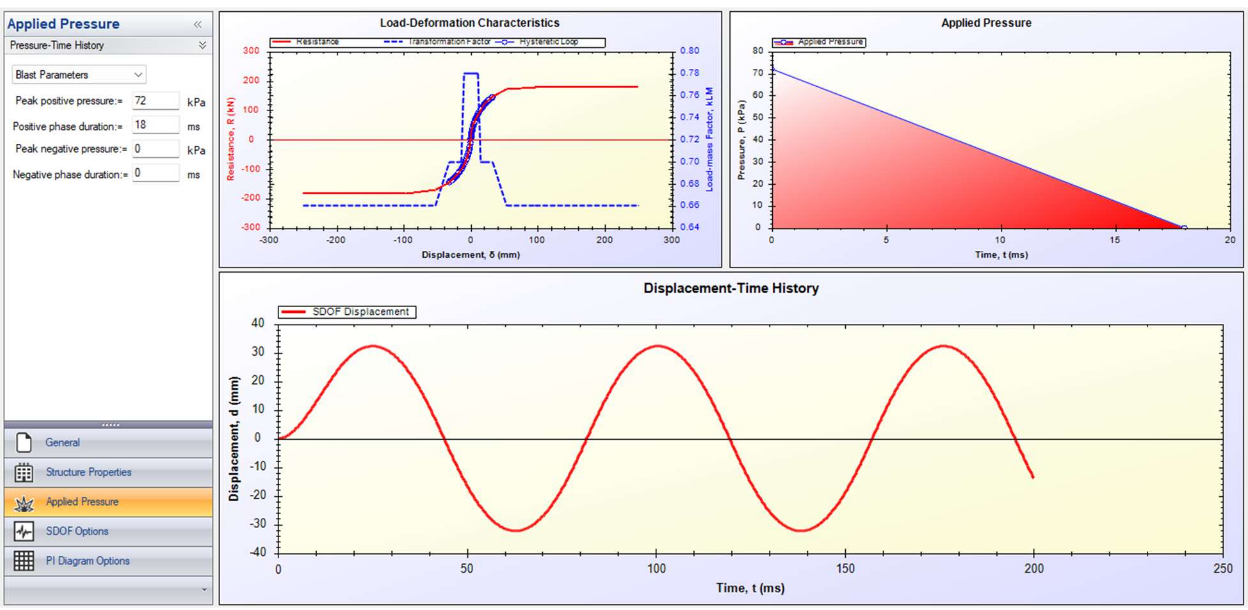

Figure A-6. Wall-2-2 readings

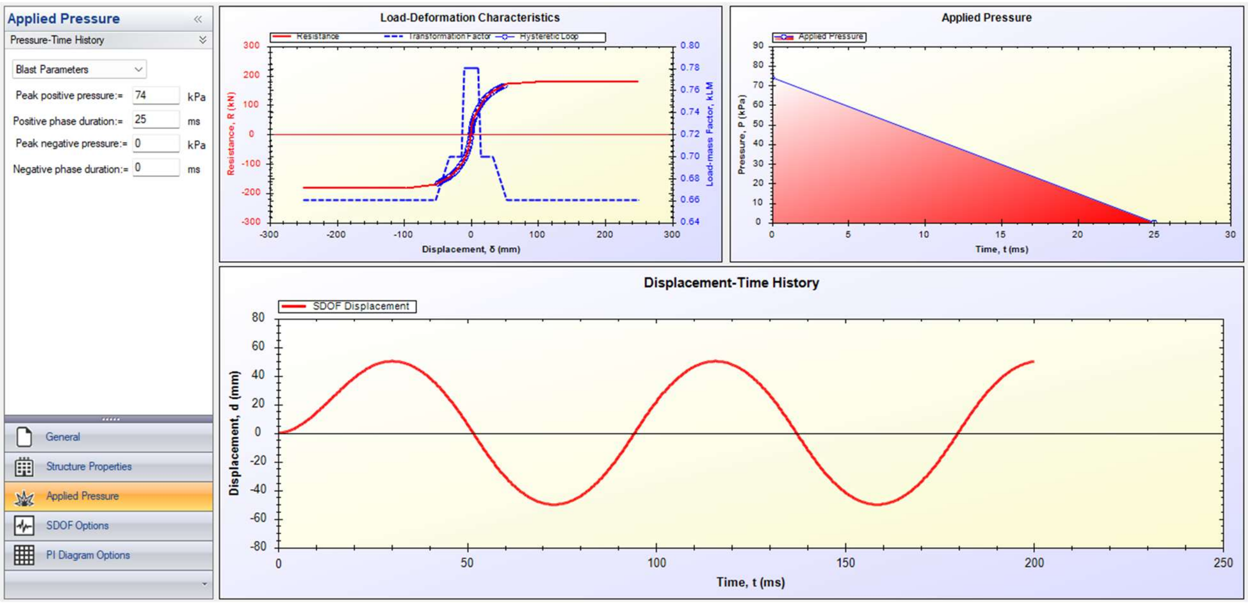

Figure A-7. Wall-2-3 readings

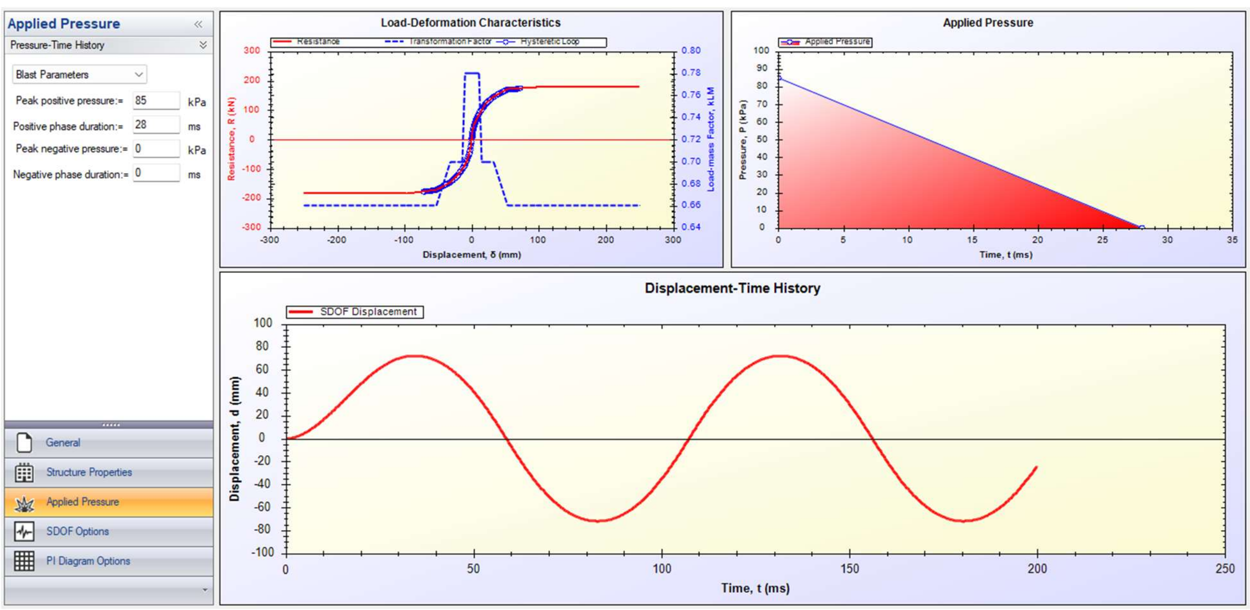

Figure A-8. Wall-2-4 readings

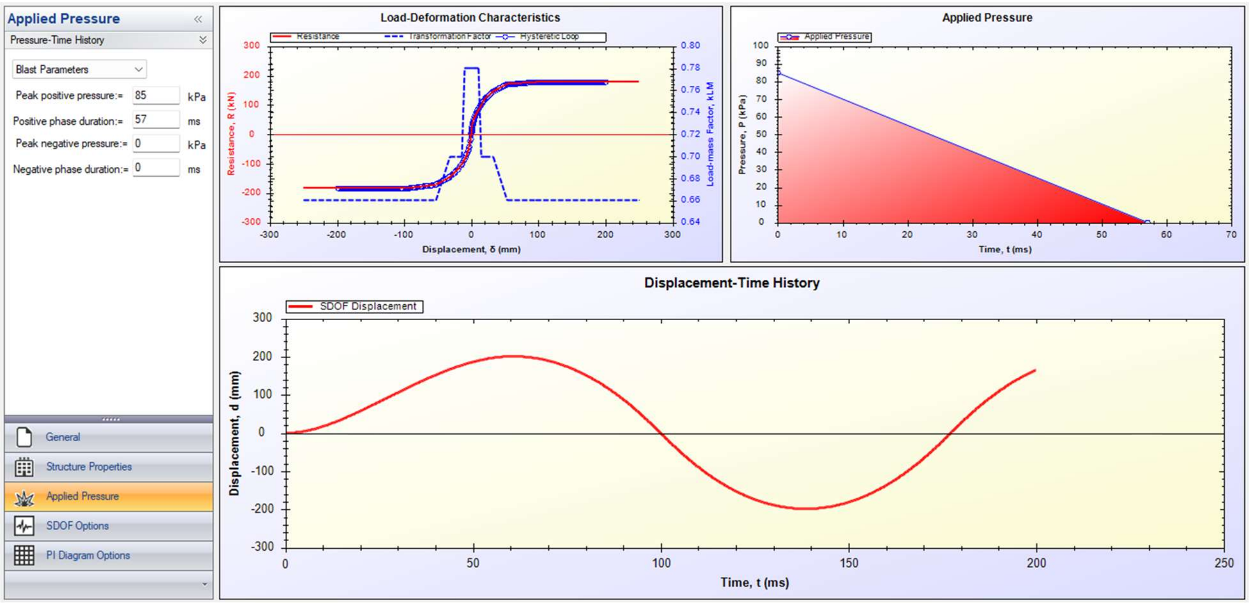

Figure A-9. Wall-2-5 readings

A.3 Wall-3

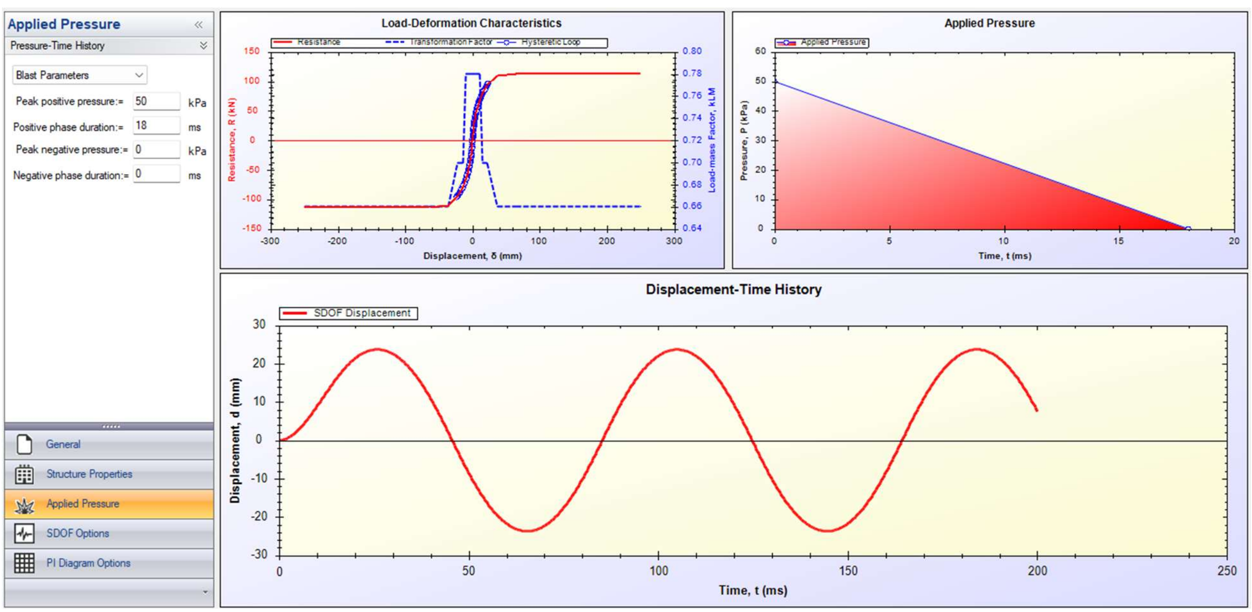

Figure A-10. Wall-3-1 readings

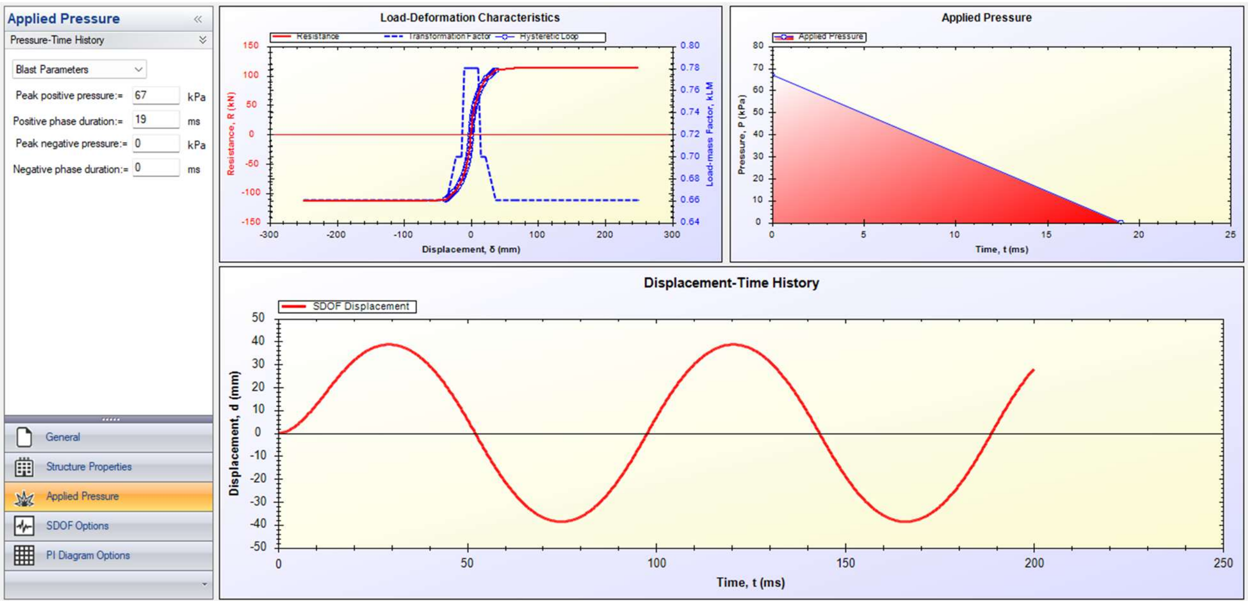

Figure A-11. Wall-3-2 readings

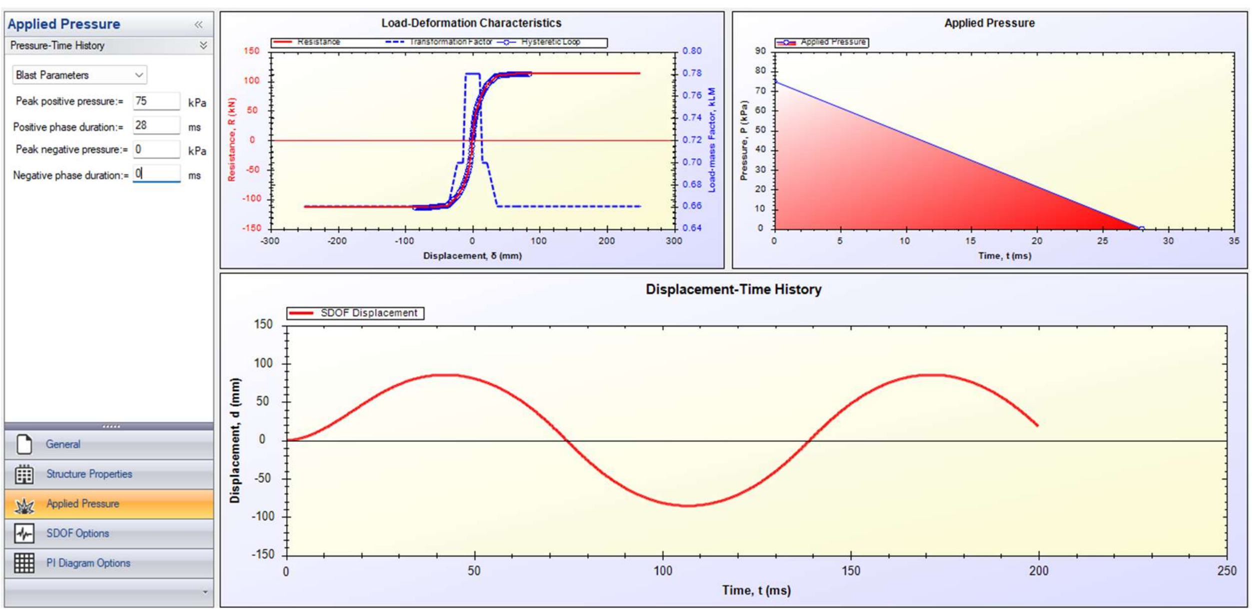

Figure A-12. Wall-3-3 readings

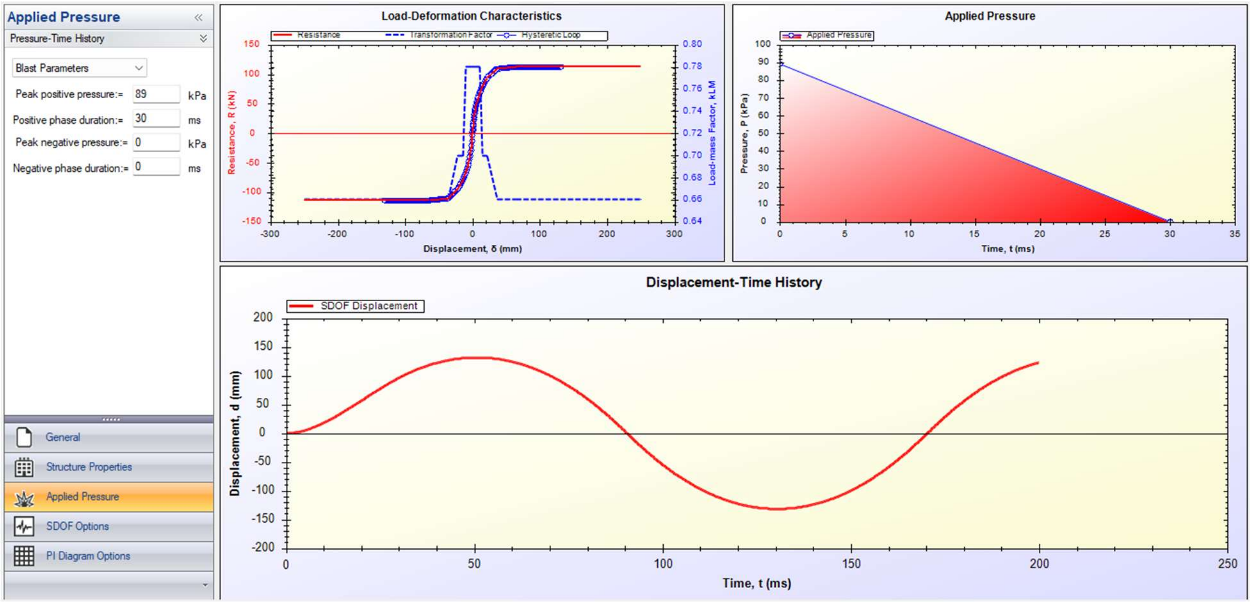

Figure A-13. Wall-3-4 readings

APPENDIX B. RC-BLAST SDOF ANALYSIS FOR LOAD BEARING RETROFITTED WALLS

B.1 Wall-4

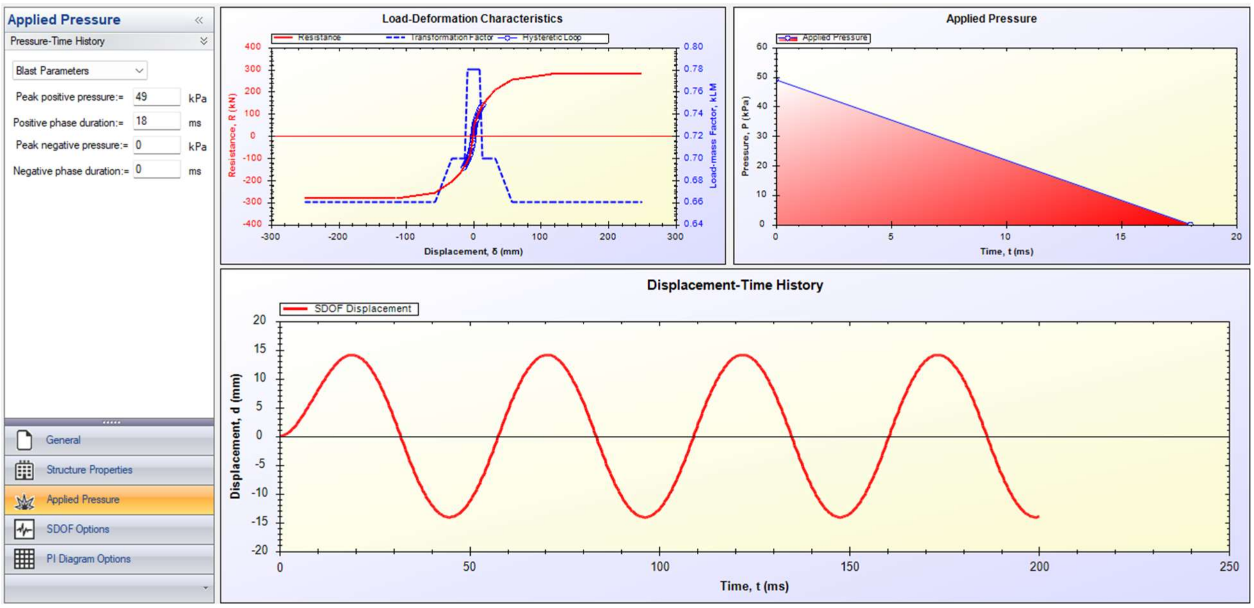

Figure B-1. Wall-4-1 readings

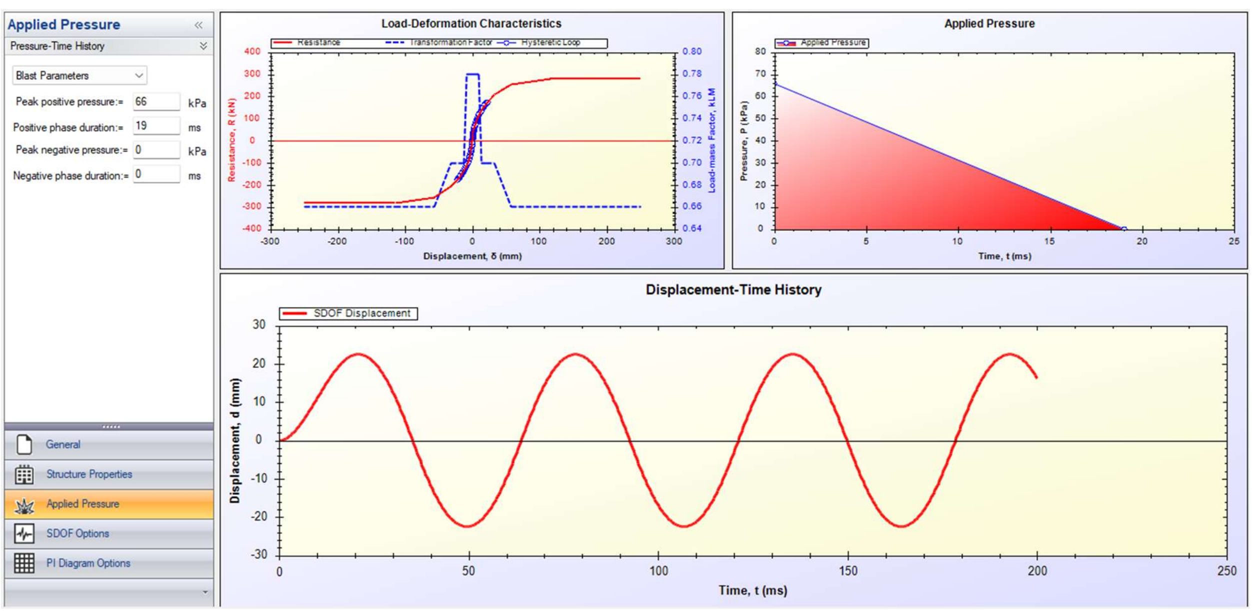

Figure B-2. Wall-4-2 readings

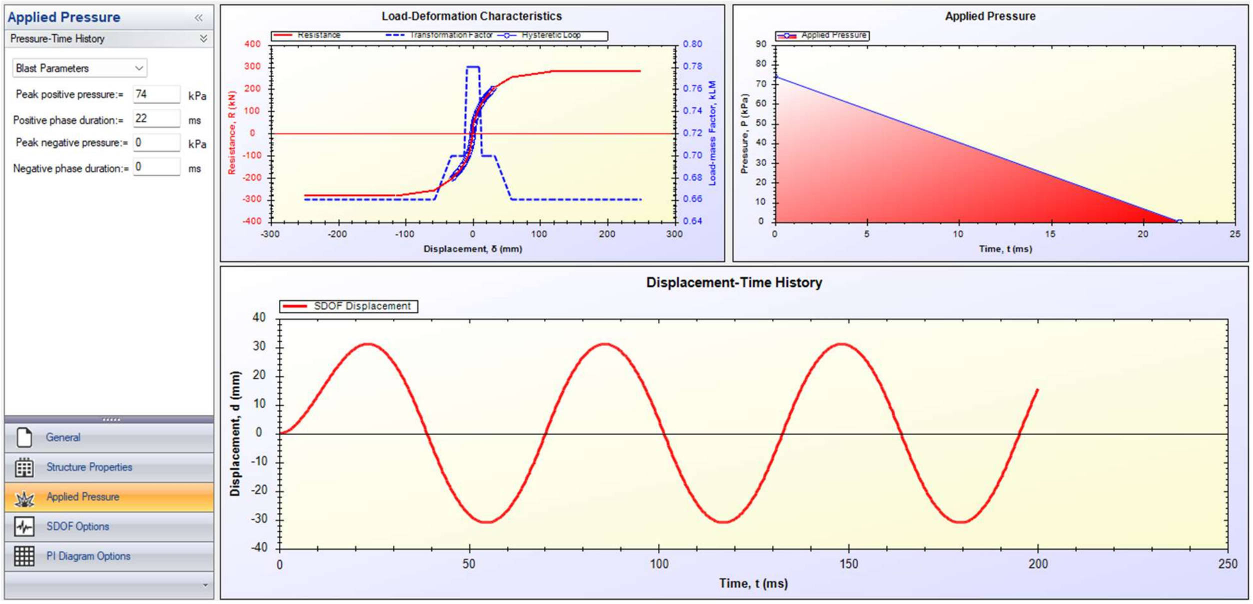

Figure B-3. Wall-4-3 readings

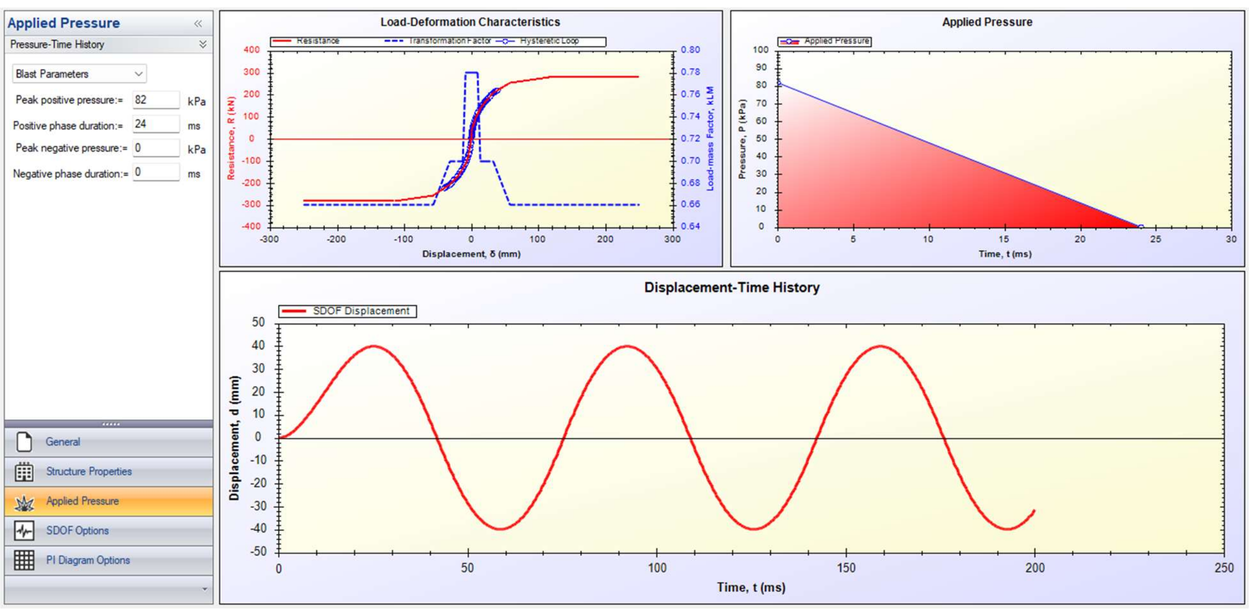

Figure B-4. Wall-4-4 readings

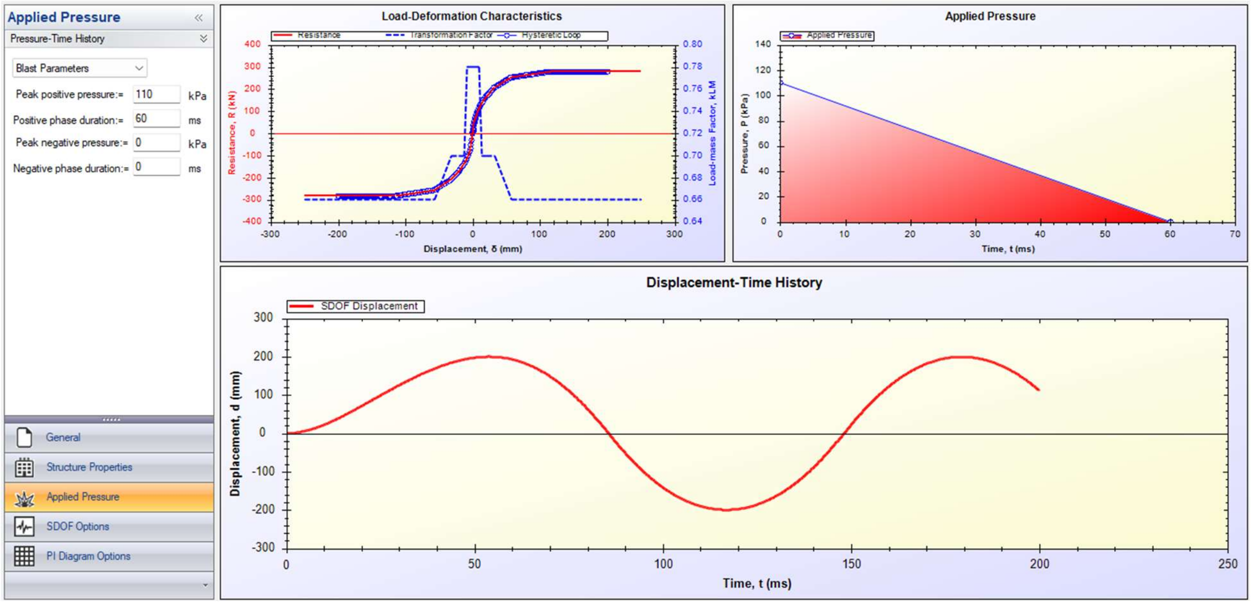

Figure B-5. Wall 4-5 readings

B.2 Wall-5

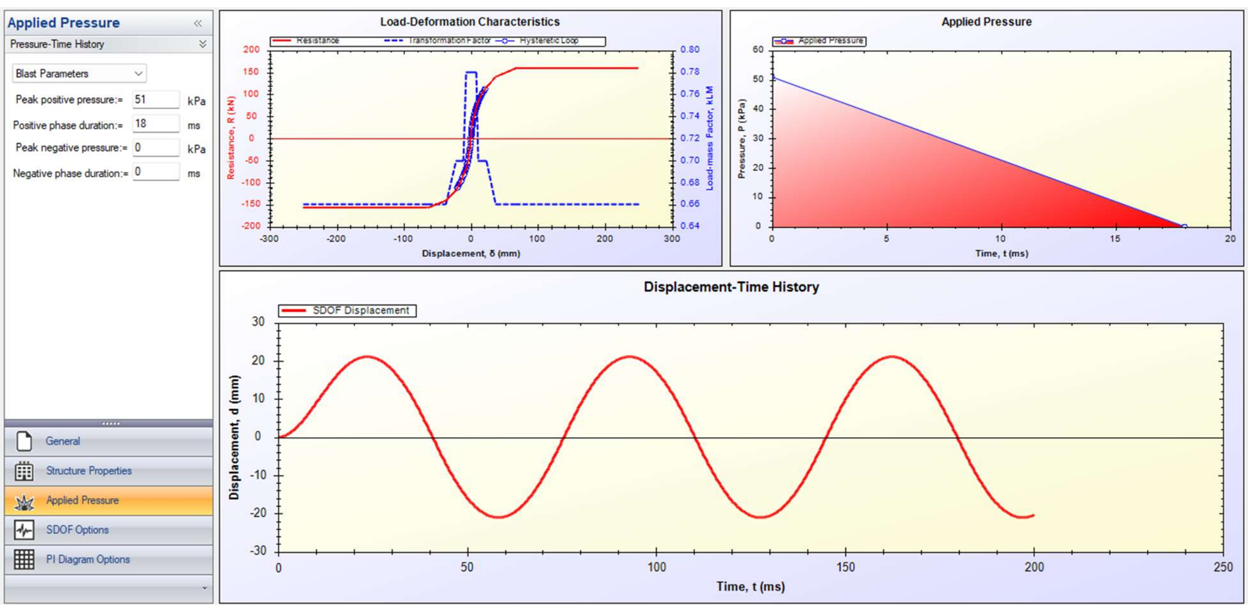

Figure B-6. Wall-5-1 readings

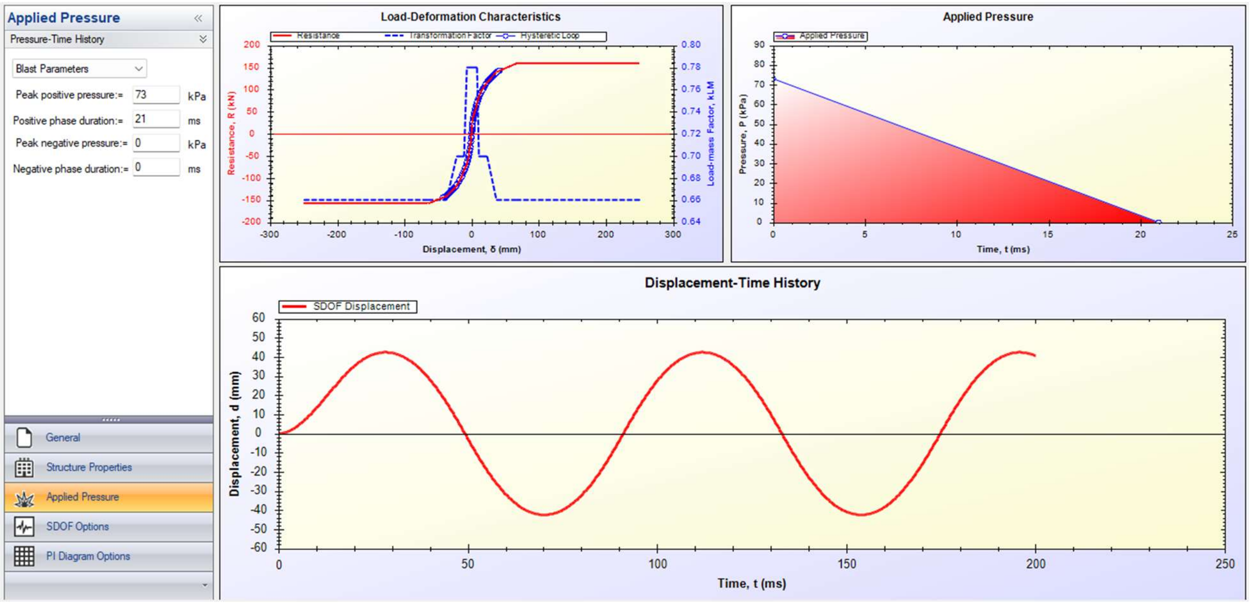

Figure B-7. Wall-5-2 readings

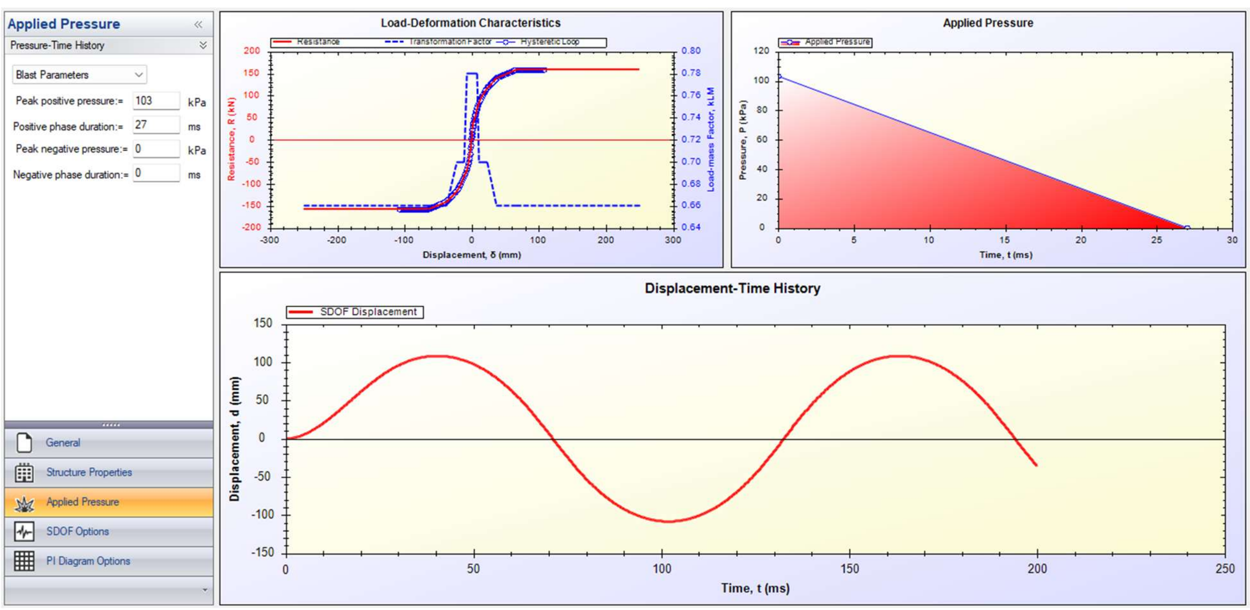

Figure B-8. Wall-5-3 readings

B.3 Wall-6

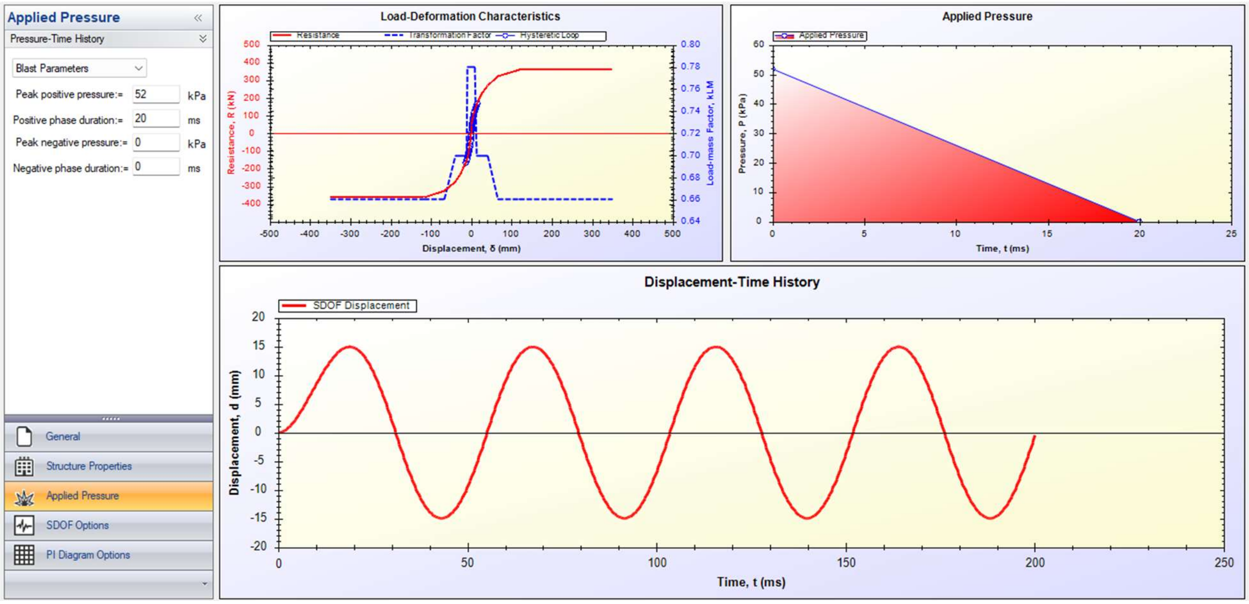

Figure B-9. Wall-6-1 readings

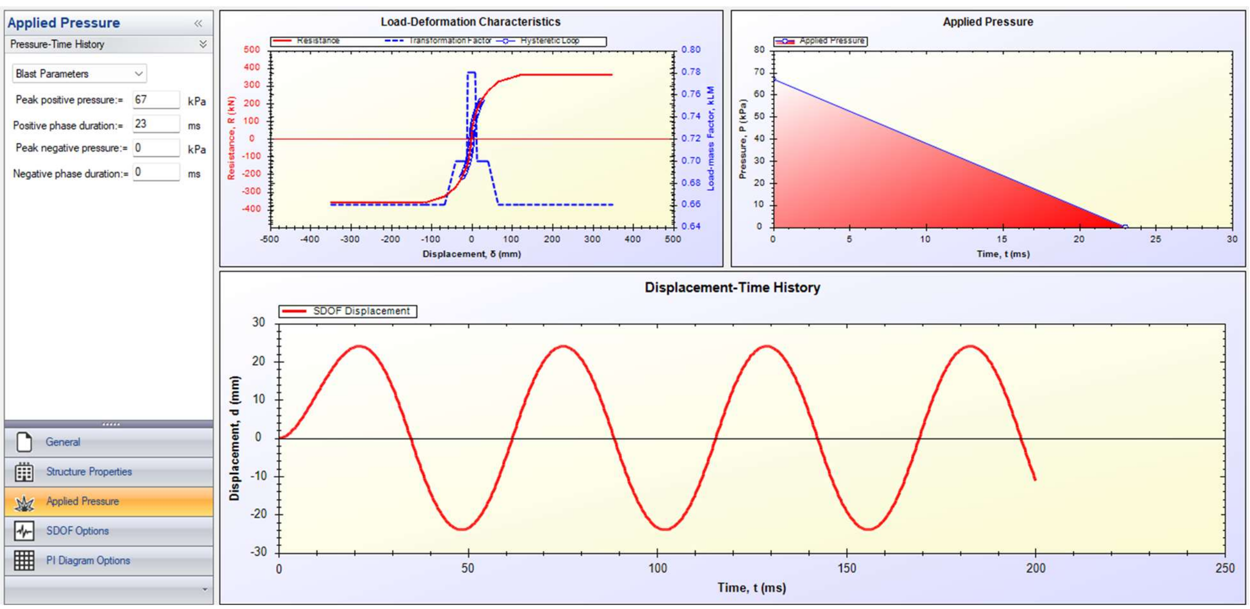

Figure B-10. Wall-6-2 readings

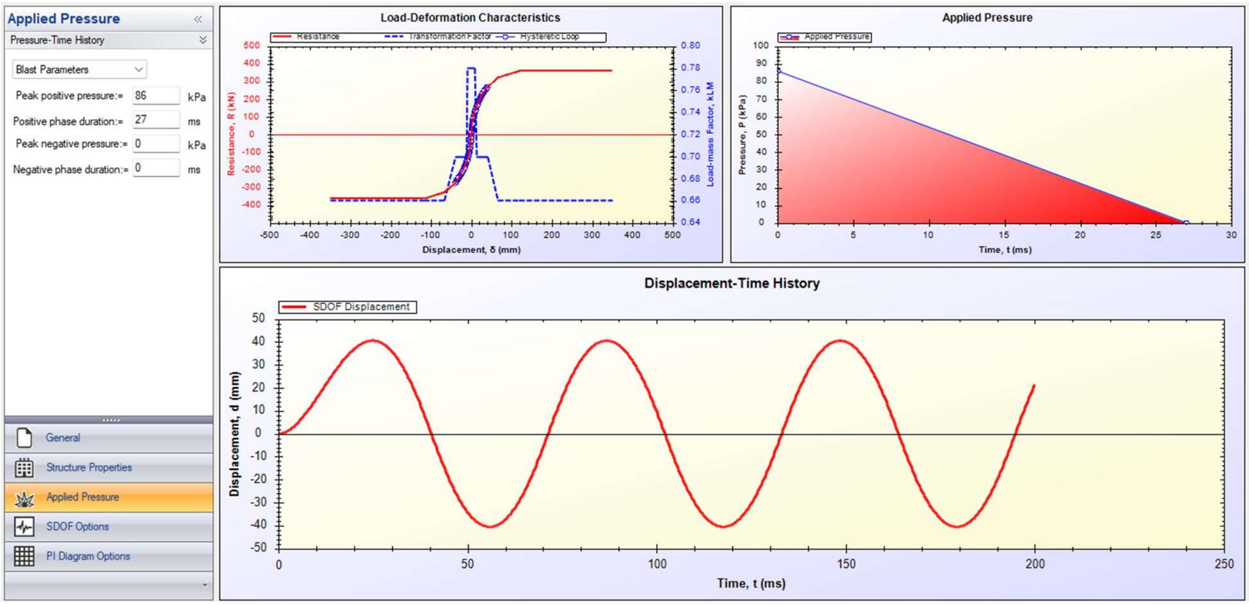

Figure B-11. Wall-6-3 readings

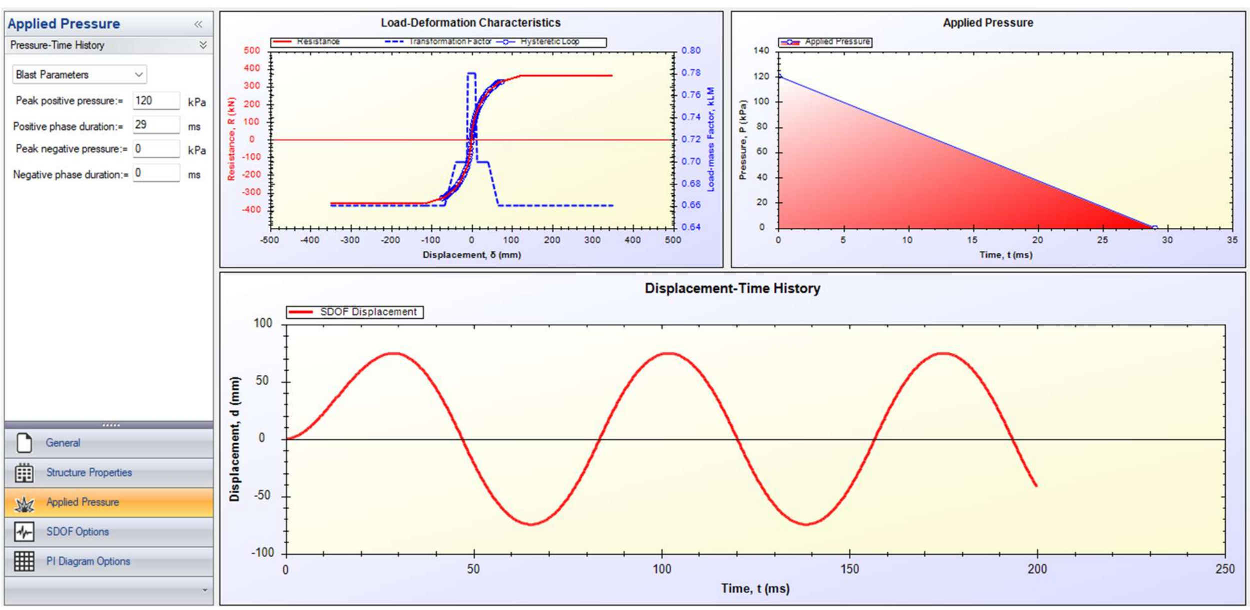

Figure B-12. Wall-6-4 readings

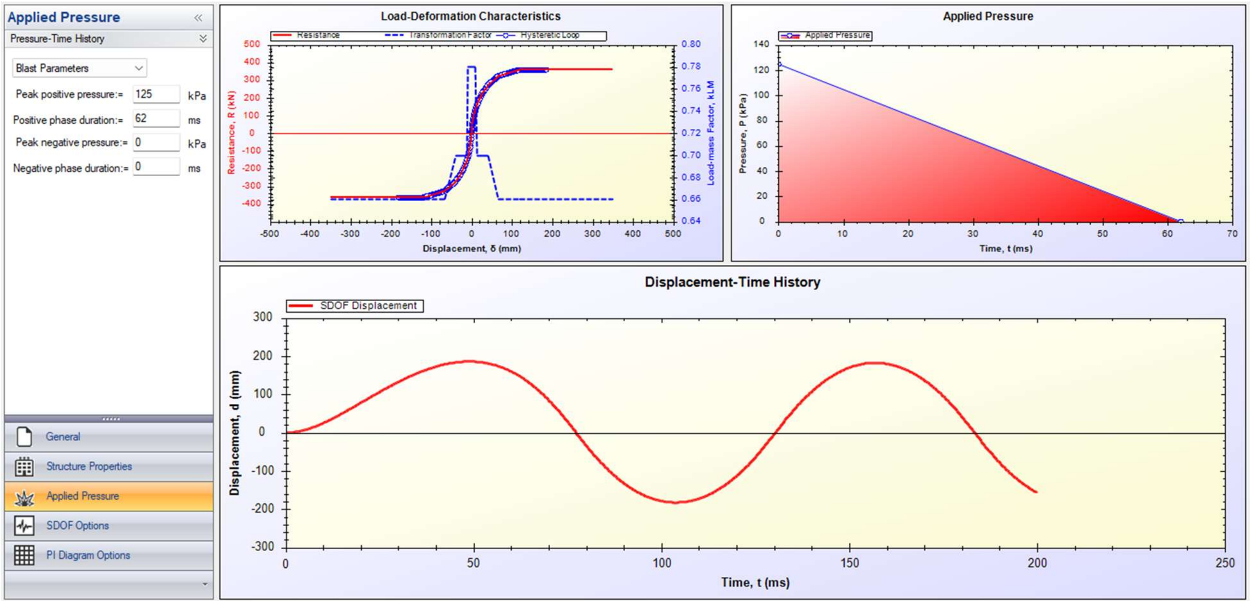

Figure B-13. Wall-6-5 readings

APPENDIX C: PARAMETRIC STUDIES

C.1 RC Blast SDOF Analysis of Increase in Stainless Steel Percentage

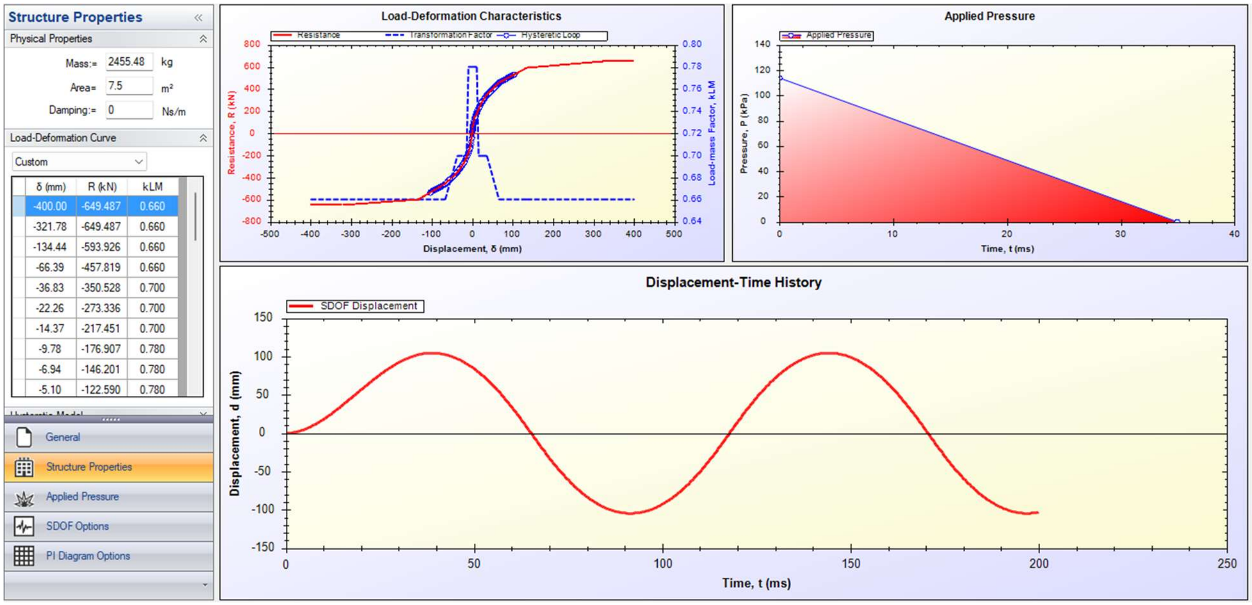

Figure C-1. RC blast sdof analysis on stainless steel percentage at 4.1mm strand diameter

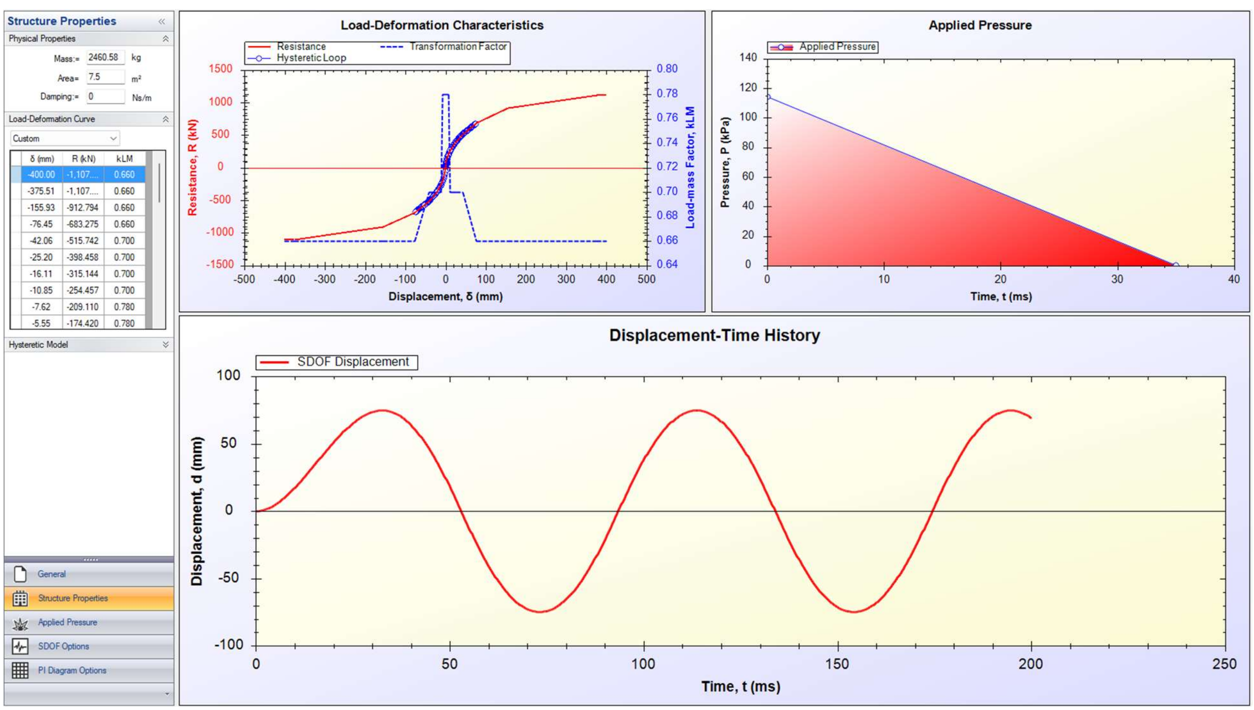

Figure C-2. RC blast sdof analysis on stainless steel percentage at 5.1mm strand diameter

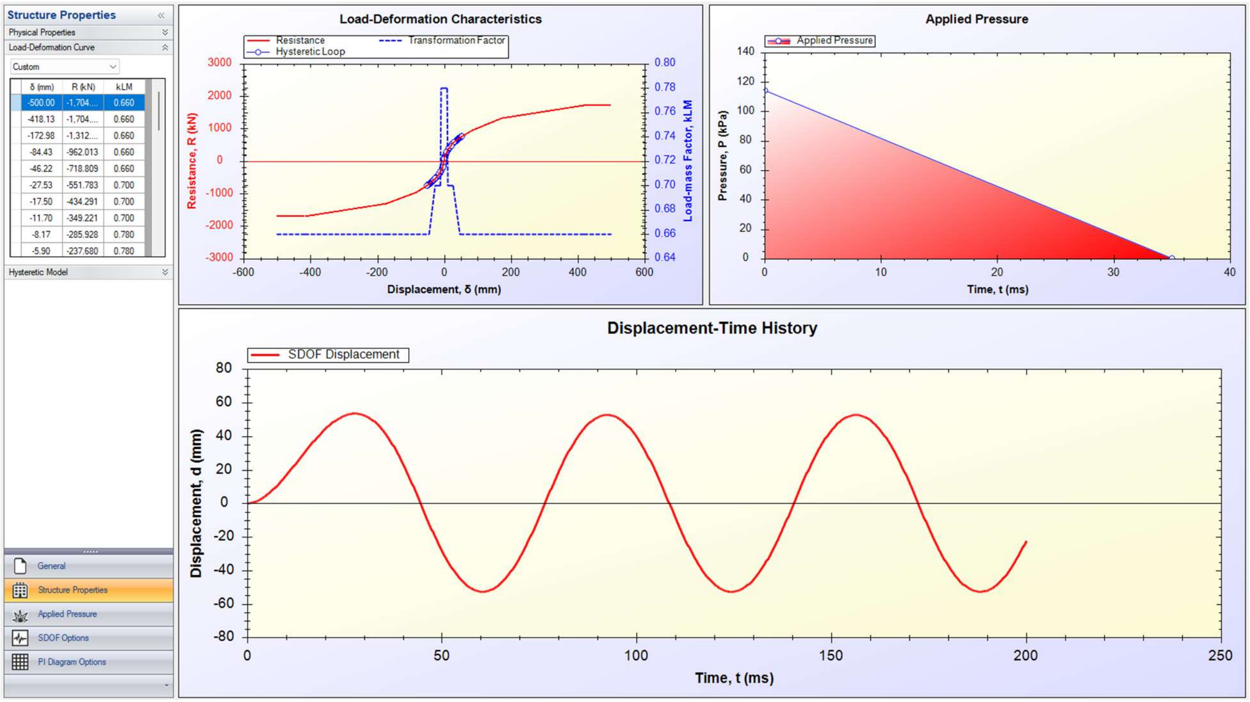

Figure C-3. RC blast sdof analysis on stainless steel percentage at 6.1mm strand diameter

C.2 RC Blast SDOF Analysis of Varied Wall Thickness

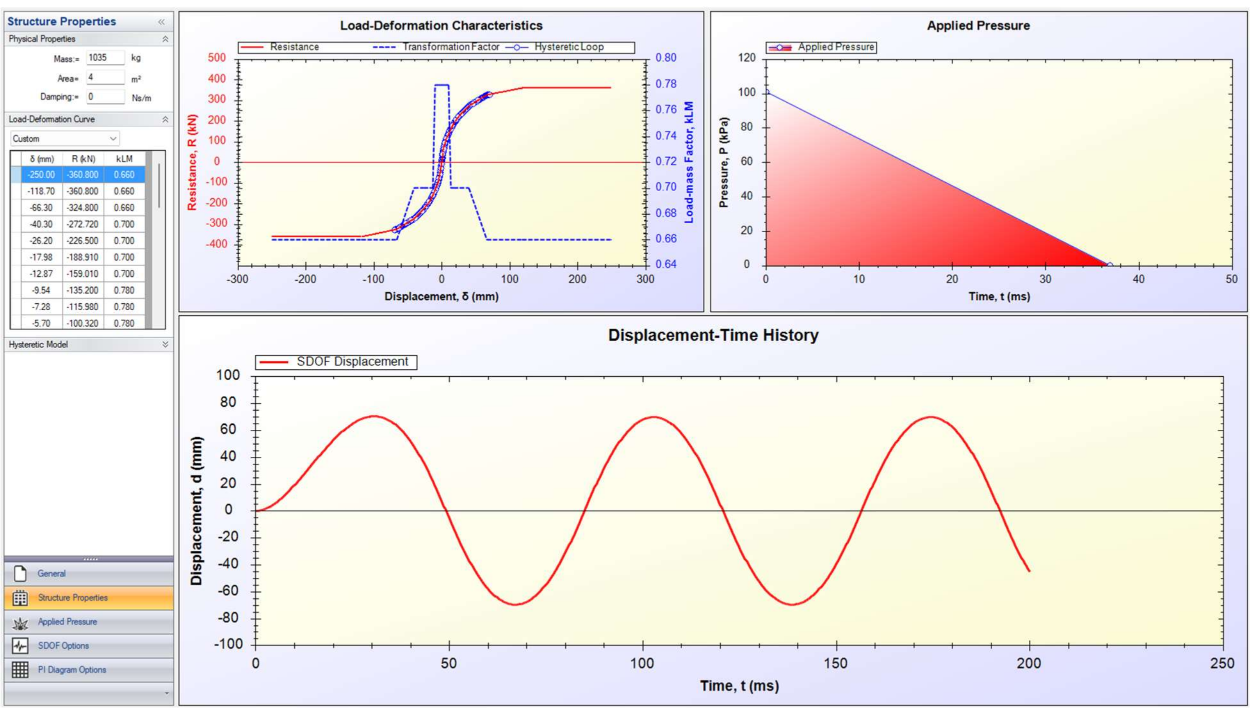

Figure C-4. RC blast sdof analysis on wall thickness of 90mm

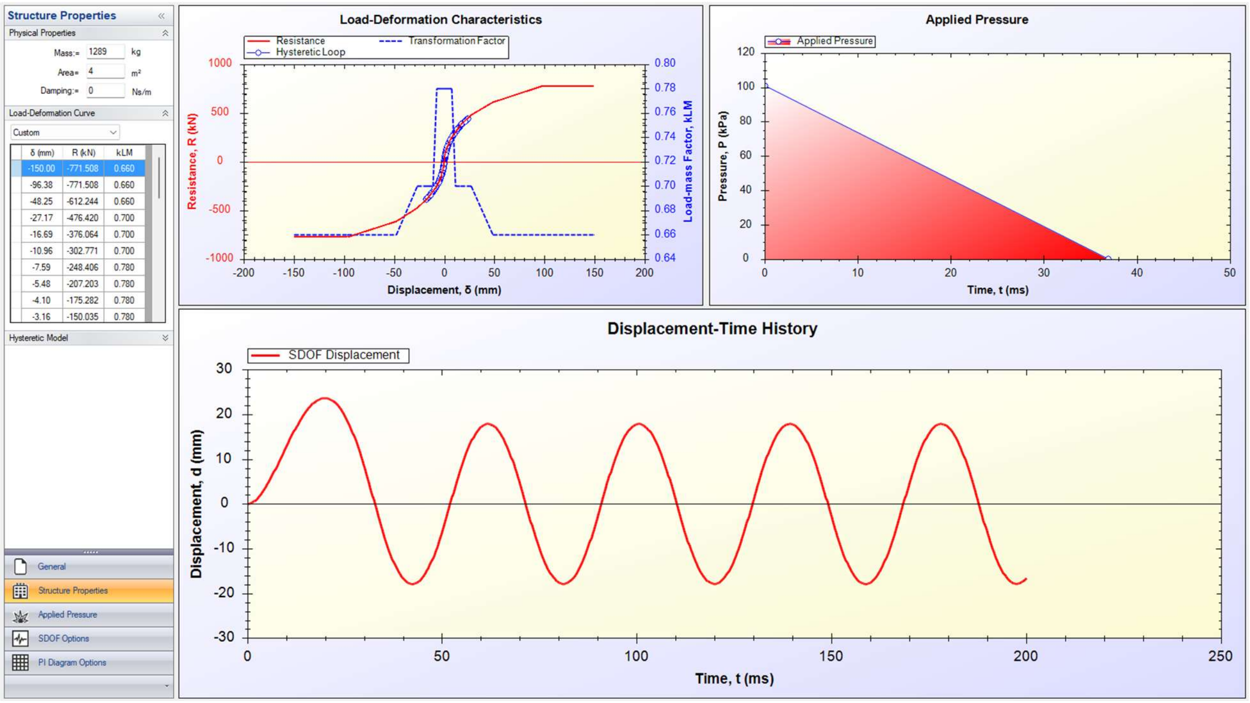

Figure C-5. RC blast sdof analysis on wall thickness of 140mm

C.3 RC Blast SDOF Analysis of Varied Wall Aspect Ratio

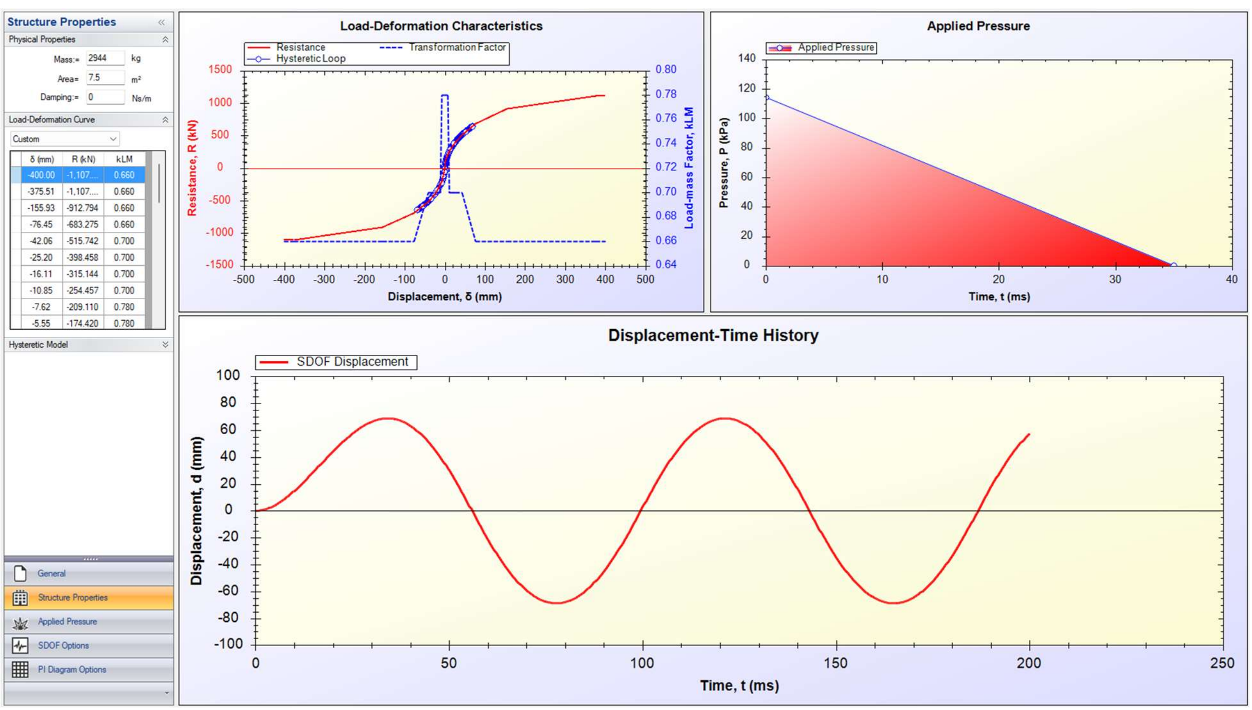

Figure C-6. RC blast sdof analysis on the wall aspect ratio of 1.2

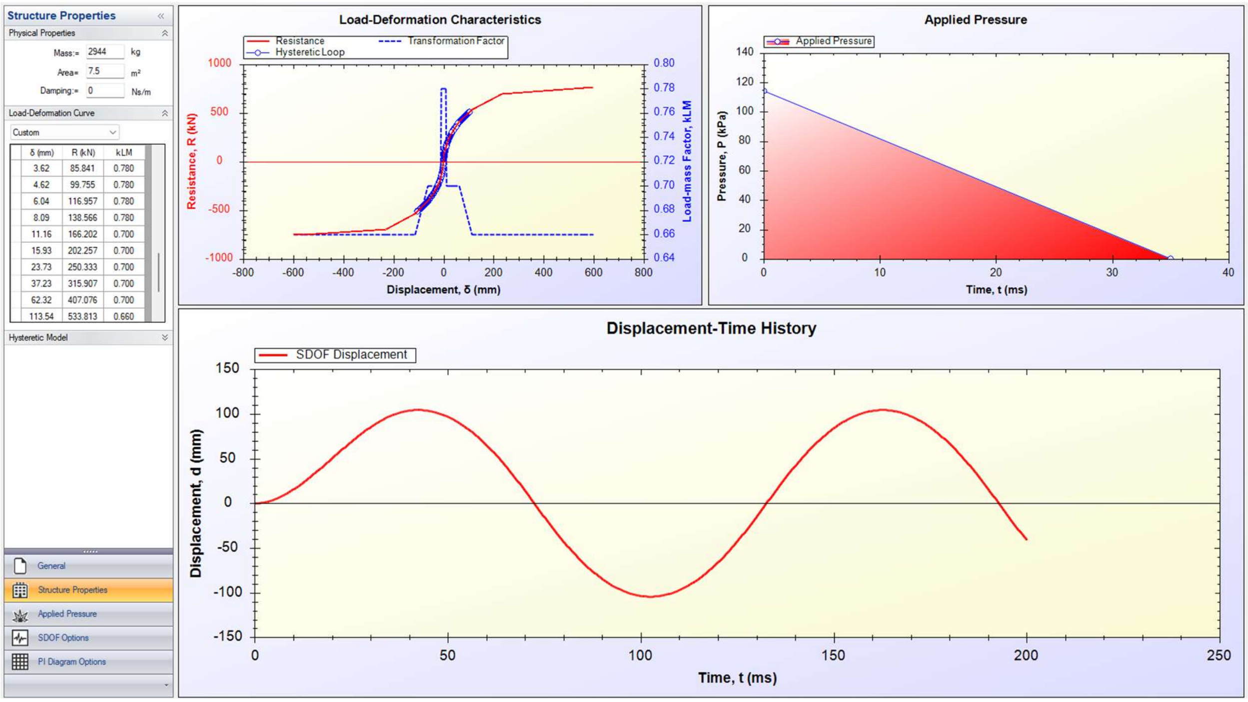

Figure C-7. RC blast sdof analysis on the wall aspect ratio of 0.8

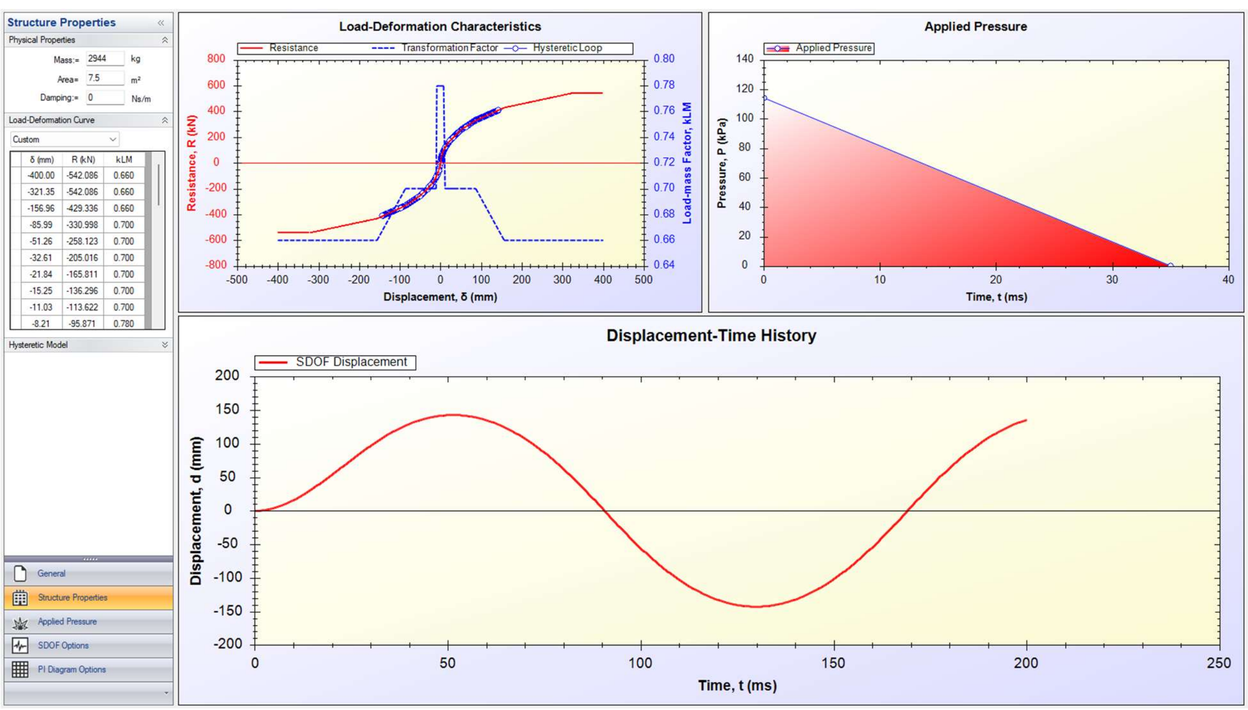

Figure C-8. RC blast sdof analysis on the wall aspect ratio of 0.6

C.4 RC Blast SDOF Analysis of Varied Axial Loading

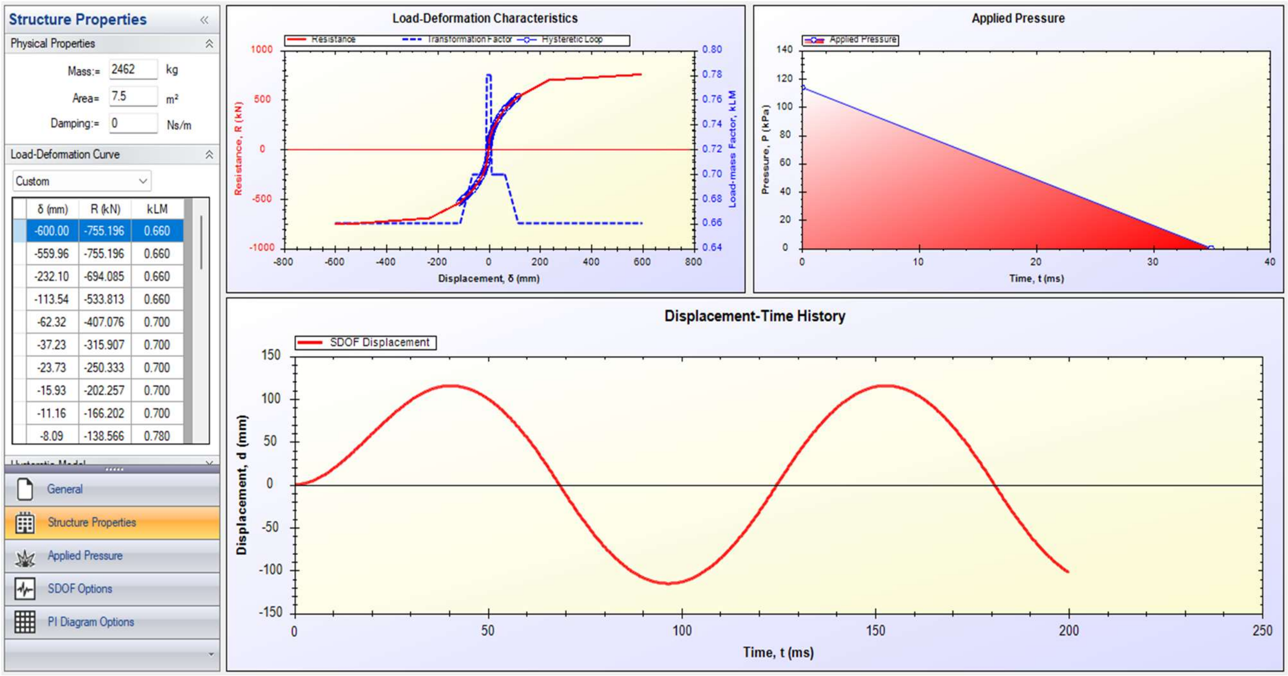

Figure C-9. RC blast sdof analysis of wall with axial load 120 kN

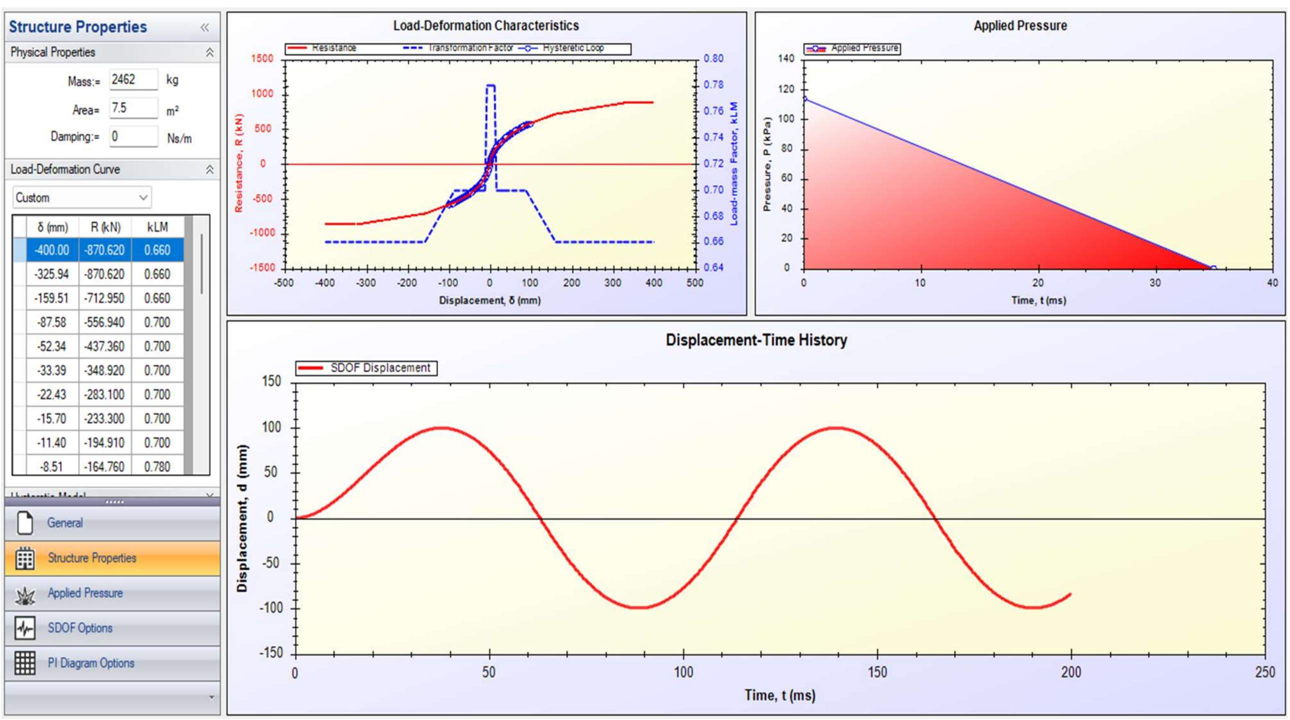

Figure C-10. RC blast sdof analysis of wall with axial load 180 kN

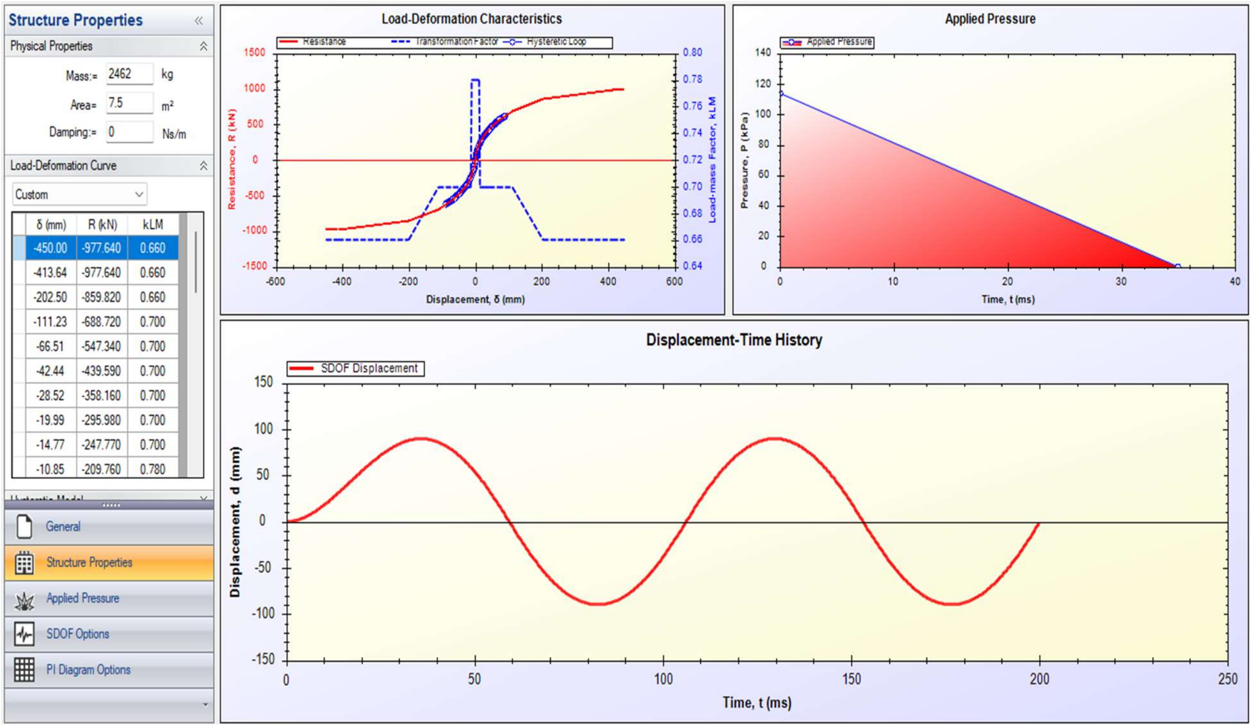

Figure C-11. RC blast sdof analysis of wall with axial load 240 kN